



ATLAS Note

GROUP-2017-XX



4th May 2021

Draft version 0.1

1

2

3

4

5

6

**A Deep Learning Approach to Differential
Measurements of Higgs - Top Interactions in
Multilepton Final States using the ATLAS
Detector at the LHC**

The ATLAS Collaboration

7 Several theories Beyond the Standard Model predict a modification of the momentum spec-
8 trum of the Higgs Boson, without a significantly altered rate of Higgs produced in association
9 with top quark pairs ($t\bar{t}H$). This provides a physical observable that can be used to search
10 for new physics based on data collected by the LHC. This thesis presents techniques and
11 preliminary results for a differential measurement of the Higgs transverse momentum in $t\bar{t}H$
12 events with multiple leptons in the final state, using data collected at an energy of $\sqrt{s} = 13$
13 TeV by the ATLAS detector at the LHC.

14 This thesis also details a measurement of $WZ +$ heavy flavor production, a significant back-
15 ground to $t\bar{t}H$ that is poorly understood. This study targets events with three leptons and one
16 or two jets in the final state, using 140 fb^{-1} of $\sqrt{s} = 13 \text{ TeV}$ data. A measured cross-section
17 of $X \pm X \text{ fb}$ ($X \pm X \text{ fb}$) is observed for $WZ + b$ ($WZ + \text{charm}$) with 1 associated jet and $X \pm X$
18 fb ($X \pm X \text{ fb}$) for $WZ + b$ ($WZ + \text{charm}$) with 2 assoicated jets.

19 Because of the challenges inherent in reconstructing the Higgs in multilepton final states, a
20 deep learning approach is used to predict the momentum spectrum of the Higgs for these
21 events. The regressed Higgs p_T spectrum is fit to data for events with two same-sign leptons
22 or three leptons in the final state. The fit is used to extract normalization factors for high
23 ($p_T(H) > 150 \text{ GeV}$) and low ($p_T(H) < 150 \text{ GeV}$) momentum $t\bar{t}H$ events. Preliminary
24 results are presented for 80 fb^{-1} of data, with projected results shown for 140 fb^{-1} .

© 2021 CERN for the benefit of the ATLAS Collaboration.

25 Reproduction of this article or parts of it is allowed as specified in the CC-BY-4.0 license.

26 **Contents**

27	I Introduction	7
28	1 Introduction	7
29	II Theoretical Motivation	10
30	2 The Standard Model and the Higgs Boson	10
31	2.1 The Forces and Particles of the Standard Model	10
32	2.2 The Higgs Mechanism	13
33	2.2.1 The Higgs Field	13
34	2.2.2 Electroweak Symmetry Breaking	15
35	2.3 $t\bar{t}H$ Production	18
36	2.4 WZ + Heavy Flavor Production	21
37	2.5 Extensions to the Standard Model	22
38	III The LHC and the ATLAS Detector	27
39	3 The LHC	27
40	4 The ATLAS Detector	30
41	4.1 Inner Detector	31
42	4.2 Calorimeters	32
43	4.3 Muon Spectrometer	33
44	4.4 Trigger System	34
45	IV Measurement of WZ + Heavy Flavor	36
46	5 Introduction	36
47	6 Data and Monte Carlo Samples	37
48	6.1 Data Samples	37
49	6.2 Monte Carlo Samples	38
50	7 Object Reconstruction	39
51	7.1 Light leptons	39
52	7.2 Jets	40
53	7.3 B-tagged Jets	41
54	7.4 Missing transverse energy	42
55	7.5 Overlap removal	43

56	8 Event Selection and Signal Region Definitions	43
57	8.1 Event Preselection	44
58	8.2 Fit Regions	46
59	8.3 Non-Prompt Lepton Estimation	48
60	8.3.1 $t\bar{t}$ Validation	48
61	8.3.2 Z+jets Validation	49
62	9 tZ Interference Studies and Separation Multivariate Analysis	50
63	10 Data and Monte Carlo Samples	54
64	10.1 Data Samples	54
65	10.2 Monte Carlo Samples	54
66	11 Object Reconstruction	55
67	11.1 Light leptons	56
68	11.2 Jets	57
69	11.3 B-tagged Jets	57
70	11.4 Missing transverse energy	59
71	11.5 Overlap removal	59
72	12 Event Selection and Signal Region Definitions	60
73	12.1 Event Preselection	60
74	12.2 Fit Regions	63
75	12.3 Non-Prompt Lepton Estimation	64
76	12.3.1 $t\bar{t}$ Validation	65
77	12.3.2 Z+jets Validation	66
78	13 tZ Interference Studies and Separation Multivariate Analysis	66
79	14 Systematic Uncertainties	70
80	15 Results	74
81	15.1 1-jet Fit Results	75
82	15.2 2-jet Fit Results	84
83	V Differential Studies of $t\bar{t}H$ Multilepton	93
84	16 Data and Monte Carlo Samples	93
85	16.1 Data Samples	94
86	16.2 Monte Carlo Samples	94
87	17 Object Reconstruction	98
88	17.1 Trigger Requirements	98
89	17.2 Light Leptons	99

90	17.3 Jets	100
91	17.4 B-tagged Jets	100
92	17.5 Missing Transverse Energy	101
93	17.6 Overlap removal	101
94	18 Higgs Momentum Reconstruction	102
95	18.1 Physics Object Truth Matching	104
96	18.2 Truth Level Studies	105
97	18.3 b-jet Identification	105
98	18.3.1 2lSS Channel	106
99	18.3.2 3l Channel	110
100	18.4 Higgs Reconstruction	113
101	18.4.1 2lSS Channel	114
102	18.4.2 3l Semi-leptonic Channel	118
103	18.4.3 3l Fully-leptonic Channel	122
104	18.5 p_T Prediction	126
105	18.5.1 2lSS Channel	127
106	18.5.2 3l Semi-leptonic Channel	130
107	18.5.3 3l Fully-leptonic Channel	134
108	18.6 3l Decay Mode	137
109	19 Signal Region Definitions	139
110	19.1 Pre-MVA Event Selection	140
111	19.2 Event MVA	145
112	19.3 Signal Region Definitions	154
113	20 Systematic Uncertainties	155
114	21 Results	162
115	21.1 Results - 79.8 fb^{-1}	163
116	21.2 Projected Results - 139 fb^{-1}	168
117	VI Conclusion	173
118	Appendices	180
119	.1 Non-prompt lepton MVA	180
120	.2 Non-prompt CR Modelling	185
121	.3 tZ Interference Studies	190
122	.4 Alternate tZ Inclusive Fit	194
123	.4.1 tZ Inclusive Fit	195
124	.4.2 Floating tZ	196
125	.5 DSID list	197

126	A Machine Learning Models	220
127	A.1 Higgs Reconstruction Model Details	220
128	A.1.1 b-jet Identification Features - 2lSS	220
129	A.1.2 b-jet Identification Features - 3l	224
130	A.1.3 Higgs Reconstruction Features - 2lSS	229
131	A.1.4 Higgs Reconstruction Features - 3lS	234
132	A.1.5 Higgs Reconstruction Features - 3lF	239
133	A.2 Background Rejection MVA Details	243
134	A.2.1 Background Rejection MVA Features - 2lSS	243
135	A.2.2 Background Rejection MVA Features - 3l	247
136	A.3 Truth Level Studies	252
137	A.4 Alternate b-jet Identification Algorithm	253
138	A.5 Binary Classification of the Higgs p_T	254
139	A.6 Impact of Alternative Jet Selection	256

140 Part I

141 Introduction

142 1 Introduction

143 Particle physics is an attempt to describe the fundamental building blocks of the universe and
144 their interactions. The Standard Model (SM) - our best current theory of fundamental particle
145 physics - does a remarkable job of that. All known fundamental particles and (almost) all of the
146 forces underlying their interactions can be explained by the SM, and the predictions from this
147 theory agree with experiment to an incredibly precise degree. This is especially true since the
148 Higgs Boson, the last piece of the SM predicted decades before, was finally discovered at the
149 Large Hadron Collider (LHC) in 2012 [1].

150 Despite the success of the SM, there remains significant work to be done. For one, the
151 SM is incomplete: it fails to provide a description of gravity, to give an explanation for the
152 observation of Dark Matter, or to provide a mechanism for neutrinos to gain mass. Further, a
153 Higgs Boson with a mass of around 125 GeV, as observed at the LHC, gives rise to what is
154 known a hierarchy problem - such a low mass Higgs requires a seemingly unnatural level of “fine
155 tuning” that is unexplained by the SM.

156 A promising avenue for addressing these problems is to study the properties of the Higgs
157 Boson and the way it interacts with other particles, in part simply because these interactions

158 have not been measured before. Its interactions with the Top Quark are a particularly promising
159 place to look. Because the Higgs Field is responsible for allowing particle to acquire mass, the
160 strength of a particle's interaction with the Higgs Boson is proportional to its mass. As the most
161 massive of the fundamental particles, the Top Quark has the strongest coupling to the Higgs
162 Boson, meaning any new physics in the Higgs sector is likely to present itself most prominently
163 in its interaction with the Top Quark.

164 These interactions can be measured by directly by studying the production of a Higgs
165 Boson in association with a pair of Top Quarks ($t\bar{t}H$). While studies have been done measuring
166 the overall rate of $t\bar{t}H$ production, there are several theories of physics Beyond the Standard
167 Model (BSM) that would affect the kinematics of $t\bar{t}H$ production without altering its overall
168 rate. This dissertation attempts to make a differential measurement of the kinematics of the
169 Higgs Boson in $t\bar{t}H$ events in order to search for these BSM effects.

170 The proton-proton collision data collected by the ATLAS detector at the LHC from 2015-
171 2018 provides the opportunity to make this measurement for the first time. The unprecedented
172 energy achieved by the LHC during this period greatly increase the rate at which $t\bar{t}H$ events are
173 produced, and the large amount of data collected provides the necessary statistics for a differential
174 measurement to be performed.

175 A study of $t\bar{t}H$ events with multiple leptons in the final state is performed, using 139 fb^{-1}
176 of data from proton-proton collisions at an energy $\sqrt{s} = 13 \text{ TeV}$ collected by the ATLAS detector
177 from 2015-2018. Events are separated into channels based on the number of light leptons in the

178 final state - either two same-sign leptons, or three leptons. A deep neural network is used to
179 reconstruct the momentum of the Higgs Boson in each event. This momentum spectrum is fit to
180 data for each analysis channel in order to search for evidence of these BSM effects.

181 An additional study of WZ produced in association with a heavy flavor jet (including both
182 b-jets and charm jets) is also included. This process mimics the final state of $t\bar{t}H$ multilpjet
183 events, making it an irreducible background for that analysis. However, this process is poorly
184 understood, and difficult to simulate accurately, introducing large systematic uncertainties for
185 analyses that include it as a background. A measurement of WZ + heavy flavor in the fully
186 leptonic decay mode is performed in an attempt to reduce this uncertainty.

187 This dissertation begins with a brief explanation of the SM, its limitations, and the theor-
188 etical motivation behind this work in Part II. This is followed by a description of the LHC and
189 the ATLAS detector in Part III. Part IV details a measurement of WZ + heavy flavor. Studies
190 of differential measurements of $t\bar{t}H$ are then described in Part V, and preliminary results are
191 presented. Finally, the results of these studies are summarized in the conclusion, Part VI.

192 Part II**193 Theoretical Motivation****194 2 The Standard Model and the Higgs Boson**

195 The Standard Model of particle physics (SM) is a Quantum Field Theory (QFT) describing the
196 known fundamental particles and their interactions. It accounts for three of the four known
197 fundamental force - electromagnetism, the weak nuclear force, and the strong nuclear force, but
198 not gravity. Further, the SM describes a mechanism for combining the weak and electromagnetic
199 forces into a singular interaction, known as the electroweak force. It is a non-Abelian gauge
200 theory, invariant under the Lie Group $SU(3)_C \otimes SU(2)_L \otimes U(1)_Y$, where C refers to color
201 charge, L, the helicity of the particle, and Y, the hypercharge.

202 2.1 The Forces and Particles of the Standard Model

203 The SM particles, summarized in Figure 2.1, can be classified into two general categories based
204 on their spin: fermions, and bosons.

Standard Model of Elementary Particles

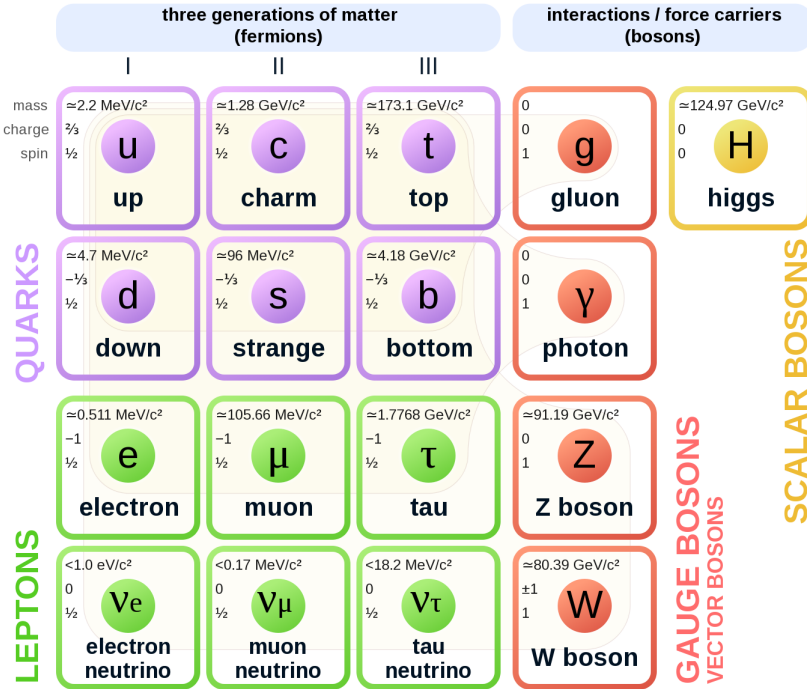


Figure 2.1: A summary of the particles of the Standard Model, including their mass, charge and spin, with the fermions listed on the left, and the bosons on the right. [2]

205 Fermions are particles with $\frac{1}{2}$ -integer spin, which according to the spin-statistics theorem,
 206 causes them to comply with the Pauli-exclusion principle. They can be separated into two groups,
 207 leptons and quarks, each of which consist of three generations of particles with increasing mass.

208 Leptons are fermions which interact via the electroweak force, but not the strong force.
 209 The three generation of leptons consist of the electron and electron neutrino, the muon and muon
 210 neutrino, the tau and tau neutrino. The quarks, by contrast, do interact via the strong force - which
 211 is to say they have color charge - in addition to the electroweak force. The three generations
 212 include the up and down quarks, the strange and charm quarks, and the top and bottom quarks.

213 Each of these generations form left-handed doublets invariant under SU(2) transfor-

214 mations. For the leptons these doublets are:

$$\begin{pmatrix} e^- \\ \nu_e \end{pmatrix}_L, \begin{pmatrix} \mu^- \\ \nu_\mu \end{pmatrix}_L, \begin{pmatrix} \tau^- \\ \nu_\tau \end{pmatrix}_L \quad (2.1)$$

215 And for the quarks:

$$\begin{pmatrix} u \\ d \end{pmatrix}_L, \begin{pmatrix} s \\ c \end{pmatrix}_L, \begin{pmatrix} t \\ b \end{pmatrix}_L \quad (2.2)$$

216 For both leptons and quarks, the heavier generations can decay into the lighter generation

217 of particles, while the first generation does not decay. Hence, ordinary matter generally consists

218 of this first generation of fermions - electrons, up quarks, and down quarks. Each of these

219 fermions has a corresponding anti-particle, which has an equal mass as its partner but opposite

220 charge. The fermions acquire their mass via the Higgs Mechanism, except for the neutrinos,

221 whose mass has been experimentally confirmed but is not accounted for in the SM.

222 Bosons, by contrast, have integer spin, and are therefore unconstrained by the Pauli-

223 exclusion principle. The SM includes two kinds of bosons: Gauge bosons, which are spin-1

224 particles that mediate the interactions between the fermions, and a single scalar, i.e. spin-0,

225 particle - the Higgs Boson. Of the gauge bosons, the W^+ , W^- and Z bosons - which are the

²²⁶ mass eigenstates of the electroweak bosons - mediate the weak interaction, while the photon
²²⁷ mediates the electric force, and the gluon mediates the strong force.

²²⁸ **2.2 The Higgs Mechanism**

²²⁹ A key feature of the SM is the gauge invariance of its Lagrangian. However, any terms added to
²³⁰ the Lagrangian giving mass to the the gauge bosons would violate this underlying symmetry of
²³¹ the theory. This presents a clear problem with the theory: The experimental observation that the
²³² W and Z bosons have mass seems to contradict the basic structure of the SM.

²³³ Rather than abandoning gauge invariance, an alternative way for particles to acquire mass
²³⁴ beyond adding a simple mass term to the Lagrangian was theorized by Higgs, Englert and Brout
²³⁵ in 1964 [3]. This procedure for introducing masses for the gauge bosons while preserving local
²³⁶ gauge invariance, known as the Higgs mechanism, was incorporated into the electroweak theory
²³⁷ by Weinberg in 1967 [4].

²³⁸ **2.2.1 The Higgs Field**

²³⁹ The Higgs mechanism introduces a complex scalar SU(2) doublet, Φ , with the form:

$$\Phi = \begin{pmatrix} \phi^+ \\ \phi^0 \end{pmatrix}_L \quad (2.3)$$

240 This field introduces a scalar potential to the Lagrangian of the form:

$$V(\Phi) = \mu^2 |\Phi^\dagger \Phi| + \lambda (|\Phi^\dagger \Phi|)^2 \quad (2.4)$$

241 Where μ and λ are free parameters of the new field. This represents the most general
 242 potential allowed while preserving $SU(2)_L$ invariance and renormalizability. In the case that
 243 $\mu^2 < 0$, this potential takes the form shown in Figure 2.2.

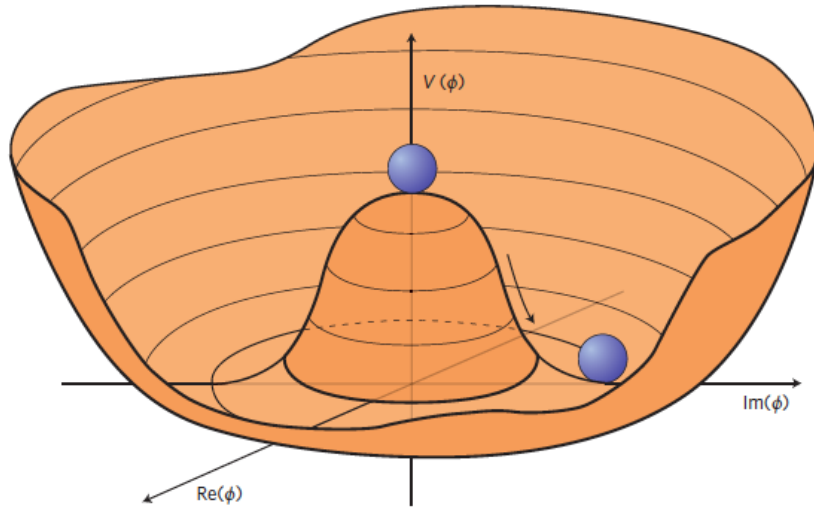


Figure 2.2: The value of the Higgs potential, $V(\Phi)$ as a function of Φ , for the case that $\mu^2 < 0$ [5].

244 The significant feature of this potential is that its minimum does not occur for a value of
 245 $\Phi = 0$. Instead, it is minimized when $|\Phi^\dagger \Phi| = -\mu^2/\lambda$. This means that in its ground state, the
 246 Higgs field takes on a non-zero value - referred to as a vacuum expectation value (VEV). So while
 247 the Higgs potential is globally symmetric, about the minimum this symmetry is broken. Since

²⁴⁸ the minimum is determined only by $\Phi^\dagger \Phi$, there is some ambiguity in the particular definition of

²⁴⁹ the VEV, but it is generally represented as

$$\langle \Phi \rangle = \frac{1}{\sqrt{2}} \begin{pmatrix} 0 \\ v \end{pmatrix} \quad (2.5)$$

²⁵⁰ The full value of Φ can be written as

$$\langle \Phi \rangle = \frac{1}{\sqrt{2}} \begin{pmatrix} 0 \\ v + H/\sqrt{2} \end{pmatrix} \quad (2.6)$$

²⁵¹ with v being the value of the VEV, and H being the real value of the scalar field.

²⁵² 2.2.2 Electroweak Symmetry Breaking

²⁵³ The Electroweak (EWK) interaction is described in the SM by a $SU(2)_L \otimes U(1)_Y$ gauge theory.

²⁵⁴ This theory predicts three $SU(2)_L$ gauge boson, $W_\mu^1, W_\mu^2, W_\mu^3$, and a single $U(1)_Y$ gauge boson,

²⁵⁵ B_μ . The couplings of these bosons to the Higgs field show up in the kinetic terms of the scalar

²⁵⁶ field Φ in the Lagrangian:

$$(D_\mu \Phi)^\dagger (D^\mu \Phi) = |(\partial_\mu - \frac{i g}{2} W_\mu^a \sigma^a - \frac{i g'}{2} B_\mu Y) \phi|^2 \quad (2.7)$$

257 Here D_μ represents the covariant derivative required to preserve gauge invariance, g and
 258 g' represent coupling constant of the gauge bosons, σ^a denotes the Pauli matrices of $SU(2)$,
 259 and Y represents the hypercharge of $U(1)$. The terms in this interaction which contribute to the
 260 masses of the gauge bosons can be written as:

$$\frac{1}{2}(0, v) \left(\frac{g}{2} W_\mu^a \sigma^a - \frac{g'}{2} B_\mu \right)^2 \begin{pmatrix} 0 \\ v \end{pmatrix} \quad (2.8)$$

261 Expanding these terms into the mass eigenstates of the electroweak interaction yields four
 262 physical gauge bosons, two charged and two neutral, which are linear combinations of the fields
 263 W_μ^1 , W_μ^2 , W_μ^3 , and B_μ :

$$\begin{aligned} W_\mu^\pm &= \frac{1}{\sqrt{2}} (W_\mu^1 \pm i W_\mu^2) \\ Z^\mu &= \frac{1}{\sqrt{(g^2 + g'^2)}} (-g' B_\mu + g W_\mu^3) \\ A^\mu &= \frac{1}{\sqrt{(g^2 + g'^2)}} (g B_\mu + g' W_\mu^3) \end{aligned} \quad (2.9)$$

264 And the masses of these fields are given by:

$$\begin{aligned} M_W^2 &= \frac{1}{4} g^2 v^2 \\ M_Z^2 &= \frac{1}{4} (g^2 + g'^2) v^2 \\ M_A^2 &= 0 \end{aligned} \quad (2.10)$$

265 This produces exactly the particles we observe - three massive gauge bosons and a single
 266 massless photon. The massless photon represents the portion of the gauge symmetry, a single
 267 $U(1)$ of the electromagnetic force, that remains unbroken by the VEV.

268 Interactions with the Higgs field also lead to the generation of the fermion masses, which
 269 in the Lagrangian take the form:

$$-\lambda_\psi(\bar{\psi}_L \phi \psi_R + \bar{\psi}_R \phi^\dagger \psi_L) \quad (2.11)$$

270 After symmetry breaking has occurred and ϕ has taken on the value of the VEV as written
 271 in equation 2.5, the mass terms of the fermions become $\lambda_\psi v$. Written this way, the fermion
 272 masses are proportional to their Yukawa coupling to the VEV, λ_ψ .

273 Based on the equation 2.6, an additional mass term, $\mu^2 H^2$ arises from the potential $V(\Phi)$.
 274 This term can be understood as an excitation of the Higgs field, a scalar boson with mass $M_H = \mu$.
 275 This is the Higgs boson, which comes about as a natural prediction of electroweak symmetry
 276 breaking.

277 The fermions' Yukawa couplings to the VEV take the same form as the fermions' coupling
 278 to the Higgs boson - λ_ψ . Therefore, the strength of a fermion's interaction with the Higgs is
 279 directly proportional to its mass. We now have a model that predicts a Higgs boson with mass
 280 $M_H = \mu$, which interacts with the fermions with coupling strength λ_ψ . Because μ and λ_ψ are

²⁸¹ free parameters of the theory, the mass of the Higgs boson and its interactions with the fermions

²⁸² must be measured experimentally.

²⁸³ **2.3 $t\bar{t}H$ Production**

²⁸⁴ The strength of a particles interaction with the Higgs, given by its Yukawa coupling, is propor-
²⁸⁵ tionate to its mass. The top quark - as the heaviest known particle - has the strongest interaction,
²⁸⁶ making this interaction particularly interesting to study. While several processes involve interac-
²⁸⁷ tions between the Higgs and the top, some Higgs production modes include the top interaction
²⁸⁸ only as a part of a loop diagram, such as the gluon-gluon fusion diagram shown in Figure 2.3.

²⁸⁹ This process therefore only allows for an indirect probe of the Higgs-top Yukawa coupling, as
²⁹⁰ the flavor of the quark in this diagram is not unique.

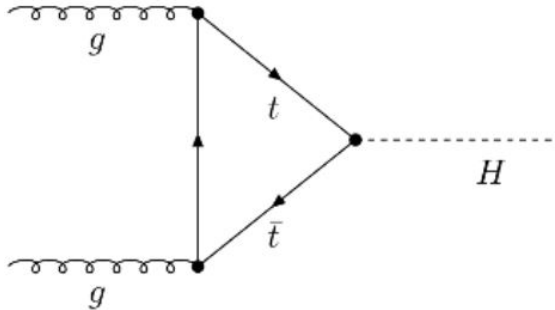


Figure 2.3: Diagram of a Higgs boson produced via gluon-gluon fusion.

²⁹¹ Studying the Higgs produced in association with top quark pairs, $t\bar{t}H$, allows this interac-
²⁹² tion to be measured directly. This process, as shown in Figure 2.4, involves a unique coupling
²⁹³ between the Higgs and the top, which can be identified by the top quark pair in the final state.

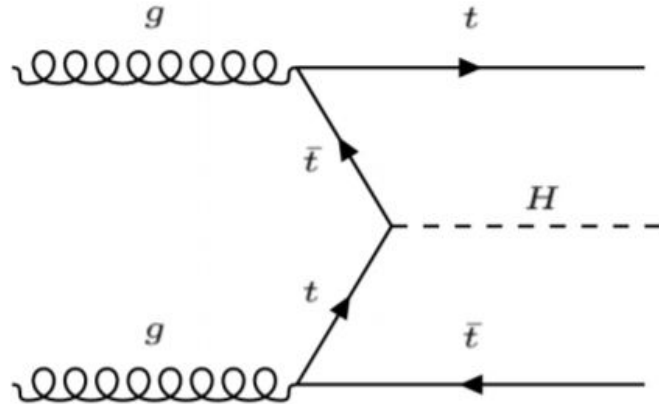


Figure 2.4: Diagram of a Higgs boson produced in association with a pair of top quarks.

294 The Higgs boson, as well as the top quarks, have very short lifetimes - on the order of
 295 10^{-22} s and 10^{-25} s respectively - meaning they can only be observed via their decay products.
 296 Measuring this process is therefore a matter of identifying events with final states consistent with
 297 $t\bar{t}H$ production.

298 Studies of $t\bar{t}H$ production have been reported by the ATLAS collaboration for $H \rightarrow b\bar{b}$,
 299 $H \rightarrow \gamma\gamma$ and multilepton (encompassing $H \rightarrow W^+W^-$, $H \rightarrow ZZ$ and $H \rightarrow \tau^-\tau^+$, with
 300 $H \rightarrow ZZ \rightarrow 4l$ as a separate analysis) decay modes. While the branching ratio of $H \rightarrow W^+W^-$
 301 is smaller than $H \rightarrow b\bar{b}$ (see Table 2.3), it produces a clearer signal, as $H \rightarrow b\bar{b}$ suffers from
 302 large $t\bar{t}$ backgrounds. On the other hand, $H \rightarrow \gamma\gamma$ produces the most easily identifiable signal,
 303 but has a much smaller branching ratio than $H \rightarrow W^+W^-$. Therefore, compared with other final
 304 states of $t\bar{t}H$, the $t\bar{t}H$ – ML channel is an attractive candidate for study, as it involves a good
 305 balance between statistical power and identifiability.

Decay Mode	Branching Ratio (%)
$H \rightarrow b\bar{b}$	58.2
$H \rightarrow WW^*$	21.4
$H \rightarrow gg$	8.19
$H \rightarrow \tau\tau$	6.27
$H \rightarrow c\bar{c}$	2.89
$H \rightarrow ZZ^*$	2.62
$H \rightarrow \gamma\gamma$	0.227

Table 1: Summary of the predominant SM Higgs ($m_H = 125$ GeV) branching ratios. Particles with a star imply off-shell decays.

306 Searches for $t\bar{t}H$ production typically target a measurement of the signal strength para-
 307 meter, $\mu_{t\bar{t}H}$, which measures the ratio of the observed cross-section and the expected cross-section
 308 according to the SM.

$$\mu_{t\bar{t}H} = \frac{\sigma_{t\bar{t}H}^{\text{obs.}}}{\sigma_{t\bar{t}H}^{\text{SM}}} \quad (2.12)$$

309 $t\bar{t}H$ production was observed by ATLAS using up to 79.8 fb^{-1} of data collected at \sqrt{s}
 310 $= 13 \text{ TeV}$, based on a combination of five Higgs decay modes: $b\bar{b}$, WW^* , $\tau^-\tau^+$, $\gamma\gamma$, and ZZ^*
 311 [6]. A significance of 5.8σ was observed, compared to a 4.9σ expected significance. Since then,
 312 two analyses have published updated results ($H \rightarrow \gamma\gamma$ and $H \rightarrow ZZ^* \rightarrow 4l$) with the full Run 2
 313 dataset, representing 139 fb^{-1} . Studies are still ongoing in the remaining channels.

314 This thesis focuses on $t\bar{t}H$ events with multiple leptons in the final state, $t\bar{t}H - ML$,
 315 specifically targeting events with two same-sign leptons (2lSS) or three leptons (3l) in the

316 final state. This includes $H \rightarrow W^+W^-$ events, where at least one of the W bosons decays
317 leptonically.

318 **2.4 WZ + Heavy Flavor Production**

319 Part IV is dedicated to a measurement of WZ produced in association with a heavy flavor jet
320 - namely, a charm or b-jet - in the fully leptonic channel. In the instance that both the W
321 and Z bosons decay leptonically, this process produces a final state similar to $t\bar{t}H$, making it
322 an irreducible background for $t\bar{t}H$ – ML specifically, and any analysis that includes multiple
323 leptons and b-tagged jets in the final state more broadly.

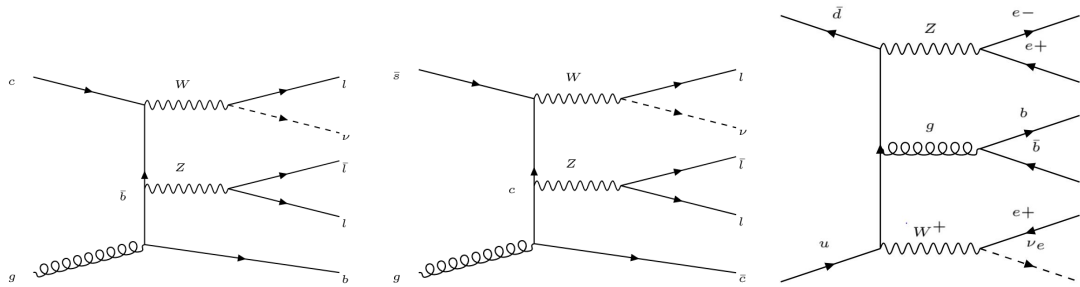


Figure 2.5: Example Feynman diagrams of $WZ +$ heavy flavor production

324 The b-jets produced in this process can be thought of in two different ways: either as
325 originating from the quark “sea” of the initial state hadrons, or as the result of a gluon from
326 one the colliding protons splitting into $b\bar{b}$ pairs. However, the heavy flavor contribution to the
327 parton distribution function (PDF) of the proton is uncertain, and simulations of this process
328 disagree depending on which of these two approaches one considers. This makes $WZ +$ heavy

329 flavor difficult to accurately simulate, and introduces a large uncertainty for any analysis which
330 includes it as a background, motivating a measurement of this process.

331 **2.5 Extensions to the Standard Model**

332 While the SM has been tested to great precision, particularly at the LHC, it is generally accepted
333 that it is only valid up to a certain energy scale. It is assumed that above a certain energy, at the
334 scale where something like a Grand Unified Theory (GUT) or quantum gravity become relevant,
335 the SM will not be applicable. Further, there are several experimental observations that the SM
336 fails to explain. For example, the SM predicts neutrinos to be massless, despite experimental
337 observation to the contrary, and fails to explain the observation of dark matter and dark energy.

338 Another example, relevant to the Higgs sector, is known as the hierarchy problem: large
339 quantum corrections to the Higgs mass from loop diagrams, such as those shown in Figure 2.6,
340 are many orders of magnitude larger than the Higgs mass itself. The observed value of the Higgs
341 mass therefore requires extremely precise cancellation between these corrections and the bare
342 mass of the Higgs, a cancellation which seems unnatural and suggests something missing in our
343 theoretical picture.

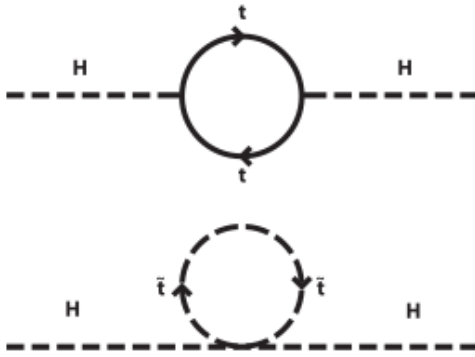


Figure 2.6: Above diagram is the leading order correction to the Higgs mass via a top quark loop, and below is the stop squark loop, coming from a supersymmetric extension of the SM, that provides a potential cancellation of the top diagram.

344 Because so many of the properties of the Higgs boson have not yet been studied, its
 345 interactions are a promising place to search for new physics that could resolve some of the
 346 limitations of the SM. As explained above, the interactions of the Higgs with the top quark, as in
 347 $t\bar{t}H$ production, are particularly interesting: As the most massive particle in the Standard Model,
 348 the top quark is the most strongly interacting with the Higgs. Therefore, any new physics effects
 349 are likely to be seen most prominently in this interaction.

350 These interactions can be measured directly by studying the production of a Higgs Boson
 351 in association with a pair of Top Quarks ($t\bar{t}H$). While this process has been observed by both
 352 the ATLAS [7] and CMS [8] collaborations, these analyses have focused on measuring the
 353 overall rate of $t\bar{t}H$ production. There are several theories of physics Beyond the Standard Model
 354 (BSM), however, that would affect the kinematics of $t\bar{t}H$ production without altering its overall
 355 rate [9].

356 An Effective Field Theory approach can be used to model the low energy effects of new,
 357 high energy physics, by parameterizing BSM effects as higher dimensional operators. These
 358 additional operators can then be added to the SM Lagrangian to write an effective Lagrangian
 359 that accounts for the effects of these higher energy physics. The lowest order of these that could
 360 contribute to Higgs-top couplings are dimension-six, as represented in Equation 2.13.

$$\mathcal{L}_{\text{eff}} = \mathcal{L}_{\text{SM}} + \frac{f}{\Lambda} O^6 \quad (2.13)$$

361 Here Λ represents the energy scale of the new physics, and f is a Wilson coefficient which
 362 represents the strength of the effective coupling. An experimental observation of any non-zero
 363 value of f would be a sign of BSM physics.

364 The addition of these operators can be shown to modify the transverse momentum (p_T)
 365 spectrum of the Higgs Boson in Higg-top interactions, without effecting the overall rate of $t\bar{t}H$
 366 production [10]. The possible impact of these higher order effects on the Higgs p_T spectrum are
 367 shown in Figure 2.7.

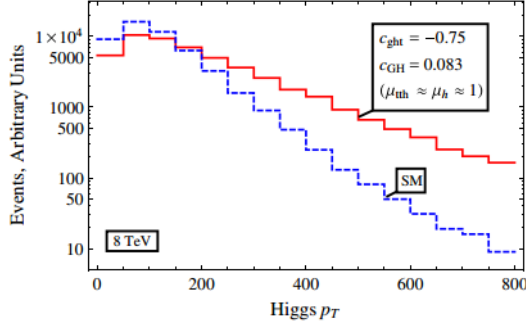


Figure 2.7: The momentum spectrum of the Higgs boson produced via top-quarks with (red) and without (blue) the presence of dimension-six operators.

368 This provides a clear, physics observable that could be used to search for evidence of
 369 BSM physics. The energy and luminosity produced by the LHC now make such a measurement
 370 possible. Reconstructing the momentum spectrum of the Higgs in $t\bar{t}H$ events therefore provides
 371 a means to search for new physics in the Higgs sector.

372 Reconstructing the Higgs is a particular challenge in the multilepton channels of $t\bar{t}H$, due
 373 to an ambiguity arising from multiple sources of missing energy. In the $H \rightarrow \gamma\gamma$ channel, the
 374 kinematics of the Higgs can be fully reconstructed from the two photons. The same is true of
 375 $H \rightarrow b\bar{b}$, though with the additional challenge of identifying which two of the four b-quarks in
 376 the final state originated from the Higgs. By contrast, the two channels (2lSS and 3l) targeted
 377 by this analysis include at least one neutrino originating from the Higgs decay.

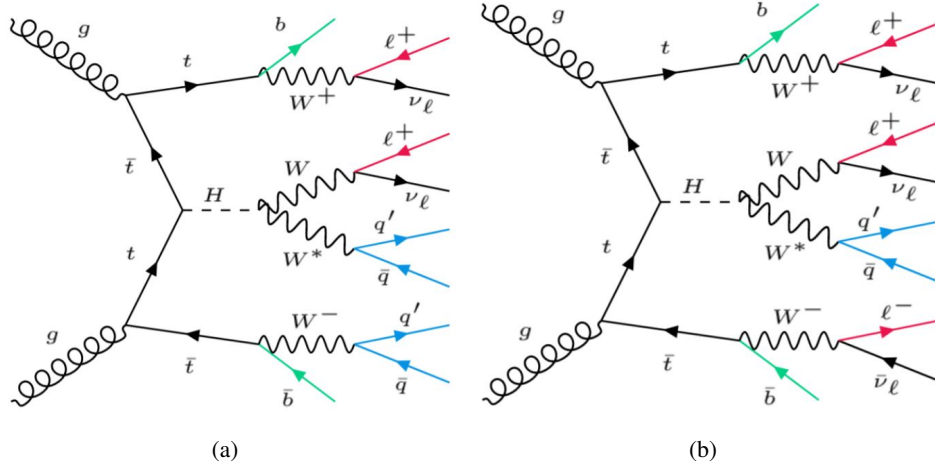


Figure 2.8: Feynman diagrams of $t\bar{t}H$ production with (a) two same-sign leptons and (b) three leptons in the final state.

378 Neutrinos are not detected by ATLAS; instead, their presence is inferred from missing
 379 transverse energy in the detector, E_{miss}^T . The two channels targeted here include not just a
 380 neutrino from the Higgs decay, but at least one additional neutrino from the decay of the top-
 381 quarks. This makes disentangling the contribution of the Higgs decay to E_{miss}^T , and thereby fully
 382 reconstructing the Higgs, impossible.

383 This challenge motivates the use of more sophisticated machine learning techniques when
 384 attempting to perform differential measurements of the Higgs p_T spectrum in the multi-lepton
 385 channels of $t\bar{t}H$.

Part III**387 The LHC and the ATLAS Detector****388 3 The LHC**

389 The Large Hadron Collider (LHC) is a particle accelerator consisting of a 27 km ring, designed
390 to collide protons at high energy. Located outside of Geneva, Switzerland and buried about 100
391 m underground, it consists of a ring of superconducting magnets which are used to accelerate
392 opposing beams of protons - or lead ions - which collide at the center of one of the various
393 detectors located around the LHC ring which record the result of these collisions. These
394 detectors include two general purpose detectors, ATLAS and CMS, which are designed to make
395 precision measurements of a broad range of physics phenomenon, and two more specialized
396 experiments, LHCb and ALICE, which are optimized to study b-quarks and heavy-ion physics,
397 respectively.

398 The LHC first began running in 2009 at a proton-proton center of mass energy of $\sqrt{s} = 8$
399 TeV. It operated at this energy from 2009 to 2012, known as Run 1, and data collected during
400 this period was used in discovering the Higgs Boson. The LHC began running again in 2015,
401 and collected data at an increased energy of $\sqrt{s} = 13$ TeV until 2018, a period referred to as Run
402 2.

403 The LHC consists of a chain of accelerators, which accelerate the protons to higher and

higher energies until they are injected into the main ring. This process is summarized in figure 3.1. Protons extracted from a tank of ionized hydrogen are fed into a linear accelerator, LINAC2, where they reach an energy of 50 MeV. From there, they enter a series of three separate circular accelerators, before being injected into the main accelerator ring at an energy of 450 GeV. Within the main ring protons are separated into two separate beams moving in opposite directions, and their energy is increased to their full collision energy. Radiofrequency cavities are used to accelerate these particles and sort them into bunches. From 2015-2018, these bunches consisted of around 100 billion protons each with an energy of 6.5 TeV per proton, which collided at a rate of 40 MHz, or every 25 ns.

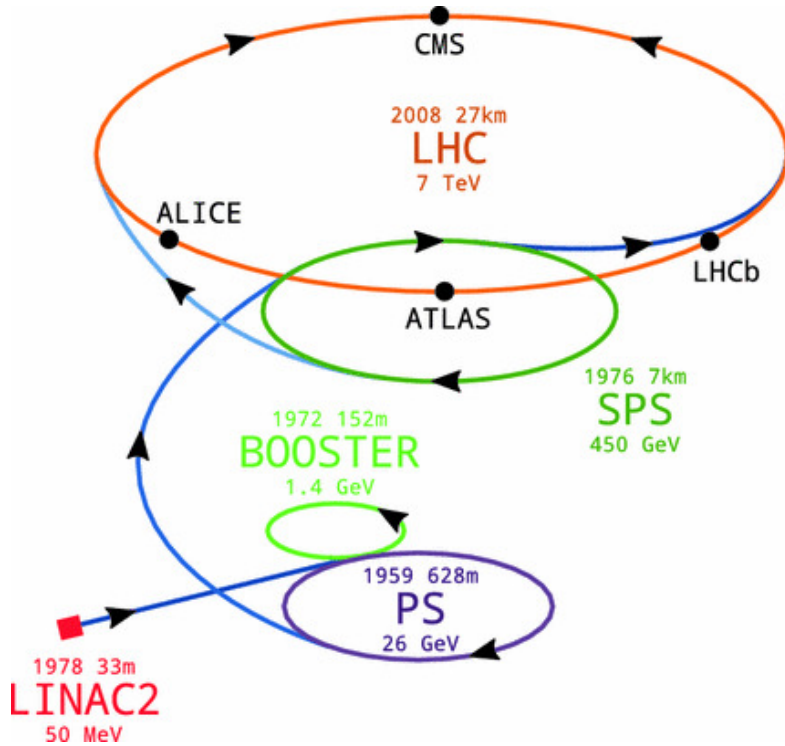


Figure 3.1: A summary of the accelerator chain used to feed protons into the LHC [11].

413 Because these proton bunches consist of a large number of particles, each bunch crossing
 414 consists of not just one, but several direct proton-proton collisions. The number of interactions
 415 that occur per bunch crossing, μ , is known as pileup. During Run 2, the average pileup for bunch
 416 crossings was around $\langle \mu \rangle = 35$, with values typically ranging between 10 and 70.

417 The amount of data collected by the LHC is measured in terms of luminosity, which is the
 418 ratio of the number of events detected per unit time, $\frac{dN}{dt}$, and the interaction cross-section, σ .

$$\mathcal{L} = \frac{1}{\sigma} \frac{dN}{dt} \quad (3.1)$$

419 The design luminosity of the LHC is $10^{34} \text{ cm}^{-2}\text{s}^{-1}$, however the LHC has achieved a
 420 luminosity of over $2 \times 10^{34} \text{ cm}^{-2}\text{s}^{-1}$. The total luminosity is then this instantaneous luminosity
 421 integrated over time.

$$\mathcal{L}_{\text{int}} = \int \mathcal{L} dt \quad (3.2)$$

422 The integrated luminosity collected by the ATLAS detector as of the end of 2018 is around
 423 140 fb^{-1} , exceeding the expected integrated luminosity of 100 fb^{-1} .

424 4 The ATLAS Detector

425 ATLAS (a not terribly natural acronym for “A Toroidal LHC Apparatus”) is a general purpose
 426 detector designed to maximize the detection efficiency of all physics objects, including leptons,
 427 jets, and photons. This means it is capable of measuring all SM particles, with the exception of
 428 neutrinos, the presence of which can be inferred based on missing transverse momentum. The
 429 detector measures 44 m long, and 25 m tall.

430 The ATLAS detector consists of multiple concentric layers, each of which serves a different
 431 purpose in reconstructing collisions. At the very center of the detector is the interaction point
 432 where the proton beams of the LHC collide.

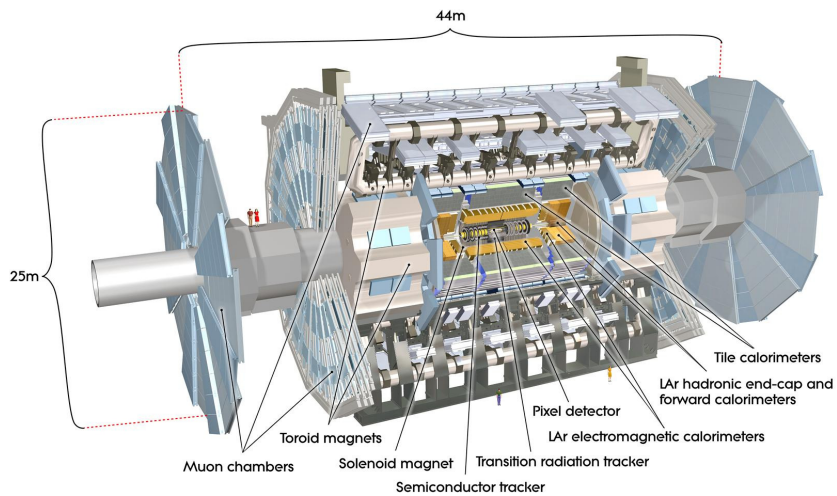


Figure 4.1: Cutaway view of the ATLAS detector, with labels of its major components [12].

433 **4.1 Inner Detector**

434 Just surrounding the interaction point is the Inner Detector, designed to track the path of charged
435 particles moving through the detector. An inner solenoid surrounding the Innder Detector is
436 used to produces a magnetic field of 2 T. This large magnetic field causes the path of charged
437 particles moving through the Inner Detector to bend. Because this magnetic field is uniform and
438 well known, it can be used in conjunction with the curvature of a particles path to measure its
439 charge and momentum.

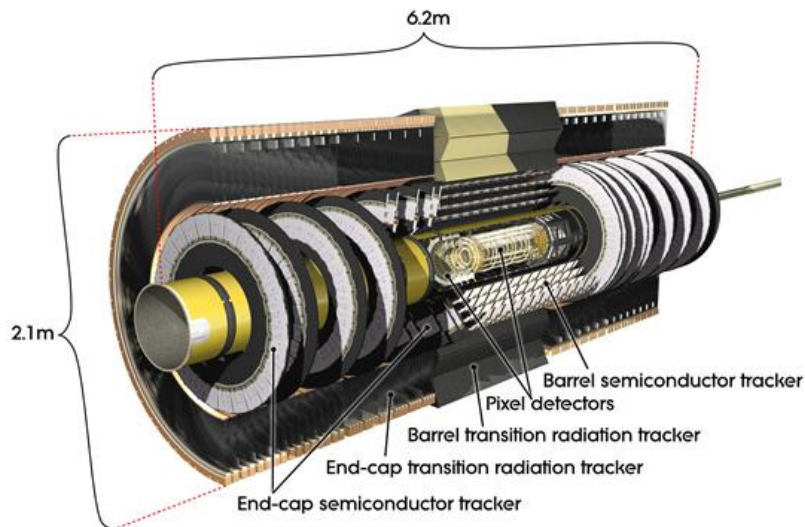


Figure 4.2: Cutaway view of the Inner Detector [13].

440 The Inner Detector consists of three components - the Pixel Detector, the Semi-Conductor
441 Tracker (SCT), and the Transition Radiation Tracker (TRT). The Pixel Detector is the innermost
442 of these, beginning just 33.25 mm away from the beam line. It consists of three silicon layers
443 along the barrel, as well as three endcap layers, covering a range of $|\eta| < 2.5$.

444 The Semiconductor Tracker (SCT) is similar to the Pixel detector, but uses long strips of
 445 silicon rather than small pixels to cover a larger spatial area. It includes over 6 million readout
 446 strips, allowing the position of charged particles to be measured to an accuracy of 17 μm .

447 The outermost component of the inner detector, the TRT consists of around 300,000 straw
 448 tubes filled with ionizable gas, which produces current through a wire in the center of each tube
 449 when a charged particle passes through. Between these staws are layers of material designed
 450 to produce transition radiation from ultrarelativistic particles as they pass through each material
 451 boundary, amplifying the signal. The position uncertainty in the TRT is higher than the other
 452 two, on the order of 200 μm , but covering a much larger area.

453 4.2 Calorimeters

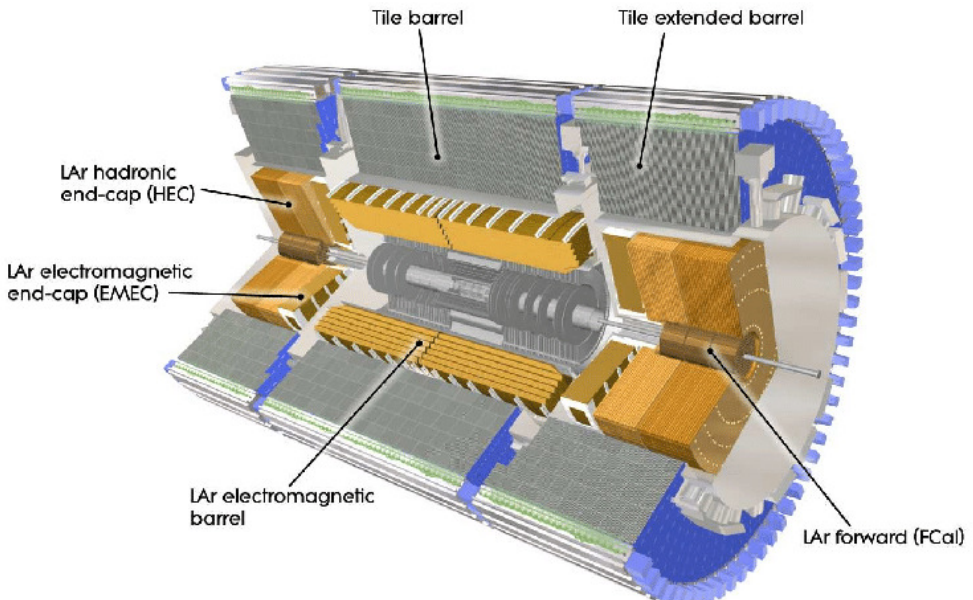


Figure 4.3: Cutaway view of the calorimeter system of the ATLAS detector [13].

454 Situated outside the Inner Detector are two concentric calorimeters. The inner calorimeter
455 uses liquid argon (LAr) to measure the energy of particles that interact electromagnetically,
456 which includes photons and any charged particle. The LAr calorimeter is made of heavy metals,
457 primarily lead and copper, which causes electromagnetically interacting particles to shower,
458 depositing their energy in the detector. The showering of the high energy particles that pass
459 through the calorimeter cause the liquid argon to ionize, and the ionized electrons are detected
460 by electronic readouts. The LAr calorimeter consists of around 180,000 readout channels.

461 The outer calorimeter measures the energy from particles that pass through the EM
462 calorimeter, and measures the energy of particles that interact via the strong force. This is
463 primarily hadrons. It is composed of steel plates designed to cause hadronic showering and
464 around 500,000 scintillating tiles as the active material. The signals from the hadronic calorimeter
465 are read out by photomultiplier tubes (PMTs).

466 **4.3 Muon Spectrometer**

467 Because muons are heavier than electrons and photons, and do not interact via the strong force,
468 they generally pass through the detector without being stopped by the calorimeters. The outermost
469 components of the detector are designed specifically to measure the energy and momentum of
470 muons produced in the LHC. The muon spectrometer consists of tracking and triggering systems.

471 The largest of the subdetectors, it extends from the outside of the calorimeter system, about a
472 4.25 m radius from the beam line, to a radius of 11 m. This large detector system is necessary

473 to accurately measure the momentum of muons, which is essential not only for measurements
474 involving the muons themselves, but also to accurately estimate the missing energy in each
475 event.

476 Two large toroidal magnets within the muon system generate a large magnetic field which
477 covers an area 26 m long with a radius of 10 m. Because the area covered by this magnet system
478 is so large, a uniform magnetic field like the one produced in the Inner Detector is impractical.
479 Instead, the magnetic field that exists in the muon spectrometer ranges between 2 T and 8 T, and
480 is much less uniform. The path of the muons passing through the spectrometer is bent by this
481 field, allowing their charge to be determined.

482 1200 tracking chambers are placed in the muon system in order to precisely measure the
483 tracks of muons with high spatial resolution. The path of the muons are tracked by Monitored
484 Drift Tubes, which are drift chambers formed by aluminum tubes and filled with ionizing gas.
485 These tubes produce a multi-layer spatial resolution on the order of 50 μm .

486 **4.4 Trigger System**

487 Because of the high collision rate and large amount of data collected by the various subdetectors,
488 ATLAS produces far more data than can actually be stored. Each event produces around 25 Mb
489 of raw data, which multiplied by the bunch crossing rate of 40 MHz, comes out to around a
490 petabyte of data every second. The information from every event cannot practically be stored,

491 therefore a sophisticated trigger system is employed in real time to determine whether events are
492 sufficiently interesting to be worth storing.

493 The trigger system in ATLAS involves multiple levels, each of which select out which
494 events move on to the next level of scrutiny. The level-1 trigger uses hardware information from
495 the calorimeters and muon spectrometer to select events that contain candidates for particles
496 commonly used in analysis, such as energetic leptons and jets. The level-1 trigger reduces the
497 rate of events from 40 MHz to around 100 kHz.

498 Events that pass the level-1 trigger move to the High-Level Trigger (HLT). The HLT takes
499 place outside of the detector in software, and looks for properties such as a large amount of
500 missing transverse energy, well defined leptons, and multiple high energy jets. Events that pass
501 the HLT are stored and used for analysis. Because the specifics of the HLT are determined by
502 software rather than hardware, the thresholds can be changed throughout the run of the detector
503 in response to run conditions such as changes to pileup and luminosity. After the HLT is applied,
504 the event rate is reduced to around 1000 per second, which are recorded for analysis.

505 Part IV**506 Measurement of WZ + Heavy Flavor****507 5 Introduction**

508 The production of WZ in association with a heavy flavor jet represents an important background
509 for many major analyses. This includes any process with leptons and b-jets in the final state,
510 such as $t\bar{t}H$, $t\bar{t}W$, and $t\bar{t}Z$. While precise measurements have been made of WZ production
511 [14], WZ + heavy flavor remains poorly understood. This is largely because the QCD processes
512 involved in the production of the b-jet make it difficult to simulate accurately. This introduces a
513 large uncertainty for analyses that include this process as a background.

514 Motivated by its relevance to the $t\bar{t}H$ multilepton analysis, we perform a study of the fully
515 leptonic decay mode of this channel; that is, events where both the W and Z decay leptonically.
516 Because WZ has no associated jets at leading order, while the major backgrounds for this channel
517 tend to have high jet multiplicity, events with more than two jets are rejected. This gives a final
518 state signature of three leptons and one or two jets.

519 Events that meet this selection criteria are sorted into pseudo-continuous b-tagging regions
520 based on the DL1r b-tag score of their associated jets. This is done to separate WZ + b-jet events
521 from WZ + charm and WZ + light jets. These regions are fit to data in order to make a more
522 accurate estimate of the contribution of WZ + heavy-flavor, where heavy-flavor jets include

523 b-jets and charm jets. The full Run-2 dataset collected by the ATLAS detector, representing 139
524 fb^{-1} of data from pp collisions at $\sqrt{s} = 13 \text{ TeV}$, is used for this study.

525 Section 10 details the data and Monte Carlo (MC) samples used in the analysis. The
526 reconstruction of various physics objects is described in Section 11. Section 12 describes the
527 event selection applied to these samples, along the definitions of the various regions used in
528 the fit. The multivariate analysis techniques used to separate the tZ background from WZ +
529 heavy flavor are described in Section 13. Section 20 describes the various sources of systematic
530 uncertainties considered in the fit. Finally, the results of the analysis are summarized in Section
531 21, followed by a brief conclusion in Section ??.

532 **The current state of the analysis shows blinded results for the full 2018 dataset.**
533 **Regions containing >5% WZ+b events are blinded, and results are from Asimov, MC only**
534 **fits.**

535 6 Data and Monte Carlo Samples

536 6.1 Data Samples

537 This study uses a sample of proton-proton collision data collected by the ATLAS detector from
538 2015 through 2018 at an energy of $\sqrt{s} = 13 \text{ TeV}$, which represents an integrated luminosity of
539 139 fb^{-1} . This data set was collected with a bunch crossing rate of 25 ns. All data used in this
540 analysis was verified by data quality checks.

541 **6.2 Monte Carlo Samples**

542 Several different generators were used to produce Monte Carlo simulations of the signal and
543 background processes. For all samples, the response of the ATLAS detector is simulated using
544 Geant4. The WZ signal samples are simulated using Sherpa 2.2.2 [15]. Specific information
545 about the Monte Carlo samples being used can be found in Table 22.

Table 2: The configurations used for event generation of signal and background processes, including the event generator, matrix element (ME) order, parton shower algorithm, and parton distribution function (PDF).

Process	Event generator	ME order	Parton Shower	PDF
WZ, VV	SHERPA 2.2.2	MEPS NLO	SHERPA	CT10
tZ	MG5_AMC	NLO	PYTHIA 8	CTEQ6L1
t̄tW	MG5_AMC (SHERPA 2.1.1)	NLO (LO multileg)	PYTHIA 8 (SHERPA)	NNPDF 3.0 NLO (NNPDF 3.0 NLO)
t̄t(Z/γ* → ll)	MG5_AMC	NLO	PYTHIA 8	NNPDF 3.0 NLO
t̄tH	MG5_AMC (MG5_AMC)	NLO (NLO)	PYTHIA 8 (HERWIG++)	NNPDF 3.0 NLO [16] (CT10 [17])
tHqb	MG5_AMC	LO	PYTHIA 8	CT10
tHW	MG5_AMC (SHERPA 2.1.1)	NLO (LO multileg)	HERWIG++ (SHERPA)	CT10 (NNPDF 3.0 NLO)
tWZ	MG5_AMC	NLO	PYTHIA 8	NNPDF 2.3 LO
t̄t̄t, t̄tt̄t̄t̄	MG5_AMC	LO	PYTHIA 8	NNPDF 2.3 LO
t̄tW+W-	MG5_AMC	LO	PYTHIA 8	NNPDF 2.3 LO
t̄t	POWHEG-BOX v2 [18]	NLO	PYTHIA 8	NNPDF 3.0 NLO
t̄t̄γ	MG5_AMC	LO	PYTHIA 8	NNPDF 2.3 LO
s-, t-channel, Wt single top	POWHEG-BOX v1 [19]	NLO	PYTHIA 6	CT10
qqVV, VVV Z → l+l-	SHERPA 2.2.1	MEPS NLO	SHERPA	NNPDF 3.0 NLO

546 7 Object Reconstruction

547 All regions defined in this analysis share a common lepton, jet, and overall event preselection.
 548 The selection applied to each physics object is detailed here; the event preselection, and the
 549 selection used to define the various fit regions, is described in Section 12.

550 All events are required to be selected by dilepton triggers. The p_T thresholds of the
 551 dilepton trigger on two electrons were 12 GeV in 2015, 17 GeV in 2016, and 24 GeV in 2017 and
 552 2018, while for the dimuon triggers the p_T thresholds on the leading (sub-leading) muon were
 553 18 GeV (8 GeV) in 2015, and 22 GeV (8 GeV) in 2016-2018. For the electron+muon triggers,
 554 the p_T thresholds on the electron (muon) were 17 GeV (14 GeV) for all datasets.

555 7.1 Light leptons

556 Electron candidates are reconstructed from energy clusters in the electromagnetic calorimeter
 557 that are associated with charged particle tracks reconstructed in the inner detector [20]. Electron
 558 candidates are required to have $p_T > 10$ GeV and $|\eta_{\text{cluster}}| < 2.47$. Muon candidates are
 559 reconstructed by combining inner detector tracks with track segments or full tracks in the muon
 560 spectrometer [21]. Muon candidates are required to have $p_T > 10$ GeV and $|\eta| < 2.5$. Candidates
 561 in the transition region between different electromagnetic calorimeter components, $1.37 <$
 562 $|\eta_{\text{cluster}}| < 1.52$, are rejected. A multivariate likelihood discriminant combining shower shape
 563 and track information is used to distinguish real electrons from hadronic showers (fake electrons).
 564 To further reduce the non-prompt electron contribution, the track is required to be consistent

565 with originating from the primary vertex; requirements are imposed on the transverse impact
 566 parameter significance ($|d_0|/\sigma_{d_0} < 5$) and the longitudinal impact parameter ($|\Delta z_0 \sin \theta_\ell| < 0.5$
 567 mm). Electron candidates are required to pass TightLH identification.

568 Muon candidates are reconstructed by combining inner detector tracks with track segments
 569 or full tracks in the muon spectrometer [21]. Muon candidates are required to have $p_T > 10$ GeV
 570 and $|\eta| < 2.5$. The longitudinal impact parameter is the same for both electrons and muons, while
 571 muons are required to pass a slightly tighter transverse impact parameter, $|d_0|/\sigma_{d_0} < 3$. Muons
 572 are also required to pass Medium ID requirements.

573 Leptons are additionally required to pass a non-prompt BDT selection developed by the
 574 $t\bar{t}H$ multilepton/ $t\bar{t}W$ analysis group. This BDT and the WPs used are summarized in Appendix
 575 .1, and described in detail in [22]. Optimized working points and scale factors for this BDT are
 576 taken from that analysis.

577 7.2 Jets

578 Jets are reconstructed from calibrated topological clusters built from energy deposits in the
 579 calorimeters [23], using the anti- k_t algorithm with a radius parameter $R = 0.4$. Particle Flow, or
 580 PFlow, jets are used in the analysis, which are hadronic objects reconstructed using information
 581 from both the tracker and the calorimeter. Jets with energy contributions likely arising from noise
 582 or detector effects are removed from consideration [24], and only jets satisfying $p_T > 25$ GeV
 583 and $|\eta| < 2.5$ are used in this analysis. For jets with $p_T < 60$ GeV and $|\eta| < 2.4$, a jet-track

584 association algorithm is used to confirm that the jet originates from the selected primary vertex,
 585 in order to reject jets arising from pileup collisions [25].

586 **7.3 B-tagged Jets**

587 In order to make a measurement of $WZ +$ heavy flavor it is necessary to distinguish these events
 588 from $WZ +$ light jets. For this purpose, the DL1r b-tagging algorithm is used to distinguish
 589 heavy flavor jets from lighter ones. The DL1r algorithm uses jet kinematics, particularly jet
 590 vertex information, as input for a neural network which assigns each jet a score designed to
 591 reflect how likely that jet is to have originated from a b-quark.

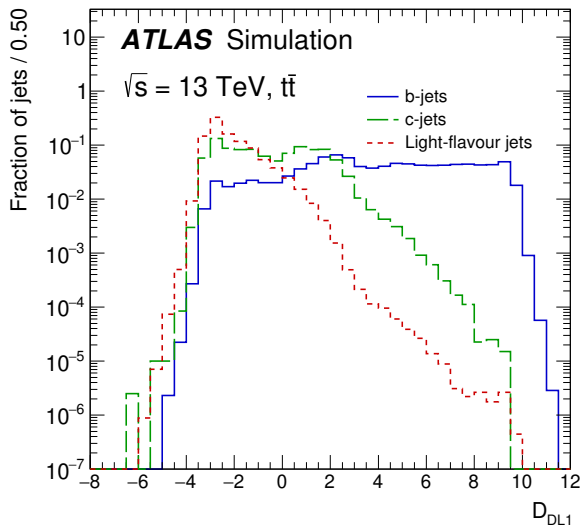


Figure 7.1: Output distribution of the DL1r algorithm for b-jets, charm jets, and light jets

592 From the output of the BDT, calibrated working points (WPs) are developed based on the
 593 efficiency of truth b-jets at particular values of the DL1r algorithm. The working points used in

594 this analysis are summarized in Table 9.

WP	none	loose	medium	tight	tightest
b eff.	-	85%	77%	70%	60%

Table 3: B-tagging Working Points by tightness and b-jet efficiency

595 A tighter WP will accept fewer b-jets, but reject a higher fraction of charm and light jets.

596 Generally, analyses that include b-jets will use a fixed working point, for example, requiring that
 597 a jet pass the 70% threshold. By instead treating these working point as bins, e.g. events with
 598 jets that fall between the 85% and 77% WPs fall into one bin, while events with jets passing the
 599 60% WP fall into another, and looking at the full psuedo-continuous DL1r spectrum of the jets,
 600 additional information can be gained. The psuedo-continuous b-tag spectrum is used in this case
 601 to separate out WZ + b, WZ + charm, and WZ + light.

602 7.4 Missing transverse energy

603 Missing transverse momentum (E_T^{miss}) is used as part of the event selection. The missing
 604 transverse momentum vector is defined as the inverse of the sum of the transverse momenta of
 605 all reconstructed physics objects as well as remaining unclustered energy, the latter of which is
 606 estimated from low- p_T tracks associated with the primary vertex but not assigned to a hard object,
 607 with object definitions taken from [26]. Light leptons considered in the E_T^{miss} reconstruction are
 608 required to have $p_T > 10 \text{ GeV}$, while jets are required to have $p_T > 20 \text{ GeV}$.

609 **7.5 Overlap removal**

610 To avoid double counting objects and remove leptons originating from decays of hadrons, overlap
 611 removal is performed in the following order: any electron candidate within $\Delta R = 0.1$ of another
 612 electron candidate with higher p_T is removed; any electron candidate within $\Delta R = 0.1$ of a muon
 613 candidate is removed; any jet within $\Delta R = 0.3$ of an electron candidate is removed; if a muon
 614 candidate and a jet lie within $\Delta R = \min(0.4, 0.04 + 10[\text{GeV}]/p_T(\text{muon}))$ of each other, the jet
 615 is kept and the muon is removed.

616 This algorithm is applied to the preselected objects. The overlap removal procedure is
 617 summarized in Table 25.

Keep	Remove	Cone size (ΔR)
electron	electron (low p_T)	0.1
muon	electron	0.1
electron	jet	0.3
jet	muon	$\min(0.4, 0.04 + 10[\text{GeV}]/p_T(\text{muon}))$
electron	tau	0.2

Table 4: Summary of the overlap removal procedure between electrons, muons, and jets.

618 **8 Event Selection and Signal Region Definitions**

619 Event are required to pass a preselection described in Section 12.1 and summarized in Table 11.
 620 Those that pass this preselection are divided into various fit regions described in Section 12.2,
 621 based on the number of jets in the event, and the b-tag score of those jets.

622 8.1 Event Preselection

623 Events are required to include exactly three reconstructed light leptons passing the requirement
 624 described in 11.1, which have a total charge of ± 1 .

625 The leptons are ordered in the analysis code as 0, 1, and 2. Lepton 0 is the lepton whose
 626 charge is opposite the other two. Lepton 1 is the lepton closest to the opposite charge lepton, i.e.
 627 the smallest ΔR , leaving lepton 2 as the lepton further from the opposite charge lepton. Lepton
 628 0 is required to have $p_T > 10$ GeV, while the same sign leptons, 1 and 2, are required to have
 629 $p_T > 20$ GeV to reduce the contribution of non-prompt leptons.

630 The invariant mass of at least one pair of opposite sign, same flavor leptons is required
 631 to fall within 10 GeV of the mass of the Z boson, 91.2 GeV. Events where one of the opposite
 632 sign pairs have an invariant mass less than 12 GeV are rejected in order to suppress low mass
 633 resonances.

634 An additional requirement is placed on the missing transverse energy, $E_T^{\text{miss}} > 20$ GeV,
 635 and the transverse mass of the W candidate, $m(E_T^{\text{miss}} + l_{\text{other}}) > 30$ GeV, where E_T^{miss} is the
 636 missing transverse energy, and l_{other} is the lepton not included in the Z-candidate.

637 Events are required to have one or two reconstructed jets passing the selection described
 638 in Section 11.2. Events with more than two jets are rejected in order to reduce the contribution
 639 of backgrounds such as $t\bar{t}Z$ and $t\bar{t}W$, which tend to have higher jet multiplicity.

Event Selection
Exactly three leptons with charge ± 1
Two same-charge leptons with $p_T > 20 \text{ GeV}$
One opposite charge lepton with $p_T > 10 \text{ GeV}$
$m(l^+l^-)$ within 10 GeV of 91.2 GeV
Transverse mass of W-candidate, $m_T(E_T^{\text{miss}} + \text{lep}_{\text{other}}) > 30 \text{ GeV}$
Missing transverse energy, $E_T^{\text{miss}} > 20 \text{ GeV}$
One or two jets with $p_T > 25 \text{ GeV}$

Table 5: Summary of the selection applied to events for inclusion in the fit

640 The event yields in the preselection region for both data and Monte Carlo are summarized
 641 in Table 12.1, which shows good agreement between data and Monte Carlo, and demonstrates
 642 that this region consists primarily of WZ events. The WZ events are split into WZ + b, WZ +
 643 c, and WZ + l based on the truth flavor of the associated jet in the event. In this ordering b-jet
 644 supersede charm, which supersides light. That is, WZ + l events contain no charm and no b jets
 645 at truth level, WZ + c contain at least one truth charm and no b-jets, and WZ + b contains at least
 646 one truth b-jet.

Process	Events
WZ + b	167.6 ± 6.5
WZ + c	1080 ± 40
WZ + l	7220 ± 310
Other VV	850 ± 140
t̄tW	16.8 ± 2.3
t̄tZ	115 ± 17
rare Top	2.2 ± 0.1
Single top	0.10 ± 0.45
Three top	0.01 ± 0.01
Four top	0.02 ± 0.01
t̄tWW	0.23 ± 0.05
Z + jets	600 ± 260
V + γ	37 ± 54
tZ	190 ± 70
tW	5.5 ± 1.2
WtZ	25.8 ± 1.1
VVV	26.2 ± 0.9
VH	94 ± 7
t̄t	108.68 ± 8
t̄tH	4.3 ± 0.5
Total	10600 ± 530
Data	10574

Table 6: Event yields in the preselection region at 139.0 fb^{-1}

647 Here Other VV represents diboson processes other than WZ, and consists predominantly
 648 of $ZZ \rightarrow ll\bar{l}\bar{l}$ events where one of the leptons is not reconstructed.

649 8.2 Fit Regions

650 Once preselection has been applied, the remaining events are categorized into one of twelve
 651 orthogonal regions. The regions used in the fit are summarized in Table 13.

Table 7: A list of the regions used in the fit and the selection used for each.

Region	Selection
1j, <85%	$N_{\text{jets}} = 1, n\text{Jets_DL1r_85} = 0$
1j, 85%-77%	$N_{\text{jets}} = 1, n\text{Jets_DL1r_85} = 1, n\text{Jets_DL1r_77}=0$
1j, 77%-70%	$N_{\text{jets}} = 1, n\text{Jets_DL1r_77} = 1, n\text{Jets_DL1r_70}=0$
1j, 70%-60%	$N_{\text{jets}} = 1, n\text{Jets_DL1r_70} = 1, n\text{Jets_DL1r_60}=0$
1j, >60%	$N_{\text{jets}} = 1, n\text{Jets_DL1r_60} = 1, tZ \text{ BDT} > 0.725$
1j tZ CR	$N_{\text{jets}} = 1, n\text{Jets_DL1r_60} = 1, tZ \text{ BDT} < 0.725$
2j, <85%	$N_{\text{jets}} = 2, n\text{Jets_DL1r_85} = 0$
2j, 85%-77%	$N_{\text{jets}} = 2, n\text{Jets_DL1r_85} >= 1, n\text{Jets_DL1r_77}=0$
2j, 77%-70%	$N_{\text{jets}} = 2, n\text{Jets_DL1r_77} >= 1, n\text{Jets_DL1r_70}=0$
2j, 70%-60%	$N_{\text{jets}} = 2, n\text{Jets_DL1r_70} >= 1, n\text{Jets_DL1r_60}=0$
2j, >60%	$N_{\text{jets}} = 2, n\text{Jets_DL1r_60} >= 1, tZ \text{ BDT} > 0.725$
2j tZ CR	$N_{\text{jets}} = 2, n\text{Jets_DL1r_60} >= 1, tZ \text{ BDT} < 0.725$

652 The working points discussed in Section 11.3 are used to separate events into fit regions
 653 based on the highest working point reached by a jet in each event. Because the background
 654 composition differs significantly based on the number of b-jets, events are further subdivided
 655 into 1-jet and 2-jet regions in order to minimize the impact of background uncertainties.

656 An unfolding procedure is performed to account for differences in the number of recon-
 657 structed jets compared to the number of truth jets in each event. In order to account for migration
 658 of WZ+1-jet and WZ+2-jet events between the 1-jet and 2-jet bins at reco level, the signal
 659 samples are separated based on the number of truth jets. Events with 0 jets or more than 3 jets at
 660 truth level, yet fall within one of the categories listed in Table 13, are categorized as WZ + other,
 661 and treated as a background. The composition of the number of truth jets in each reco jet bin is
 662 taken from MC, with uncertainties in these estimates described in detail in Section 20.

663 An additional tZ control region is created based on the BDT described in Section 13. The

664 region with 1-jet passing the 60% working point is split in two - a signal enriched region of
665 events with a BDT score greater than 0.03, and a tZ control region including events with less
666 than 0.03. This cutoff is arrived at by performing an Asimov fit with a variety of cutoffs, and
667 selecting the value that produces the highest significance for the measurement of WZ + b.

668 **8.3 Non-Prompt Lepton Estimation**

669 Two processes act as sources of non-prompt leptons appear in the analysis: $t\bar{t}$ and Z+jet
670 production both produce two prompt leptons, and each contribute to the 3l region when an
671 additional non-prompt lepton appears in the event. The contribution of these processes is
672 estimated with Monte Carlo simulations, which are validated using enriched control regions.

673 The modelling in the Z+jets and $t\bar{t}$ CRs is further validated for each of the pseudo-
674 continuous b-tag regions used in the analysis. The relevant lepton p_T spectrum in each b-tag
675 region is shown in Appendix .2 for these CRs after the correction factors derived below have
676 been applied.

677 **8.3.1 $t\bar{t}$ Validation**

678 $t\bar{t}$ events can produce two prompt leptons from the decay of each of the tops. These top decays
679 produce two b-quarks, the decay of which can produce additional non-prompt leptons, which
680 occasionally pass the event preselection. In order to validate that the Monte Carlo accurately

681 simulates this process accurately, the MC prediction in a non-prompt $t\bar{t}$ enriched control region

682 is compared to data.

683 The $t\bar{t}$ control region is similar to the preselection region - three leptons meeting the

684 criteria described in Section 12 are required, and the requirements on E_T^{miss} remain the same.

685 However, the selection requiring a lepton pair form a Z-candidate are reversed. Events where the

686 invariant mass of any two opposite sign, same flavor leptons falls within 10 GeV of 91.2 GeV are

687 rejected. This ensures the $t\bar{t}$ control region is orthogonal to the preselection region.

688 Further, because the jet multiplicity of $t\bar{t}$ events tends to be higher than WZ, the number

689 of jets in each event is required to be greater than 1. As b-jets are almost invariably produced

690 from top decays, at least one b-tagged jet passing the 70% DL1r WP in each event is required.

691 Data is compared to MC predictions in the region for a variety of kinematic variable, as well

692 as various b-tag WPs. A constant normalization discrepancy between data and MC predictions

693 of approximately 10% is found, which is accounted for by applying a constant correction factor

694 of 0.9 to the $t\bar{t}$ MC prediction. As data and MC are found to agree within 20% for each of

695 the b-tag WPs considered, a 20% systematic uncertainty on the $t\bar{t}$ prediction is included for the

696 analysis.

697 **8.3.2 Z+jets Validation**

698 Similar to $t\bar{t}$, a non-prompt Z+jets control region is produced in order to validate the MC

699 predictions. The lepton requirements remain the same as the preselection region. Because no

700 neutrinos are present for this process, the E_T^{miss} cut is reversed, requiring $E_T^{\text{miss}} < 30 \text{ GeV}$. This
 701 also ensures this control region is orthogonal to the preselection region. Further, the number of
 702 jets in each event is required to be greater than or equal to one.

703 While there is general agreement between data and MC within statistical uncertainty, the
 704 shape of the p_T spectrum of the lepton from the W is found to differ. To account for this
 705 discrepancy, a variable correction factor is applied to Z+jets. χ^2 minimization of the W lepton
 706 p_T spectrum is performed to derive a correction factor of $1.53 - 6.6 * 10^{-6}(\text{lep}_\text{Pt}_W)$.

707 The uncertainty in the Z + jets prediction is evaluated by comparing data to MC for each
 708 of the continuous b-tag WPs. For each of the regions considered, the data falls within 25% of
 709 the MC prediction once this correction factor has been applied. Therefore, a 25% systematic
 710 uncertainty is applied to Z + jets in the analysis.

711 9 tZ Interference Studies and Separation Multivariate Analysis

712 An important process to consider in this analysis is tZ: the top almost always decays into a W
 713 boson and b-quark, and when both the W and Z decay leptonically, this gives three leptons and
 714 a heavy flavor jet in the final state. Because tZ can produce a final state identical to the signal,
 715 it represents a predominant background in the most signal enriched regions. That is, the region
 716 with one jet passing the 60% DL1r WP. Therefore, a boosted decision tree (BDT) algorithm is
 717 trained using XGBoost [27] to separate WZ + heavy flavor from tZ. The result of this BDT is

⁷¹⁸ used to create a tZ enriched region in the fit, reducing its impact on the measurement of WZ +
⁷¹⁹ heavy flavor.

⁷²⁰ The following kinematic variables are used as inputs to train this BDT:

- ⁷²¹ • The invariant mass of the reconstructed top candidate
- ⁷²² • p_T of each of the leptons, jet
- ⁷²³ • The invariant mass of each combination of lepton pairs, $M(l\bar{l})$
- ⁷²⁴ • E_T^{miss}
- ⁷²⁵ • Distance between each combination of leptons, $\Delta R(l\bar{l})$
- ⁷²⁶ • Distance between each lepton and the jet, $\Delta R(lj)$

⁷²⁷ Here the top candidate is reconstructed based on the procedure described in section 6.1 of
⁷²⁸ [28]. Broadly, the mass of the top quark candidate is reconstructed from the jet, the lepton not
⁷²⁹ included in the Z-candidate, and a reconstructed neutrino. In the case that there is one jet in the
⁷³⁰ event, there is only possible b-jet candidate. For events with two jets, the jet with the highest
⁷³¹ DL1r score is used.

⁷³² The training samples included only events meeting the requirements of the 1-jet, >60%
⁷³³ region, i.e. passing all the selection described in section 12 and having exactly one jet which
⁷³⁴ passes the tightest (60%) DL1r working point. A sample of 20,000 background (tZ) and signal

735 (WZ+b) Monte Carlo events are used to train the BDT. And additional 5,000 events are reserved
 736 for testing the model, in order to prevent over-fitting. A total of 750 decision trees with a
 737 maximum depth of 6 branches are used to build the model. These parameters are chosen
 738 empirically, by training several models with different parameters and selecting the one that gave
 739 the best separation for the test sample.

740 The results of the BDT training are shown in figure 13.1. The output scores for both signal
 741 and background events is shown on the left. The right shows the receiving operating characteristic
 742 (ROC) curve that results from the MVA. The ROC curve represents the background rejection
 743 as a function of signal efficiency, where each point on the curve represents a different response
 744 score. The ROC curve of the BDT is compared to the performance of using an optimal set of flat
 745 selections on the same set of input variables.

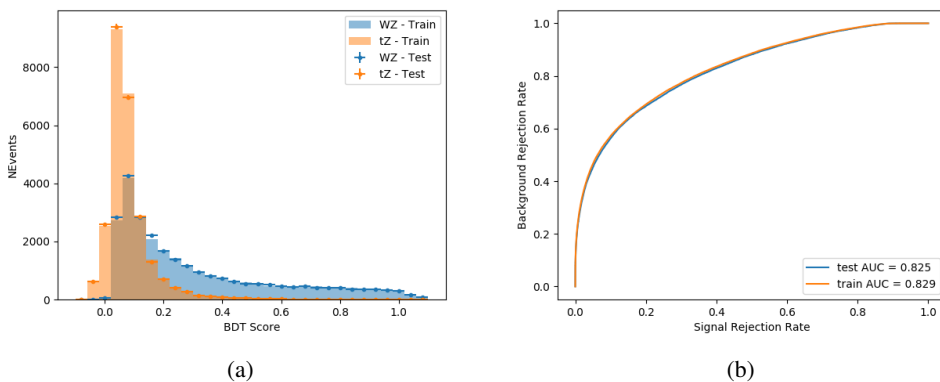


Figure 9.1: Distribution of the BDT response for signal and background events on the left, the ROC curve for the BDT on the right.

746 The relative important of each input feature in the model, measured by how often they
 747 appeared in the decision trees, is shown in figure 13.2.

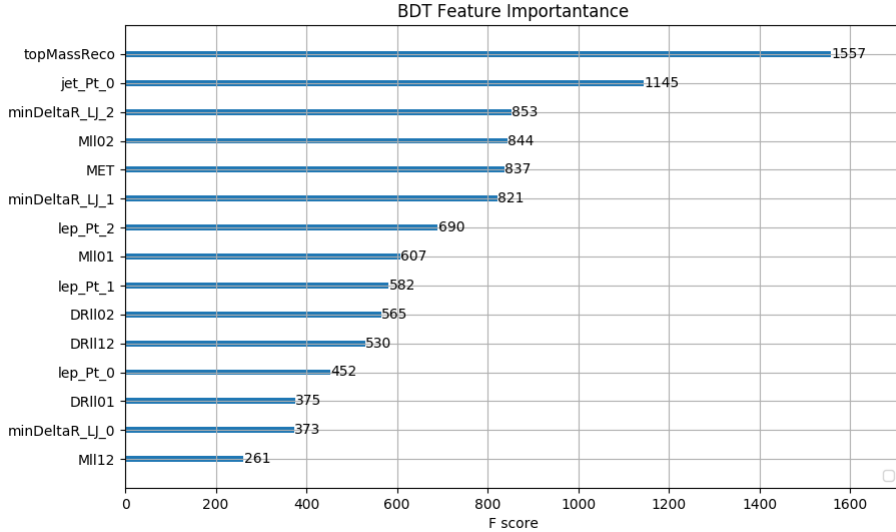


Figure 9.2: Relative importance of each input feature in the model.

748 These results suggest that some amount of separation can be achieved between these two
 749 processes, with a high BDT score selecting a set of events that is pure in $WZ + b$. A BDT score
 750 of 0.725 is selected as a cutoff, where events with scores higher than this form a signal enriched
 751 region, and events with scores lower than this form a $t\bar{Z}$ control region. This cutoff is selected by
 752 varying the value of this cutoff in stat-only Asimov fits, and selecting the value that minimizes
 753 the statistical uncertainty on $WZ + b$.

754 10 Data and Monte Carlo Samples**755 10.1 Data Samples**

756 This study uses a sample of proton-proton collision data collected by the ATLAS detector from
757 2015 through 2018 at an energy of $\sqrt{s} = 13$ TeV, which represents an integrated luminosity of
758 139 fb^{-1} . This data set was collected with a bunch crossing rate of 25 ns. All data used in this
759 analysis was verified by data quality checks.

760 10.2 Monte Carlo Samples

761 Several different generators were used to produce Monte Carlo simulations of the signal and
762 background processes. For all samples, the response of the ATLAS detector is simulated using
763 Geant4. The WZ signal samples are simulated using Sherpa 2.2.2 [15]. Specific information
764 about the Monte Carlo samples being used can be found in Table 22.

Table 8: The configurations used for event generation of signal and background processes, including the event generator, matrix element (ME) order, parton shower algorithm, and parton distribution function (PDF).

Process	Event generator	ME order	Parton Shower	PDF
WZ, VV	SHERPA 2.2.2	MEPS NLO	SHERPA	CT10
tZ	MG5_AMC	NLO	PYTHIA 8	CTEQ6L1
t̄tW	MG5_AMC (SHERPA 2.1.1)	NLO (LO multileg)	PYTHIA 8 (SHERPA)	NNPDF 3.0 NLO (NNPDF 3.0 NLO)
t̄t(Z/γ* → ll)	MG5_AMC	NLO	PYTHIA 8	NNPDF 3.0 NLO
t̄tH	MG5_AMC (MG5_AMC)	NLO (NLO)	PYTHIA 8 (HERWIG++)	NNPDF 3.0 NLO [16] (CT10 [17])
tHqb	MG5_AMC	LO	PYTHIA 8	CT10
tHW	MG5_AMC (SHERPA 2.1.1)	NLO (LO multileg)	HERWIG++ (SHERPA)	CT10 (NNPDF 3.0 NLO)
tWZ	MG5_AMC	NLO	PYTHIA 8	NNPDF 2.3 LO
t̄t̄t, t̄t̄t̄t̄	MG5_AMC	LO	PYTHIA 8	NNPDF 2.3 LO
t̄tW+W-	MG5_AMC	LO	PYTHIA 8	NNPDF 2.3 LO
t̄t	POWHEG-BOX v2 [18]	NLO	PYTHIA 8	NNPDF 3.0 NLO
t̄t̄γ	MG5_AMC	LO	PYTHIA 8	NNPDF 2.3 LO
s-, t-channel, Wt single top	POWHEG-BOX v1 [19]	NLO	PYTHIA 6	CT10
qqVV, VVV				
Z → l+l-	SHERPA 2.2.1	MEPS NLO	SHERPA	NNPDF 3.0 NLO

11 Object Reconstruction

All regions defined in this analysis share a common lepton, jet, and overall event preselection.

767 The selection applied to each physics object is detailed here; the event preselection, and the

selection used to define the various fit regions, is described in Section 12.

All events are required to be selected by dilepton triggers. The p_T thresholds of the

770 dilepton trigger on two electrons were 12 GeV in 2015, 17 GeV in 2016, and 24 GeV in 2017 and

771 2018, while for the dimuon triggers the p_T thresholds on the leading (sub-leading) muon were

772 18 GeV (8 GeV) in 2015, and 22 GeV (8 GeV) in 2016-2018. For the electron+muon triggers,

773 the p_T thresholds on the electron (muon) were 17 GeV (14 GeV) for all datasets.

774 **11.1 Light leptons**

775 Electron candidates are reconstructed from energy clusters in the electromagnetic calorimeter

776 that are associated with charged particle tracks reconstructed in the inner detector [20]. Electron

777 candidates are required to have $p_T > 10$ GeV and $|\eta_{\text{cluster}}| < 2.47$. Muon candidates are

778 reconstructed by combining inner detector tracks with track segments or full tracks in the muon

779 spectrometer [21]. Muon candidates are required to have $p_T > 10$ GeV and $|\eta| < 2.5$. Candidates

780 in the transition region between different electromagnetic calorimeter components, $1.37 <$

781 $|\eta_{\text{cluster}}| < 1.52$, are rejected. A multivariate likelihood discriminant combining shower shape

782 and track information is used to distinguish real electrons from hadronic showers (fake electrons).

783 To further reduce the non-prompt electron contribution, the track is required to be consistent

784 with originating from the primary vertex; requirements are imposed on the transverse impact

785 parameter significance ($|d_0|/\sigma_{d_0} < 5$) and the longitudinal impact parameter ($|\Delta z_0 \sin \theta_\ell| < 0.5$

786 mm). Electron candidates are required to pass TightLH identification.

787 Muon candidates are reconstructed by combining inner detector tracks with track segments

788 or full tracks in the muon spectrometer [21]. Muon candidates are required to have $p_T > 10$ GeV

789 and $|\eta| < 2.5$. The longitudinal impact parameter is the same for both electrons and muons, while

790 muons are required to pass a slightly tighter transverse impact parameter, $|d_0|/\sigma_{d_0} < 3$. Muons
791 are also required to pass Medium ID requirements.

792 Leptons are additionally required to pass a non-prompt BDT selection developed by the
793 $t\bar{t}H$ multilepton/ $t\bar{t}W$ analysis group. This BDT and the WPs used are summarized in Appendix
794 .1, and described in detail in [22]. Optimized working points and scale factors for this BDT are
795 taken from that analysis.

796 **11.2 Jets**

797 Jets are reconstructed from calibrated topological clusters built from energy deposits in the
798 calorimeters [23], using the anti- k_t algorithm with a radius parameter $R = 0.4$. Particle Flow, or
799 PFlow, jets are used in the analysis, which are hadronic objects reconstructed using information
800 from both the tracker and the calorimeter. Jets with energy contributions likely arising from noise
801 or detector effects are removed from consideration [24], and only jets satisfying $p_T > 25$ GeV
802 and $|\eta| < 2.5$ are used in this analysis. For jets with $p_T < 60$ GeV and $|\eta| < 2.4$, a jet-track
803 association algorithm is used to confirm that the jet originates from the selected primary vertex,
804 in order to reject jets arising from pileup collisions [25].

805 **11.3 B-tagged Jets**

806 In order to make a measurement of $WZ +$ heavy flavor it is necessary to distinguish these events
807 from $WZ +$ light jets. For this purpose, the DL1r b-tagging algorithm is used to distinguish

808 heavy flavor jets from lighter ones. The DL1r algorithm uses jet kinematics, particularly jet
 809 vertex information, as input for a neural network which assigns each jet a score designed to
 810 reflect how likely that jet is to have originated from a b-quark.

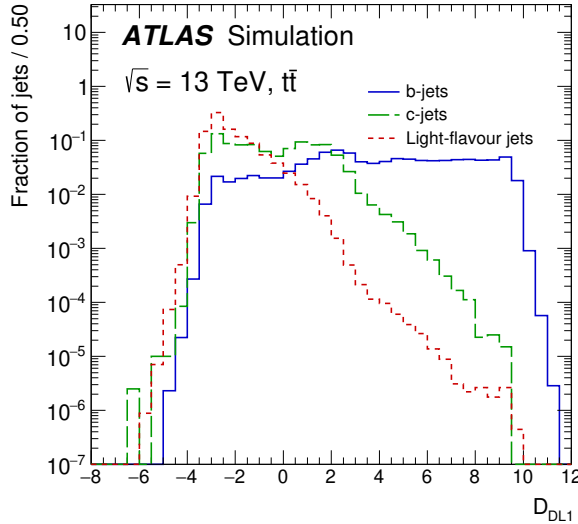


Figure 11.1: Output distribution of the DL1r algorithm for b-jets, charm jets, and light jets

811 From the output of the BDT, calibrated working points (WPs) are developed based on the
 812 efficiency of truth b-jets at particular values of the DL1r algorithm. The working points used in
 813 this analysis are summarized in Table 9.

WP	none	loose	medium	tight	tightest
b eff.	-	85%	77%	70%	60%

Table 9: B-tagging Working Points by tightness and b-jet efficiency

814 A tighter WP will accept fewer b-jets, but reject a higher fraction of charm and light jets.
 815 Generally, analyses that include b-jets will use a fixed working point, for example, requiring that

816 a jet pass the 70% threshold. By instead treating these working point as bins, e.g. events with
817 jets that fall between the 85% and 77% WPs fall into one bin, while events with jets passing the
818 60% WP fall into another, and looking at the full psuedo-continuous DL1r spectrum of the jets,
819 additional information can be gained. The psuedo-continuous b-tag spectrum is used in this case
820 to separate out WZ + b, WZ + charm, and WZ + light.

821 **11.4 Missing transverse energy**

822 Missing transverse momentum (E_T^{miss}) is used as part of the event selection. The missing
823 transverse momentum vector is defined as the inverse of the sum of the transverse momenta of
824 all reconstructed physics objects as well as remaining unclustered energy, the latter of which is
825 estimated from low- p_T tracks associated with the primary vertex but not assigned to a hard object,
826 with object definitions taken from [26]. Light leptons considered in the E_T^{miss} reconstruction are
827 required to have $p_T > 10$ GeV, while jets are required to have $p_T > 20$ GeV.

828 **11.5 Overlap removal**

829 To avoid double counting objects and remove leptons originating from decays of hadrons, overlap
830 removal is performed in the following order: any electron candidate within $\Delta R = 0.1$ of another
831 electron candidate with higher p_T is removed; any electron candidate within $\Delta R = 0.1$ of a muon
832 candidate is removed; any jet within $\Delta R = 0.3$ of an electron candidate is removed; if a muon

833 candidate and a jet lie within $\Delta R = \min(0.4, 0.04 + 10[\text{GeV}]/p_T(\text{muon}))$ of each other, the jet
834 is kept and the muon is removed.

835 This algorithm is applied to the preselected objects. The overlap removal procedure is
836 summarized in Table 25.

Keep	Remove	Cone size (ΔR)
electron	electron (low p_T)	0.1
muon	electron	0.1
electron	jet	0.3
jet	muon	$\min(0.4, 0.04 + 10[\text{GeV}]/p_T(\text{muon}))$
electron	tau	0.2

Table 10: Summary of the overlap removal procedure between electrons, muons, and jets.

837 12 Event Selection and Signal Region Definitions

838 Event are required to pass a preselection described in Section 12.1 and summarized in Table 11.
839 Those that pass this preselection are divided into various fit regions described in Section 12.2,
840 based on the number of jets in the event, and the b-tag score of those jets.

841 12.1 Event Preselection

842 Events are required to include exactly three reconstructed light leptons passing the requirement
843 described in 11.1, which have a total charge of ± 1 .

844 The leptons are ordered in the analysis code as 0, 1, and 2. Lepton 0 is the lepton whose
 845 charge is opposite the other two. Lepton 1 is the lepton closest to the opposite charge lepton, i.e.
 846 the smallest ΔR , leaving lepton 2 as the lepton further from the opposite charge lepton. Lepton
 847 0 is required to have $p_T > 10$ GeV, while the same sign leptons, 1 and 2, are required to have
 848 $p_T > 20$ GeV to reduce the contribution of non-prompt leptons.

849 The invariant mass of at least one pair of opposite sign, same flavor leptons is required
 850 to fall within 10 GeV of the mass of the Z boson, 91.2 GeV. Events where one of the opposite
 851 sign pairs have an invariant mass less than 12 GeV are rejected in order to suppress low mass
 852 resonances.

853 An additional requirement is placed on the missing transverse energy, $E_T^{\text{miss}} > 20$ GeV,
 854 and the transverse mass of the W candidate, $m(E_T^{\text{miss}} + l_{\text{other}}) > 30$ GeV, where E_T^{miss} is the
 855 missing transverse energy, and l_{other} is the lepton not included in the Z-candidate.

856 Events are required to have one or two reconstructed jets passing the selection described
 857 in Section 11.2. Events with more than two jets are rejected in order to reduce the contribution
 858 of backgrounds such as $t\bar{t}Z$ and $t\bar{t}W$, which tend to have higher jet multiplicity.

Event Selection

- Exactly three leptons with charge ± 1
 - Two same-charge leptons with $p_T > 20$ GeV
 - One opposite charge lepton with $p_T > 10$ GeV
 - $m(l^+l^-)$ within 10 GeV of 91.2 GeV
 - Transverse mass of W-candidate, $m_T(E_T^{\text{miss}} + \text{lep}_{\text{other}}) > 30$ GeV
 - Missing transverse energy, $E_T^{\text{miss}} > 20$ GeV
 - One or two jets with $p_T > 25$ GeV
-

Table 11: Summary of the selection applied to events for inclusion in the fit

859 The event yields in the preselection region for both data and Monte Carlo are summarized
 860 in Table 12.1, which shows good agreement between data and Monte Carlo, and demonstrates
 861 that this region consists primarily of WZ events. The WZ events are split into WZ + b, WZ +
 862 c, and WZ + l based on the truth flavor of the associated jet in the event. In this ordering b-jet
 863 supersede charm, which supersides light. That is, WZ + l events contain no charm and no b jets
 864 at truth level, WZ + c contain at least one truth charm and no b-jets, and WZ + b contains at least
 865 one truth b-jet.

Process	Events
WZ + b	167.6 ± 6.5
WZ + c	1080 ± 40
WZ + l	7220 ± 310
Other VV	850 ± 140
$t\bar{t}W$	16.8 ± 2.3
$t\bar{t}Z$	115 ± 17
rare Top	2.2 ± 0.1
Single top	0.10 ± 0.45
Three top	0.01 ± 0.01
Four top	0.02 ± 0.01
$t\bar{t}WW$	0.23 ± 0.05
Z + jets	600 ± 260
V + γ	37 ± 54
tZ	190 ± 70
tW	5.5 ± 1.2
WtZ	25.8 ± 1.1
VVV	26.2 ± 0.9
VH	94 ± 7
t \bar{t}	108.68 ± 8
t $\bar{t}H$	4.3 ± 0.5
Total	10600 ± 530
Data	10574

Table 12: Event yields in the preselection region at 139.0 fb^{-1}

866 Here Other VV represents diboson processes other than WZ, and consists predominantly

867 of $ZZ \rightarrow llll$ events where one of the leptons is not reconstructed.

868 12.2 Fit Regions

869 Once preselection has been applied, the remaining events are categorized into one of twelve
870 orthogonal regions. The regions used in the fit are summarized in Table 13.

Table 13: A list of the regions used in the fit and the selection used for each.

Region	Selection
1j, <85%	$N_{\text{jets}} = 1, n\text{Jets}_{\text{DL1r}_85} = 0$
1j, 85%-77%	$N_{\text{jets}} = 1, n\text{Jets}_{\text{DL1r}_85} = 1, n\text{Jets}_{\text{DL1r}_77} = 0$
1j, 77%-70%	$N_{\text{jets}} = 1, n\text{Jets}_{\text{DL1r}_77} = 1, n\text{Jets}_{\text{DL1r}_70} = 0$
1j, 70%-60%	$N_{\text{jets}} = 1, n\text{Jets}_{\text{DL1r}_70} = 1, n\text{Jets}_{\text{DL1r}_60} = 0$
1j, >60%	$N_{\text{jets}} = 1, n\text{Jets}_{\text{DL1r}_60} = 1, tZ \text{ BDT} > 0.725$
1j tZ CR	$N_{\text{jets}} = 1, n\text{Jets}_{\text{DL1r}_60} = 1, tZ \text{ BDT} < 0.725$
2j, <85%	$N_{\text{jets}} = 2, n\text{Jets}_{\text{DL1r}_85} = 0$
2j, 85%-77%	$N_{\text{jets}} = 2, n\text{Jets}_{\text{DL1r}_85} \geq 1, n\text{Jets}_{\text{DL1r}_77} = 0$
2j, 77%-70%	$N_{\text{jets}} = 2, n\text{Jets}_{\text{DL1r}_77} \geq 1, n\text{Jets}_{\text{DL1r}_70} = 0$
2j, 70%-60%	$N_{\text{jets}} = 2, n\text{Jets}_{\text{DL1r}_70} \geq 1, n\text{Jets}_{\text{DL1r}_60} = 0$
2j, >60%	$N_{\text{jets}} = 2, n\text{Jets}_{\text{DL1r}_60} \geq 1, tZ \text{ BDT} > 0.725$
2j tZ CR	$N_{\text{jets}} = 2, n\text{Jets}_{\text{DL1r}_60} \geq 1, tZ \text{ BDT} < 0.725$

871 The working points discussed in Section 11.3 are used to separate events into fit regions
872 based on the highest working point reached by a jet in each event. Because the background
873 composition differs significantly based on the number of b-jets, events are further subdivided
874 into 1-jet and 2-jet regions in order to minimize the impact of background uncertainties.

875 An unfolding procedure is performed to account for differences in the number of recon-
876 structed jets compared to the number of truth jets in each event. In order to account for migration

877 of WZ+1-jet and WZ+2-jet events between the 1-jet and 2-jet bins at reco level, the signal
878 samples are separated based on the number of truth jets. Events with 0 jets or more than 3 jets at
879 truth level, yet fall within one of the categories listed in Table 13, are categorized as WZ + other,
880 and treated as a background. The composition of the number of truth jets in each reco jet bin is
881 taken from MC, with uncertainties in these estimates described in detail in Section 20.

882 An additional tZ control region is created based on the BDT described in Section 13. The
883 region with 1-jet passing the 60% working point is split in two - a signal enriched region of
884 events with a BDT score greater than 0.03, and a tZ control region including events with less
885 than 0.03. This cutoff is arrived at by performing an Asimov fit with a variety of cutoffs, and
886 selecting the value that produces the highest significance for the measurement of WZ + b.

887 **12.3 Non-Prompt Lepton Estimation**

888 Two processes act as sources of non-prompt leptons appear in the analysis: $t\bar{t}$ and Z+jet
889 production both produce two prompt leptons, and each contribute to the 31 region when an
890 additional non-prompt lepton appears in the event. The contribution of these processes is
891 estimated with Monte Carlo simulations, which are validated using enriched control regions.

892 The modelling in the Z+jets and $t\bar{t}$ CRs is further validated for each of the pseudo-
893 continuous b-tag regions used in the analysis. The relevant lepton p_T spectrum in each b-tag
894 region is shown in Appendix .2 for these CRs after the correction factors derived below have
895 been applied.

896 12.3.1 $t\bar{t}$ Validation

897 $t\bar{t}$ events can produce two prompt leptons from the decay of each of the tops. These top decays
 898 produce two b-quarks, the decay of which can produce additional non-prompt leptons, which
 899 occasionally pass the event preselection. In order to validate that the Monte Carlo accurately
 900 simulates this process accurately, the MC prediction in a non-prompt $t\bar{t}$ enriched control region
 901 is compared to data.

902 The $t\bar{t}$ control region is similar to the preselection region - three leptons meeting the
 903 criteria described in Section 12 are required, and the requirements on E_T^{miss} remain the same.
 904 However, the selection requiring a lepton pair form a Z-candidate are reversed. Events where the
 905 invariant mass of any two opposite sign, same flavor leptons falls within 10 GeV of 91.2 GeV are
 906 rejected. This ensures the $t\bar{t}$ control region is orthogonal to the preselection region.

907 Further, because the jet multiplicity of $t\bar{t}$ events tends to be higher than WZ, the number
 908 of jets in each event is required to be greater than 1. As b-jets are almost invariably produced
 909 from top decays, at least one b-tagged jet passing the 70% DL1r WP in each event is required.

910 Data is compared to MC predictions in the region for a variety of kinematic variable, as well
 911 as various b-tag WPs. A constant normalization discrepancy between data and MC predictions
 912 of approximately 10% is found, which is accounted for by applying a constant correction factor
 913 of 0.9 to the $t\bar{t}$ MC prediction. As data and MC are found to agree within 20% for each of
 914 the b-tag WPs considered, a 20% systematic uncertainty on the $t\bar{t}$ prediction is included for the
 915 analysis.

916 **12.3.2 Z+jets Validation**

917 Similar to $t\bar{t}$, a non-prompt Z +jets control region is produced in order to validate the MC
 918 predictions. The lepton requirements remain the same as the preselection region. Because no
 919 neutrinos are present for this process, the E_T^{miss} cut is reversed, requiring $E_T^{\text{miss}} < 30 \text{ GeV}$. This
 920 also ensures this control region is orthogonal to the preselection region. Further, the number of
 921 jets in each event is required to be greater than or equal to one.

922 While there is general agreement between data and MC within statistical uncertainty, the
 923 shape of the p_T spectrum of the lepton from the W is found to differ. To account for this
 924 discrepancy, a variable correction factor is applied to Z +jets. χ^2 minimization of the W lepton
 925 p_T spectrum is performed to derive a correction factor of $1.53 - 6.6 * 10^{-6}(\text{lep}_\text{Pt}_W)$.

926 The uncertainty in the $Z + \text{jets}$ prediction is evaluated by comparing data to MC for each
 927 of the continuous b-tag WPs. For each of the regions considered, the data falls within 25% of
 928 the MC prediction once this correction factor has been applied. Therefore, a 25% systematic
 929 uncertainty is applied to $Z + \text{jets}$ in the analysis.

930 **13 tZ Interference Studies and Separation Multivariate Analysis**

931 An important process to consider in this analysis is tZ : the top almost always decays into a W
 932 boson and b-quark, and when both the W and Z decay leptonically, this gives three leptons and
 933 a heavy flavor jet in the final state. Because tZ can produce a final state identical to the signal,

934 it represents a predominant background in the most signal enriched regions. That is, the region
 935 with one jet passing the 60% DL1r WP. Therefore, a boosted decision tree (BDT) algorithm is
 936 trained using XGBoost [27] to separate WZ + heavy flavor from tZ. The result of this BDT is
 937 used to create a tZ enriched region in the fit, reducing its impact on the measurement of WZ +
 938 heavy flavor.

939 The following kinematic variables are used as inputs to train this BDT:

- 940 • The invariant mass of the reconstructed top candidate
- 941 • p_T of each of the leptons, jet
- 942 • The invariant mass of each combination of lepton pairs, $M(l\bar{l})$
- 943 • E_T^{miss}
- 944 • Distance between each combination of leptons, $\Delta R(l\bar{l})$
- 945 • Distance between each lepton and the jet, $\Delta R(lj)$

946 Here the top candidate is reconstructed based on the procedure described in section 6.1 of
 947 [28]. Broadly, the mass of the top quark candidate is reconstructed from the jet, the lepton not
 948 included in the Z-candidate, and a reconstructed neutrino. In the case that there is one jet in the
 949 event, there is only possible b-jet candidate. For events with two jets, the jet with the highest
 950 DL1r score is used.

951 The training samples included only events meeting the requirements of the 1-jet, >60%
952 region, i.e. passing all the selection described in section 12 and having exactly one jet which
953 passes the tightest (60%) DL1r working point. A sample of 20,000 background (tZ) and signal
954 (WZ+b) Monte Carlo events are used to train the BDT. And additional 5,000 events are reserved
955 for testing the model, in order to prevent over-fitting. A total of 750 decision trees with a
956 maximum depth of 6 branches are used to build the model. These parameters are chosen
957 empirically, by training several models with different parameters and selecting the one that gave
958 the best separation for the test sample.

959 The results of the BDT training are shown in figure 13.1. The output scores for both signal
960 and background events is shown on the left. The right shows the receiving operating characteristic
961 (ROC) curve that results from the MVA. The ROC curve represents the background rejection
962 as a function of signal efficiency, where each point on the curve represents a different response
963 score. The ROC curve of the BDT is compared to the performance of using an optimal set of flat
964 selections on the same set of input variables.

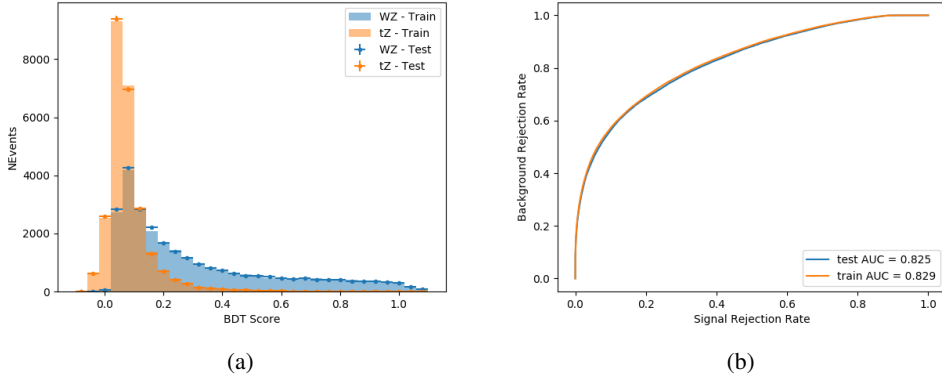


Figure 13.1: Distribution of the BDT response for signal and background events on the left, the ROC curve for the BDT on the right.

965 The relative important of each input feature in the model, measured by how often they
 966 appeared in the decision trees, is shown in figure 13.2.

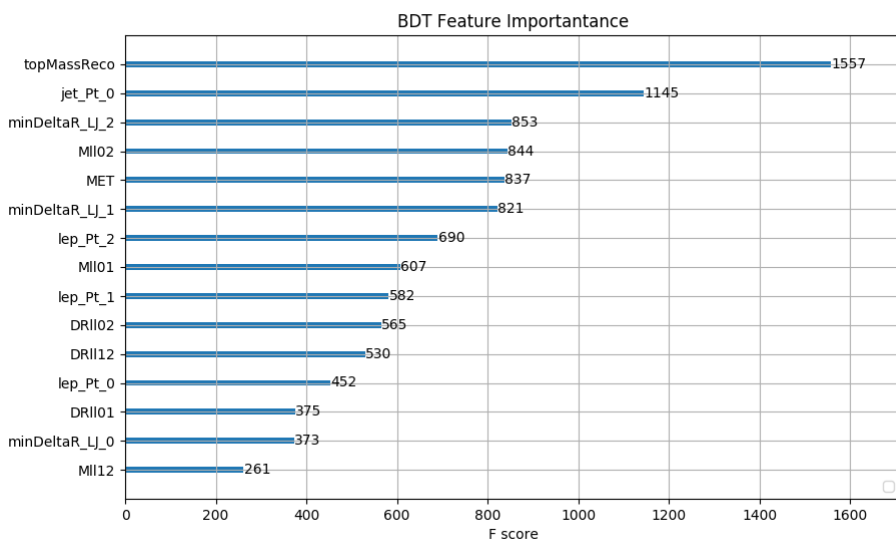


Figure 13.2: Relative importance of each input feature in the model.

967 These results suggest that some amount of separation can be achieved between these two
968 processes, with a high BDT score selecting a set of events that is pure in $WZ + b$. A BDT score
969 of 0.725 is selected as a cutoff, where events with scores higher than this form a signal enriched
970 region, and events with scores lower than this form a $t\bar{Z}$ control region. This cutoff is selected by
971 varying the value of this cutoff in stat-only Asimov fits, and selecting the value that minimizes
972 the statistical uncertainty on $WZ + b$.

973 **14 Systematic Uncertainties**

974 The systematic uncertainties that are considered are summarized in Table 43. These are imple-
975 mented in the fit either as a normalization factors or as a shape variation or both in the signal
976 and background estimations. The numerical impact of each of these uncertainties is outlined in
977 Section 21.

Table 14: Sources of systematic uncertainty considered in the analysis.

Systematic uncertainty	Components
Luminosity	1
Pileup reweighting	1
Physics Objects	
Electron	6
Muon	15
Jet energy scale	28
Jet energy resolution	8
Jet vertex fraction	1
Jet flavor tagging	131
E_T^{miss}	3
Total (Experimental)	194
Signal Modeling	
Shape modelling	3
Renormalization and factorization scales	5
nJet Migration	5
Background Modeling	
Cross section	15
Renormalization and factorization scales	12
Total (Signal and background modeling)	35
Total (Overall)	230

978 The uncertainty in the combined integrated luminosity is derived from a calibration of the
 979 luminosity scale performed for 13 TeV proton-proton collisions [29], [30].

980 The experimental uncertainties are related to the reconstruction and identification of light
 981 leptons and b-tagging of jets, and to the reconstruction of E_T^{miss} . The sources which contribute to
 982 the uncertainty in the jet energy scale (JES) [31] are decomposed into uncorrelated components
 983 and treated as independent sources of uncertainty in the analysis. These are treated as 30
 984 nuisance parameters included in the fit. A similar approach is used for the jet energy resolution

985 (JER) uncertainty, which is decomposed into 8 JER uncertainty components included as NPs in
986 the fit.

987 The uncertainties in the b-tagging efficiencies measured in dedicated calibration analyses
988 [32] are also decomposed into uncorrelated components. The large number of components for
989 b-tagging is due to the calibration of the distribution of the MVA discriminant.

990 Theoretical uncertainties applied to MC predictions, including cross section, PDF, and scale
991 uncertainties are taken from theory calculations, with the exception of non-prompt and dibo-
992 son backgrounds. The cross-section uncertainty on tZ is taken from [33]. Derivation of the
993 non-prompt background uncertainties, Z+jets and tt>, are explained in Section 12.3. These
994 normalization uncertainties are chosen so as to account for the complete uncertainty in the
995 non-prompt contribution, and therefore no additional modelling uncertainties are considered for
996 Z+jets and tt>.

997 The other VV + heavy flavor processes (namely VV+b and VV+charm, which primarily
998 consist of ZZ events) are also poorly understood, because these processes involve the same
999 physics as WZ + heavy flavor, and have also not been measured. Therefore, a conservative 50%
1000 uncertainty is applied to those samples. While this uncertainty is large, it is found to have little
1001 impact on the significance of the final result.

1002 The theory uncertainties applied to the predominate background estimates are summarized
1003 in Table 48.

Process	X-section [%]
tZ	X-sec: ± 15.2 QCD Scale: $^{+5.2}_{-1.3}$ PDF($+\alpha_S$): ± 1.2
t̄t H (aMC@NLO+Pythia8)	QCD Scale: $^{+5.8}_{-9.2}$ PDF($+\alpha_S$): ± 3.6
t̄t Z (aMC@NLO+Pythia8)	QCD Scale: $^{+9.6}_{-11.3}$ PDF($+\alpha_S$): ± 4
t̄t W (aMC@NLO+Pythia8)	QCD Scale: $^{+12.9}_{-11.5}$ PDF($+\alpha_S$): ± 3.4
VV + b/charm (Sherpa 2.2.1)	± 50
VV + light (Sherpa 2.2.1)	± 6
t̄t	± 20
Z + jets	± 25
Others	± 50

Table 15: Summary of theoretical uncertainties for MC predictions in the analysis.

1004 Additional signal uncertainties are estimated by comparing estimates from the nominal Sherpa
 1005 WZ samples with alternate WZ samples generated with Powheg+PYTHIA8. Separate systemat-
 1006 ics are included in the fit for WZ + b, WZ + charm and WZ + light, where the distribution among
 1007 each of the fit regions is varied based on the prediction of the Powheg sample.

1008 A similar approach is taken to account for uncertainties in migrations between the number of
 1009 reco and truth jets. The fraction of events with 1 truth jet which fall into the 1 jet bin versus the
 1010 2 jet bin at reco level is compared for Sherpa and Powheg. The same is done for events with 2
 1011 truth jets. A systematic is included where events are shifted between the 1-jet and 2-jet regions
 1012 based on the differences between these two shapes. This is done independently for each of the
 1013 WZ + b, WZ + charm, and WZ + light templates.

1014 Additional systematics are included to account for the uncertainty in the contamination of
 1015 0 jet and 3 or more jet events (as defined at truth level) in the 1 and 2 reco jet bins. Because these
 1016 events fall outside the scope of this measurement, these events are included as a background.
 1017 As such, a normalization, rather than a shape, uncertainty is applied for this background. The
 1018 number of WZ events with 0-jets and $>=3$ -jets in the reconstructed 1-jet and 2-jet regions are
 1019 compared for Sherpa and Powheg, and these differences are taken as separate normalization
 1020 systematics on the yield of WZ+0-jet and WZ+ $>=3$ -jet events.

1021 15 Results

1022 A separate maximum-likelihood fit is performed over the 1-jet and 2-jet fit regions in order to
 1023 extract the best-fit value of the WZ + b-jet and WZ + charm jet contributions. The WZ + b,
 1024 WZ + charm and WZ + light contributions are allowed to float, with the remaining background
 1025 contributions are held fixed. **The current fit strategy treats the WZ + b-jet contribution as**
 1026 **the parameter of interest, with the normalization of the WZ + charm and the WZ + light**
 1027 **contributions taken as systematic uncertainties. This could however be adjusted, depending**
 1028 **on whether it is decided the goal of the analysis should be to measure WZ+b specifically or**
 1029 **WZ + heavy flavor overall.** The result of the fit is used to extract the cross-section of WZ +
 1030 heavy-flavor production.

1031 A maximum likelihood fit to data is performed simultaneously in the regions described
 1032 in Section 12. The parameters μ_{WZ+b} , $\mu_{WZ+charm}$, $\mu_{WZ+light}$, where $\mu = \sigma_{\text{observed}}/\sigma_{\text{SM}}$, are

1033 extracted from the fit.

1034 The Asimov fit for 1-jet events gives an expected μ value of $1.00^{+0.37}_{-0.35}(\text{stat})^{+0.24}_{-0.22}(\text{sys})$ for
 1035 WZ + b. The fitted cross-section modifiers for WZ + charm and WZ + light are $1.00 \pm 0.17 \pm 0.15$
 1036 and $1.00 \pm 0.04 \pm 0.07$, respectively.

1037 The expected cross-section of WZ+b with 1 associated jet obtained from the fit is
 1038 $1.74^{+0.65}_{-0.61}(\text{stat})^{+0.42}_{-0.37}(\text{sys})$ fb with an expected significance of 2.2σ . The expected cross-sectin
 1039 of WZ + charm is measured to be $14.6 \pm 2.5(\text{stat}) \pm 2.1(\text{sys})$ fb, with a correlation of -0.23.

1040 For 2-jet events, the fit gives an expected μ value of $1.00^{+0.34}_{-0.33}(\text{stat})^{+0.29}_{-0.28}(\text{sys})$ for WZ +
 1041 b. The fitted cross-section modifiers for WZ + charm and WZ + light are $1.00 \pm 0.17 \pm 0.15$ and
 1042 $1.00 \pm 0.04 \pm 0.08$, respectively.

1043 The expected WZ + b cross-section in the 2-jet region is $2.46^{+0.83}_{-0.81}(\text{stat})^{+0.073}_{-0.68}(\text{sys})$ fb
 1044 with an expected significance of 2.6σ . The 2-jet expected cross-section of WZ + charm is
 1045 $12.7 \pm 2.2(\text{stat}) \pm 2.0(\text{sys})$ fb, and the correlation between WZ + charm and WZ + b is -0.26.

1046 15.1 1-jet Fit Results

1047 **The results of the fit are currently blinded.**

1048 The pre-fit yields in each of the regions used in the fit are shown in Table 15.1, and
 1049 summarized in Figure 15.1.

Sample	1j, <85% WP	1j, 77%-85% WP	1j, 70%-77% WP	1j, 60%-70% WP	1j, >60% WP	tZ CR
WZ + b - 1j	8.1 ± 1.6	4.7 ± 0.5	4.6 ± 0.4	5.1 ± 0.4	18.2 ± 2.4	4.8 ± 0.6
WZ + c - 1j	260 ± 22	81 ± 6	43.1 ± 3.6	25.8 ± 2.6	9.4 ± 1.8	2.9 ± 0.6
WZ + l - 1j	3090 ± 250	91 ± 13	17 ± 3	4.9 ± 1.6	1.3 ± 0.4	0.2 ± 0.1
WZ + b - 2j	1.10 ± 0.37	0.44 ± 0.11	0.39 ± 0.06	0.62 ± 0.14	2.1 ± 0.5	0.59 ± 0.14
WZ + c - 2j	21 ± 5	5.6 ± 1.2	3.0 ± 0.7	2.0 ± 0.5	0.70 ± 0.20	0.30 ± 0.08
WZ + l - 2j	250 ± 60	5.7 ± 1.6	0.73 ± 0.53	0.31 ± 0.15	0.07 ± 0.06	0.01 ± 0.01
WZ - Other	13 ± 5	1.4 ± 0.4	0.42 ± 0.08	0.2 ± 0.01	0.30 ± 0.05	0.67 ± 0.15
Other VV	6.2 ± 0.6	0.2 ± 0.4	0.2 ± 0.04	0.07 ± 0.1	0.1 ± 0.1	0.1 ± 0.2
ZZ	336 ± 26	17.8 ± 2.1	4.3 ± 0.6	1.7 ± 0.5	0.36 ± 0.08	0.10 ± 0.03
t̄W	1.1 ± 0.2	0.2 ± 0.1	0.3 ± 0.1	0.4 ± 0.1	1.5 ± 0.3	0.7 ± 0.2
t̄Z	6.8 ± 1.2	1.4 ± 0.3	1.0 ± 0.2	1.2 ± 0.2	4.4 ± 0.8	3.2 ± 0.6
Z + jets	169 ± 38	8.9 ± 1.9	3.7 ± 0.8	3.3 ± 0.7	3.2 ± 0.7	0.8 ± 0.17
V + γ	45 ± 28	1.9 ± 2.4	0.1 ± 0.1	0.02 ± 0.01	1.0 ± 0.9	0.02 ± 0.03
tZ	24.3 ± 4.3	5.5 ± 1.1	4.1 ± 0.8	5.9 ± 1.1	10.7 ± 2.0	23 ± 4
tW	1.4 ± 0.8	0.2 ± 0.5	0.0 ± 0.2	0.7 ± 0.6	0.26 ± 0.42	0.39 ± 0.41
WtZ	2.3 ± 1.2	0.6 ± 0.3	0.3 ± 0.21	0.27 ± 0.2	1.1 ± 0.7	0.6 ± 0.5
VVV	12.4 ± 0.5	0.93 ± 0.06	0.35 ± 0.03	0.13 ± 0.02	0.14 ± 0.03	0.02 ± 0.01
VH	40 ± 6	2.6 ± 1.4	0.9 ± 0.8	0.7 ± 0.8	0.5 ± 0.6	0.0 ± 0.0
t̄t	12.1 ± 1.6	2.9 ± 0.6	2.5 ± 0.5	2.8 ± 0.5	11.2 ± 1.4	10.9 ± 1.5
t̄tH	0.24 ± 0.03	0.05 ± 0.01	0.04 ± 0.01	0.06 ± 0.01	0.20 ± 0.03	0.13 ± 0.02
Total	5010 ± 260	227 ± 24	88 ± 12	57 ± 8	76 ± 16	53 ± 8

Table 16: Pre-fit yields in each of the 1-jet fit regions.

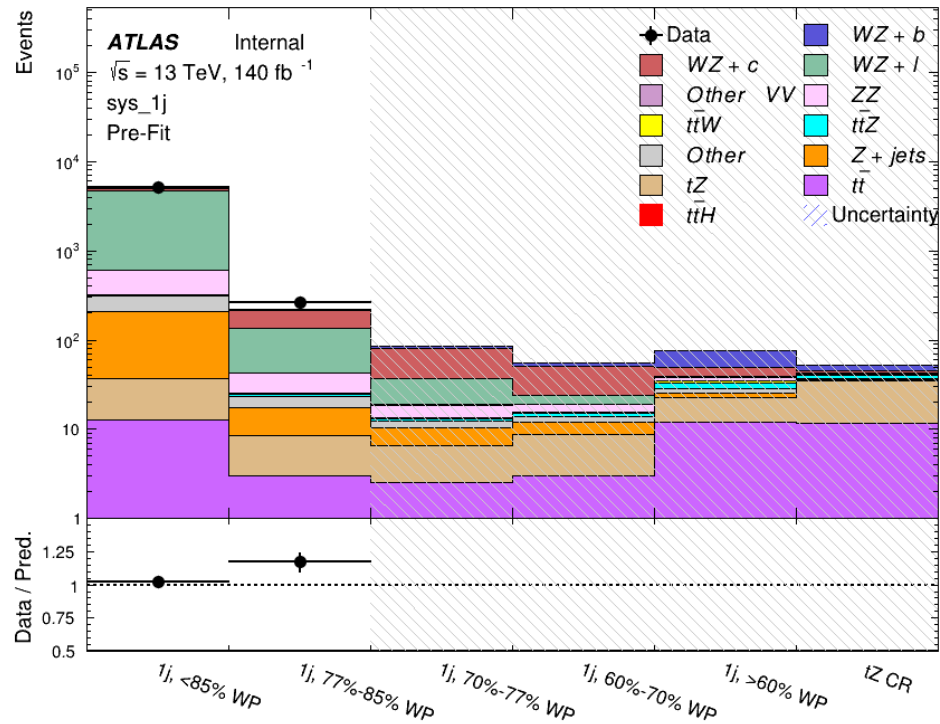


Figure 15.1: Pre-fit summary of the 1-jet fit regions.

1051

The post-fit yields in each region are summarized in Figure 15.1.

1052

	1j, <85% WP	1j, 77%-85% WP	1j, 70%-77% WP	1j, 60%-70% WP	1j, >60% WP	tZ CR
WZ + b	8.1 ± 4.9	4.7 ± 2.0	4.6 ± 2.0	5.1 ± 2.1	18 ± 10	5.0 ± 2.5
WZ + c	260 ± 60	80 ± 14	43 ± 7	26 ± 5	9.4 ± 2.3	2.9 ± 0.7
WZ + l	3090 ± 130	90 ± 11	17.3 ± 2.8	4.9 ± 1.6	1.3 ± 0.4	0.23 ± 0.1
WZ + b - 2j	1.10 ± 0.37	0.44 ± 0.11	0.39 ± 0.06	0.62 ± 0.14	2.1 ± 0.5	0.59 ± 0.1
WZ + c - 2j	21 ± 5	5.6 ± 1.2	3.0 ± 0.7	2.0 ± 0.5	0.70 ± 0.20	0.30 ± 0.0
WZ + l - 2j	250 ± 60	5.7 ± 1.6	0.73 ± 0.53	0.31 ± 0.15	0.07 ± 0.06	0.01 ± 0.0
WZ - Other	13 ± 5	1.4 ± 0.4	0.42 ± 0.08	0.2 ± 0.01	0.30 ± 0.05	0.67 ± 0.1
Other VV	6.2 ± 0.6	0.92 ± 0.07	0.02 ± 0.01	0.01 ± 0.01	0.01 ± 0.01	0.01 ± 0.0
ZZ	346 ± 57	19 ± 5	4.3 ± 0.8	2.7 ± 0.5	2.4 ± 0.1	2.1 ± 0.6
t̄tW	1.09 ± 0.21	0.2 ± 0.1	0.1 ± 0.1	0.4 ± 0.1	1.5 ± 0.3	0.1 ± 0.2
t̄tZ	6.8 ± 1.2	1.4 ± 0.3	1.0 ± 0.2	1.2 ± 0.2	4.4 ± 0.7	3.2 ± 0.5
rare Top	0.14 ± 0.04	0.04 ± 0.02	0.04 ± 0.0	0.1 ± 0.03	0.14 ± 0.04	0.15 ± 0.0
t̄tWW	0.04 ± 0.03	0.01 ± 0.02	0.01 ± 0.01	0.01 ± 0.01	0.01 ± 0.02	0.01 ± 0.0
Z + jets	169 ± 37	8.9 ± 1.9	3.7 ± 0.8	3.3 ± 0.7	3.2 ± 0.7	0.8 ± 0.2
W + jets	0.01 ± 0.01	0.01 ± 0.0				
V + γ	46 ± 28	1.9 ± 2.4	0.1 ± 0.1	0.0 ± 0.2	1.0 ± 0.9	0.0 ± 0.0
tZ	24 ± 4	5.5 ± 1.0	4.1 ± 0.8	5.9 ± 1.1	10.7 ± 1.8	23.3 ± 3.7
tW	1.37 ± 0.82	0.18 ± 0.26	0.01 ± 0.12	0.67 ± 0.64	0.26 ± 0.42	0.39 ± 0.4
WtZ	2.3 ± 1.2	0.6 ± 0.3	0.3 ± 0.2	0.3 ± 0.2	1.1 ± 0.6	0.6 ± 0.3
VVV	12.4 ± 0.4	0.9 ± 0.1	0.4 ± 0.1	0.13 ± 0.02	0.14 ± 0.03	0.02 ± 0.0
VH	40 ± 6	2.6 ± 1.4	0.9 ± 0.8	0.7 ± 0.8	0.4 ± 0.6	0.01 ± 0.0
t̄t	12.1 ± 1.6	2.9 ± 0.6	2.5 ± 0.5	2.8 ± 0.5	11.2 ± 1.5	10.9 ± 1.4
t̄tH	0.24 ± 0.03	0.05 ± 0.01	0.04 ± 0.01	0.06 ± 0.01	0.20 ± 0.03	0.13 ± 0.0
Total	5100 ± 110	227 ± 12	87 ± 6	56.7 ± 4.4	76 ± 9	52.5 ± 4.2

Table 17: Post-fit yields in each of the 1-jet fit regions.

1053

A post-fit summary plot of the 1-jet fitted regions is shown in Figure 15.2:

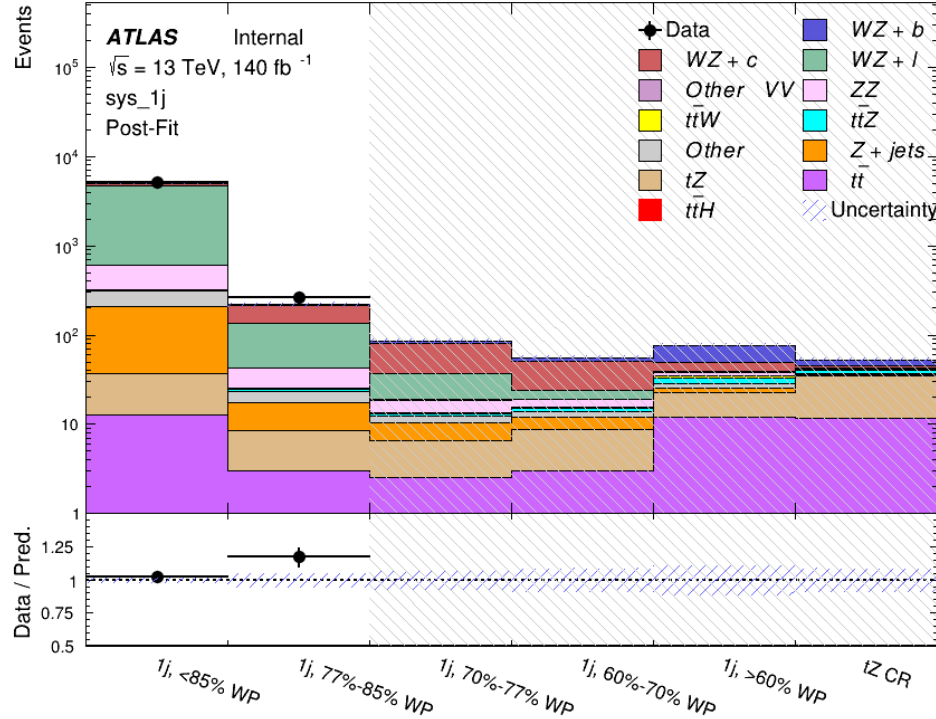


Figure 15.2: Post-fit summary of the 1-jet fit regions.

1054 As described in Section 20, there are 226 systematic uncertainties that are considered
 1055 as NPs in the fit. These NPs are constrained by Gaussian or log-normal probability density
 1056 functions. The latter are used for normalisation factors to ensure that they are always positive.
 1057 The expected number of signal and background events are functions of the likelihood. The prior
 1058 for each NP is added as a penalty term, decreasing the likelihood as it is shifted away from its
 1059 nominal value.

1060 The impact of each NP is calculated by performing the fit with the parameter of interest held
 1061 fixed, varied from its fitted value by its uncertainty, and calculating $\Delta\mu$ relative to the baseline

1062 fit. The impact of the most significant sources of systematic uncertainties is summarized in Table

1063 [18.](#)

Uncertainty Source	$\Delta\mu$	
WZ + light cross-section	0.13	-0.12
WZ + charm cross-section	-0.10	0.12
Jet Energy Scale	0.08	0.13
tZ cross-section	-0.10	0.10
Jet Energy Resolution	-0.10	0.10
Luminosity	-0.08	0.09
Other Diboson + b cross-section	-0.07	0.07
Flavor tagging	0.05	0.05
t <bar>t} cross-section</bar>	-0.05	0.05
WZ cross-section - QCD scale	-0.04	0.03
Total Systematic Uncertainty	0.28	0.32

Table 18: Summary of the most significant sources of systematic uncertainty on the measurement of WZ + b with exactly one associated jet.

1064 The ranking and impact of those nuisance parameters with the largest contribution to the

1065 overall uncertainty is shown in Figure [15.3](#).

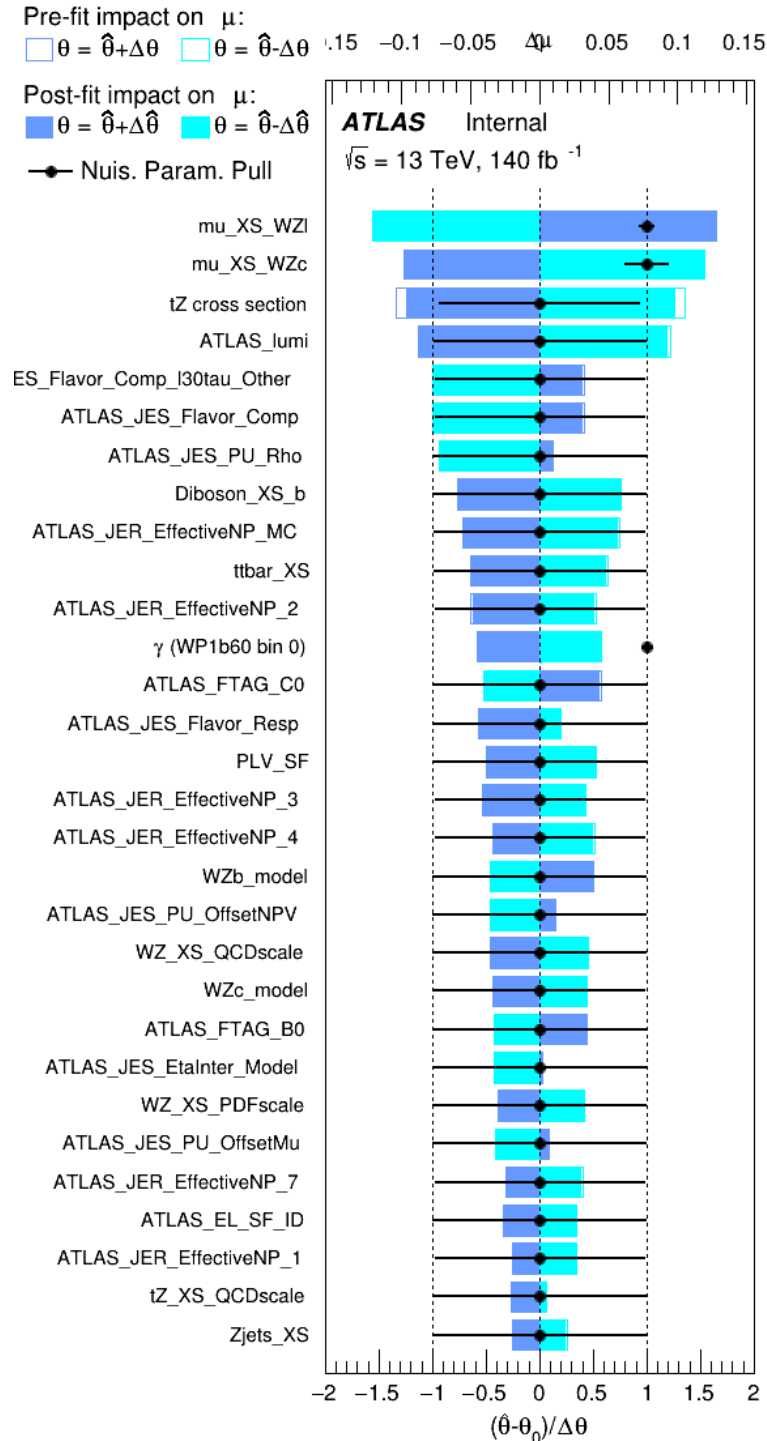


Figure 15.3: Impact of systematic uncertainties on the signal-strength of $WZ + b$ for events with exactly one jet

1066 The large impact of the Jet Energy Scale and Jet Flavor Tagging is unsurprising, as the
 1067 shape of the fit regions depends heavily on the modeling of the jets. The other major sources
 1068 of uncertainty come from background modelling and cross-section uncertainty. The pie charts
 1069 in Figure 15.4 show that for the modelling uncertainties that contribute most correspond to the
 1070 most significant backgrounds.

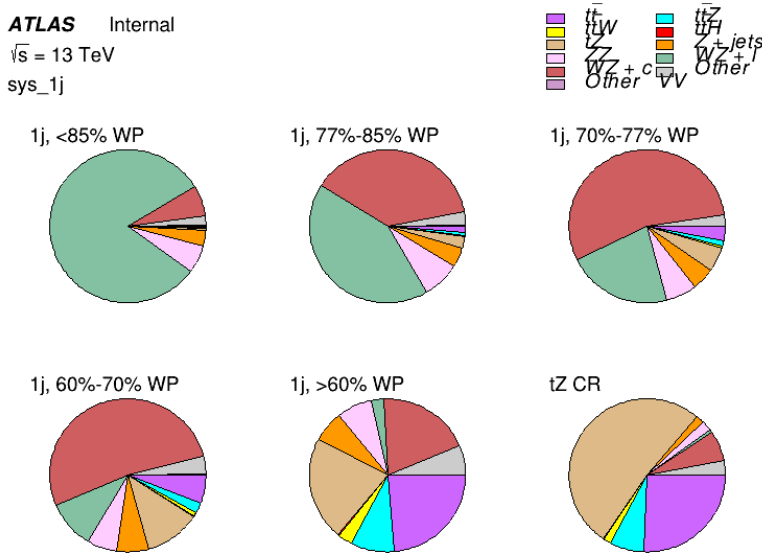


Figure 15.4: Post-fit background composition of the fit regions.

1071 The correlations between these nuisance parameters are summarized in Figure 15.5.

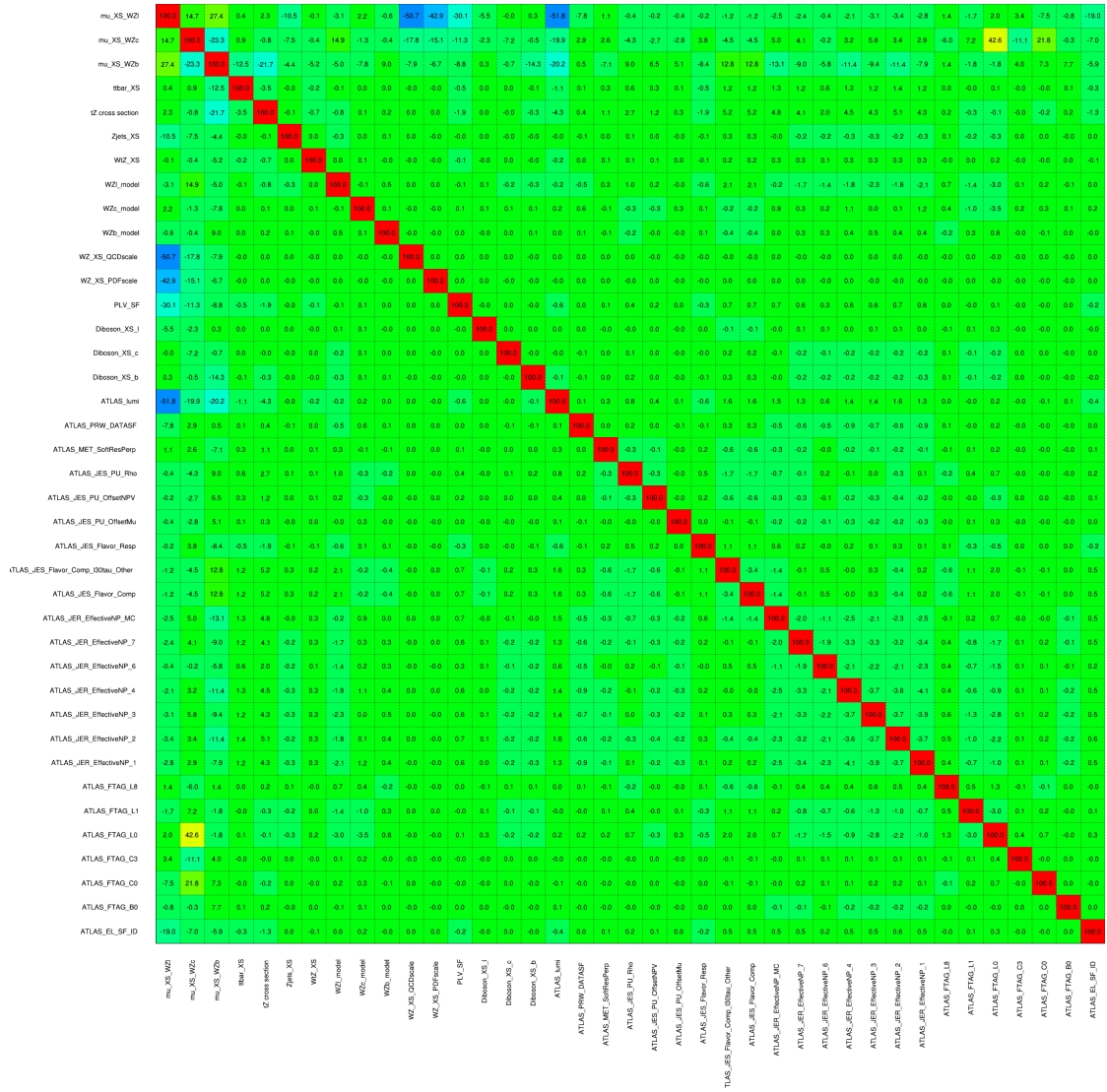


Figure 15.5: Correlations between nuisance parameters

1072 The negative correlations between $\mu_{WZ+charm}$ and μ_{WZ+b} and $\mu_{WZ+light}$ are expected:
1073 WZ + charm is present in both the WZ + b and WZ + light enriched regions, therefore increasing
1074 the fraction of charm requires increasing the fraction of WZ + b and WZ + light. This reasoning
1075 also explains the positive correlation between μ_{WZ+b} and $\mu_{WZ+light}$.

1076 Two of the major backgrounds in the region with the highest purity of $WZ + b$ are tZ and
1077 Other $VV + b$, explaining the negative correlations between μ_{WZ+b} and the tZ cross section, and
1078 the $VV + b$ cross section.

1079 The high correlation between the luminosity and $\mu_{WZ+light}$ arises from the fact that the
1080 uncertainty on $\mu_{WZ+light}$ is very low (around 4%). Small changes in luminosity cause a change
1081 in the yield of $WZ + light$ that is large compared to its uncertainty, producing a large correlation
1082 between these two parameters.

1083 **15.2 2-jet Fit Results**

1084 **The results of the fit are currently blinded.**

1085 Pre-fit yields in each of the 2-jet fit regions are shown in Figure 15.2.

	2j, <85% WP	2j, 77%-85% WP	2j, 70%-77% WP	2j, 60%-70% WP	2j, >60% WP	tZ CR 2j
WZ + b - 2j	3.1 ± 1.6	6.7 ± 0.5	5.6 ± 0.4	8.0 ± 0.6	31 ± 2	14 ± 1
WZ + c - 2j	180 ± 20	54 ± 6	41 ± 3	24 ± 3	11 ± 2	4.8 ± 0.6
WZ + l - 2j	1250 ± 150	90 ± 14	18 ± 3	5.8 ± 1.4	1.4 ± 0.4	0.25 ± 0.1
WZ + b - 1j	3.4 ± 0.6	1.52 ± 0.35	1.58 ± 0.23	1.95 ± 0.39	6.7 ± 1.1	1.9 ± 0.6
WZ + c - 1j	56 ± 14	17.6 ± 4.0	8.6 ± 2.2	6.3 ± 1.8	3.0 ± 0.9	0.7 ± 0.2
WZ + l - 1j	427 ± 120	24 ± 7	4.7 ± 2.3	1.6 ± 0.7	0.3 ± 0.2	0.01 ± 0.0
WZ - Other	129 ± 29	6.1 ± 4.6	1.2 ± 0.3	0.3 ± 0.2	2.9 ± 0.5	3.6 ± 0.6
Other VV	7.63 ± 0.63	0.6 ± 0.5	0.16 ± 0.03	0.01 ± 0.01	0.1 ± 0.1	0.1 ± 0.1
ZZ	135 ± 20	14.1 ± 3.2	4.7 ± 0.8	4.0 ± 0.6	4.1 ± 0.7	3.1 ± 0.5
t̄tW	0.8 ± 0.2	0.4 ± 0.1	0.5 ± 0.1	0.7 ± 0.2	4.3 ± 0.6	3.9 ± 0.6
t̄tZ	14.7 ± 2.2	5.6 ± 0.8	4.5 ± 0.7	6.5 ± 1.1	25.4 ± 4.0	21.9 ± 3.4
rare Top	0.14 ± 0.04	0.07 ± 0.03	0.03 ± 0.02	0.09 ± 0.03	0.37 ± 0.07	0.6 ± 0.1
t̄tWW	0.04 ± 0.03	0.02 ± 0.02	0.01 ± 0.01	0.01 ± 0.00	0.03 ± 0.03	0.01 ± 0.0
Z + jets	110.0 ± 22.9	9.6 ± 2.0	2.1 ± 0.50	1.6 ± 0.4	5.1 ± 1.1	1.5 ± 0.3
W + jets	0.0 ± 0.0	0.0 ± 0.0	0.0 ± 0.0	0.0 ± 0.0	0.0 ± 0.0	0.0 ± 0.0
V + γ	25 ± 18	0.5 ± 0.2	0.1 ± 0.1	0.1 ± 0.1	0.0 ± 0.02	0.05 ± 0.0
tZ	15.9 ± 2.9	6.9 ± 1.3	5.1 ± 1.0	8.0 ± 1.5	18.7 ± 3.2	36.4 ± 6.1
tW	0.9 ± 0.7	0.2 ± 0.3	0.0 ± 0.1	0.0 ± 0.0	0.8 ± 0.6	0.2 ± 0.2
WtZ	4.9 ± 2.5	1.5 ± 0.8	1.1 ± 0.6	1.3 ± 0.7	4.6 ± 2.4	3.3 ± 1.7
VVV	7.4 ± 0.3	1.0 ± 0.1	0.4 ± 0.1	0.2 ± 0.1	0.13 ± 0.03	0.04 ± 0.0
VH	19.5 ± 4.2	2.8 ± 1.6	0.7 ± 0.7	0.1 ± 0.2	0.0 ± 0.0	0.0 ± 0.0
t̄t	0.7 ± 0.4	0.1 ± 0.1	0.05 ± 0.06	0.15 ± 0.13	0.8 ± 0.5	2.3 ± 1.2
t̄t	6.8 ± 1.0	2.4 ± 0.5	1.8 ± 0.4	3.3 ± 0.6	8.4 ± 1.2	13.6 ± 1.1
t̄tH	0.4 ± 0.1	0.2 ± 0.1	0.16 ± 0.02	0.23 ± 0.03	0.94 ± 0.11	1.03 ± 0.1
Total	2580 ± 160	229 ± 24	89 ± 13	69 ± 11	120 ± 15	108 ± 11

Table 19: Pre-fit yields in each of the 2-jet fit regions.

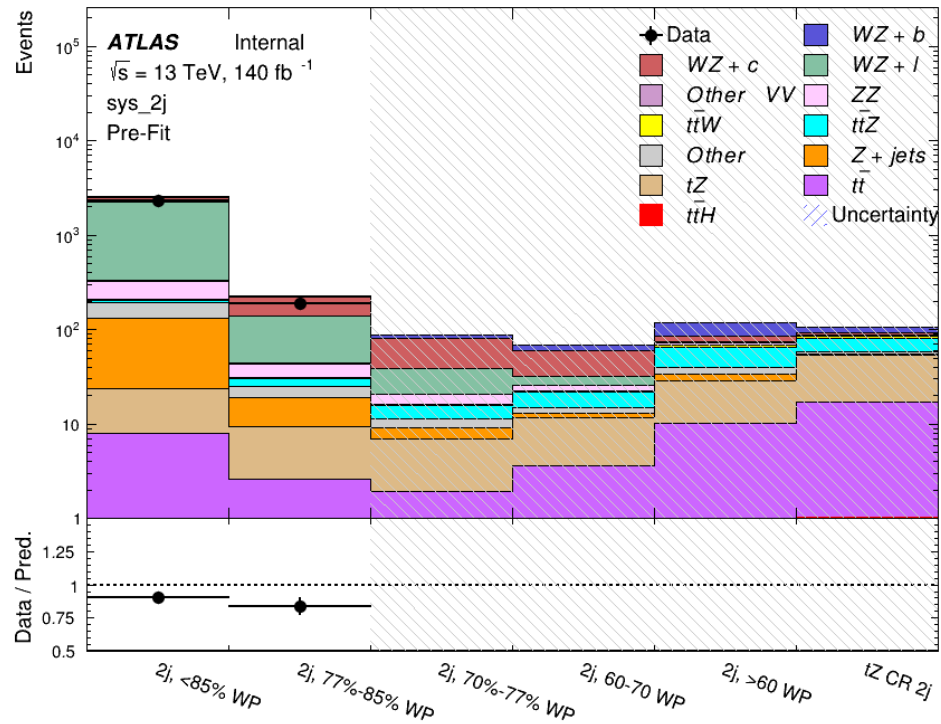


Figure 15.6: Pre-fit summary of the 2-jet fit regions.

1086

The post-fit yields in each region are summarized in Figure 15.2.

	2j, <85% WP	2j, 77%-85% WP	2j, 70%-77% WP	2j, 60%-70% WP	2j, >60% WP	tZ CR 2j
WZ + b	13 ± 6	6.7 ± 2.9	5.8 ± 2.5	8.0 ± 3.5	31 ± 13	14 ± 5
WZ + c	260 ± 60	77 ± 15	41 ± 8	26 ± 5	10.9 ± 2.4	4.8 ± 1.1
WZ + l	1860 ± 90	90 ± 12	17.6 ± 2.8	5.8 ± 1.3	1.4 ± 0.4	0.3 ± 0.2
WZ + b - 1j	3.4 ± 0.6	1.52 ± 0.35	1.58 ± 0.23	1.95 ± 0.39	6.7 ± 1.1	1.9 ± 0.6
WZ + c - 1j	56 ± 14	17.6 ± 4.0	8.6 ± 2.2	6.3 ± 1.8	3.0 ± 0.9	0.7 ± 0.2
WZ + l - 1j	427 ± 120	24 ± 7	4.7 ± 2.3	1.6 ± 0.7	0.3 ± 0.2	0.01 ± 0.0
WZ - Other	129 ± 29	6.1 ± 4.6	1.2 ± 0.3	0.3 ± 0.2	2.9 ± 0.5	3.6 ± 0.6
Other VV	7.6 ± 0.6	0.3 ± 0.3	0.3 ± 0.1	0.1 ± 0.06	0.03 ± 0.02	0.1 ± 0.1
ZZ	145 ± 30	11.3 ± 4.4	2.7 ± 1.6	1.0 ± 0.3	4.0 ± 0.1	2.4 ± 0.1
t̄tW	0.8 ± 0.2	0.4 ± 0.1	0.54 ± 0.12	0.74 ± 0.15	4.3 ± 0.6	3.9 ± 0.6
t̄tZ	14.7 ± 2.2	5.6 ± 0.8	4.5 ± 0.7	6.5 ± 1.0	25.4 ± 3.9	21.9 ± 3.0
rare Top	0.14 ± 0.04	0.07 ± 0.03	0.03 ± 0.02	0.09 ± 0.03	0.4 ± 0.1	0.6 ± 0.1
t̄tWW	0.04 ± 0.03	0.02 ± 0.02	0.01 ± 0.01	0.01 ± 0.01	0.03 ± 0.03	0.01 ± 0.0
Z + jets	110 ± 23	9.6 ± 2.0	2.1 ± 0.5	1.6 ± 0.4	5.1 ± 1.1	1.5 ± 0.3
W + jets	0.0 ± 0.0	0.0 ± 0.0				
V + γ	25 ± 19	0.5 ± 0.2	0.1 ± 0.1	0.13 ± 0.14	0.0 ± 0.02	0.05 ± 0.0
tZ	15.9 ± 2.7	6.9 ± 1.2	5.1 ± 0.9	8.0 ± 1.4	18.7 ± 3.0	36 ± 6
tW	0.1 ± 0.7	0.2 ± 0.3	0.0 ± 0.1	0.0 ± 0.0	0.8 ± 0.6	0.2 ± 0.2
WtZ	4.9 ± 2.5	1.5 ± 0.8	1.1 ± 0.6	1.3 ± 0.7	4.6 ± 2.3	3.3 ± 1.7
VVV	7.4 ± 0.3	1.0 ± 0.1	0.36 ± 0.03	0.19 ± 0.03	0.13 ± 0.03	0.04 ± 0.0
VH	19 ± 4	2.8 ± 1.6	0.7 ± 0.7	0.1 ± 0.2	0.0 ± 0.0	0.0 ± 0.0
t̄t	6.8 ± 1.0	2.4 ± 0.5	1.8 ± 0.4	3.3 ± 0.6	8.4 ± 1.2	13.6 ± 1.7
t̄tH	0.40 ± 0.05	0.19 ± 0.03	0.16 ± 0.02	0.23 ± 0.03	0.94 ± 0.11	1.03 ± 0.1
Total	2580 ± 60	229 ± 11	89 ± 6	69.1 ± 4.1	120 ± 10	108 ± 6

Table 20: Post-fit yields in each of the 2-jet fit regions.

1087

A post-fit summary of the fitted regions is shown in Figure 15.7:

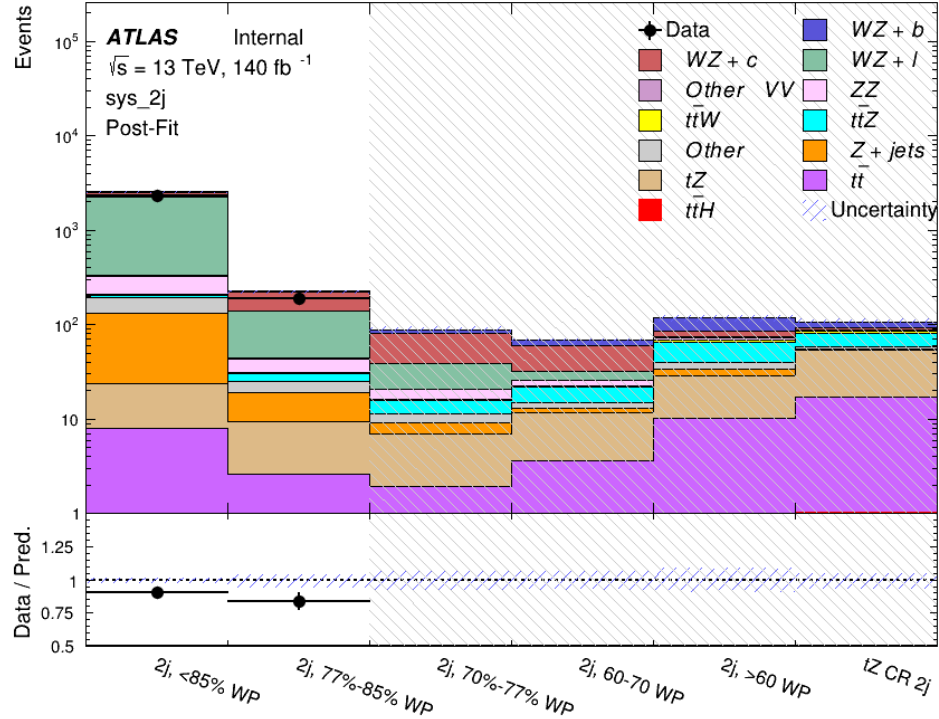


Figure 15.7: Post-fit summary of the fit over 2-jet regions.

1088 The same set of systematic uncertainties consider for the 1-jet fit are included in the 2-jet
 1089 fit as well. The impact of the most significant systematic uncertainties is summarized in Table
 1090 [21](#).

Uncertainty Source	$\Delta\mu$	
WZ + c cross-section	-0.1	0.14
Luminosity	-0.11	0.12
tZ cross-section	-0.11	0.11
Jet Energy Scale	-0.11	0.11
ttZ cross-section - QCD scale	-0.08	0.09
WZ + l cross-section	0.08	-0.07
WtZ cross-section	-0.07	0.07
Flavor tagging	0.05	0.05
Other VV + b cross-section	-0.05	0.05
Jet Energy Resolution	-0.04	0.04
Total	0.29	0.31

Table 21: Summary of the most significant sources of systematic uncertainty on the measurement of WZ + b 2-jet events.

¹⁰⁹¹ The ranking and impact of those nuisance parameters with the largest contribution to the
¹⁰⁹² overall uncertainty is shown in Figure 15.8.

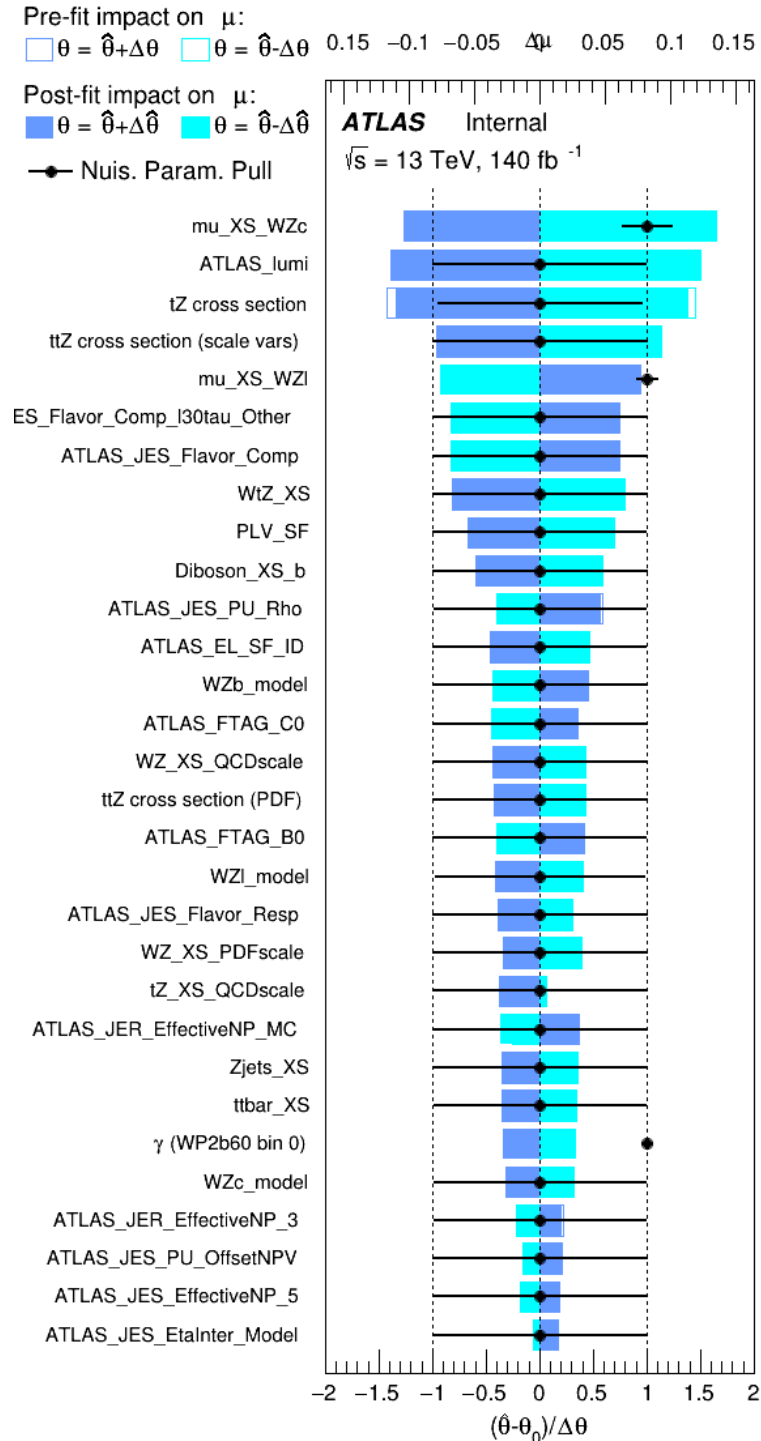


Figure 15.8: Impact of systematic uncertainties on the signal-strength of $WZ + b$ in 2-jet events.

1093 The large impact of the Jet Energy Scale and Jet Flavor Tagging is unsurprising, as the
 1094 shape of the fit regions depends heavily on the modeling of the jets. The other major sources
 1095 of uncertainty come from background modelling and cross-section uncertainty. The pie charts
 1096 in Figure 15.9 show that for the modelling uncertainties that contribute most correspond to the
 1097 most significant backgrounds.

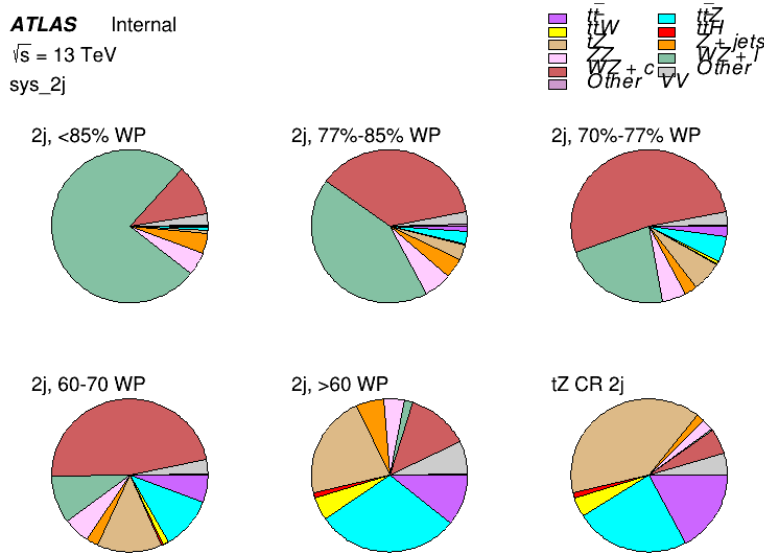


Figure 15.9: Post-fit background composition of the 2-jet fit regions.

1098 The correlations between these nuisance parameters are summarized in Figure 15.10.

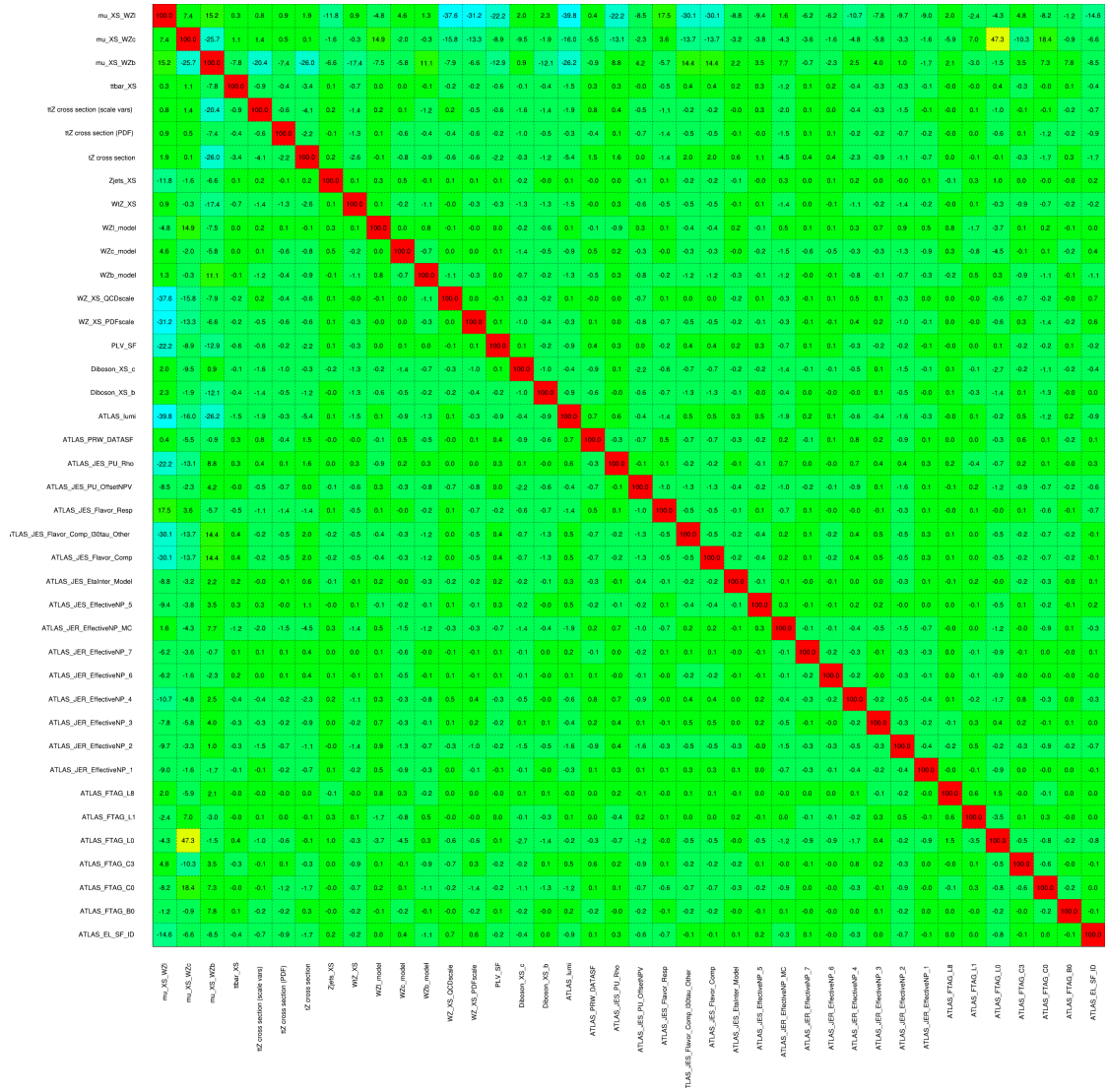


Figure 15.10: Correlations between nuisance parameters in the 2-jet fit

1099

As in the 1-jet case, no significant, unexpected correlations are found between nuisance

1100 parameters.

Part V**Differential Studies of $t\bar{t}H$ Multilepton****16 Data and Monte Carlo Samples**

1104 For both data and Monte Carlo (MC) simulations, samples were prepared in the xAOD format,
1105 which was used to produced a xAOD based on the HIGG8D1 derivation framework. This framework
1106 was designed for the main $t\bar{t}H$ multi-lepton analysis. Because this analysis targets events with
1107 multiple light leptons, as well as tau hadrons, this framework skims the dataset of any events that
1108 do not meet at least one of the following requirements:

- 1109 • at least two light leptons within a range $|\eta| < 2.6$, with leading lepton $p_T > 15$ GeV and
1110 subleading lepton $p_T > 5$ GeV
- 1111 • at least one light lepton with $p_T > 15$ GeV within a range $|\eta| < 2.6$, and at least two hadronic
1112 taus with $p_T > 15$ GeV.

1113 Samples were then generated from these HIGG8D1 derivations using AnalysisBase version
1114 21.2.127. A ptag of p4133 was used for MC samples, and p4134 for data.

1115 16.1 Data Samples

1116 The study uses proton-proton collision data collected by the ATLAS detector from 2015 through
 1117 2018, which represents an integrated luminosity of 139 fb^{-1} and an energy of $\sqrt{s} = 13 \text{ TeV}$. All
 1118 data used in this analysis was included in one of the following Good Run Lists:

- 1119 • data15_13TeV.periodAllYear_DetStatus-v79-repro20-02_DQDefects-00-02-02
 1120 _PHYS_StandardGRL_All_Good_25ns.xml
- 1121 • data16_13TeV.periodAllYear_DetStatus-v88-pro20-21_DQDefects-00-02-04
 1122 _PHYS_StandardGRL_All_Good_25ns.xml
- 1123 • data17_13TeV.periodAllYear_DetStatus-v97-pro21-13_Unknown_PHYS_StandardGRL
 1124 _All_Good_25ns_Triggerno17e33prim.xml
- 1125 • data18_13TeV.periodAllYear_DetStatus-v102-pro22-04_Unknown_PHYS_StandardGRL
 1126 _All_Good_25ns_Triggerno17e33prim.xml

1127 16.2 Monte Carlo Samples

1128 Several Monte Carlo (MC) generators were used to simulate both signal and background pro-
 1129 cesses. For all of these, the effects of the ATLAS detector are simulated in Geant4. The specific
 1130 event generator used for each of these MC samples is listed in Table 22. A Higgs mass of 125
 1131 GeV is assumed in all simulations.

Table 22: The configurations used for event generation of signal and background processes, including the event generator, matrix element (ME) order, parton shower algorithm, and parton distribution function (PDF).

Process	Event generator	ME order	Parton Shower	PDF
$t\bar{t}H$	MG5_AMC	NLO	PYTHIA 8	NNPDF 3.0 NLO [16]
	(MG5_AMC)	(NLO)	(HERWIG++)	(CT10 [17])
$t\bar{t}W$	MG5_AMC	NLO	PYTHIA 8	NNPDF 3.0 NLO
	(SHERPA 2.1.1)	(LO multileg)	(SHERPA)	(NNPDF 3.0 NLO)
$t\bar{t}(Z/\gamma^* \rightarrow ll)$	MG5_AMC	NLO	PYTHIA 8	NNPDF 3.0 NLO
	SHERPA 2.2.2	MEPS NLO	SHERPA	CT10
$t\bar{t}$	POWHEG-BOX v2 [18]	NLO	PYTHIA 8	NNPDF 3.0 NLO
$t\bar{t}\gamma$	MG5_AMC	LO	PYTHIA 8	NNPDF 2.3 LO
tZ	MG5_AMC	LO	PYTHIA 6	CTEQ6L1
$tHqb$	MG5_AMC	LO	PYTHIA 8	CT10
tHW	MG5_AMC	NLO	HERWIG++	CT10
	(SHERPA 2.1.1)	(LO multileg)	(SHERPA)	(NNPDF 3.0 NLO)
tWZ	MG5_AMC	NLO	PYTHIA 8	NNPDF 2.3 LO
$t\bar{t}t, t\bar{t}t\bar{t}$	MG5_AMC	LO	PYTHIA 8	NNPDF 2.3 LO
$t\bar{t}W^+W^-$	MG5_AMC	LO	PYTHIA 8	NNPDF 2.3 LO
s-, t-channel, Wt single top qqVV, VVV $Z \rightarrow l^+l^-$	POWHEG-BOX v1 [19]	NLO	PYTHIA 6	CT10
	SHERPA 2.2.1	MEPS NLO	SHERPA	NNPDF 3.0 NLO

1132 The signal sample ($t\bar{t}H$) is modelled at NLO with POWHEG-BOX v2 using the NNPDF2.0
 1133 parton distribution function (PDF) [34]. Parton showering and hadronisation were modelled
 1134 with PYTHIA 8.2 [35]. The $t\bar{t}H$ sample is normalized to a cross-section of 507^{+35}_{-50} fb based on
 1135 NLO calculations. Uncertainties are based on varying the QCD factorisation and renormalisation
 1136 scale, as well as uncertainties in the PDF and α_s .

1137 The $t\bar{t}W$ background is simulated using Sherpa 2.2.1 with the NNPDF3.0 NLO PDF. The
 1138 matrix element is calculated with up to one additional parton at NLO, and up to two at LO. As
 1139 explained in detail in [7], the $t\bar{t}W$ contribution predicted by MC is found disagree significantly

1140 with what is observed in data. While an effort is currently being undertaken to measure $t\bar{t}W$ more
1141 accurately, the approach used by the 79.8 fb^{-1} $t\bar{t}H$ analysis is used here: A normalization
1142 factor of 1.68 is applied to the MC estimate of $t\bar{t}W$ and additional systematic uncertainties on
1143 $t\bar{t}W$ are included to account for this modelling discrepancy, as outlined in Section 20.

1144 The $t\bar{t}(Z/\gamma^*)$ process is simulated with the **MADGRAPH5_AMC@NLO** generator, using
1145 NNPDF3.0. Diboson processes are generated with **SHERPA 2.2.2** at NLO precision for one extra
1146 parton, and at LO for up to three extra partons.

1147 The estimation of the “fake” or non-prompt background - with leptons from hadron decays
1148 or photon conversions - is done primarily using an inclusive $t\bar{t}$ sample. This sample is generated
1149 using **POWHEG**, with **PYTHIA8** performing the parton shower and fragmentation.

1150 While the main $t\bar{t}H$ analysis is currently refining a data-driven approach for estimating
1151 the contribution of events with non-prompt leptons, at the time of this note this strategy has not
1152 been completely developed for the full Run-2 dataset. Therefore, the non-prompt contribution
1153 is estimated with MC, while applying normalization corrections and systematic uncertainties
1154 derived from data driven techniques developed for the 79.8 fb^{-1} $t\bar{t}H/t\bar{t}W$ analysis [7]. The
1155 primary contribution to the non-prompt lepton background is from $t\bar{t}$ production, with V+jets
1156 and single-top as much smaller sources. Likelihood fits over several control regions enriched with
1157 these non-prompt backgrounds are fit to data in order to derive normalization factors for these
1158 backgrounds. The specific normalization factors and uncertainties applied to the non-prompt
1159 contributions are listed in Section 20.

¹¹⁶⁰ Other background processes, such as tH , tZ , $t\bar{t}WW$ and $t\bar{t}t\bar{t}$, are expected to make minor
¹¹⁶¹ contributions to the total background. The generators and setting used for these backgrounds are
¹¹⁶² summarized in Table ??.

¹¹⁶³ The specific DSIDs used in the analysis are listed below:

Sample	DSID
$t\bar{t}H$	345873-5, 346343-5
VV	364250-364254, 364255, 363355-60, 364890
$t\bar{t}W$	413008
$t\bar{t}Z$	410156, 410157, 410218-20
low mass $t\bar{t}Z$	410276-8
Rare Top	410397, 410398, 410399
single Top	410658-9, 410644-5
three Top	304014
four Top	410080
$t\bar{t}WW$	410081
$Z + \text{jets}$	364100-41
low mass $Z + \text{jets}$	364198-215
$W + \text{jets}$	364156-97
$V\gamma$	364500-35
tZ	410560
tW	410013-4
WtZ	410408
VVV	364242-9
VH	342284-5
WtH	341998
$t\bar{t}\gamma$	410389
$t\bar{t}$	410470

Table 23: List of Monte Carlo samples by data set ID used in the analysis.

1164 17 Object Reconstruction

1165 All analysis channels considered in this note share a common object selection for leptons and
1166 jets, as well as a shared trigger selection.

1167 17.1 Trigger Requirements

1168 Events are required to be selected by dilepton triggers, as summarized in Table 24.

Dilepton triggers (2015)	
$\mu\mu$ (asymm.)	HLT_mu18_mu8noL1
ee (symm.)	HLT_2e12_lhloose_L12EM10VH
$e\mu, \mu e$ (\sim symm.)	HLT_e17_lhloose_mu14
Dilepton triggers (2016)	
$\mu\mu$ (asymm.)	HLT_mu22_mu8noL1
ee (symm.)	HLT_2e17_lhvloose_nod0
$e\mu, \mu e$ (\sim symm.)	HLT_e17_lhloose_nod0_mu14
Dilepton triggers (2017)	
$\mu\mu$ (asymm.)	HLT_mu22_mu8noL1
ee (symm.)	HLT_2e24_lhvloose_nod0
$e\mu, \mu e$ (\sim symm.)	HLT_e17_lhloose_nod0_mu14
Dilepton triggers (2018)	
$\mu\mu$ (asymm.)	HLT_mu22_mu8noL1
ee (symm.)	HLT_2e24_lhvloose_nod0
$e\mu, \mu e$ (\sim symm.)	HLT_e17_lhloose_nod0_mu14

Table 24: List of lowest p_T -threshold, un-prescaled dilepton triggers used for 2015-2018 data taking.

1169 **17.2 Light Leptons**

1170 Electron candidates are reconstructed from energy clusters in the electromagnetic calorimeter
1171 that are associated with charged particle tracks reconstructed in the inner detector [20]. Electron
1172 candidates are required to have $p_T > 10 \text{ GeV}$ and $|\eta_{\text{cluster}}| < 2.47$. Candidates in the transition
1173 region between different electromagnetic calorimeter components, $1.37 < |\eta_{\text{cluster}}| < 1.52$, are
1174 rejected. A multivariate likelihood discriminant combining shower shape and track information
1175 is used to distinguish prompt electrons from nonprompt leptons, such as those originating from
1176 hadronic showers. Electron candidate are also required to pass TightLH identification.

1177 To further reduce the non-prompt contribution, the track of each electron is required to
1178 originate from the primary vertex; requirements are imposed on the transverse impact parameter
1179 significance ($|d_0|/\sigma_{d_0}$) and the longitudinal impact parameter ($|\Delta z_0 \sin \theta_\ell|$).

1180 Muon candidates are reconstructed by combining inner detector tracks with track segments
1181 or full tracks in the muon spectrometer [21]. Muon candidates are required to have $p_T > 10 \text{ GeV}$
1182 and $|\eta| < 2.5$. Muons are required to Medium ID requirements.

1183 All leptons are required to pass a non-prompt BDT selection developed by the main
1184 $t\bar{t}H - \text{ML}/t\bar{t}W$ analysis, described in detail in [7]. Optimized working points and scale factors
1185 for this BDT are taken from that analysis. This BDT and the WPs used are summarized in
1186 Appendix [1](#),

1187 17.3 Jets

1188 Jets are reconstructed from calibrated topological clusters built from energy deposits in the
1189 calorimeters [23], using the anti- k_t algorithm with a radius parameter $R = 0.4$. Particle Flow, or
1190 PFlow, jets are used in the analysis, which are hadronic objects reconstructed using information
1191 from both the tracker and the calorimeter. Jets with energy contributions likely arising from noise
1192 or detector effects are removed from consideration [24], and only jets satisfying $p_T > 25$ GeV
1193 and $|\eta| < 2.5$ are used in this analysis. For jets with $p_T < 60$ GeV and $|\eta| < 2.4$, a jet-track
1194 association algorithm is used to confirm that the jet originates from the selected primary vertex,
1195 in order to reject jets arising from pileup collisions [25].

1196 17.4 B-tagged Jets

1197 Each analysis channel used in this analysis includes b-jets in the final state. These are identified
1198 using the DL1r b-tagging algorithm, which uses jet vertex and kinematic information to distin-
1199 guish heavy and light flavored jets. These features are used as inputs to a neural network, the
1200 output of which is used to form calibrated working points (WPs) based on how likely a jet is to
1201 have originated from a b-quark. This analysis uses the 70% DL1r WP - implying an efficiency of
1202 70% for truth b-jets - for selecting b-tagged jets.

1203 17.5 Missing Transverse Energy

1204 Because all $t\bar{t}H - ML$ channels considered include multiple neutrinos, missing transverse
1205 energy (E_T^{miss}) is present in each event. The missing transverse momentum vector is defined as
1206 the inverse of the sum of the transverse momenta of all reconstructed physics objects as well
1207 as remaining unclustered energy, the latter of which is estimated from low- p_T tracks associated
1208 with the primary vertex but not assigned to a hard object [26].

1209 17.6 Overlap removal

1210 To avoid double counting objects and remove leptons originating from decays of hadrons, overlap
1211 removal is performed in the following order: any electron candidate within $\Delta R = 0.1$ of another
1212 electron candidate with higher p_T is removed; any electron candidate within $\Delta R = 0.1$ of a muon
1213 candidate is removed; any jet within $\Delta R = 0.3$ of an electron candidate is removed; if a muon
1214 candidate and a jet lie within $\Delta R = \min(0.4, 0.04 + 10[\text{GeV}] / p_T(\text{muon}))$ of each other, the jet
1215 is kept and the muon is removed.

1216 This algorithm is applied to the preselected objects. The overlap removal procedure is
1217 summarized in Table 25.

Keep	Remove	Cone size (ΔR)
electron	electron (low p_T)	0.1
muon	electron	0.1
electron	jet	0.3
jet	muon	$\min(0.4, 0.04 + 10[\text{GeV}]/p_T(\text{muon}))$
electron	tau	0.2

Table 25: Summary of the overlap removal procedure between electrons, muons, and jets.

1218 18 Higgs Momentum Reconstruction

1219 Reconstructing the momentum of the Higgs boson is a particular challenge for channels with
 1220 leptons in the final state: Because all channels include at least two neutrinos in the final state, the
 1221 Higgs can never be fully reconstructed. However, the momentum spectrum can be well predicted
 1222 by a neural network when provided with the kinematics of the Higgs Boson decay products - as
 1223 verified by studies detailed in Appendix A.3. With this in mind, several layers of MVAs are used
 1224 to reconstruction the Higgs momentum:

1225 The first layer is a model designed to select which jets are most likely to be the b-jets that
 1226 came from the top decay, detailed in Section 18.3. As described in Section 18.4, the kinematics
 1227 of these jets and possible Higgs decay products are fed into the second layer, which is designed
 1228 to identify the decay products of the Higgs Boson itself. The kinematics of the particles this
 1229 layer identifies as most likely to have originated from the Higgs decay are then fed into yet
 1230 another neural-network, which predicts the momentum of the Higgs (18.5). For the 3l channel,
 1231 an additional MVA is used to determine the decay mode of the Higgs boson in the 3l channel
 1232 (18.6).

1233 Models are trained on Monte Carlo simulations of $t\bar{t}H$ events generated using MG5_AMC.

1234 Specifically, events DSIDs 346343-5, 345873-5, and 345672-4 are used for training in order to

1235 increase the statistics of the training sample.

1236 For all of these models, the Keras neural network framework, with Tensorflow 2.0 as the

1237 backend, is used, and the number of hidden layers and nodes are determined using grid search

1238 optimization. Each neural network uses the LeakyReLU activation function, a learning rate of

1239 0.01, and the Adam optimization algorithm, as alternatives are found to either decrease or have

1240 no impact on performance. Batch normalization is applied after each layer in order to stabilize

1241 the model and decrease training time. For the classification algorithms (b-jet matching, Higgs

1242 reconstruction, and 3l decay identification) binary-cross entropy is used as the loss function,

1243 while the p_T reconstruction algorithm uses MSE.

1244 The specific inputs features used for each model are arrived at through a process of trial

1245 and error - features considered potentially useful are tried, and those that are found to increase

1246 performance are included. While each model includes a relatively large number of features,

1247 some using upwards of 30, this inclusive approach is found to maximize the performance of

1248 each model while decreasing the variance compared to a reduced number of inputs. Each input

1249 feature is validated by comparing MC simulations to 79.8 fb^{-1} of data, as shown in the sections

1250 below.

1251 18.1 Physics Object Truth Matching

1252 Machine Learning algorithms are trained to identify the decay products of the Higgs Boson using
1253 MC simulations of $t\bar{t}H$ events. The kinematics of the reconstructed physics objects, as well as
1254 event level variables, are used as inputs, with the parent ID taken from the truth record used to
1255 label the data. The objects considered include light leptons and jets.

1256 Reconstructed physics objects are matched to particle level objects, in order to identify the
1257 parent particle of these reconstructed objects. Reconstructed jets are matched to truth jets based
1258 on the requirements that the reco jet and truth jet fall within $\Delta R < 0.4$, and the two objects have
1259 a p_T that agrees within 10%. Truth level and reco level leptons are required to have the same
1260 flavor, a $\Delta R < 0.1$, and p_T that agree within 10%. Events where no match can be found between
1261 the particle level decay products of the Higgs and the reconstructed objects are not included in
1262 training.

1263 Leptons considered as possible Higgs and top decay candidates are required to pass the
1264 selection described in Section 17.2. For jets, however, it is found that a large fraction that
1265 originate from either the top decay or the Higgs decay fall outside the selection described in
1266 Section 17.3. Specifically, jets from the Higgs decay tend to be soft, with 32% having $p_T <$
1267 25 GeV. Therefore jets with $p_T < 15$ GeV are considered as possible candidates in the models
1268 described below. By contrast, less than 5% of the jets originating from the Higgs fall below
1269 this p_T threshold. The jets are found to be well modeled even down to this low p_T threshold,
1270 as shown in Section 19.1. The impact of using different p_T selection for the jet candidates is

1271 considered in detail in Section A.6. As they are expected to originate from the primary vertex,

1272 jets are also required to pass a JVT cut.

1273 18.2 Truth Level Studies

1274 Attempts to identify the decay products of the Higgs are motivated by the ability to reconstruct

1275 the Higgs momentum based on their kinematics. In order to demonstrate that this is case, the

1276 kinematics of reconstructed objects that are truth matched to the Higgs decay are used as inputs

1277 to a neural network which is designed to predict of the momentum of the Higgs. This is done in

1278 the 2lSS channel -

1279 18.3 b-jet Identification

1280 Including the kinematics of the b-jets that originate from the top decay is found to improve the

1281 identification of the Higgs decay products, and improve the accuracy with which the Higgs

1282 momentum can be reconstructed. Because these b-jets are reconstructed by the detector with

1283 high efficiency (just over 90% of the time), and can be identified relatively consistently, the first

1284 step in reconstructing the Higgs is selecting the b-jets from the top decay.

1285 Exactly two b-jets are expected in the final state of $t\bar{t}H$ – ML events. However, in both

1286 the 3l and 2lSS channels, only one or more b-tagged jets are required (where the 70% DL1r b-tag

1287 working point is used). Therefore, for events which have exactly one, or more than two, b-tagged

1288 jets, deciding which combination of jets correspond to the top decay is non-trivial. Further,

1289 events with 1 b-tagged jet represent just over half of all $t\bar{t}H - ML$ events. Of those, both b-jets
 1290 are reconstructed by the detector 75% of the time. Therefore, rather than adjusting the selection
 1291 to require exactly 2 b-tagged jets, and losing more than half of the signal events, a neural network
 1292 is used to predict which pair of jets is most likely to correspond to truth b-jets.

1293 Once the network is trained, all possible pairings of jets are fed into the model, and the pair
 1294 of jets with the highest output score are taken to be b-jets in successive steps of the analysis.

1295 18.3.1 2ISS Channel

1296 For the 2ISS channel, the input features shown in Table 26 are used for training. Here j_0 and j_1
 1297 are the two jet candidates, while l_0 and l_1 are the two leptons in the event, both ordered by p_T . jet
 1298 DL1r is an integer corresponding to the calibrated b-tagging working points reached by each jet,
 1299 where 5 represents the tightest working point and 1 represents the loosest. The variables nJets
 1300 DL1r 60% and nJets DL1r 85% represent the number of jets in the event passing the 60% and
 1301 85% b-tag working points, respectively.

jet p_T 0	jet p_T 1	Lepton p_T 0
Lepton p_T 1	jet η 0	jet η 1
$\Delta R(j_0)(j_1)$	$M(j_0j_1)$	$\Delta R(l_0)(j_0)$
$\Delta R(l_0)(j_1)$	$\Delta R(l_1)(j_0)$	$\Delta R(l_1)(j_1)$
$M(l_0j_0)$	$M(l_0j_1)$	$M(l_1j_0)$
$M(l_1j_1)$	jet DL1r 0	jet DL1r 1
nJets OR DL1r 85	nJets OR DL1r 60	$\Delta R(j_0l_0)(j_1l_1)$
$\Delta R(j_0l_1)(j_1l_0)$	$p_T(j_0j_1l_0l_1 E_T^{\text{miss}})$	$M(j_0j_1l_0l_1 E_T^{\text{miss}})$
$\Delta\phi(j_0)(E_T^{\text{miss}})$	$\Delta\phi(j_1)(E_T^{\text{miss}})$	HT jets
nJets	E_T^{miss}	

Table 26: Input features used in the b-jet identification algorithm for the 2ISS channel

1302 As there are far more incorrect combinations than correct ones, by a factor of more than
 1303 20:1, the training set is resampled to reduce the fraction of incorrect combinations. A random
 1304 sample of 5 million incorrect entries are used for training, along with close 1 million correct
 1305 entries. 10% of the dataset is set aside for testing, leaving around 5 million datapoints for
 1306 training.

1307 The difference between the distributions for a few of these features for the "correct" (i.e.
 1308 both jets are truth b-jets), and "incorrect" combinations are shown in Figure 18.1. The correct and
 1309 incorrect contributions are scaled to the same integral, so as to better demonstrate the differences
 1310 in the distributions.

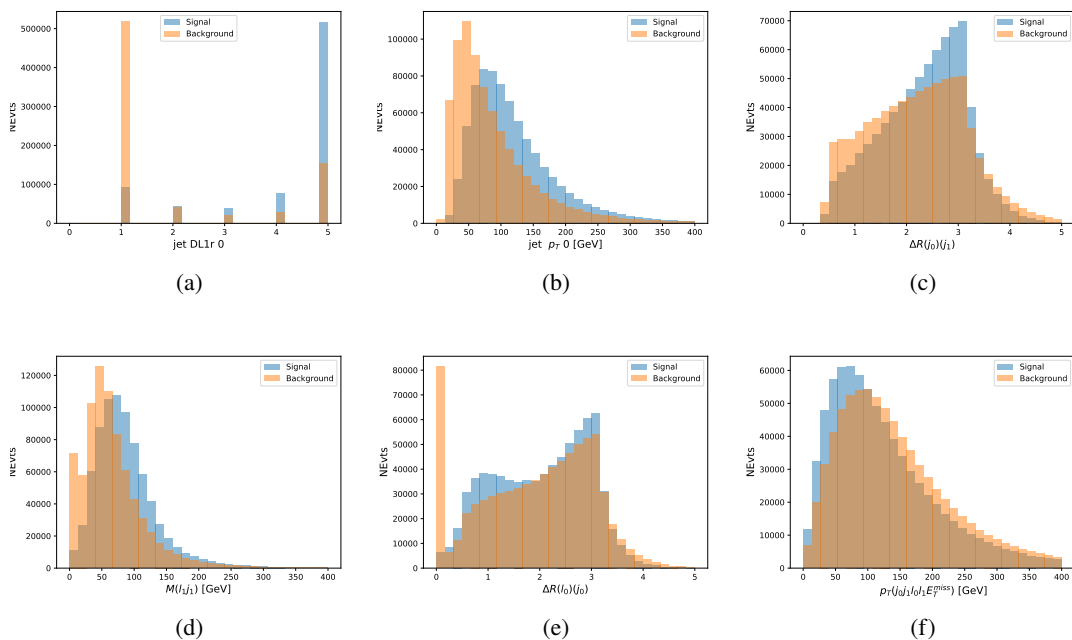


Figure 18.1: Input features for top2ISS training. The signal in blue represents events where both jet candidates are truth b-jets from top decays, and the orange is all other combinations. Each are scaled to the same number of events. (a) shows the DL1r working point of leading jet, (b) shows the p_T of the leading jet, (c) shows the ΔR of the two jets, (d) the invariant mass of lepton 1 and jet 1, (e) the ΔR of lepton 0 and jet 0, and (f) the p_T of both jets, both leptons, and the E_T^{miss} .

1311 The modeling of these inputs is validated against data, with Figure 18.2 showing good
 1312 general agreement between data and MC. Plots for the complete list of features can found in
 1313 Section A.

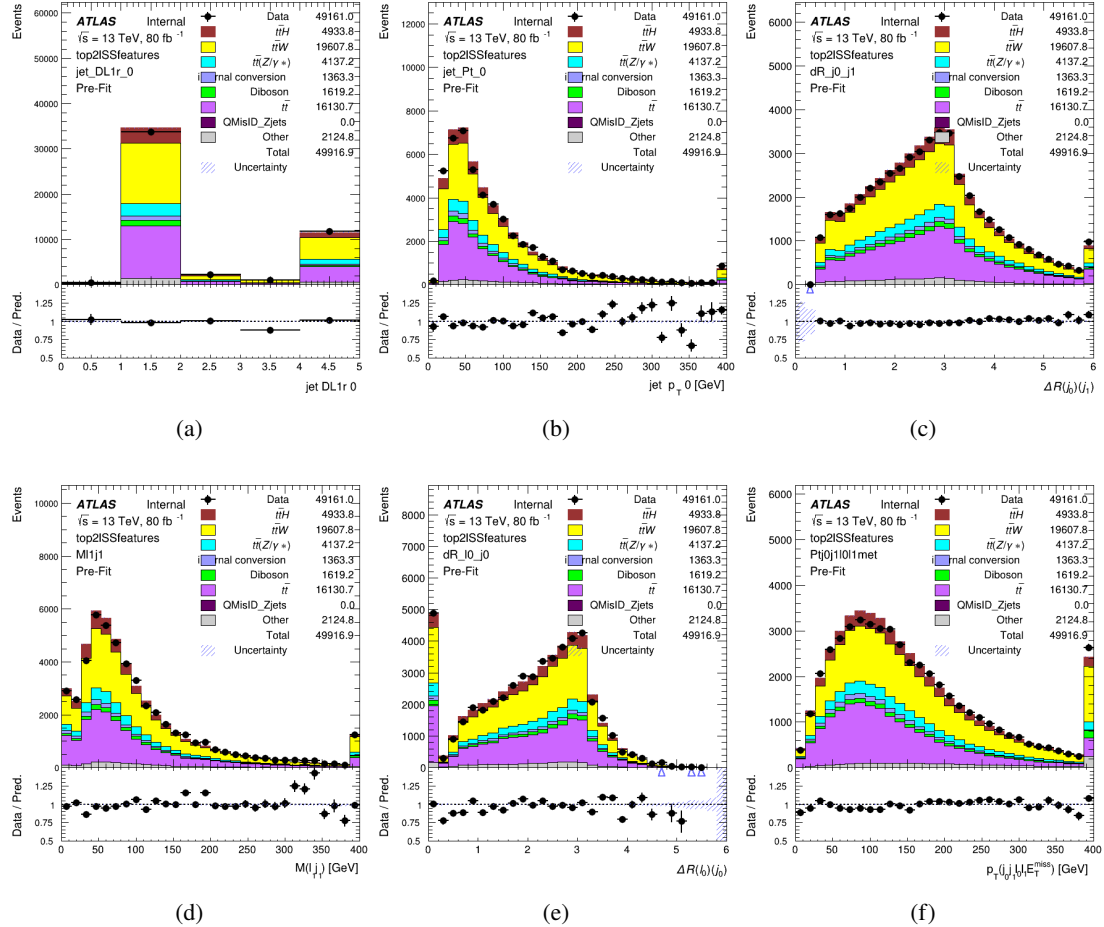


Figure 18.2: Data/MC comparisons of input features for top2ISS training for 79.8 fb^{-1} of data. (a) shows the DL1r working point of leading jet, (b) shows the p_T of the leading jet, (c) shows the ΔR of the two jets, (d) the invariant mass of lepton 1 and jet 1, (e) the ΔR of lepton 0 and jet 0, and (f) the p_T of both jets, both leptons, and the E_T^{miss} .

1314 Based on the results of grid search evaluation, the optimal architecture is found to include
 1315 5 hidden layers with 40 nodes each. No regularizer or dropout is added to the network, as

1316 overfitting is found to not be an issue. The output score distribution as well as the ROC curve for
 1317 the trained model are shown in Figure 18.3.1. The model is found to identify the correct pairing
 1318 of jets for 73% of 2lSS signal events on test data.

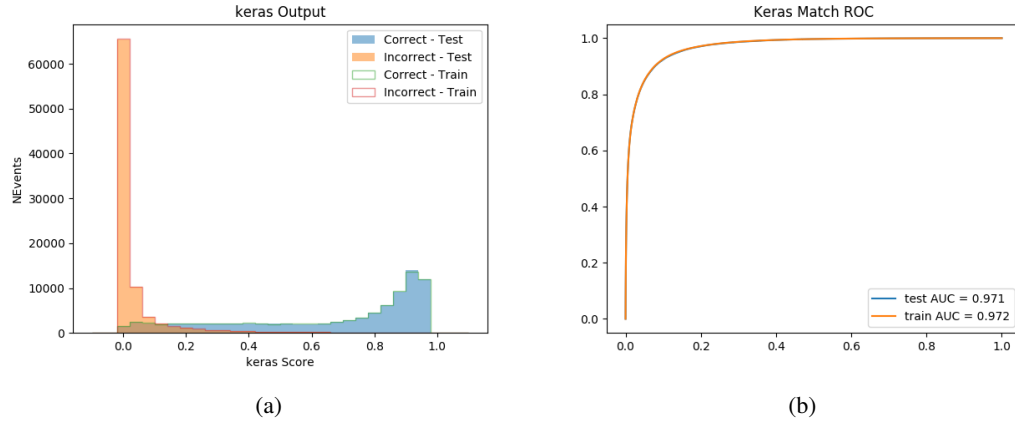


Figure 18.3: Results of the b-jet identification algorithm for the 2lSS channel, showing (a) the output score of the NN for correct and incorrect combinations of jets. (b) the ROC curve of the output, showing background rejection as a function of signal efficiency

1319 For point of comparison, a "naive" approach to identify b-jets is used as well: The two
 1320 jets which pass the highest DL1r b-tag working point are assumed to be the b-jets from the top
 1321 decay. In the case that multiple jets meet the same b-tag working point, the jet with higher p_T is
 1322 used. This method identifies the correct jet pair 65% of the time.

1323 The accuracy of the model for different values of n-bjets, compared to this naive approach,
 1324 is shown in Table 27.

b-jet Selection	Neural Network	Naive
1 b-jet	58.6%	42.1%
2 b-jets	88.4%	87.1%
≥ 3 b-jets	61.7%	53.3%
Overall	73.9%	67.2%

Table 27: Accuracy of the NN in identifying b-jets from tops in 2ISS events, overall and split by the number of b-tagged jets in the event, compared to the accuracy of taking the two highest b-tagged jets.

1325 18.3.2 3l Channel

1326 The input features used in the 3l channel are listed in Table 28, with the same naming convention
 1327 as the 2ISS channel.

jet p_T 0	jet p_T 1	jet η 0
jet η 1	Lepton p_T 0	Lepton p_T 1
Lepton p_T 2	$\Delta R(j_0)(j_1)$	$M(j_0 j_1)$
$\Delta R(l_0)(j_0)$	$\Delta R(l_1)(j_0)$	$\Delta R(l_2)(j_0)$
$\Delta R(l_0)(j_1)$	$\Delta R(l_1)(j_1)$	$\Delta R(l_2)(j_1)$
$M(l_0 j_0)$	$M(l_1 j_0)$	$M(l_2 j_0)$
$M(l_0 j_1)$	$M(l_1 j_1)$	$M(l_2 j_1)$
$\Delta R(j_0 l_0)(j_1 l_1)$	$\Delta R(j_0 l_0)(j_1 l_2)$	$\Delta R(j_0 l_1)(j_1 l_0)$
$\Delta R(j_0 l_2)(j_1 l_0)$	jet DL1r 0	jet DL1r 1
$p_T(j_0 j_1 l_0 l_1 l_2 E_T^{\text{miss}})$	$M(t j_0 j_1 l_0 l_1 l_2 E_T^{\text{miss}})$	$\Delta\phi(j_0)(E_T^{\text{miss}})$
$\Delta\phi(j_1)(E_T^{\text{miss}})$	HT Lepton	HT jets
nJets	E_T^{miss}	nJets OR DL1r 85
nJets OR DL1r 60		

Table 28: Input features for the b-jet identification algorithm in the 3l channel.

1328 A few of these features are shown in Figure 18.4, comparing the distributions for correct
 1329 and incorrect combinations of jets.

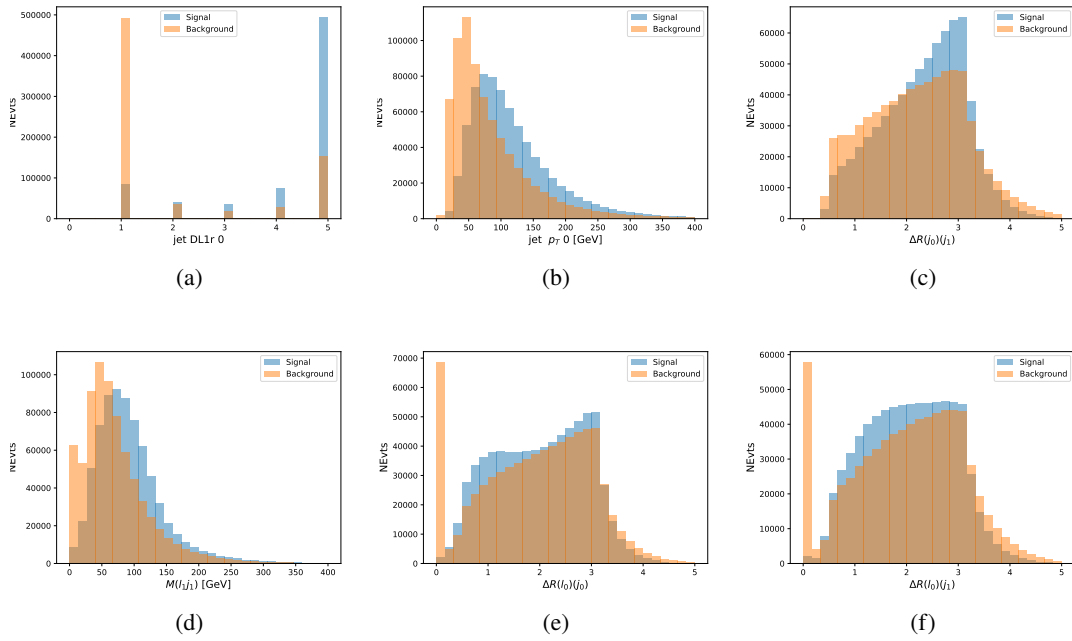


Figure 18.4: Input features for top3l training. The signal in blue represents events where both jet candidates are truth b-jets from top decays, and the orange is all other combinations. Scaled to the same number of events. (a) show the DL1r WP of jet 0, (b) the p_T of jet 0, (c) ΔR between jet 0 and jet 1, (d) the invariant mass of lepton 1 and jet 1, (e) ΔR between lepton 0 and jet 0, and (f) ΔR between lepton 0 and jet 1

1330 The modeling of these inputs is validated against data, with Figure 18.5 showing good
 1331 general agreement between data and MC. Plots for the complete list of features can found in
 1332 Section A.

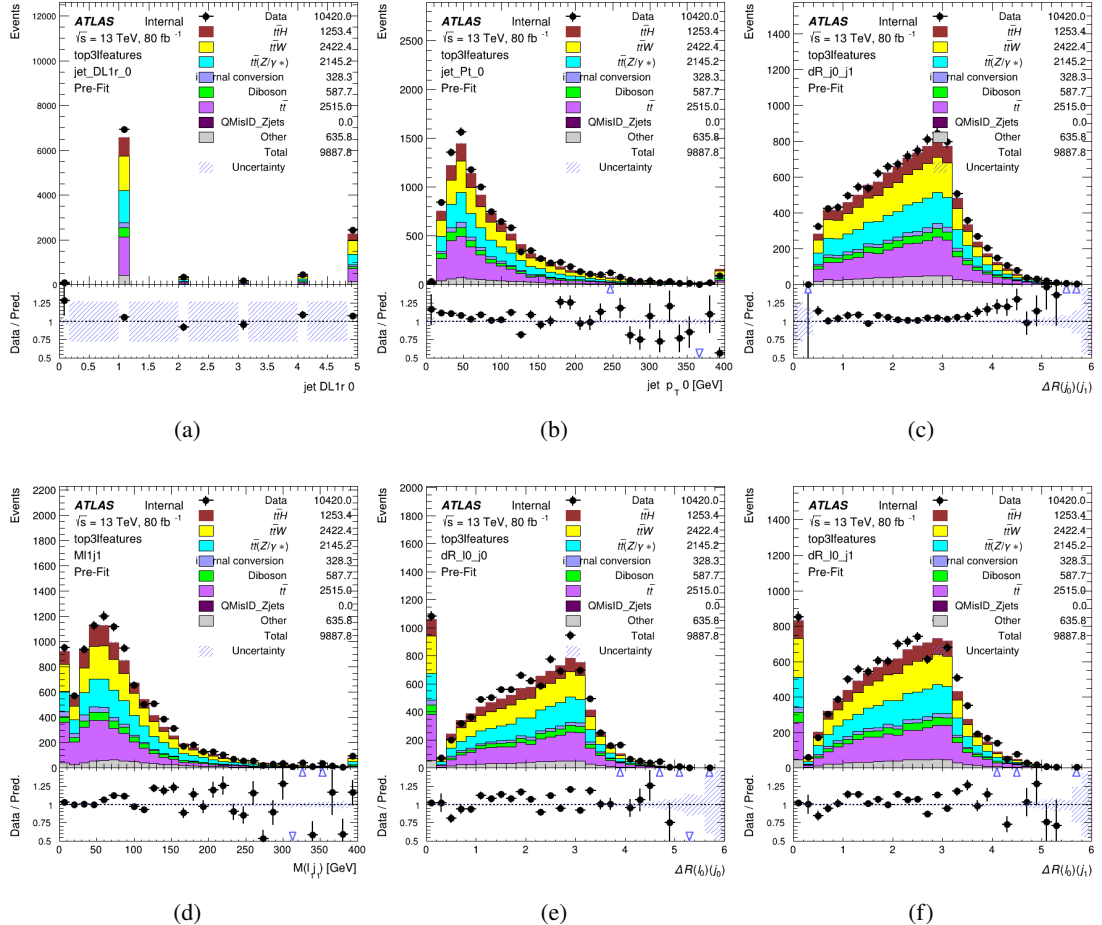


Figure 18.5: Data/MC comparisons of input features for top3l training for 79.8 fb^{-1} of data. (a) show the DL1r WP of jet 0, (b) the p_T of jet 0, (c) ΔR between jet 0 and jet 1, (d) the invariant mass of lepton 1 and jet 1, (e) ΔR between lepton 0 and jet 0, and (f) ΔR between lepton 0 and jet 1

Again, the dataset is downsized to reduce the ratio of correct and incorrect combination from 20:1, to 5:1. Around 7 million events are used for training, with 10% set aside for testing. Based on the results of grid search evaluation, the optimal architecture is found to include 5 hidden layers with 60 nodes each. The output score distribution as well as the ROC curve for the trained model are shown in Figure 18.3.2.

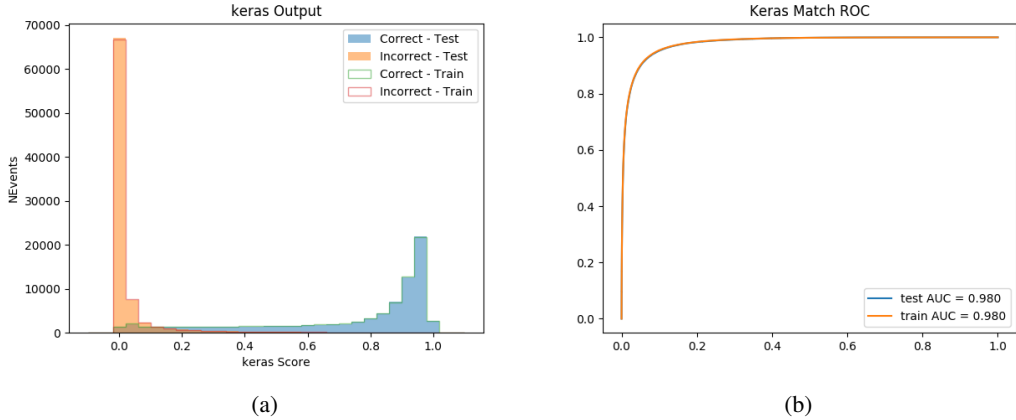


Figure 18.6: Results of the b-jet identification algorithm for the 3l channel, showing (a) the output score of the NN for correct and incorrect combinations of jets. (b) the ROC curve of the output, showing background rejection as a function of signal efficiency

1338 This procedure is found to identify the correct pairing of jets for nearly 80% of 3l signal
 1339 events. The accuracy of the model is summarized in Table 29.

Table 29: Accuracy of the NN in identifying b-jets from tops, compared to the naive method of taking the highest b-tagged jets.

	NN	Naive
1 b-jet	69.0%	48.9%
2 b-jets	89.6%	88.3%
≥ 3 b-jets	55.7%	52.3%
Overall	79.8%	70.2%

1340 18.4 Higgs Reconstruction

1341 Techniques similar to the b-jet identification algorithms are employed to select the decay products
 1342 of the Higgs: kinematics of all possible combinations of reconstructed objects are fed into a neural
 1343 network to determine which of those is most likely to be the decay products of the Higgs.

1344 Again separate models are used for the 2lSS and 3l channels, while the 3l channel has now
1345 been split into two: $t\bar{t}H$ events with three leptons in the final state include both instances where
1346 the Higgs decays into a lepton (and a neutrino) and a pair of jets, and instances where the Higgs
1347 decays to two leptons.

1348 3l events are therefore categorized as either semi-leptonic (3lS) or fully-leptonic (3lF). In
1349 the semi-leptonic case the reconstructed decay products consist of two jets and a single lepton.
1350 For the fully-leptonic case, the decay products include 2 of the three leptons associated with the
1351 event. For training the models, events are separated into these two categories using truth level
1352 information. A separate MVA, described in Section 18.6, is used to make this distinction at reco
1353 level and determine which model to use.

1354 For all channels, the models described in Section 18.3 are used to identify b-jet candidates,
1355 whose kinematics are used to identify the Higgs decay products. These jets are not considered
1356 as possible candidates for the Higgs decay, justified by the fact that these models are found to
1357 misidentify jets from the Higgs decay as jets from the top decay less than 1% of the time.

1358 **18.4.1 2lSS Channel**

1359 For the 2lSS channel, the Higgs decay products include one light lepton and two jets. The neural
1360 network is trained on the kinematics of different combinations of leptons and jets, as well as the
1361 b-jets identified in Section 18.3, with the specific input features listed in Table 30.

Lepton p_T H	Lepton p_T T	jet p_T 0
jet p_T 1	top p_T 0	top p_T 1
top η 0	top η 1	jet η 0
jet η 1	jet Phi 0	jet Phi 1
Lepton η H	Lepton heta T	$\Delta R(j_0)(j_1)$
$\Delta R(l_H)(j_0)$	$\Delta R(l_H)(j_1)$	$M(j_0 j_1)$
$M(l_H j_0)$	$M(l_H j_1)$	$\Delta R(l_H)(b_0)$
$\Delta R(l_H)(b_1)$	$\Delta R(l_T)(b_0)$	$\Delta R(l_T)(b_1)$
$\Delta R(j_0 j_1)(l_H)$	$\Delta R(j_0 j_1)(l_T)$	$\Delta R(j_0 j_1)(b_0)$
$\Delta R(j_0 j_1)(b_1)$	$\Delta R(j_0)(b_0)$	$\Delta R(j_0)(b_1)$
$\Delta R(j_1)(b_0)$	$\Delta R(j_1)(b_1)$	$M(j_0 j_1 l_H)$
$p_T(j_0 j_1 l_H l_T b_0 b_1 E_T^{\text{miss}})$	topScore	E_T^{miss}
nJets	HT jets	

Table 30: Input features used to identify the Higgs decay products in 2ISS events

1362 Here j_0 and j_1 , and l_H are the jet and lepton decay candidates, respectively. The other
 1363 lepton in the event is labeled l_T , as it is assumed to have come from the decay of one of the top
 1364 quarks. b_0 and b_1 are the two b-jets identified by the b-jet identification algorithm. The b-jet
 1365 Reco Score is the output of the b-jet reconstruction algorithm.

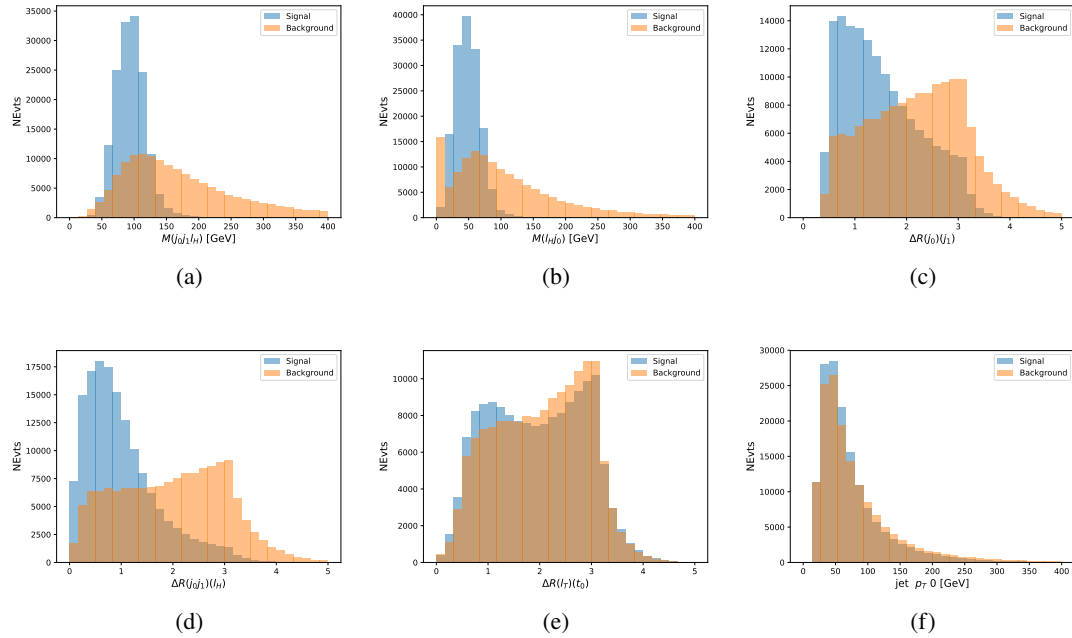


Figure 18.7: Input features for higgs2lSS training. The signal in blue represents events where both jet candidates are truth b-jets from top decays, and the orange is all other combinations. Scaled to the same number of events. (a) shows the invariant mass of the two jet candidates and the lepton candidate, (b) the invariant mass of jet 0 and the lepton candidate, (c) ΔR between the jet candidates, (d) ΔR between jet 0 + jet 1 and the lepton candidate, (e) ΔR between the lepton from the top and the leading b-jet, (f) the p_T of jet 0.

1366 The modeling of these inputs is validated against data, with Figure 18.2 showing good
 1367 general agreement between data and MC. Plots for the complete list of features can found in
 1368 Section A.

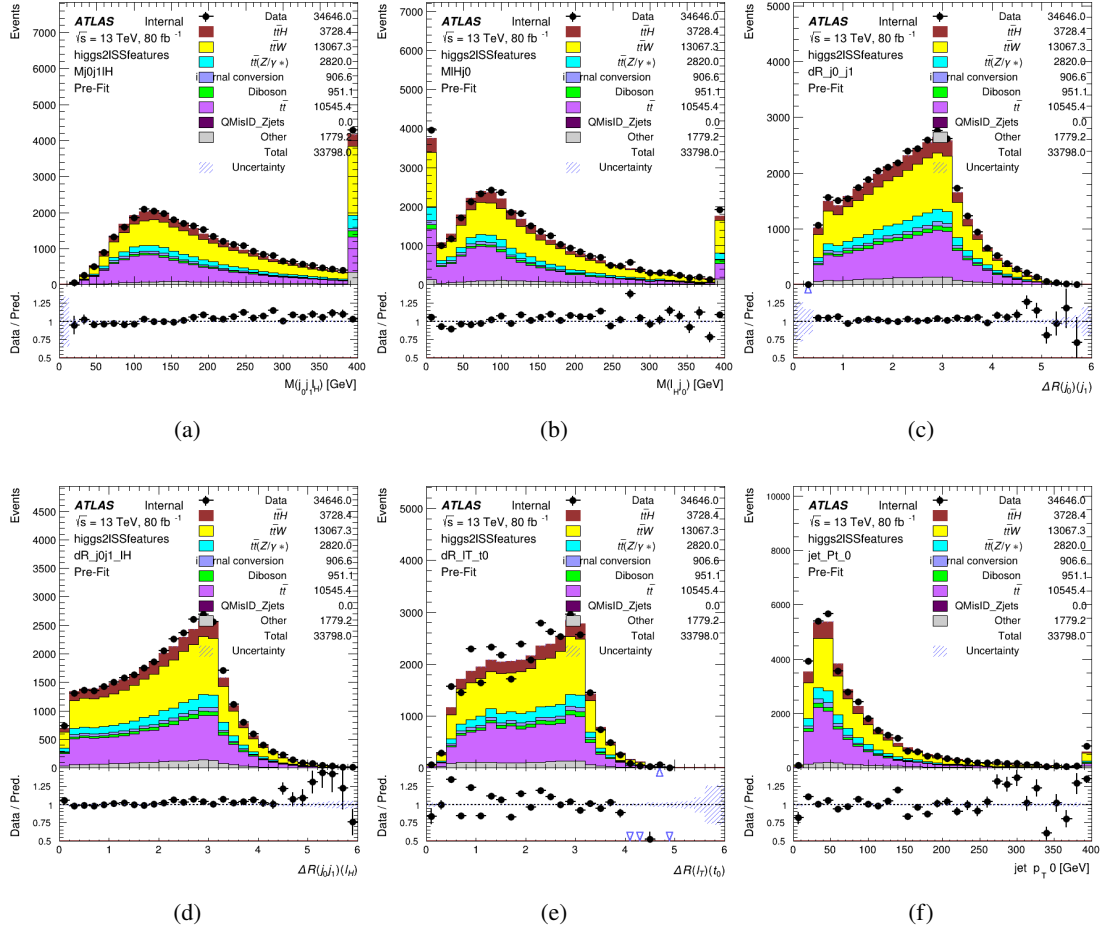


Figure 18.8: Data/MC comparisons of input features for higgs2ISS training for 79.8 fb^{-1} of data. (a) shows the invariant mass of the two jet candidates and the lepton candidate, (b) the invariant mass of jet 0 and the lepton candidate, (c) ΔR between the jet candidates, (d) ΔR between jet 0 + jet 1 and the lepton candidate, (e) ΔR between the lepton from the top and the leading b-jet, (f) the p_T of jet 0.

1369 A neural network consisting of 7 hidden layers with 60 nodes each is trained on around 2
 1370 million events, with an additional 200,000 reserved for testing the model. In order to compensate
 1371 for large number of incorrect combinations, these have been downsampled such that the correct
 1372 combinations represent over 10% of the training set. The output of the NN is summarized in
 1373 Figure 18.4.1.

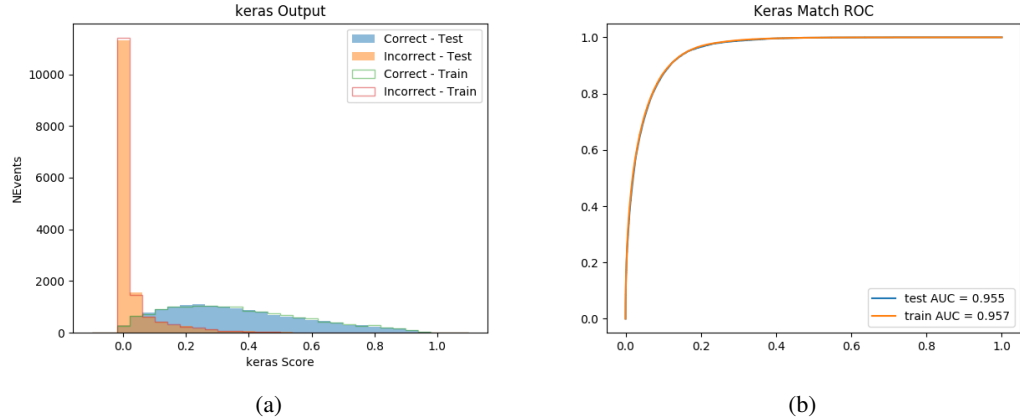


Figure 18.9: Result of the Higgs reconstruction algorithm in the 2lSS channel, showing (a) the output score of the NN for correct and incorrect combinations of jets scaled to an equal number of events, and (b) the ROC curve of the output, showing background rejection as a function of signal efficiency

1374 The neural network identifies the correct combination 55% of the time. It identifies the
 1375 correct lepton 85% of the time, and selects the correct lepton and at least one of the correct jets
 1376 81% of the time.

1377 18.4.2 3l Semi-leptonic Channel

1378 For 3l $t\bar{t}H$ where the Higgs decay semi-leptonically, the decay products include one of the three
 1379 leptons and two jets. In this case, the other two leptons originated from the decay of the tops,
 1380 meaning the opposite-sign (OS) lepton cannot have come from the Higgs. This leaves only the two
 1381 same-sign (SS) leptons as possible Higgs decay products.

Lepton $p_T H$	Lepton $p_T T_0$	Lepton $p_T T_1$
jet $p_T 0$	jet $p_T 1$	top $p_T 0$
top $p_T 1$	jet $\eta 0$	jet $\eta 1$
jet $\phi 0$	jet $\phi 1$	$\Delta R(j_0)(j_1)$
$M(j_0 j_1)$	$\Delta R(l_H)(j_0)$	$\Delta R(l_H)(j_1)$
$\Delta R(j_0 j_1)(l_H)$	$\Delta R(j_0 j_1)(l_{T_1})$	$\Delta R(l_{T_0})(l_{T_1})$
$\Delta R(l_H)(l_{T_1})$	$M(j_0 j_1 l_{T_0})$	$M(j_0 j_1 l_{T_1})$
$M(j_0 j_1 l_H)$	$\Delta R(j_0 j_1 l_H)(l_{T_0})$	$\Delta R(j_0 j_1 l_H)(l_{T_1})$
$\Delta\phi(j_0 j_1 l_H)(E_T^{\text{miss}})$	$p_T(j_0 j_1 l_H l_{T_0} l_{T_1} b_0 b_1 E_T^{\text{miss}})$	$M(j_0 j_1 b_0)$
$M(j_0 j_1 b_1)$	$\Delta R(l_{T_0})(b_0)$	$\Delta R(l_{T_0})(b_1)$
$\Delta R(l_{T_1})(b_0)$	$\Delta R(l_{T_1})(b_1)$	$\Delta R(j_0)(b_0)$
$\Delta R(j_0)(b_1)$	$\Delta R(j_1)(b_0)$	$\Delta R(j_1)(b_1)$
topScore	MET	HT jets
nJets		

Table 31: Input features used to identify the Higgs decay products in 3lS events

1382 Here j_0 and j_1 , and l_H are the jet and lepton decay candidates, respectively. The other
 1383 two leptons in the event are labeled as l_{T0} and l_{T1} . b_0 and b_1 are the two b-jets identified by
 1384 the b-jet identification algorithm. The b-jet Reco Score is the output of the Higgs reconstruction
 1385 algorithm.

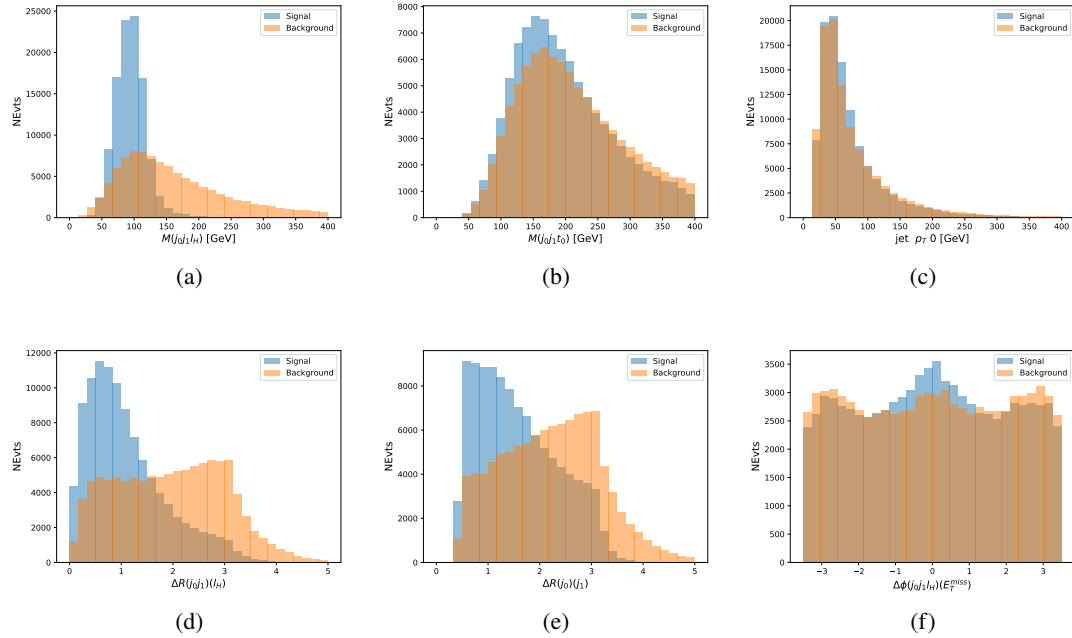


Figure 18.10: Input features for higgs3LS training. The signal in blue represents events where both jet candidates are truth b-jets from top decays, and the orange is all other combinations. Scaled to the same number of events.

1386 The modeling of these inputs is validated against data, with Figure 18.11 showing good
 1387 general agreement between data and MC. Plots for the complete list of features can found in
 1388 appendix A.1.

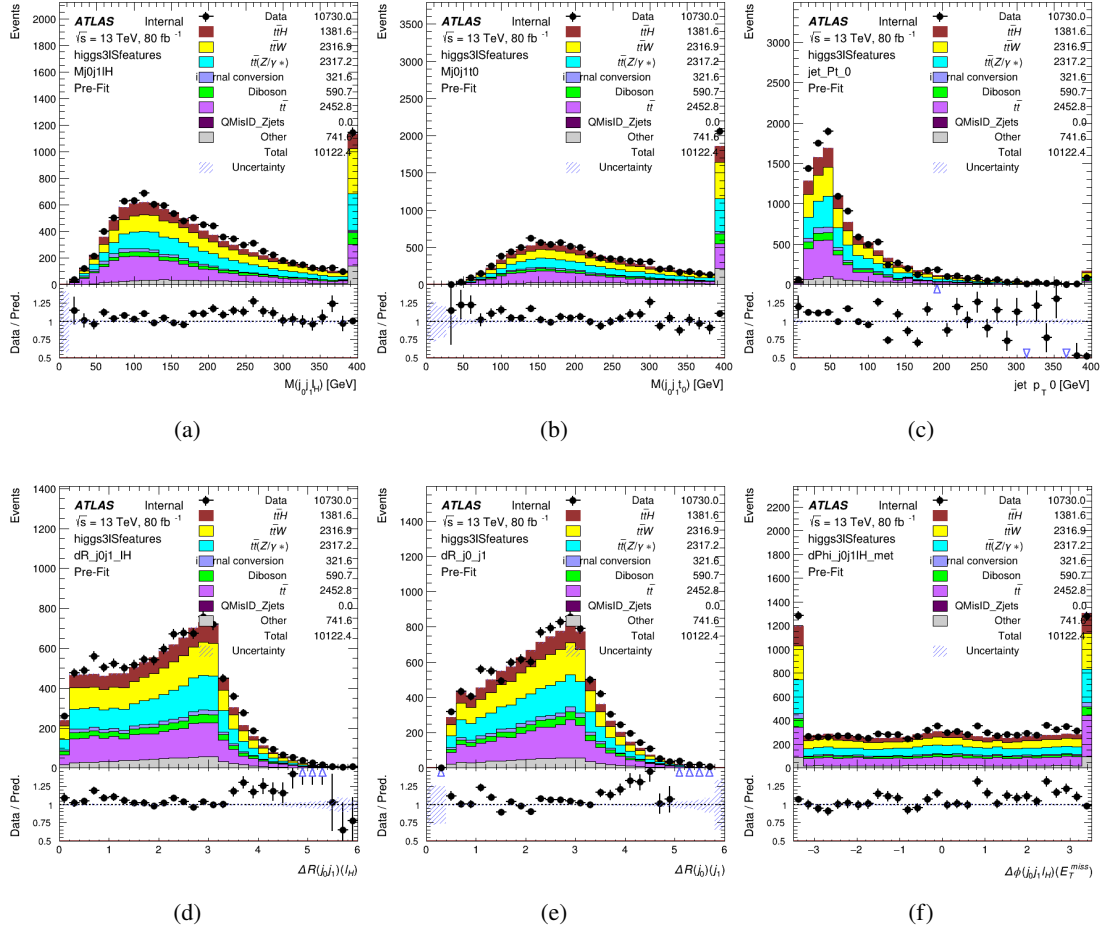


Figure 18.11: Data/MC comparisons of input features for higgs3lS training for 79.8 fb^{-1} of data.

1389 A neural network of 7 hidden layers with 70 nodes each is trained on 1.8 million events.
 1390 Once again, incorrect combinations are downsampled, such that the correct combinations are
 1391 around 10% of the training set. 10% of the dataset is reserved for testing. The output of the NN
 1392 is summarized in Figure 18.4.2.

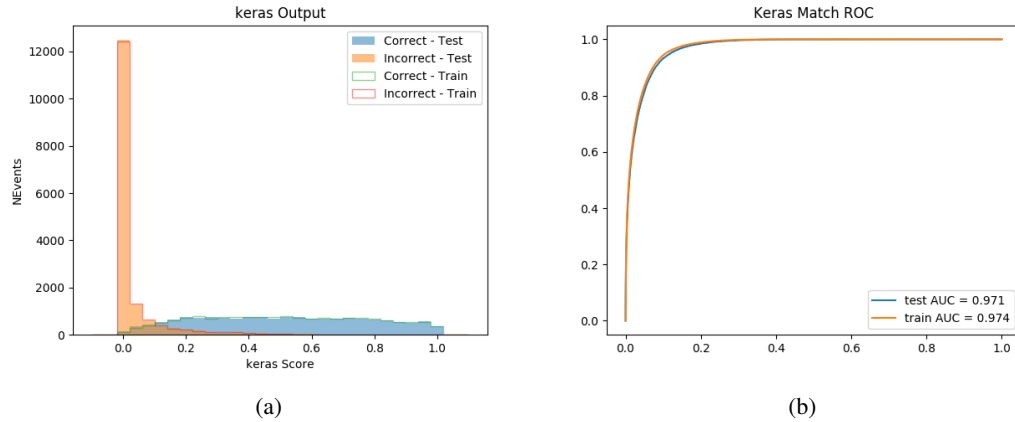


Figure 18.12: Results of the Higgs reconstruction algorithm in the 3lS channel, showing (a) the output score of the NN for correct and incorrect combinations of jets, scaled to an equal number of entries., (b) the ROC curve of the output, showing background rejection as a function of signal efficiency

1393 The neural network identifies the correct combination 64% of the time. It identifies the
1394 correct lepton 85% of the time, and selects the correct lepton and at least one of the correct jets
1395 83% of the time.

18.4.3 3l Fully-leptonic Channel

1397 In the fully-leptonic 3l case, the goal is identify which two of the three leptons originated from
1398 the Higgs decay. Since one of these two must be the OS lepton, this problem is reduced to
1399 determining which of the two SS leptons originated from the Higgs. The kinematics of both
1400 possibilities are used for training, one where the SS lepton from the Higgs is correctly labeled,
1401 and one where it is not.

Lepton $p_T H_1$	Lepton $p_T H_0$	Lepton $p_T T$
top $p_T 0$	top $p_T 1$	$\Delta\phi(l_{H_1})(E_T^{\text{miss}})$
$\Delta\phi(l_T)(E_T^{\text{miss}})$	$M(l_{H_0}l_{H_1})$	$M(l_{H_1}l_T)$
$M(l_{H_0}l_T)$	$\Delta R(l_{H_0})(l_{H_1})$	$\Delta R(l_{H_1})(l_T)$
$\Delta R(l_{H_0})(l_T)$	$\Delta R(l_{H_0}l_{H_1})(l_T)$	$\Delta R(l_{H_0}l_T)(l_{H_1})$
$\Delta R(l_{H_0}l_{H_1})(b_0)$	$\Delta R(l_{H_0}l_{H_1})(b_1)$	$\Delta R(l_{H_0}b_0)$
$M(l_{H_0}b_0)$	$\Delta R(l_{H_0}b_1)$	$M(l_{H_0}b_1)$
$\Delta R(l_{H_1}b_0)$	$M(l_{H_1}b_0)$	$\Delta R(l_{H_1}b_1)$
$M(l_{H_1}b_1)$	E_T^{miss}	topScore

Table 32: Input features used to identify the Higgs decay products in 3lF events

1402 Here l_{H0} and l_{H1} are the Higgs decay candidates. The other lepton in the event is labeled
 1403 l_T . b_0 and b_1 are the two b-jets identified by the b-jet identification algorithm. The b-jet Reco
 1404 Score is the output of the Higgs reconstruction algorithm.

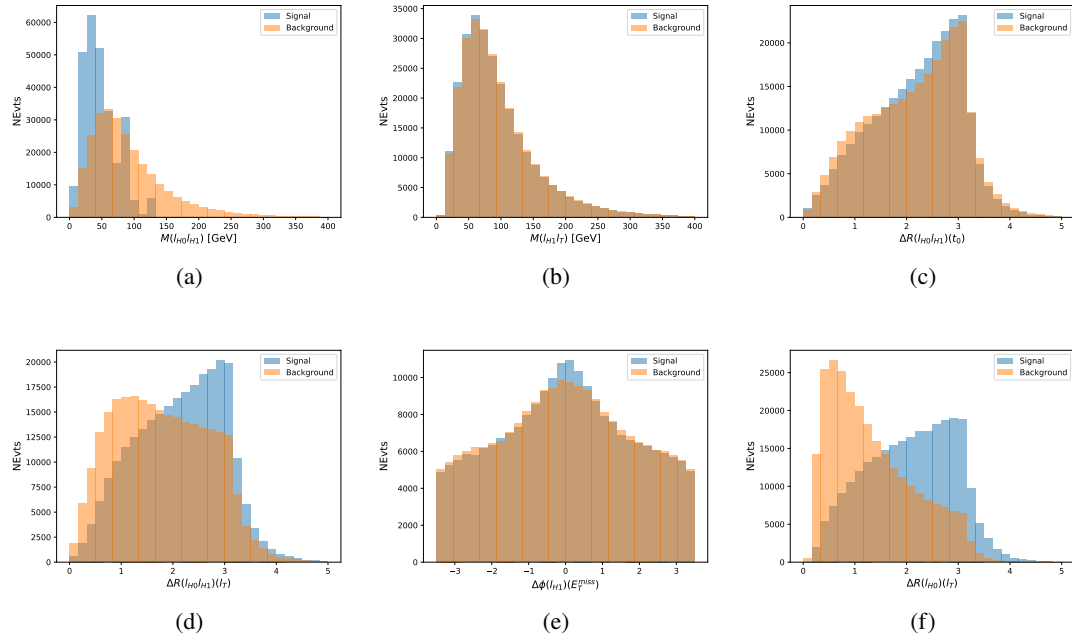


Figure 18.13: Input features for higgs3IF training. The signal in blue represents events where both jet candidates are truth b-jets from top decays, and the orange is all other combinations. Scaled to the same number of events.

1405 The modeling of these inputs is validated against data, with Figure 18.14 showing good
 1406 general agreement between data and MC. Plots for the complete list of features can found in
 1407 Section A.

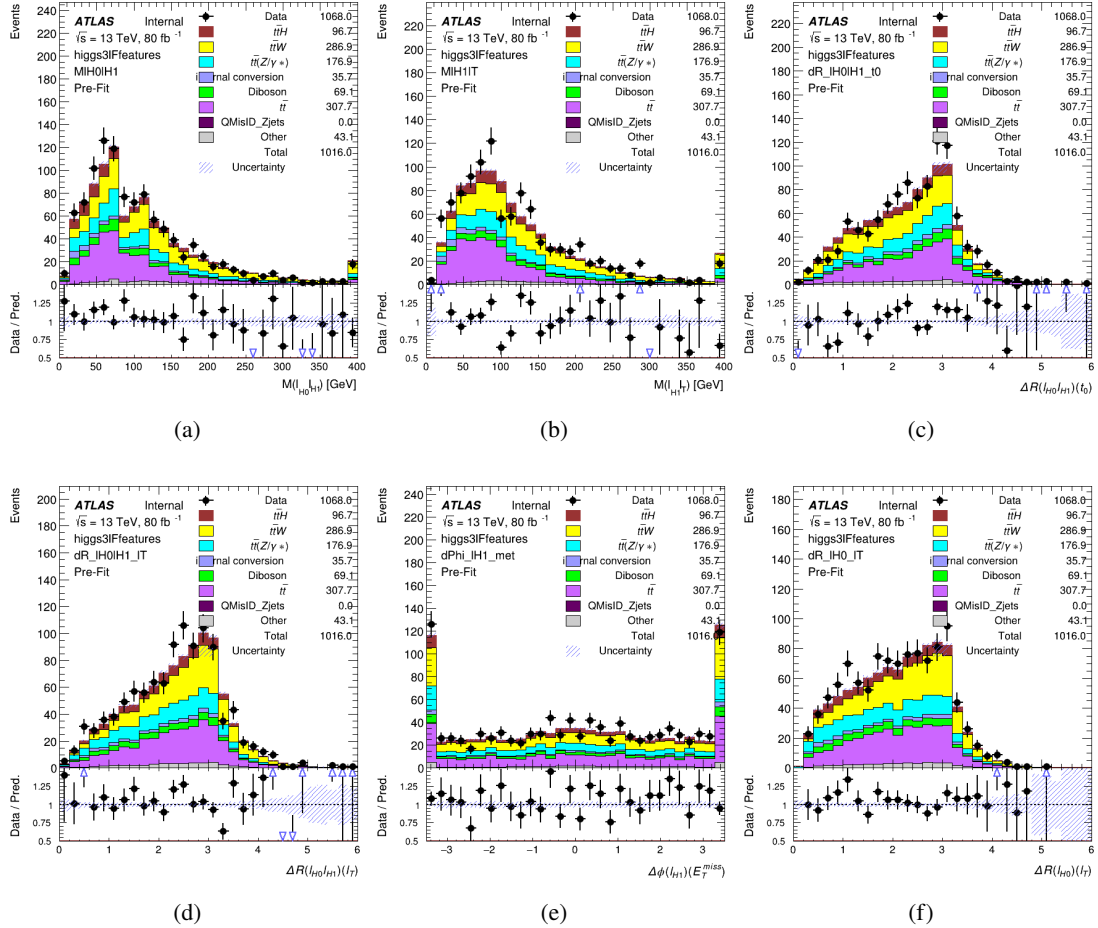


Figure 18.14: Data/MC comparisons of input features for higgs3lF training for 79.8 fb^{-1} of data.

1408 A neural network consisting of 5 nodes and 60 hidden units is trained on 800,000 events,

1409 with 10% of the dataset reserved for testing. The output of the model is summarized in Figure

1410 **18.4.3.**

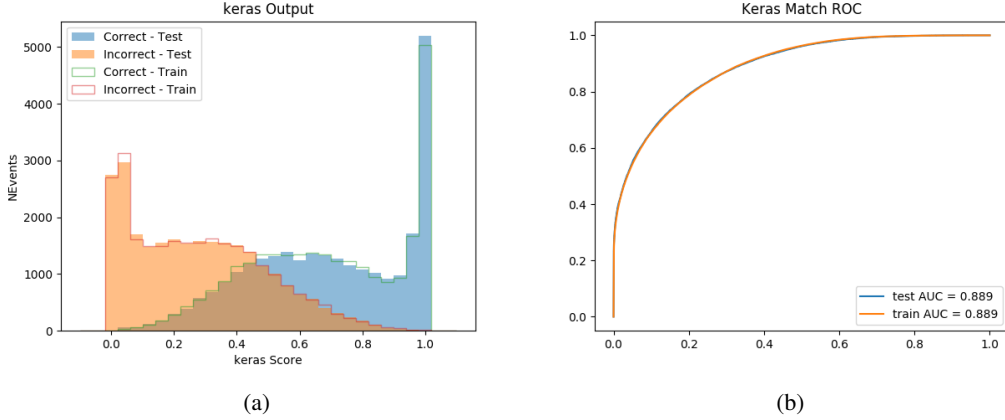


Figure 18.15: (a) the output score of the NN for correct and incorrect combinations of jets. (a) the ROC curve of the output, showing background rejection as a function of signal efficiency

1411 The correct lepton is identified by the model for 80% of events in the testing data set.

1412 **18.5 p_T Prediction**

1413 Once the most probable decay products have been identified, their kinematics are used as inputs
 1414 to a regression model which attempts to predict the momentum of the Higgs Boson. Once again,
 1415 a DNN is used. Input variables representing the b-jets and leptons not from the Higgs decay
 1416 are included as well, as these are found to improve performance. The truth p_T of the Higgs,
 1417 as predicted by MC, are used as labels. Separate models are built for each channel - 2lSS, 3l
 1418 Semi-leptonic and 3l Fully-leptonic.

1419 As a two-bin fit is targeted for the final result, some metrics evaluating the performance
 1420 of the models aim to show how well it distinguished between "high p_T " and "low p_T " events. A

1421 cutoff point of 150 GeV is used to define these two categories.

1422 Because the analysis uses a two bin fit of the Higgs p_T , the momentum reconstruction
1423 could be treated as a binary classification problem, rather than a regression problem. This
1424 approach is explored in detail in Section A.5, and is found not to provide any significant increase
1425 in sensitivity. The regression approach is used because it provides more flexibility for future
1426 analyses, as it is independent of the cutoff between high and low p_T , as well as the number of
1427 bins. Further, a regression allows the output of the neural network to be more clearly understood,
1428 as it can be directly compared to a physics observable.

1429 **18.5.1 2lSS Channel**

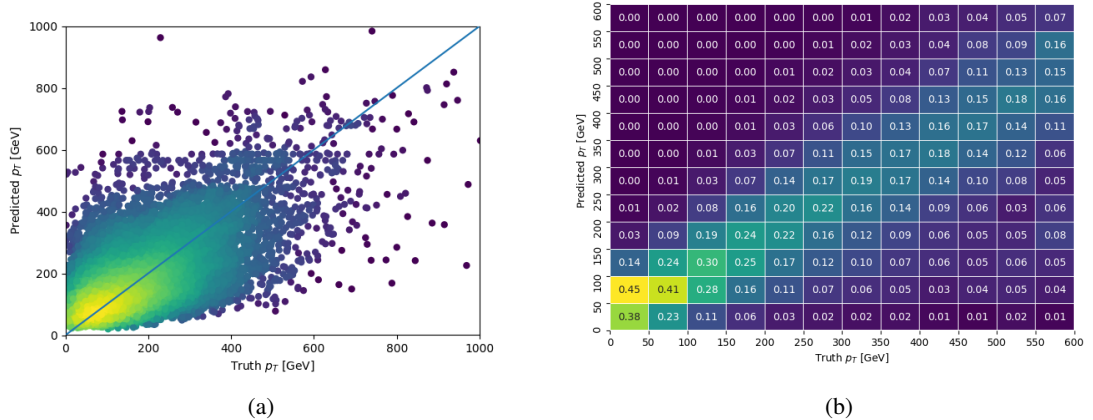
1430 The input variables listed in Table 33 are used to predict the Higgs p_T in the 2lSS channel. Here
1431 j_0 and j_1 are the two jets identified as Higgs decay products. The lepton identified as originating
1432 from the Higgs is labeled l_H , while the other lepton is labeled l_T , as it is assumed to have come
1433 from the decay of one of the top quarks. b_0 and b_1 are the two b-jets identified by the b-jet
1434 identification algorithm. The Higgs Reco Score and b-jet Reco Score are the outputs of the Higgs
1435 reconstruction algorithm, and the b-jet identification algorithm, respectively.

HT	$M(j_0 j_1)$	$M(j_0 j_1 l_H)$
$M(l_H j_0)$	$M(l_H j_1)$	$p_T(b_0 b_1)$
$p_T(j_0 j_1 l_H)$	$\Delta\phi(j_0 j_1 l_H)(E_T^{\text{miss}})$	$\Delta R(j_0)(j_1)$
$\Delta R(j_0 j_1)(l_H)$	$\Delta R(j_0 j_1 l_H)(l_T)$	$\Delta R(j_0 j_1 l_H)(b_0)$
$\Delta R(j_0 j_1 l_H)(b_1)$	$\Delta R(l_H)(j_0)$	$\Delta R(l_H)(b_0)$
$\Delta R(l_H)(b_1)$	$\Delta R(l_T)(b_0)$	$\Delta R(l_T)(b_1)$
$\Delta R(b_0)(b_1)$	Higgs Reco Score	jet η 0
jet η 1	jet Phi 0	jet Phi 1
jet p_T 0	jet p_T 1	Lepton η H
Lepton ϕ H	Lepton p_T H	Lepton p_T T
E_T^{miss}	nJets	b-jet Reco Score
b-jet p_T 0	b-jet p_T 1	

Table 33: Input features for reconstructing the Higgs p_T spectrum for 2lSS events

1436 The optimal neural network architecture for this channel is found to consist of 7 hidden
 1437 layers with 60 nodes each. The input data set includes 1.2 million events, 10% of which is used
 1438 for testing, the other 90% for training. Training is found to converge after around 150 epochs.

1439 To evaluate the performance of the model, the predicted p_T spectrum is compared to the
 1440 truth Higgs p_T in Figure 18.16. In order to visualize the model performance more clearly, in (a)
 1441 of that figure, the color of each point is determined by Kernel Density Estimation (KDE). The
 1442 color shown represents the logarithm of the output from KDE, to counteract the large number of
 1443 low p_T events. For that same reason, each column of the histogram shown in (b) of Figure 18.16
 1444 is normalized to unity. This plot therefore demonstrates what the model predicts for each slice
 1445 of truth p_T .



1447 GeV and >150 GeV. Figure 18.17 demonstrates the NN output for high and low p_T events based
 1448 on this cutoff.

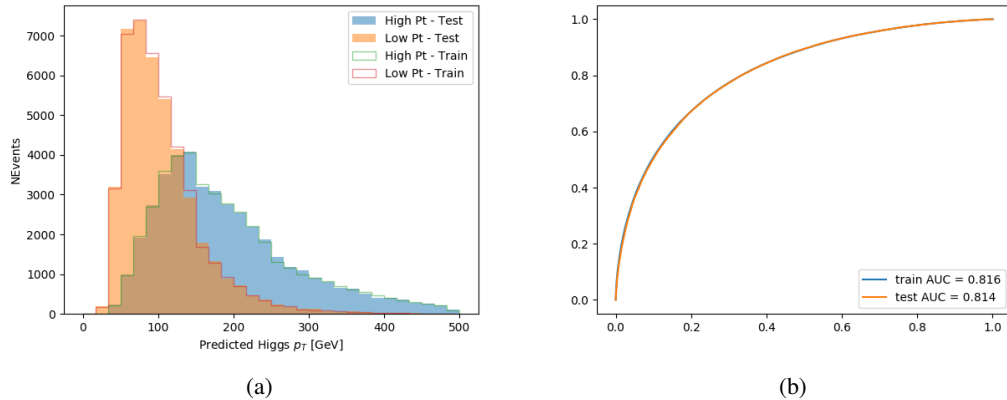


Figure 18.17: (a) shows the reconstructed Higgs p_T for 2lSS events with truth $p_T > 150$ GeV and < 150 GeV, while (b) shows the ROC curve for those two sets of events.

1449 18.5.2 3l Semi-leptonic Channel

1450 The following input features are used to predict the Higgs p_T for events in the 3lS channel:

HT jets	MET	$M(j_0 j_1)$
$M(j_0 j_1 l_H)$	$M(j_0 j_1 l_{T0})$	$M(j_0 j_1 l_{T1})$
$M(j_0 j_1 b_0)$	$M(j_0 j_1 b_1)$	$M(b_0 l_{T0})$
$M(b_0 l_{T1})$	$M(b_1 l_{T0})$	$M(b_1 l_{T1})$
$\Delta\phi(j_0 j_1 l_H)(E_T^{\text{miss}})$	$\Delta R(j_0)(j_1)$	$\Delta R(j_0 j_1)(l_H)$
$\Delta R(j_0 j_1)(l_{T1})$	$\Delta R(j_0 j_1)(b_0)$	$\Delta R(j_0 j_1)(b_1)$
$\Delta R(j_0 j_1 l_H)(l_{T0})$	$\Delta R(j_0 j_1 l_H)(l_{T1})$	$\Delta R(j_0 j_1 l_H)(b_0)$
$\Delta R(j_0 j_1 l_H)(b_1)$	$\Delta R(l_H)(j_0)$	$\Delta R(l_H)(j_1)$
$\Delta R(l_H)(l_{T1})$	$\Delta R(l_{T0})(l_{T1})$	$\Delta R(l_{T0})(b_0)$
$\Delta R(l_{T0})(b_1)$	$\Delta R(l_{T1})(b_0)$	$\Delta R(l_{T1})(b_1)$
higgsScore	jet η 0	jet η 1
jet ϕ 0	jet ϕ 1	jet p_T 0
jet p_T 1	Lepton η H	Lepton ϕ H
Lepton p_T H	Lepton p_T T0	Lepton p_T T1
nJets	topScore	b-jet p_T 0
b-jet p_T 1		

Table 34: Input features for reconstructing the Higgs p_T spectrum for 3lS events

Again, j_0 and j_1 are the two jets identified as Higgs decay products, ordered by p_T . The lepton identified as originating from the Higgs is labeled l_H , while the other two leptons are labeled l_{T0} and l_{T1} . b_0 and b_1 are the two b-jets identified by the b-jet identification algorithm. The Higgs Reco Score and b-jet Reco Score are the outputs of the Higgs reconstruction algorithm, and the b-jet identification algorithm, respectively.

The optimal neural network architecture for this channel is found to consist of 7 hidden layers with 80 nodes each. The inputdata set includes one million events, 10% of which is used for testing, the other 90% for training. Training is found to converge after around 150 epochs.

To evaluate the performance of the model, the predicted p_T spectrum is compared to the truth Higgs p_T in Figure 18.18. Once again, (a) of 18.18 shows a scatterplots of predicted vs truth p_T , where the color of each point corresponds to the log of the relative KDE at that point. Each column of the the histogram in (b) is normalized to unity, to better demonstrate the output of the NN for each slice of truth p_T .

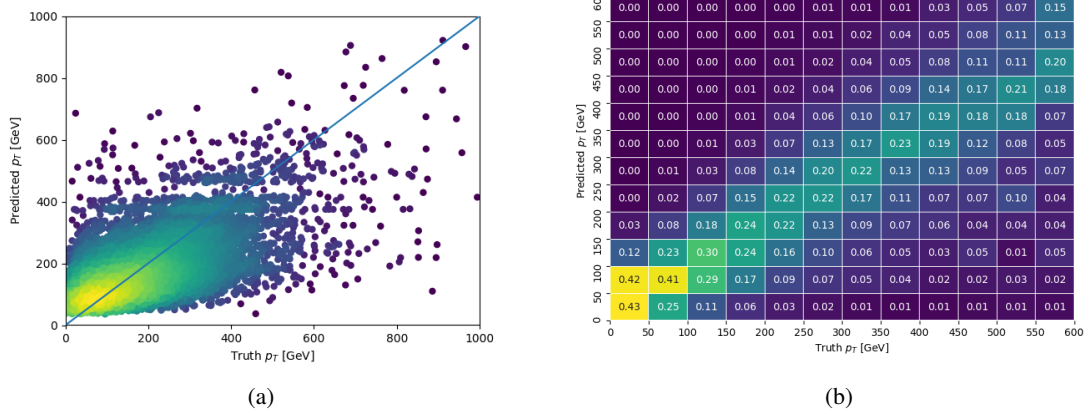


Figure 18.18: The regressed Higgs momentum spectrum as a function of the truth p_T for 3IS $t\bar{t}H$ events in (a) a scatterplot, where the color of each point represents the log of the point density, based on Gaussian Kernal Density Estimation, and (b) a histogram where each column has been normalized to one.

1464 Figure 18.19 shows (a) the output of the NN for events with truth p_T less than and greater
 1465 than 150 GeV and (b) the ROC curve demonstrating how well the NN distinguishes high and low
 1466 p_T events.

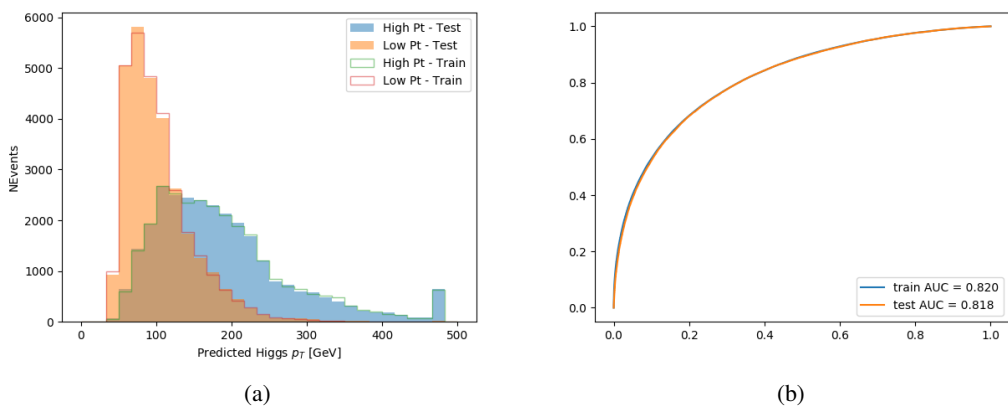


Figure 18.19: (a) shows the reconstructed Higgs p_T for 3IS events with truth $p_T > 150$ GeV and < 150 GeV, while (b) shows the ROC curve for those two sets of events.

1467 18.5.3 3l Fully-leptonic Channel

1468 The features listed in 35 are used to construct a model for predictin the Higgs p_T for 3lF events.

HT	$M(l_{H0}l_{H1})$	$M(l_{H0}l_T)$
$M(l_{H0}b_0)$	$M(l_{H0}b_1)$	$M(l_{H1}l_T)$
$M(l_{H1}b_0)$	$M(l_{H1}b_1)$	$\Delta R(l_{H0})(l_{H1})$
$\Delta R(l_{H0})(l_T)$	$\Delta R(l_{H0}l_{H1})(l_T)$	$\Delta R(l_{H0}l_T)(l_{H1})$
$\Delta R(l_{H1})(l_T)$	$\Delta R(l_{H0}b_0)$	$\Delta R(l_{H0}b_1)$
$\Delta R(l_{H1}b_1)$	$\Delta R(l_{H1}b_0)$	higgsScore
Lepton η H_0	Lepton η H_1	Lepton η T
Lepton p_T H_0	Lepton p_T H_1	Lepton p_T T
E_T^{miss}	topScore	b-jet p_T 0
b-jet p_T 1		

Table 35: Input features for reconstructing the Higgs p_T spectrum for 3lF events

1469 l_{H0} and l_{H1} represent the two leptons identified by the Higgs reconstruction model as
 1470 originating from the Higgs, while l_T is the other lepton in the event. The Higgs Reco Score and
 1471 b-jet Reco Score are the outputs of the Higgs reconstruction algorithm, and b-jet identification
 1472 algorithm, respectively.

1473 The optimal neural network architecture for this channel is found to consist of 5 hidden
 1474 layers with 40 nodes each. The input data set includes 400,000 events, 10% of which is used for
 1475 testing, the other 90% for training. Training is found to converge after around 150 epochs.

1476 The predicted transverse momentum, as a function of the truth p_T , is shown in Figure
 1477 [18.20](#).

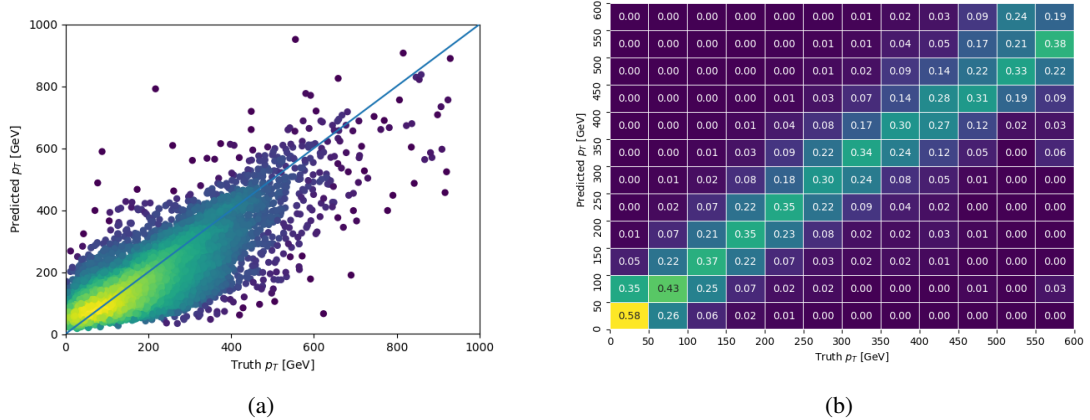


Figure 18.20: The regressed Higgs momentum spectrum as a function of the truth p_T for 3lF $t\bar{t}H$ events in (a) a scatterplot, where the color of each point represents the log of the point density, based on Gaussian Kernel Density Estimation, and (b) a histogram where each column has been normalized to one.

1478 When split into high and low p_T , based on a cutoff of 150 GeV, the

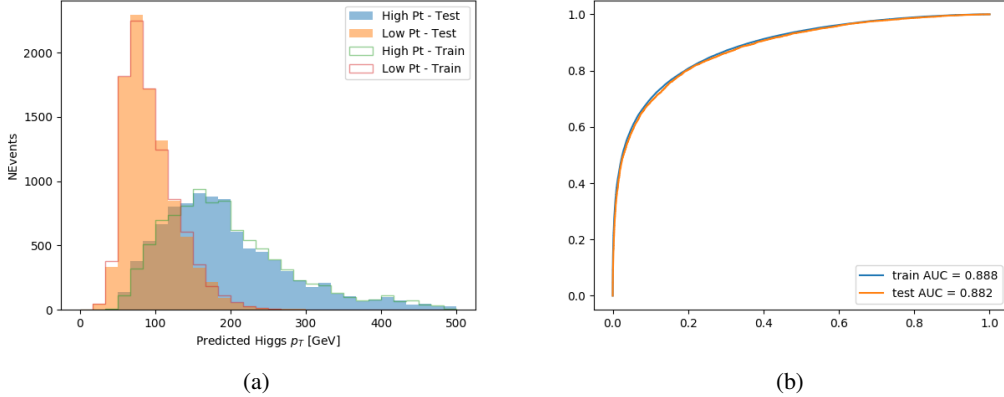


Figure 18.21: (a) shows the reconstructed Higgs p_T for 3lF events with truth $p_T > 150$ GeV and < 150 GeV, while (b) shows the ROC curve for those two sets of events.

1479 18.6 3l Decay Mode

1480 In the 3l channel, there are two possible ways for the Higgs to decay, both involving intermediate
 1481 W boson pairs: Either both W bosons decay leptonically, in which case the reconstructed decay
 1482 consists of two leptons (referred as the fully-leptonic 3l channel), or one W decays leptonically
 1483 and the other hadronically, giving two jets and one lepton in the final state (referred to as the
 1484 semi-leptonic 3l channel). In order to accurately reconstruct the Higgs, it is necessary to identify
 1485 which of these decays took place for each 3l event.

1486 The kinematics of each event, along with the output scores of the Higgs and top recon-
 1487 struction algorithms, are used to distinguish these two possible decay modes. The particular
 1488 inputs used are listed in Table 36.

HT jets	$M(l_0 t_0)$	$M(l_0 t_1)$
$M(l_1 t_0)$	$M(l_1 t_1)$	$M(l_0 l_1)$
$M(l_0 l_2)$	$M(l_1 l_2)$	$\Delta R(l_0 t_0)$
$\Delta R(l_0 t_1)$	$\Delta R(l_1 t_0)$	$\Delta R(l_1 t_1)$
$\Delta R(l l_0 1)$	$\Delta R(l l_0 2)$	$\Delta R(l l_1 2)$
Lepton η 0	Lepton η 1	Lepton η 2
Lepton ϕ 0	Lepton ϕ 1	Lepton ϕ 2
Lepton p_T 0	Lepton p_T 1	Lepton p_T 2
E_T^{miss}	nJets	nJets OR DL1r 60
nJets OR DL1r 85	score3lF	score3lS
topScore	total charge	

Table 36: Input features used to distinguish semi-leptonic and fully-leptonic Higgs decays in the 3l channel.

1489 Here l_0 is the opposite charge lepton, l_1 and l_2 are the two SS leptons order by ΔR
 1490 from lepton 0. score3lF and score3lS are the outputs of the 3lS and 3lF Higgs reconstruction
 1491 algorithms, while topScore is the output of the b-jet identification algorithm.

1492 A neural network with 5 hidden layers, each with 50 nodes, is trained to distinguish these
 1493 two decay modes. The output of the model is summarized in Figure 18.22.

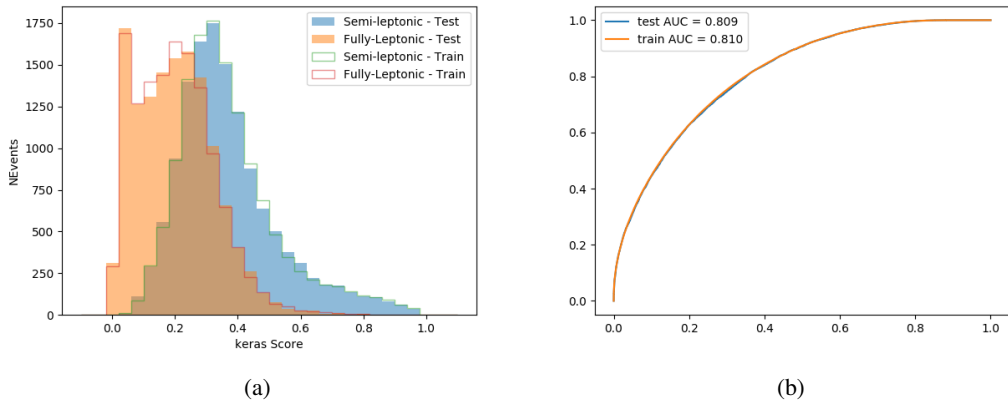


Figure 18.22: (a) shows the output of the decay separation NN for Semi-leptonic (blue) and Fully-leptonic (orange) 3l events, scaled to equal area. (b) shows the ROC curve for those two sets of events.

1494 A cutoff of 0.23 is determined to be optimal for separating 3lS and 3lF in the fit.

1495 19 Signal Region Definitions

1496 Events are divided into two channels based on the number of leptons in the final state: one with
 1497 two same-sign leptons, the other with three leptons. The 3l channel includes events where both
 1498 leptons originated from the Higgs boson as well as events where only one of the leptons

1499 19.1 Pre-MVA Event Selection

1500 A preselection is applied to define orthogonal analysis channels based on the number of leptons
1501 in each event. For the 2lSS channel, the following preselection is used:

- 1502
- Two very tight, same-charge, light leptons with $p_T > 20 \text{ GeV}$

1503

 - ≥ 4 reconstructed jets, ≥ 1 b-tagged jets

1504

 - No reconstructed tau candidates

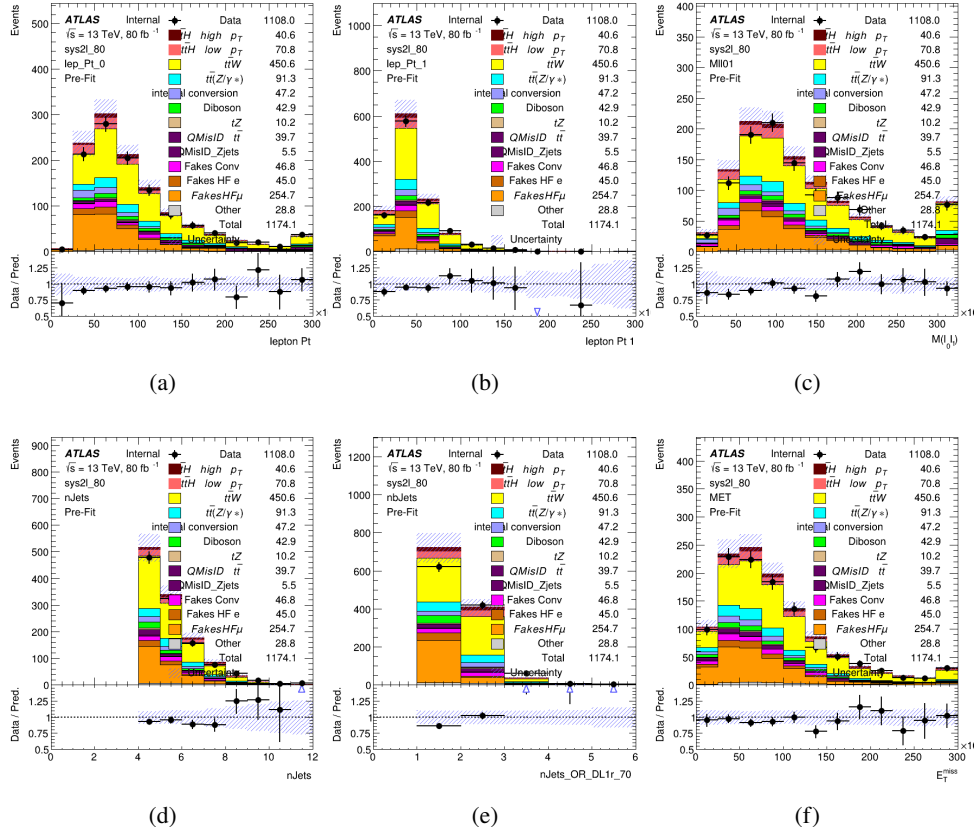
1505 The event yield after the 2lSS preselection has been applied, for MC and data at 79.8 fb^{-1} ,
1506 is shown in Table 19.1.

Process	Yield	
t̄H high p _T	41	±5
t̄H low p _T	71	±8
t̄W	450	±70
t̄(Z/γ*)	91	±11
t̄ll low mass	10	±6
Rare Top	20	±12
VV	42	±22
tZ	10	±5
QMisID	44.7	±2.7
Fakes int. conv	47	±26
Fakes ext. conv	46	±44
Fakes HF e	45	±23
Fakes HF μ	250	±50
Three top	2.2	±1.1
Four top	5.64	±0.31
t̄WW	10.9	±0.6
tW	1.2 × 10 ⁻⁵	±3.5e-06
WtZ	9.1	±0.8
VVV	0.30	±0.05
VH	0.6	±1.0
Total	1170	±120
Data	1108	

Table 37: Yields of the 2lSS preselection region

1507

Figure 19.1. Good general agreement is found.

Figure 19.1: Data/MC comparisons of the 2LSS pre-selection region. (a) and (b) show the p_T of leptons 0 and 1, (c) shows the invariant mass of lepton 0 and 1, (d) shows the jet multiplicity, (e) the b-tagged jet multiplicity, and (f) the missing transverse energy.

1508

For the 3l channel, the following selection is applied:

1509

- Three light leptons with total charge ± 1
- Same charge leptons are required to be very tight, with $p_T > 20$ GeV
- Opposite charge lepton must be loose, with $p_T > 10$ GeV

1510

1511

- 1512 • ≥ 2 reconstructed jets, ≥ 1 b-tagged jets
- 1513 • No reconstructed tau candidates
- 1514 • $|M(l^+l^-) - 91.2 \text{ GeV}| > 10 \text{ GeV}$ for all opposite-charge, same-flavor lepton pairs
- 1515 The event yield after the 31 preselection has been applied, for MC and data at 79.8 fb^{-1} ,
- 1516 is shown in Table 19.1.

Process	Yield
t̄H high p _T	20.5 ±2.3
t̄H low p _T	33.6 ±3.8
t̄W	138 ±18
t̄Z/γ	80 ±9
t̄lllowmass	3.5±2.0
rareTop	22 ±12
VV	39 ±19
tZ	9.2±4.5
QMisID	1.8±0.6
Fakes int. conv	31 ±17
Fakes ext. conv	14 ±11
Fakes HF e	20 ±10
Fakes HF μ	102 ±22
Three top	0.96±0.48
Four top	6.17±0.35
t̄WW	5.46±0.33
tW	$1.20 \times 10^{-5} \pm 3.5\text{-}06$
WtZ	8.7±0.6
VVV	0.81±0.11
VH	$1.20 \times 10^{-5} \pm 3.5\text{-}06$
Total	512 ±48
Data	535

Table 38: Yields of the 3l preselection region.

1517

Comparisons of kinematic distributions for data and MC in this region are shown in Figure

1518 19.2.

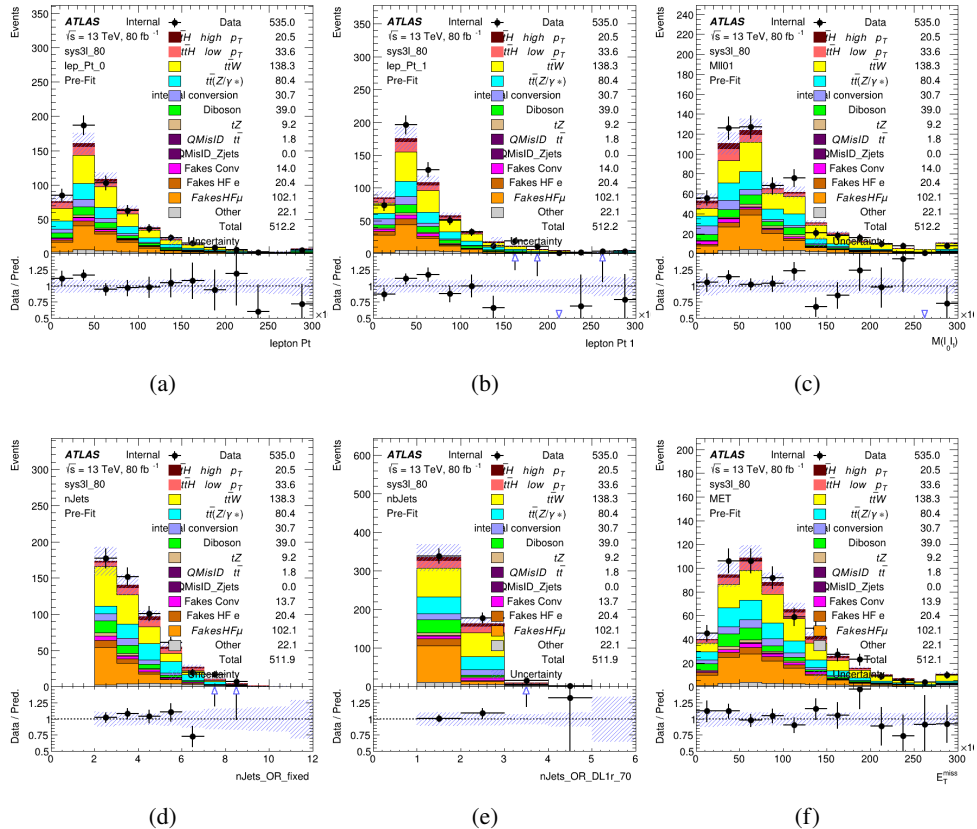


Figure 19.2: Data/MC comparisons of the 3l pre-selection region. (a) and (b) show the p_T of leptons 0 and 1, (c) shows the invariant mass of lepton 0 and 1, (d) shows the jet multiplicity, (e) the b-tagged jet multiplicity, and (f) the missing transverse energy.

1519

19.2 Event MVA

1520

Separate multi-variate analysis techniques (MVAs) are used in order to distinguish signal events from background for each analysis channel - 2lSS, 3l semi-leptonic (3lS), and 3l fully leptonic (3lF). Here events with three leptons are split into 3lS and 3lF based on the model described

1523 in 18.6. In particular, Boosted Decision Tree (BDT) algorithms are produced with XGBoost
1524 [**xgboost**] are trained using the kinematics of signal and background events derived from Monte
1525 Carlo simulations. Events are weighted in the BDT training by the weight of each Monte Carlo
1526 event.

1527 Because the background composition differs for events with a high reconstructed Higgs p_T
1528 compared to events with low reconstructed Higgs p_T , separate MVAs are produced for high and
1529 low p_T regions. This is found to provide better significance than attempting to build an inclusive
1530 model, as demonstrated in appendix A.2. A cutoff of 150 GeV is used. This gives a total of 6
1531 background rejection MVAs - explicitly, 2lSS high p_T , 2lSS low p_T , 3lS high p_T , 3lS low p_T ,
1532 3lF high p_T , and 3lF low p_T .

1533 The following features are used in both the high and low p_T 2lSS BDTs:

HT	$M(\text{lep}, E_T^{\text{miss}})$	$M(l_0 l_1)$
binHiggs p_T 2ISS	$\Delta R(l_0)(l_1)$	diLepton type
higgsRecoScore	jet η 0	jet η 1
jet ϕ 0	jet ϕ 1	jet p_T 0
jet p_T 1	Lepton η 0	Lepton η 1
Lepton ϕ 0	Lepton ϕ 1	Lepton p_T 0
Lepton p_T 1	E_T^{miss}	$\min \Delta R(l_0)(\text{jet})$
$\min \Delta R(l_1)(\text{jet})$	$\min \Delta R(\text{Lepton})(\text{bjet})$	mjjMax frwdJet
nJets	nJets OR DL1r 60	nJets OR DL1r 70
nJets OR DL1r 85	topRecoScore	

Table 39: Input features used to distinguish signal and background events in the 2ISS channel.

1534

While for each of the 31 BDTs, the features listed below are used for training:

$M(\text{lep}, E_T^{\text{miss}})$	$M(l_0 l_1)$	$M(l_0 l_1 l_2)$
$M(l_0 l_2)$	$M(l_1 l_2)$	$\text{binHiggs } p_T \text{ 3lF}$
$\text{binHiggs } p_T \text{ 3lS}$	$\Delta R(l_0)(l_1)$	$\Delta R(l_0)(l_2)$
$\Delta R(l_1)(l_2)$	decayScore	higgsRecoScore3lF
higgsRecoScore3lS	$\text{jet } \eta \text{ 0}$	$\text{jet } \eta \text{ 1}$
$\text{jet } \phi \text{ 0}$	$\text{jet } \phi \text{ 1}$	$\text{jet } p_T \text{ 0}$
$\text{jet } p_T \text{ 1}$	$\text{Lepton } \eta \text{ 0}$	$\text{Lepton } \eta \text{ 1}$
$\text{Lepton } \eta \text{ 2}$	$\text{Lepton } \phi \text{ 0}$	$\text{Lepton } \phi \text{ 1}$
$\text{Lepton } \phi \text{ 2}$	$\text{Lepton } p_T \text{ 0}$	$\text{Lepton } p_T \text{ 1}$
$\text{Lepton } p_T \text{ 2}$	E_T^{miss}	$\min \Delta R(l_0)(\text{jet})$
$\min \Delta R(l_1)(\text{jet})$	$\min \Delta R(l_2)(\text{jet})$	$\min \Delta R(\text{Lepton})(\text{bjet})$
$mjj\text{Max frwdJet}$	$n\text{Jets}$	$n\text{Jets OR DL1r 60}$
$n\text{Jets OR DL1r 70}$	$n\text{Jets OR DL1r 85}$	topScore

Table 40: Input features used to distinguish signal and background events in the 3l channel.

1535 Modelling of each of these input features is verified in Appendix A.2 by comparing data
 1536 and MC for 79.8 fb^{-1} . The BDTs are produced with a maximum tree depth of 6, using AUC as
 1537 the target loss function. The BDT response distribution and ROC curve for each model is shown
 1538 in Figures 19.3-19.5.

2lSS

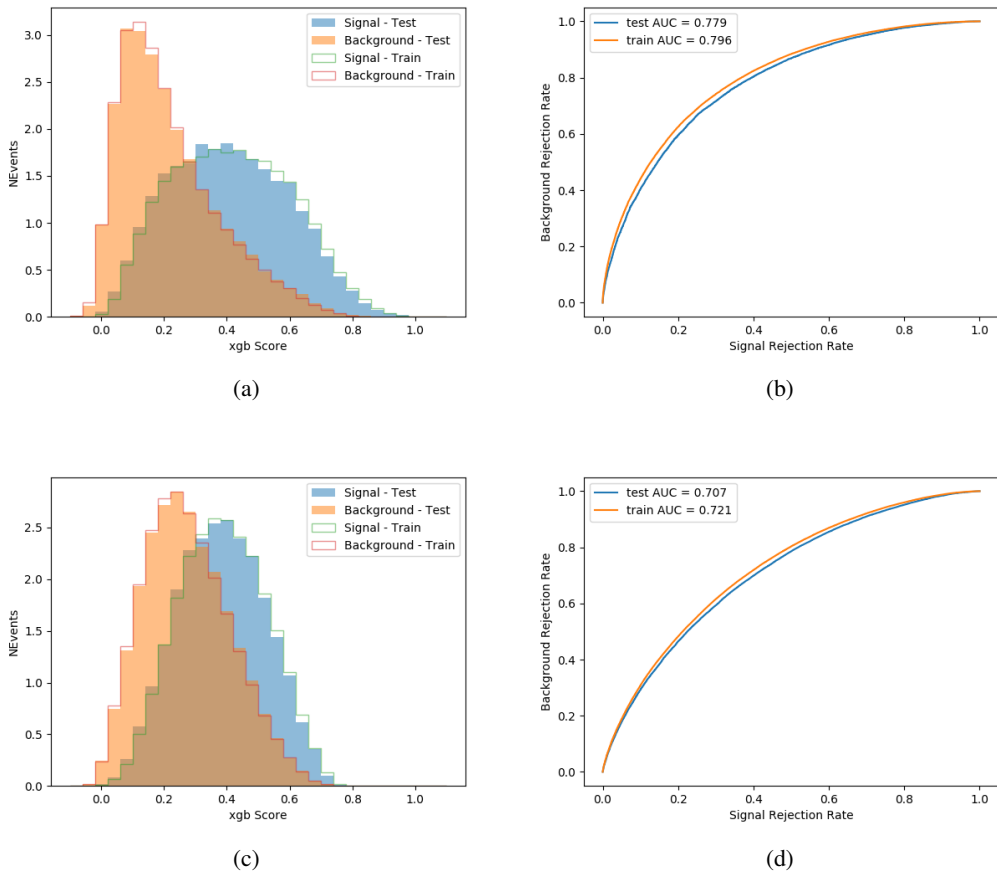


Figure 19.3: Output BDT scores of training and testing data for signal (blue) and background (orange) for 2lSS events with (a) high regressed Higgs p_T and (b) low regressed Higgs p_T . (b) and (d) show the ROC curve for the 2lSS high and low p_T models, respectively.

3l - Semileptonic

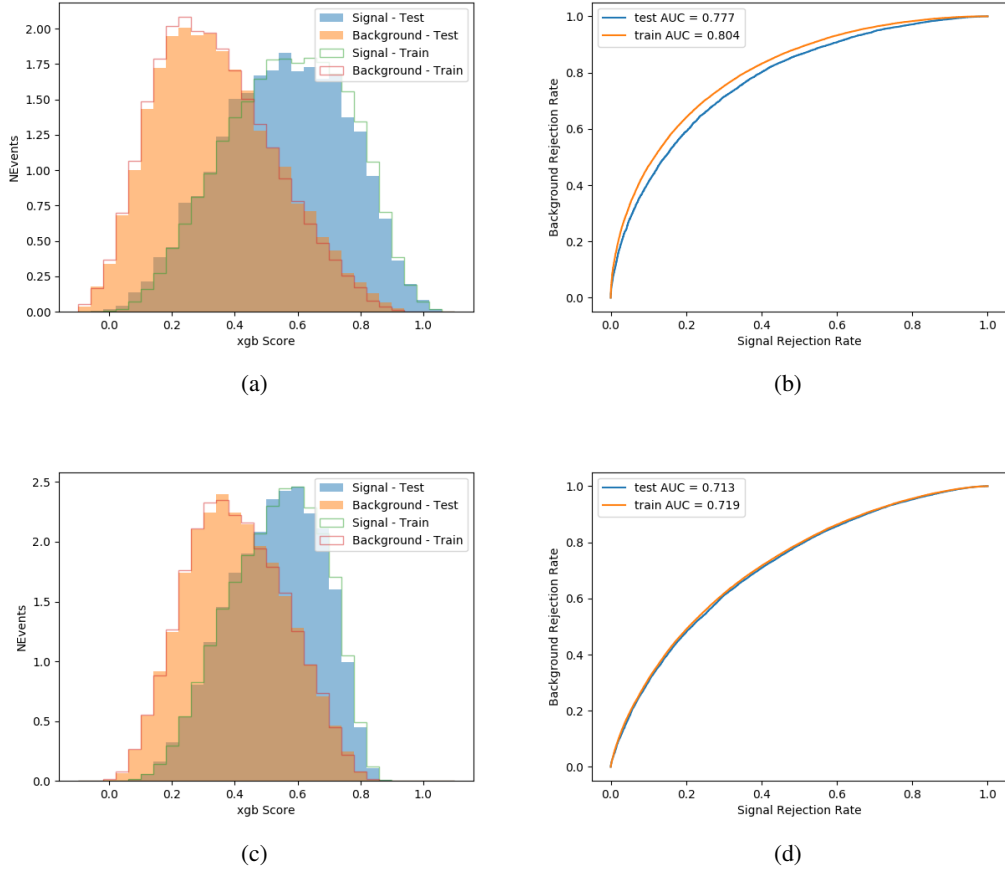


Figure 19.4: Output BDT scores of training and testing data for signal (blue) and background (orange) for 3lS events with (a) high regressed Higgs p_T and (b) low regressed Higgs p_T . (b) and (d) show the ROC curve for the 3lS high and low p_T models, respectively.

3l - Fully Leptonic

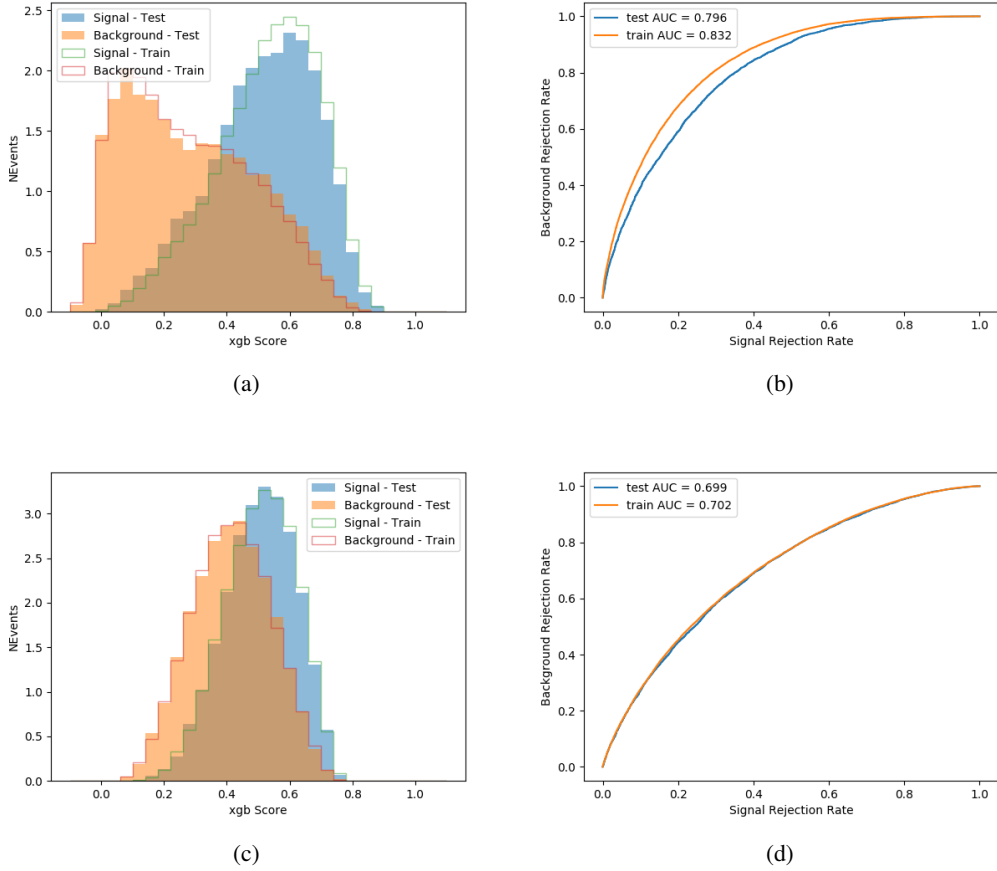


Figure 19.5: Output BDT scores of training and testing data for signal (blue) and background (orange) for 3lF events with (a) high regressed Higgs p_T and (b) low regressed Higgs p_T . (b) and (d) show the ROC curve for the 3lF high and low p_T models, respectively.

1539 Output distributions of each MVA, comparing MC predictions to data at 79.8 fb^{-1} are

1540 shown in figures 19.6-19.2.

High p_T Background Rejection BDTs

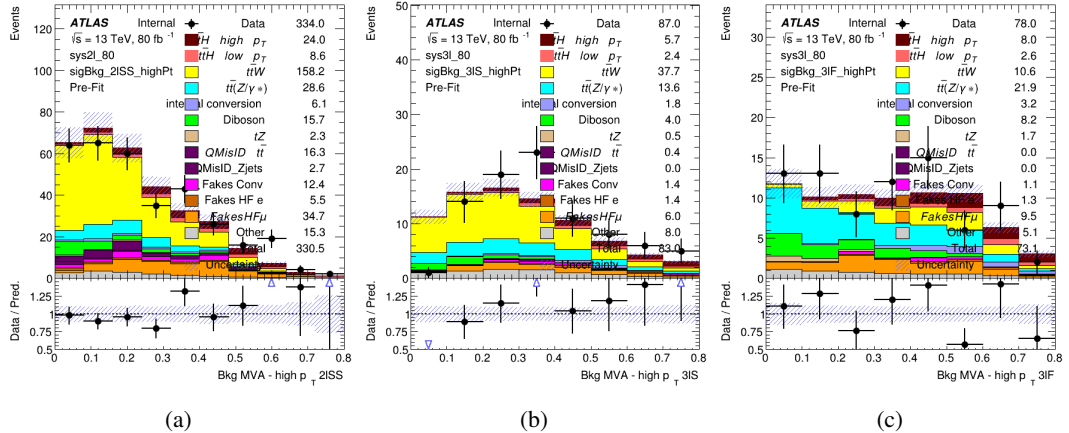


Figure 19.6: Output score of the high p_T BDTs in the (a) 2ISS, (b) 3IS, and (c) 3IF channels

Low p_T Background Rejection BDTs

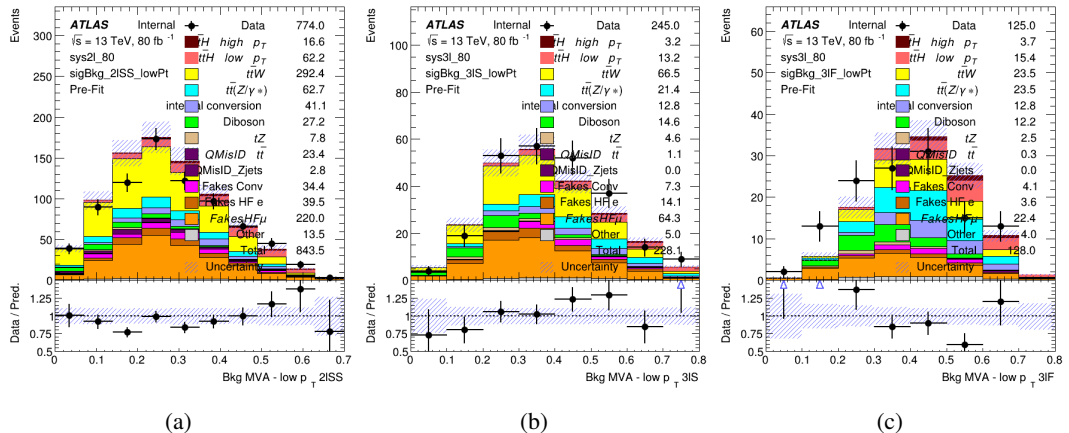


Figure 19.7: Output score of the low p_T BDTs in the (a) 2ISS, (b) 3IS, and (c) 3IF channels

1541 19.3 Signal Region Definitions

1542 Once pre-selection has been applied, channels are further refined based on the MVAs described
 1543 above. The output of the model described in Section 18.6 is used to separate the three channel
 1544 into two - Semi-leptonic and Fully-leptonic - based on the predicted decay mode of the Higgs
 1545 boson. This leaves three orthogonal signal regions - 2lSS, 3lS, and 3lF.

1546 For each event, depending on the number of leptons as well as whether the p_T of the Higgs
 1547 is predicted to be high (> 150 GeV) or low (< 150 GeV), a cut on the appropriate background
 1548 rejection MVA is applied. The particular cut values, listed in Table 41, are determined by
 1549 maximizing S/\sqrt{B} in each region.

Channel	BDT Score
2lSS high p_T	0.36
2lSS low p_T	0.34
3lS high p_T	0.51
3lS low p_T	0.43
3lF high p_T	0.33
3lF low p_T	0.41

Table 41: Cutoff values on background rejection MVA score applied to signal regions.

1550 The event preselection and MVA selection listed in Table 41 are used define the three
 1551 signal regions used in the fit. These signal region definitions are summarized in Table 42.

Region	Selection
2ISS	Two same charge tight leptons with $p_T > 20 \text{ GeV}$ $N_{\text{jets}} \geq 4, N_{\text{b-jets}} \geq 1$ b-tagged jets Zero τ_{had} $H_{p_T}^{\text{pred}} > 150 \text{ GeV}$ and BDT score > 0.36 or $H_{p_T}^{\text{pred}} < 150 \text{ GeV}$ and BDT score > 0.34
3IS	Three light leptons with total charge ± 1 Two tight SS leptons, $p_T > 20 \text{ GeV}$ One loose OS lepton, $p_T > 10 \text{ GeV}$ $N_{\text{jets}} \geq 2, N_{\text{b-jets}} \geq 1$ b-tagged jets Zero τ_{had} $ M(l^+l^-) - 91.2 \text{ GeV} > 10 \text{ GeV}$ for all OSSF lepton pairs Decay NN Score < 0.23 $H_{p_T}^{\text{pred}} > 150 \text{ GeV}$ and BDT score > 0.51 or $H_{p_T}^{\text{pred}} < 150 \text{ GeV}$ and BDT score > 0.43
3IF	Three light leptons with total charge ± 1 Two tight SS leptons, $p_T > 20 \text{ GeV}$ One loose OS lepton, $p_T > 10 \text{ GeV}$ $N_{\text{jets}} \geq 2, N_{\text{b-jets}} \geq 1$ b-tagged jets Zero τ_{had} $ M(l^+l^-) - 91.2 \text{ GeV} > 10 \text{ GeV}$ for all OSSF lepton pairs Decay NN Score > 0.23 $H_{p_T}^{\text{pred}} > 150 \text{ GeV}$ and BDT score > 0.33 or $H_{p_T}^{\text{pred}} < 150 \text{ GeV}$ and BDT score > 0.41

Table 42: Selection applied to define the three signal regions used in the fit.

20 Systematic Uncertainties

1552 The systematic uncertainties that are considered are summarized in Table 43. These are imple-
 1553 mented in the fit either as a normalization factors or as a shape variation or both in the signal
 1554 and background estimations. The numerical impact of each of these uncertainties is outlined in
 1555 section 21.
 1556

Table 43: Sources of systematic uncertainty considered in the analysis. Some of the systematic uncertainties are split into several components, as indicated by the number in the rightmost column.

Systematic uncertainty	Components
Luminosity	1
Pileup reweighting	1
Physics Objects	
Electron	6
Muon	15
Jet energy scale and resolution	28
Jet vertex fraction	1
Jet flavor tagging	131
E_T^{miss}	3
Total (Experimental)	186
Background Modeling	
Cross section	24
Renormalization and factorization scales	10
Parton shower and hadronization model	2
Shower tune	4
Total (Signal and background modeling)	40
Background Modeling	
Cross section	24
Renormalization and factorization scales	10
Parton shower and hadronization model	2
Shower tune	4
Total (Signal and background modeling)	40
Total (Overall)	226

1557 The uncertainty in the combined 2015+2016 integrated luminosity is derived from a
 1558 calibration of the luminosity scale using x-y beam-separation scans performed in August 2015
 1559 and May 2016 [29].

1560 The experimental uncertainties are related to the reconstruction and identification of light
 1561 leptons and b-tagging of jets, and to the reconstruction of E_T^{miss} . The TOTAL electron ID
 1562 correlation model is used, corresponding to 1 electron ID systematic. Electron ID is found to be

1563 a subleading systematic that is unconstrained by the fit, making it an appropriate choice for this
1564 analysis.

1565 The sources which contribute to the uncertainty in the jet energy scale [31] are decom-
1566 posed into uncorrelated components and treated as independent sources in the analysis. The
1567 CategoryReduction model is used to account for JES uncertainties, which decomposes the uncer-
1568 tainties into 30 nuisance parameters included in the fit. The SimpleJER model is used to account
1569 for jet energy resolution (JER) uncertainties, and 8 JER uncertainty components unclued as
1570 NPs in the fit.

1571 The uncertainties in the b-tagging efficiencies measured in dedicated calibration analyses
1572 [32] are also decomposed into uncorrelated components. The large number of components for
1573 b-tagging is due to the calibration of the distribution of the BDT discriminant.

1574 The systematic uncertainties associated with the signal and background processes are
1575 accounted for by varying the cross-section of each process within its uncertainty.

1576 The full list of systematic uncertainties considered in the analysis is summarized in Tables
1577 44, 45 and 46.

1578

Experimental Systematics on Leptons and E_T^{miss}			
Type	Description	Systematics Name	Application
Trigger			
Scale Factors	Trigger Efficiency	lepSFTrigTight_MU(EL)_SF_Trigger_STAT(SYST)	Event Weight
Muons			
Efficiencies	Reconstruction and Identification	lepSFObjTight_MU_SF_ID_STAT(SYST)	Event Weight
	Isolation	lepSFObjTight_MU_SF_Isol_STAT(SYST)	Event Weight
	Track To Vertex Association	lepSFObjTight_MU_SF_TTVA_STAT(SYST)	Event Weight
p_T Scale	p_T Scale	MUONS_SCALE	p_T Correction
Resolution	Inner Detector Energy Resolution	MUONS_ID	p_T Correction
	Muon Spectrometer Energy Resolution	MUONS_MS	p_T Correction
Electrons			
Efficiencies	Reconstruction	lepSFObjTight_EL_SF_ID	Event Weight
	Identification	lepSFObjTight_EL_SF_Reco	Event Weight
	Isolation	lepSFObjTight_EL_SF_Isol	Event Weight
Scale Factor	Energy Scale	EG_SCALE_ALL	Energy Correction
Resolution	Energy Resolution	EG_RESOLUTION_ALL	Energy Correction
E_T^{miss}			
Soft Tracks Terms	Resolution	MET_SoftTrk_ResoPerp	p_T Correction
	Resolution	MET_SoftTrk_ResoPara	p_T Correction
	Scale	MET_SoftTrk_ScaleUp	p_T Correction
	Scale	MET_SoftTrk_ScaleDown	p_T Correction

Table 44: Summary of experimental systematics considered for leptons and E_T^{miss} . Includes type, description, name of systematic as used in the fit, and mode of application. The mode of application indicates the systematic evaluation, e.g. as an overall event re-weighting (Event Weight) or rescaling (p_T Correction).

Experimental Systematics on Jets			
Type	Origin	Systematics Name	Application
Jet Vertex Tagger		JVT	Event Weight
Energy Scale	Calibration Method	JET_21NP_ JET_EffectiveNP_1-19	p_T Correction p_T Correction
	η inter-calibration	JET_EtaIntercalibration_Modelling JET_EtaIntercalibration_NonClosure JET_EtaIntercalibration_TotalStat	p_T Correction p_T Correction p_T Correction
	High p_T jets	JET_SingleParticle_HighPt	p_T Correction
	Pile-Up	JET_Pileup_OffsetNPV JET_Pileup_OffsetMu JET_Pileup_PtTerm JET_Pileup_RhoTopology	p_T Correction p_T Correction p_T Correction p_T Correction
	Non Closure	JET_PunchThrough_MC15	p_T Correction
	Flavour	JET_Flavor_Response JET_BJES_Response JET_Flavor_Composition	p_T Correction p_T Correction p_T Correction
Resolution		JET_JER_SINGLE_NP	Event Weight

Table 45: Jet systematics take into account effects of jets calibration method, η inter-calibration, high p_T jets, pile-up, and flavor response. They are all diagonalised into effective parameters.

Experimental Systematics on b-tagging		
Type	Origin	Systematic Name
Scale Factors	DL1r b-tagger efficiency on b originated jets in bins of η	DL1r_Continuous_EventWeight_B0-29
	DL1r b-tagger efficiency on c originated jets in bins of η	DL1r_Continuous_EventWeight_C0-19
	DL1r b-tagger efficiency on light flavoured originated jets in bins of η and p_T	DL1r_Continuous_EventWeight_Light0-79
	DL1r b-tagger extrapolation efficiency	DL1r_Continuous_EventWeight_extrapolation DL1r_Continuous_EventWeight_extrapolation_from_charm

Table 46: Summary of experimental systematics to be included for b-tagging of jets in the analysis, using the continuous DL1r tagging algorithm. All of the b-tagging related systematics are applied as event weights. From left: type, description, and the name of systematic used in the fit.

1579 As mentioned in Section 16.2, a normalization corrections and uncertainties on the estim-
 1580 ates of non-prompt leptons backgrounds are derived using data driven techniques, decribed in
 1581 detail in [7]. These are derived from a likelihood fit over various non-prompt enriched control
 1582 regions, targeting several sources of non-prompt light leptons separately: external conversion
 1583 electrons, internal conversion electrons, electrons from heavy flavor decays, and muons from
 1584 heavy flavor decays.

1585 The normalization factor and uncertainty applied to each source of non-prompt leptons is
 1586 summarized in Table 20

Processss	Normalization Factor
NF_e^{ExtCO}	1.70 ± 0.51
NF_e^{IntCO}	0.75 ± 0.26
NF_e^{HF}	1.09 ± 0.32
NF_{μ}^{HF}	1.28 ± 0.17

Table 47: Normalization factors - with statistical and systematic uncertainties - derived from the fit over fake control regions for each source of non-prompt leptons considered.

1587 In addition to those derived from the control regions, several additional uncertainties are
 1588 assigned to the non-prompt lepton background. An additional 25% uncertainty on material
 1589 conversions is assigned, based on the comparison between data and MC in a region where a
 1590 loose electron fails the photon conversion veto. A shape uncertainty of 15% (6%) is assigned to
 1591 the HF non-prompt electron (muon) background based on a comparison between data and MC
 1592 where the second leading electron (muon) is only required to be loose. As the contribution from
 1593 light non-prompt leptons is small, about 10% percent of the contribution from HF non-prompt
 1594 leptons, it is derived from the agreement between data and simulation in a LF enriched region at
 1595 low values of the non-prompt lepton BDT. The resulting uncertainty is 100%, and is taken to be
 1596 uncorrelated between internal and material conversions.

1597 Theoretical uncertainties applied to MC predictions, including cross section, PDF, and
 1598 scale uncertainties are taken from theory calculations for the predominate prompt backgrounds.
 1599 Following the nominal $t\bar{t}H$ – ML analysis, a 50% uncertainty is applied to Diboson to account
 1600 for the large uncertainty in estimating $VV +$ heavy flavor. The other “rare” background processes
 1601 - including tZ , rare top processes, $ttWW$, WtZ , VVV , $tHjb$ and WtH - are assigned an overall

¹⁶⁰² 50% normalization uncertainty as well. The theory uncertainties applied to the MC estimates

¹⁶⁰³ are summarized in Table 48.

Process	X-section [%]
t̄H (aMC@NLO+Pythia8)	QCD Scale: $^{+5.8}_{-9.2}$ PDF(+ α_S): ± 3.6
t̄Z (aMC@NLO+Pythia8)	QCD Scale: $^{+9.6}_{-11.3}$ PDF(+ α_S): ± 4
t̄W (aMC@NLO+Pythia8)	QCD Scale: $^{+12.9}_{-11.5}$ PDF(+ α_S): ± 3.4
tHjb (aMC@NLO+Pythia8)	QCD Scale: $^{+6.5}_{-14.9}$ PDF(+ α_S): ± 3.7
WtH (aMC@NLO+Pythia8)	QCD Scale: $^{+5.0}_{-6.7}$ PDF(+ α_S): ± 6.3
VV (Sherpa 2.2.1)	± 50
Others	± 50

Table 48: Summary of theoretical uncertainties for MC predictions in the analysis.

¹⁶⁰⁴ Additional uncertainties to account for t̄W mismodelling are also applied. These include
¹⁶⁰⁵ a “Generator” uncertainty, based on a comparison between the nominal Sherpa 2.2.5 sample,
¹⁶⁰⁶ and the formerly used aMC@NLO sample, and an “Extra radiation” uncertainty, which includes
¹⁶⁰⁷ renormalisation and factorisation scale variations of the Sherpa 2.2.5 sample.

¹⁶⁰⁸ 21 Results

¹⁶⁰⁹ A maximum likelihood fit is performed simultaneously over the reconstructed Higgs p_T spectrum
¹⁶¹⁰ in the three signal regions, 2lSS, 3lS, and 3lF. The signal is split into high and low p_T samples,
¹⁶¹¹ based on whether the truth p_T of the Higgs is above or below 150 GeV. The parameters $\mu_{t\bar{t}H\text{high}p_T}$
¹⁶¹² and $\mu_{t\bar{t}H\text{low}p_T}$, where $\mu = \sigma_{\text{observed}}/\sigma_{\text{SM}}$, are extracted from the fit, signifying the difference

₁₆₁₃ between the observed value and the theory prediction. Unblinded results are shown for the 79.8
₁₆₁₄ fb^{-1} data set, as well as MC only projections of results using the full Run-2, 139 fb^{-1} dataset.

₁₆₁₅ As described in Section 20, there are 229 systematic uncertainties that are considered
₁₆₁₆ as NPs in the fit. These NP s are constrained by Gaussian or log-normal probability density
₁₆₁₇ functions. The latter are used for normalisation factors to ensure that they are always positive.
₁₆₁₈ The expected number of signal and background events are functions of the likelihood. The prior
₁₆₁₉ for each NP is added as a penalty term, decreasing the likelihood as it is shifted away from its
₁₆₂₀ nominal value.

₁₆₂₁ 21.1 Results - 79.8 fb^{-1}

₁₆₂₂ As the data collected from 2015-2017 has been unblinded for $t\bar{t}H$ – ML channels, represent-
₁₆₂₃ ing 79.8 fb^{-1} , those events are unblinded. The predicted Higgs p_T spectrum is fit to data
₁₆₂₄ simultaneously in each of the three signal regions shown in Figure 21.1.

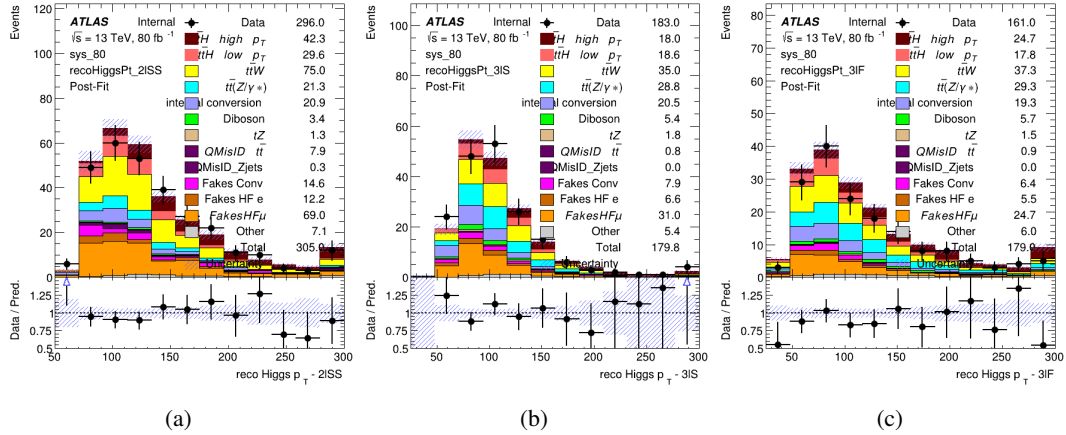


Figure 21.1: Post-fit distributions of the reconstructed Higgs p_T in the three signal regions, (a) 2ISS, (b) 3IS, and (c) 3IF, for 79.8 fb^{-1} of MC

1625

A post-fit summary of the fitted regions is shown in Figure 21.2.

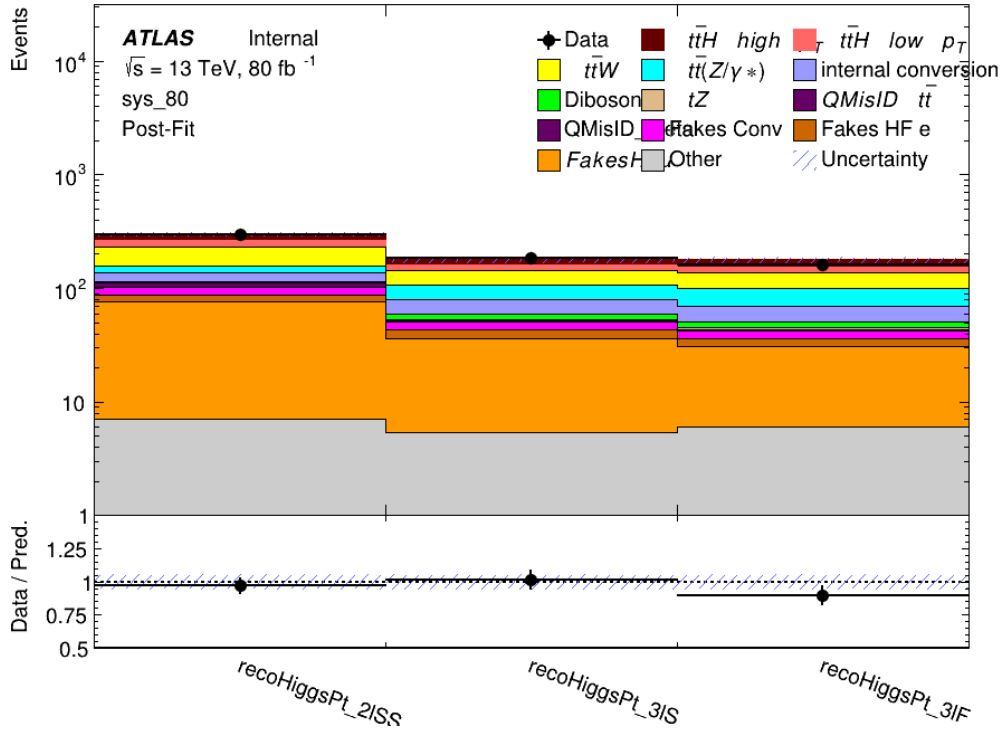


Figure 21.2: Post-fit summary of the yields in each signal region.

1626 The the measured μ values for high and low p_T Higgs production obtained from the fit
 1627 are shown in 49. A significance of 1.7σ is observed for $t\bar{t}H$ high p_T , and 2.1σ is measured for
 1628 $t\bar{t}H$ low p_T .

$$\mu_{t\bar{t}H \text{ high } p_T} = 2.1^{+0.62}_{-0.59}(\text{stat})^{+0.40}_{-0.43}(\text{sys})$$

$$\mu_{t\bar{t}H \text{ low } p_T} = 0.83^{+0.39}_{-0.40}(\text{stat})^{+0.51}_{-0.53}(\text{sys})$$

Table 49: Best fit μ values for $t\bar{t}H$ high p_T and $t\bar{t}H$ low p_T , where $\mu = \sigma_{\text{obs}}/\sigma_{\text{pred}}$

1629 The most prominent sources of systematic uncertainty, as measured by their impact on
 1630 $\mu_{t\bar{t}H \text{ high } p_T}$, are summarized in Table 50.

Uncertainty Source	$\Delta\mu$	
Jet Energy Scale	0.25	0.23
$t\bar{t}H$ cross-section (QCD scale)	-0.11	0.21
Luminosity	-0.13	0.14
Flavor Tagging	0.14	0.13
$t\bar{t}W$ cross-section (QCD scale)	-0.12	0.11
Higgs Branching Ratio	-0.1	0.11
$t\bar{t}H$ cross-section (PDF)	-0.07	0.08
Electron ID	-0.06	0.06
Non-prompt Muon Normalization	-0.05	0.06
$t\bar{t}Z$ cross-section (QCD scale)	-0.05	0.05
Diboson cross-section	-0.05	0.05
Fake muon modelling	-0.04	0.04
Total	0.40	0.43

Table 50: Summary of the most significant sources of systematic uncertainty on the measurement of $t\bar{t}H$ high p_T .

1631 The most significant sources of uncertainty on the measurement of $t\bar{t}H$ - low p_T are shown
 1632 in Table 51.

Uncertainty Source	$\Delta\mu$	
Internal Conversions	-0.26	0.26
Luminosity	-0.16	0.17
Non-prompt Muon Normalization	-0.16	0.16
t̄W cross-section (QCD scale)	-0.17	0.15
Jet Energy Scal	0.15	0.15
Non-prompt Electron Modelling	-0.13	0.14
Flavor Tagging	0.13	0.13
Non-prompt Muon Modelling	-0.12	0.13
Non-prompt Electron Normalization	-0.11	0.11
t̄Z cross-section (QCD scale)	-0.08	0.09
Diboson Cross-section	-0.07	0.07
Total	0.51	0.53

Table 51: Summary of the most significant sources of systematic uncertainty on the measurement of t̄H low p_T.

¹⁶³³ The ranking and impact of those nuisance parameters with the largest contribution to the
¹⁶³⁴ overall uncertainty is shown in Figure 21.3.

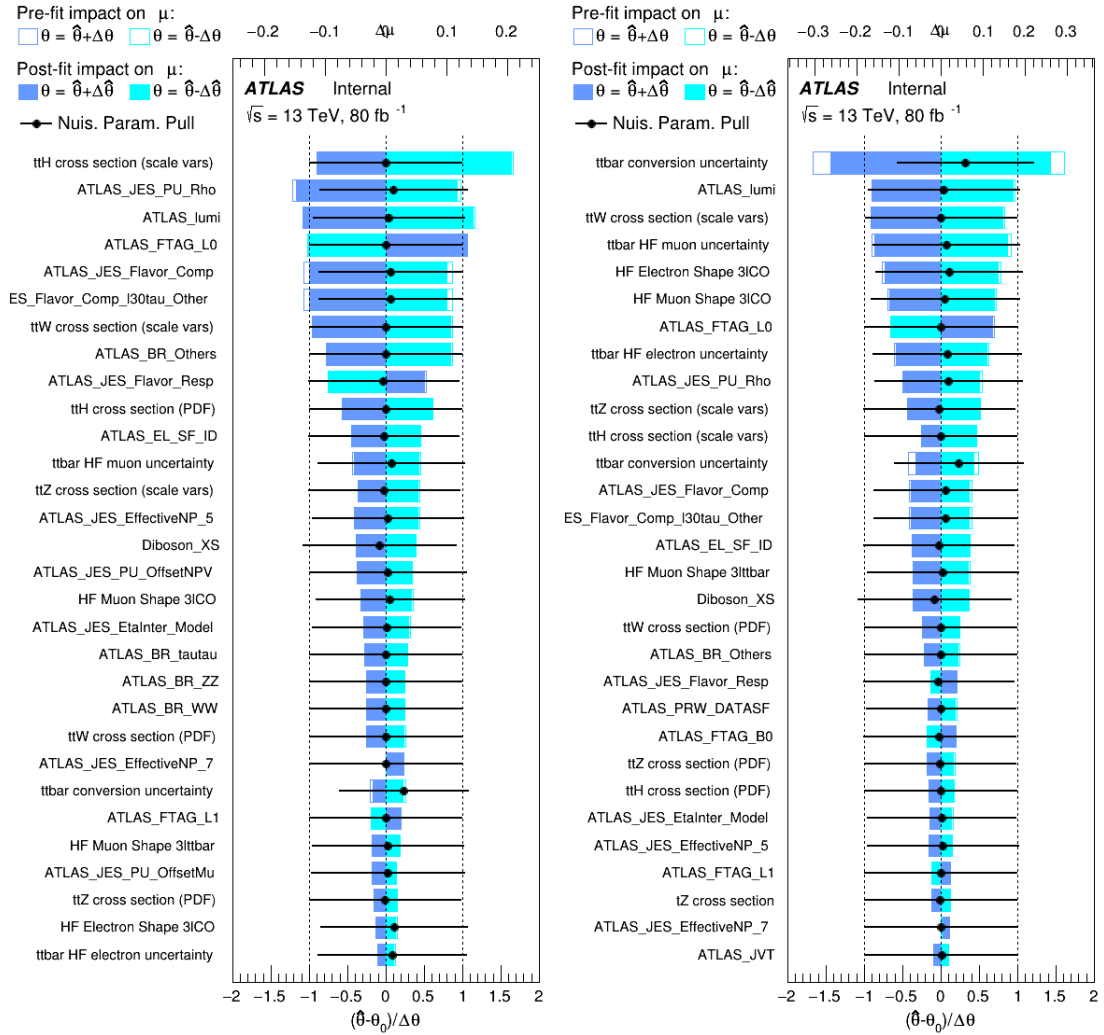


Figure 21.3: Impact of systematic uncertainties on the measurement of high p_T (left) and low p_T (right) $t\bar{t}H$ events

1635

The background composition of each of the fit regions is shown in Figure 21.4.

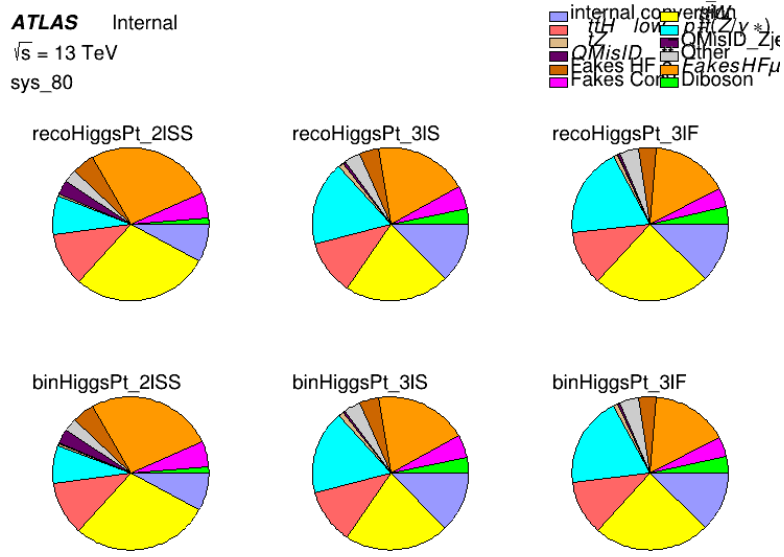


Figure 21.4: Background composition of the fit regions.

¹⁶³⁶ **21.2 Projected Results - 139 fb^{-1}**

¹⁶³⁷ As data collected in 2018 has not yet been unblinded for $t\bar{t}H$ – ML at the time of this note, data
¹⁶³⁸ from that year remains blinded. Instead, an Asimov fit is performed - with the MC prediction
¹⁶³⁹ being used both as the SM prediction as well as the data in the fit - in order to give expected
¹⁶⁴⁰ results.

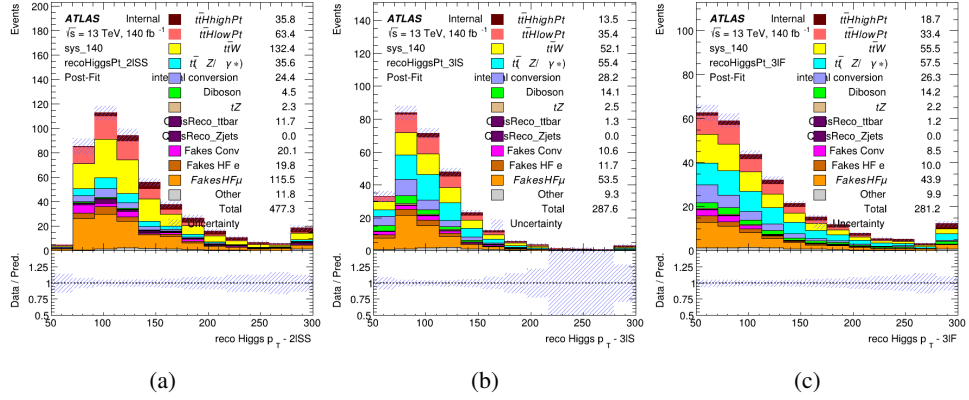


Figure 21.5: Blinded post-fit distributions of the reconstructed Higgs p_T in the three signal regions, (a) 2lSS, (b) 3lS, and (c) 3lF, for 139 fb^{-1} of data

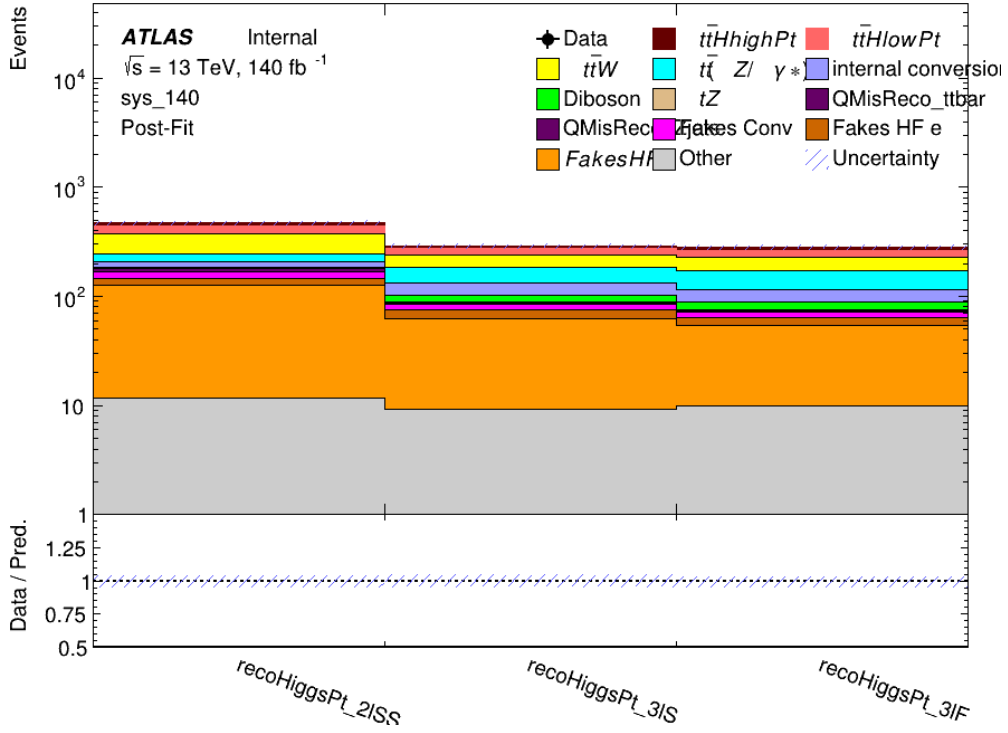


Figure 21.6: Post-fit summary of fit.

¹⁶⁴² shown in [52](#). A significance of 2.0σ is expected for $t\bar{t}H$ high p_T , and a projected significance

¹⁶⁴³ 2.3σ is extracted for $t\bar{t}H$ low p_T .

$$\mu_{t\bar{t}H \text{ high } p_T} = 1.00^{+0.45}_{-0.43} (\text{stat})^{+0.30}_{-0.31} (\text{sys})$$

$$\mu_{t\bar{t}H \text{ low } p_T} = 1.00^{+0.29}_{-0.30} (\text{stat})^{+0.48}_{-0.50} (\text{sys})$$

Table 52: Best fit μ values for $t\bar{t}H$ high p_T and $t\bar{t}H$ low p_T , where $\mu = \sigma_{\text{obs}}/\sigma_{\text{pred}}$

¹⁶⁴⁴ The most prominent sources of systematic uncertainty, as measured by their impact on

¹⁶⁴⁵ $\mu_{t\bar{t}H \text{ high } p_T}$, are summarized in Table [53](#).

Uncertainty Source	$\Delta\mu$	
Jet Energy Scale	0.19	0.17
$t\bar{t}W$ Cross-section (QCD Scale)	-0.12	0.11
Luminosity	-0.1	0.11
Flavor Tagging	0.1	0.1
$t\bar{t}H$ Cross-section (QCD Scale)	-0.05	0.1
$t\bar{t}Z$ Cross-section (QCD Scale)	-0.05	0.06
Non-prompt Muon Normalization	-0.05	0.05
Higgs Branching Ratio	-0.05	0.05
Diboson Cross-section	-0.04	0.05
Non-prompt Muon Modelling	-0.04	0.04
$t\bar{t}H$ Cross-section (PDF)	-0.03	0.04
Electron ID	-0.04	0.04
$t\bar{t}W$ Cross-section (PDF)	-0.03	0.03
Total	0.30	0.31

Table 53: Summary of the most significant sources of systematic uncertainty on the measurement of $t\bar{t}H$ high p_T .

¹⁶⁴⁶ The most significant sources of systematic uncertainty on $t\bar{t}H$ low p_T are summarized in

¹⁶⁴⁷ Table [54](#).

Uncertainty Source	$\Delta\mu$	
Internal Conversions	-0.18	0.2
Jet Energy Scale	0.19	0.16
Non-prompt Muon Normalization	-0.16	0.17
Luminosity	-0.15	0.17
t̄W Cross-section (QCD Scale)	-0.17	0.15
Non-prompt Electron Modelling	-0.13	0.14
Non-prompt Muon Modelling	-0.13	0.13
Flavor Tagging	0.13	0.12
Non-prompt Electron Normalization	-0.1	0.11
t̄Z Cross-section (QCD Scale)	-0.07	0.09
t̄H Cross-section (QCD Scale)	-0.05	0.1
Total	0.48	0.50

Table 54: Summary of the most significant sources of systematic uncertainty on the measurement of t̄H low p_T.

¹⁶⁴⁸ The ranking and impact of those nuisance parameters with the largest contribution to the
¹⁶⁴⁹ overall uncertainty is shown in Figure 21.7.

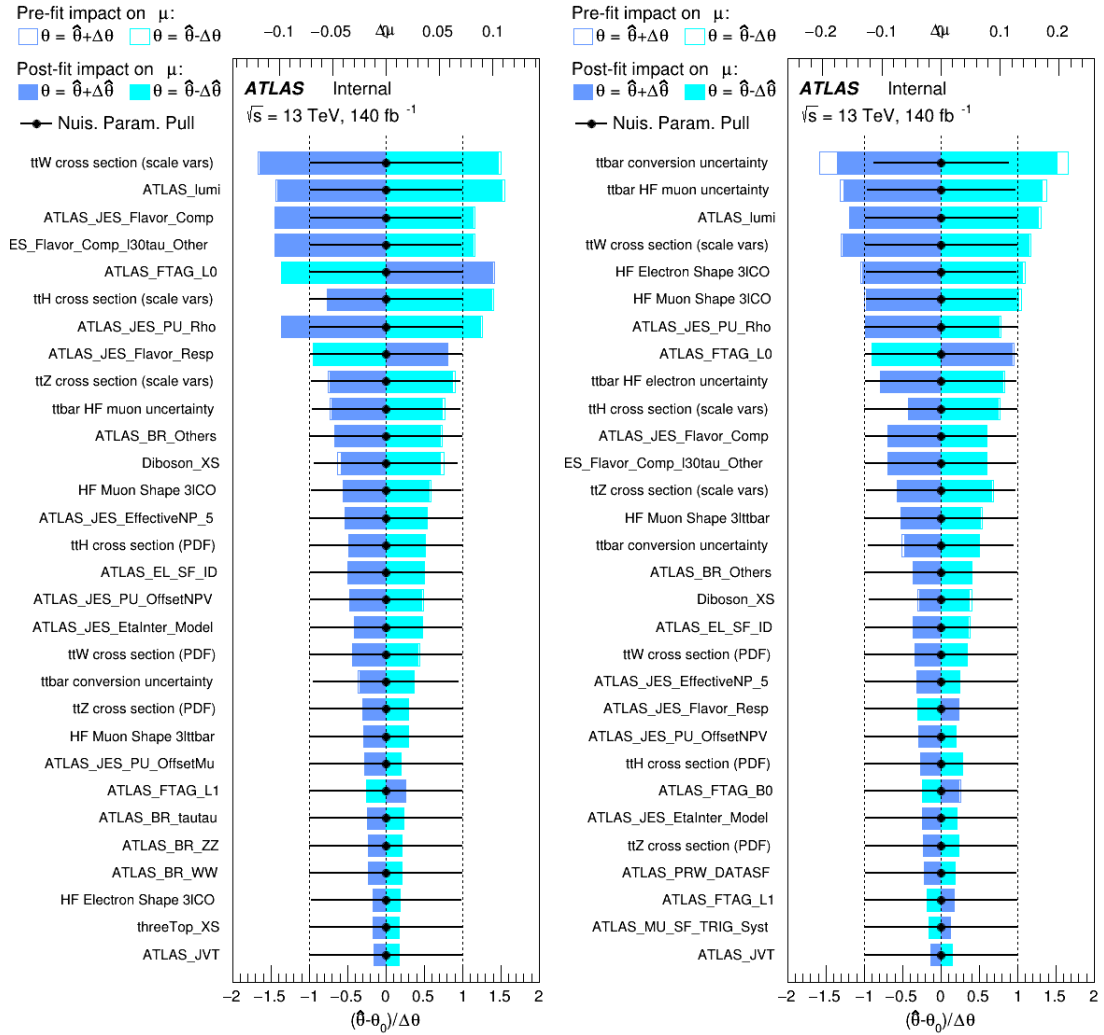


Figure 21.7: Impact of systematic uncertainties on the measurement of high p_T (left) and low p_T (right) $t\bar{t}H$ events

1650

The background composition of each of the fit regions is shown in Figure 21.8.

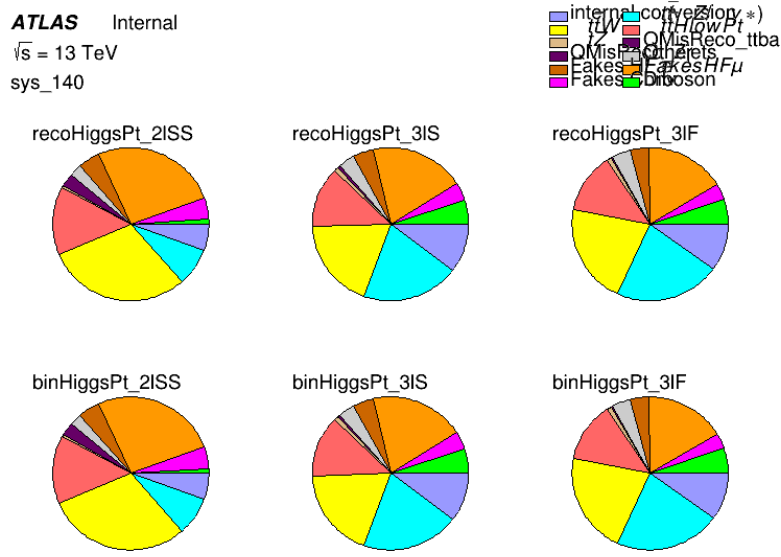


Figure 21.8: Background composition of the fit regions.

Part VI

Conclusion

As search for the effects of dimension-six operators on $t\bar{t}H$ production is performed. An effective field theory approach is used to parameterize the effects of high energy physics on the Higgs momentum spectrum. The momentum spectrum is reconstructed using various MVA techniques, and the limits on dimension-six operators are limited to X.

References

- 1657 [1] ATLAS Collaboration, *Observation of a new particle in the search for the Standard*
1658 *Model Higgs boson with the ATLAS detector at the LHC*, Phys. Lett. B **716** (2012) 1,
1659 arXiv: [1207.7214 \[hep-ex\]](https://arxiv.org/abs/1207.7214).
- 1660 [2] R. Oerter, *The theory of almost everything : the Standard Model, the unsung triumph of*
1661 *modern physics*, Pi Press, 2006, ISBN: 978-0-13-236678-6.
- 1662 [3] P. W. Higgs, *Broken Symmetries and the Masses of Gauge Bosons*,
1663 Phys. Rev. Lett. 13 (Oct, 1964) 508-509 ().
- 1664 [4] J. Goldstone, A. Salam and S. Weinberg, *Broken Symmetries*,
1665 Phys. Rev. **127** (3 1962) 965,
1666 URL: <https://link.aps.org/doi/10.1103/PhysRev.127.965>.
- 1667 [5] J. Ellis, *Higgs Physics*,
1668 (2013) 117, 52 pages, 45 figures, Lectures presented at the ESHEP 2013 School of
1669 High-Energy Physics, to appear as part of the proceedings in a CERN Yellow Report,
1670 URL: <https://cds.cern.ch/record/1638469>.
- 1671 [6] T. A. Collaboration, *Observation of Higgs boson production in association with a top*
1672 *quark pair at the LHC with the ATLAS detector*, Physics Letters B **784** (2018) 173,
1673 ISSN: 0370-2693, URL:
1674 <https://www.sciencedirect.com/science/article/pii/S0370269318305732>.

- 1676 [7] *Evidence for the associated production of the Higgs boson and a top quark pair with the*
1677 *ATLAS detector*, tech. rep. ATLAS-CONF-2017-077, CERN, 2017,
1678 URL: <https://cds.cern.ch/record/2291405>.
- 1679 [8] A. M. Sirunyan et al., *Observation of $t\bar{t}H$ Production*,
1680 *Physical Review Letters* **120** (2018), ISSN: 1079-7114,
1681 URL: <http://dx.doi.org/10.1103/PhysRevLett.120.231801>.
- 1682 [9] B. Dumont, S. Fichet and G. von Gersdorff,
1683 *A Bayesian view of the Higgs sector with higher dimensional operators*,
1684 *Journal of High Energy Physics* **2013** (2013), ISSN: 1029-8479,
1685 URL: [http://dx.doi.org/10.1007/JHEP07\(2013\)065](http://dx.doi.org/10.1007/JHEP07(2013)065).
- 1686 [10] S. Banerjee, S. Mukhopadhyay and B. Mukhopadhyaya,
1687 *Higher dimensional operators and the LHC Higgs data: The role of modified kinematics*,
1688 *Physical Review D* **89** (2014), ISSN: 1550-2368,
1689 URL: <http://dx.doi.org/10.1103/PhysRevD.89.053010>.
- 1690 [11] M. Zinser, ‘The Large Hadron Collider’, *Search for New Heavy Charged Bosons and*
1691 *Measurement of High-Mass Drell-Yan Production in Proton—Proton Collisions*,
1692 Springer International Publishing, 2018 47, ISBN: 978-3-030-00650-1,
1693 URL: https://doi.org/10.1007/978-3-030-00650-1_4.
- 1694 [12] *Detector and Technology*, URL: <https://atlas.cern/discover/detector>.
- 1695 [13] M. Marjanovic, *ATLAS Tile calorimeter calibration and monitoring systems*, 2018.

- 1696 [14] M. Aaboud et al., *Observation of electroweak $W^\pm Z$ boson pair production in association*
 1697 *with two jets in pp collisions at $\sqrt{s} = 13$ TeV with the ATLAS detector,*
 1698 **Phys. Lett. B** **793** (2019) 469, arXiv: [1812.09740 \[hep-ex\]](#).
- 1699 [15] T. Gleisberg et al., *Event generation with SHERPA 1.1*, **JHEP** **02** (2009) 007,
 1700 arXiv: [0811.4622 \[hep-ph\]](#).
- 1701 [16] R. D. Ball et al., *Parton distributions for the LHC Run II*, **JHEP** **04** (2015) 040,
 1702 arXiv: [1410.8849 \[hep-ph\]](#).
- 1703 [17] H.-L. Lai et al., *New parton distributions for collider physics*,
 1704 **Phys. Rev. D** **82** (2010) 074024, arXiv: [1007.2241 \[hep-ph\]](#).
- 1705 [18] S. Frixione, G. Ridolfi and P. Nason,
 1706 *A positive-weight next-to-leading-order Monte Carlo for heavy flavour hadroproduction*,
 1707 **JHEP** **09** (2007) 126, arXiv: [0707.3088 \[hep-ph\]](#).
- 1708 [19] E. Re, *Single-top Wt-channel production matched with parton showers using the*
 1709 *POWHEG method*, **Eur. Phys. J. C** **71** (2011) 1547, arXiv: [1009.2450 \[hep-ph\]](#).
- 1710 [20] ATLAS Collaboration, *Electron efficiency measurements with the ATLAS detector using*
 1711 *the 2015 LHC proton–proton collision data*, ATLAS-CONF-2016-024, 2016,
 1712 URL: <https://cds.cern.ch/record/2157687>.
- 1713 [21] ATLAS Collaboration, *Measurement of the muon reconstruction performance of the*
 1714 *ATLAS detector using 2011 and 2012 LHC proton–proton collision data*,
 1715 **Eur. Phys. J. C** **74** (2014) 3130, arXiv: [1407.3935 \[hep-ex\]](#).

- 1716 [22] R. Narayan et al., *Measurement of the total and differential cross sections of a*
1717 *top-quark-antiquark pair in association with a W boson in proton-proton collisions at a*
1718 *centre-of-mass energy of 13 TeV with ATLAS detector at the Large Hadron Collider,*
1719 *tech. rep. ATL-COM-PHYS-2020-217, CERN, 2020,*
1720 *URL: <https://cds.cern.ch/record/2712986>.*
- 1721 [23] ATLAS Collaboration, *Jet Calibration and Systematic Uncertainties for Jets*
1722 *Reconstructed in the ATLAS Detector at $\sqrt{s} = 13 \text{ TeV}$, ATL-PHYS-PUB-2015-015,*
1723 *2015, URL: <https://cds.cern.ch/record/2037613>.*
- 1724 [24] ATLAS Collaboration,
1725 *Selection of jets produced in 13 TeV proton–proton collisions with the ATLAS detector,*
1726 *ATLAS-CONF-2015-029, 2015, URL: <https://cds.cern.ch/record/2037702>.*
- 1727 [25] ATLAS Collaboration, *Performance of pile-up mitigation techniques for jets in pp*
1728 *collisions at $\sqrt{s} = 8 \text{ TeV}$ using the ATLAS detector, Eur. Phys. J. C **76** (2016) 581,*
1729 *arXiv: [1510.03823 \[hep-ex\]](https://arxiv.org/abs/1510.03823).*
- 1730 [26] ATLAS Collaboration, *Performance of missing transverse momentum reconstruction*
1731 *with the ATLAS detector in the first proton–proton collisions at $\sqrt{s} = 13 \text{ TeV}$,*
1732 *ATL-PHYS-PUB-2015-027, 2015, URL: <https://cds.cern.ch/record/2037904>.*
- 1733 [27] T. Chen and C. Guestrin, ‘XGBoost: A Scalable Tree Boosting System’,
1734 *Proceedings of the 22nd ACM SIGKDD International Conference on Knowledge*
1735 *Discovery and Data Mining, KDD ’16, ACM, 2016 785, ISBN: 978-1-4503-4232-2,*
1736 *URL: <http://doi.acm.org/10.1145/2939672.2939785>.*

- 1737 [28] F. Cardillo et al., *Measurement of the fiducial and differential cross-section of a top*
1738 *quark pair in association with a Z boson at 13 TeV with the ATLAS detector*, (2019),
1739 URL: <https://cds.cern.ch/record/2672207>.
- 1740 [29] ATLAS Collaboration, *Luminosity determination in pp collisions at $\sqrt{s} = 7$ TeV using*
1741 *the ATLAS detector at the LHC*, *Eur. Phys. J. C* **71** (2011) 1630,
1742 arXiv: [1101.2185 \[hep-ex\]](https://arxiv.org/abs/1101.2185).
- 1743 [30] G. Avoni et al.,
1744 *The new LUCID-2 detector for luminosity measurement and monitoring in ATLAS*,
1745 *JINST* **13** (2018) P07017.
- 1746 [31] G. Aad, T. Abajyan, B. Abbott and etal, *Jet energy resolution in proton-proton collisions*
1747 *at $\sqrt{s} = 7$ TeV recorded in 2010 with the ATLAS detector*,
1748 *The European Physical Journal C* **73** (2013) 2306, ISSN: 1434-6052,
1749 URL: <https://doi.org/10.1140/epjc/s10052-013-2306-0>.
- 1750 [32] A. Collaboration, *Performance of b -jet identification in the ATLAS experiment*,
1751 *Journal of Instrumentation* **11** (2016) P04008,
1752 URL: <http://stacks.iop.org/1748-0221/11/i=04/a=P04008>.
- 1753 [33] *Observation of the associated production of a top quark and a Z boson at 13 TeV with*
1754 *ATLAS*, (2020), URL: <https://cds.cern.ch/record/2722504>.
- 1755 [34] ATLAS Collaboration, *Comparison of Monte Carlo generator predictions from Powheg*
1756 *and Sherpa to ATLAS measurements of top pair production at 7 TeV*,
1757 ATL-PHYS-PUB-2015-011, 2015, URL: <https://cds.cern.ch/record/2020602>.

- 1758 [35] ATLAS Collaboration, *ATLAS tunes of PYTHIA 6 and Pythia 8 for MC11,*
1759 ATL-PHYS-PUB-2011-009, 2011, URL: <https://cds.cern.ch/record/1363300>.

¹⁷⁶⁰ **List of contributions**

1761

¹⁷⁶² **Appendices**

¹⁷⁶³ **.1 Non-prompt lepton MVA**

1764 A lepton MVA has been developed to better reject non-prompt leptons than standard cut
1765 based selections based upon impact parameter, isolation and PID. The name of this MVA is
1766 **PromptLeptonIso**. The full set of studies and detailed explanation can be found in [22].

1767 The decays of W and Z bosons are commonly selected by the identification of one or two
1768 electrons or muons. The negligible lifetimes of these bosons mean that the leptons produced in the
1769 decay originate from the interaction vertex and are thus labelled “prompt”. Analyses using these
1770 light leptons impose strict reconstruction quality, isolation and impact parameter requirements
1771 to remove “fake” leptons. A significant source of the fake light leptons are non-prompt leptons
1772 produced in decays of hadrons that contain bottom (b) or charm (c) quarks. Such hadrons
1773 typically have microscopically significant lifetimes that can be detected experimentally.

1774 These non-prompt leptons can also pass the tight selection criteria. In analyses that
1775 involve top (t) quarks, which decay almost exclusively into a W boson and a b quark, non-
1776 prompt leptons from the semileptonic decay of bottom and charm hadrons can be a significant
1777 source of background events. This is particularly the case in the selection of same-sign dilepton
1778 and multilepton final states.

1779 The main idea is to identify non-prompt light leptons using lifetime information associated
1780 with a track jet that matches the selected light lepton. This lifetime information is computed
1781 using tracks contained within the jet. Typically, lepton lifetime is determined using the impact
1782 parameter of the track reconstructed by the inner tracking detector which is matched to the recon-
1783 structed lepton. Using additional reconstructed charged particle tracks increases the precision of

1784 identifying the displaced decay vertex of bottom or charm hadrons that produced a non-prompt
 1785 light lepton. The MVA also includes information related to the isolation of the lepton to reject
 1786 non-prompt leptons.

1787 **PromptLeptonIso** is a gradient boosted BDT. The training of the BDT is performed on
 1788 leptons selected from the PowHEG+PYTHIA6 non-allhad $t\bar{t}$ MC sample. Eight variables are used
 1789 to train the BDT in order to discriminate between prompt and non-prompt leptons. The track
 1790 jets that are matched to the non-prompt leptons correspond to jets initiated by b or c quarks, and
 1791 may contain a displaced vertex. Consequently, three of the selected variables are used to identify
 1792 b-tag jets by standard ATLAS flavour tagging algorithms. Two variables use the relationship
 1793 between the track jet and lepton: the ratio of the lepton p_T with respect to the track jet p_T and
 1794 ΔR between the lepton and the track jet axis. Finally three additional variables test whether the
 1795 reconstructed lepton is isolated: the number of tracks collected by the track jet and the lepton
 1796 track and calorimeter isolation variables. Table 55 describes the variables used to train the BDT
 1797 algorithm. The choice of input variables has been extensively discussed with Egamma, Muon,
 1798 Tracking, and Flavour Tagging CP groups.

Variable	Description
N_{track} in track jet	Number of tracks collected by the track jet
$\text{IP2 log}(P_b/P_{\text{light}})$	Log-likelihood ratio between the b and light jet hypotheses with the IP2D algorithm
$\text{IP3 log}(P_b/P_{\text{light}})$	Log-likelihood ratio between the b and light jet hypotheses with the IP3D algorithm
$N_{\text{TrkAtVtx}} \text{ SV + JF}$	Number of tracks used in the secondary vertex found by the SV1 algorithm in addition to the number of tracks from secondary vertices found by the JetFitter algorithm with at least two tracks
$p_T^{\text{lepton}}/p_T^{\text{track jet}}$	The ratio of the lepton p_T and the track jet p_T
$\Delta R(\text{lepton}, \text{track jet})$	ΔR between the lepton and the track jet axis
$p_T^{\text{VarCone30}}/p_T$	Lepton track isolation, with track collecting radius of $\Delta R < 0.3$
$E_T^{\text{TopoCone30}}/p_T$	Lepton calorimeter isolation, with topological cluster collecting radius of $\Delta R < 0.3$

Table 55: A table of the variables used in the training of **PromptLeptonIso**.

1799 The output distribution of the BDT is shown in Figure .1.

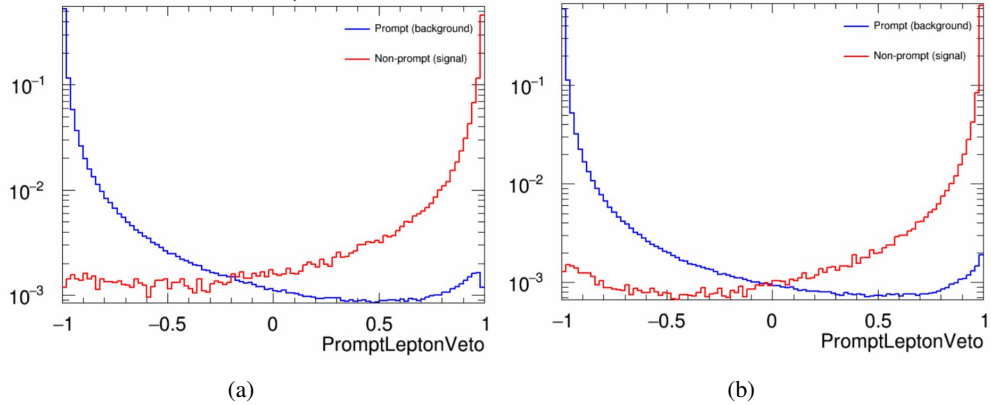


Figure .9: Distribution of the PLV BDT discriminant for (a) electrons and (b) muons

1800 The ROC curve for the BDT response, compared to the standard `FixedCutTight` WP, is
 1801 shown in figure .1, which shows a clear improvement when using this alternate training.

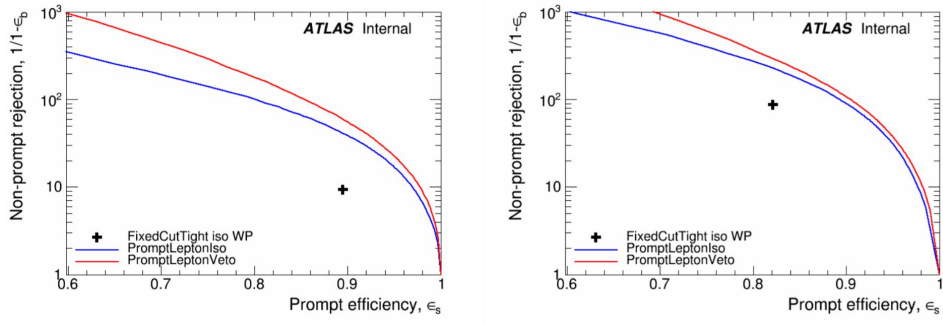


Figure .10: ROC curves for the PLV as well as the performance of the standard `FixedCutTight` WP for (left) electrons and (right) muons

1802 A cutoff value of -0.7 for electrons and -0.5 for muons are chosen as the WPs for this
 1803 MVA, based on an optimisation of S/\sqrt{B} performed in the preselection regions of the $t\bar{t}H - ML$
 1804 analysis, which have a signature similar to that of this analysis.

1805 The efficiency of the tight `PromptLeptonIso` working point is measured using the tag
1806 and probe method with $Z \rightarrow \ell^+ \ell^-$ events. Such calibration are performed by analysers from
1807 this analysis in communication with the Egamma and Muon combined performance groups. The
1808 scale factor are approximately 0.92 for $10 < p_T < 15$ GeV, and averaging at 0.98 to 0.99 for
1809 higher p_T leptons. An extra systematic is applied to muons within $\Delta R < 0.6$ of a calorimeter
1810 jet, since there is a strong dependence on the scale factor due to the presence of these jets. For
1811 electrons, the dominant systematics is coming from pile-up dependence. Overall the systematics
1812 are a maximum of 3% at low p_T and decreasing at a function of p_T .

₁₈₁₃ **.2 Non-prompt CR Modelling**

1814 In order to further validate the modeling in each of the non-prompt CRs, additional
 1815 kinematic plots are made in the Z+jets CR and $t\bar{t}$ CR in each of the continuous b-tag regions,
 1816 after the correction factors detailed in Section 12.3 have been applied.

1817 In the case of the Z+jets CR, the p_T spectrum of the lepton originating from the W
 1818 candidate is shown, as this is the distribution used to extract the scale factor applied to Z+jets.
 1819 These plots are shown in Figures .11 and .12.

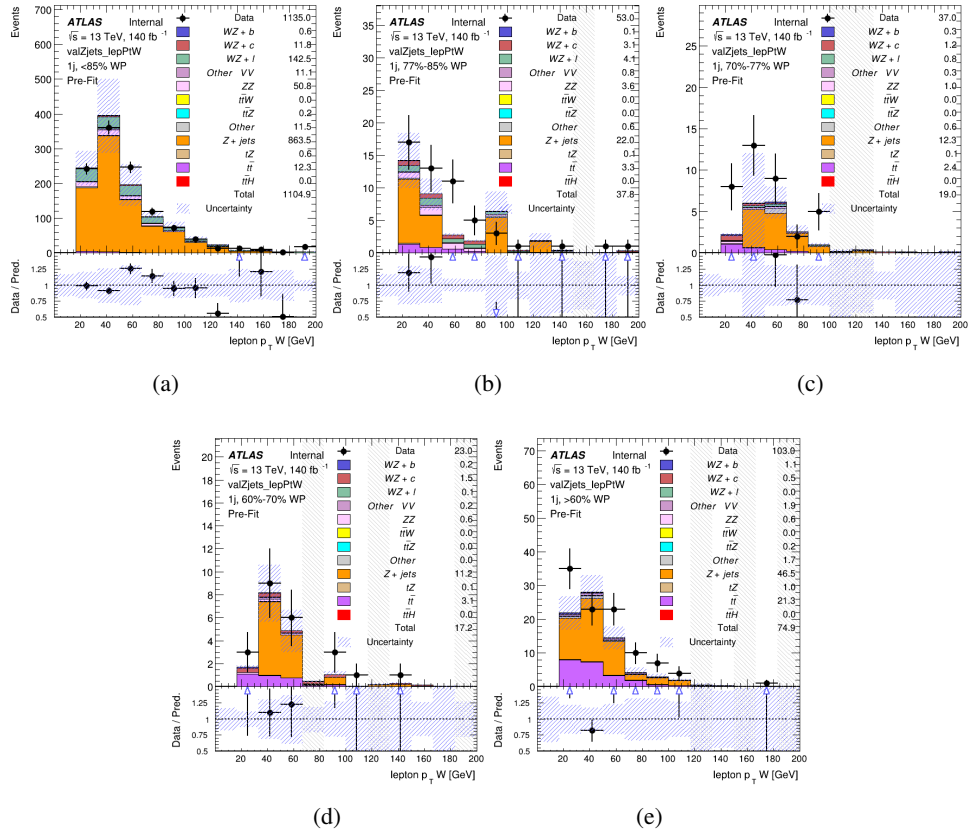


Figure .11: Comparisons between the data and MC distributions of the p_T of the lepton originating from the W-candidate in the Z+jets CR for each of the 1-jet b-tag working point regions

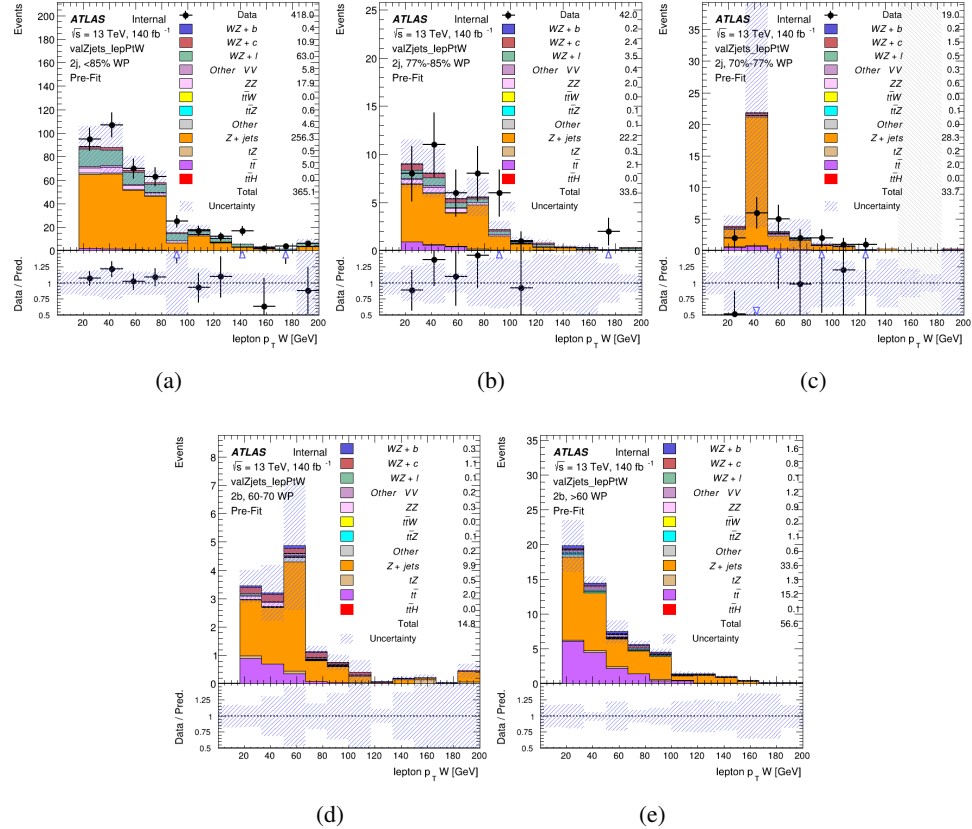


Figure .12: Comparisons between the data and MC distributions of the p_T of the lepton originating from the W-candidate in the Z+jets CR for each of the 2-jet b-tag working point regions

1820 The same is shown for the $t\bar{t}$ CR, but the p_T of the OS lepton is used instead as a
 1821 representation of the modeling, as the lepton from the W is not well defined for $t\bar{t}$ events. These
 1822 plots are shown in Figures .13 and .14.

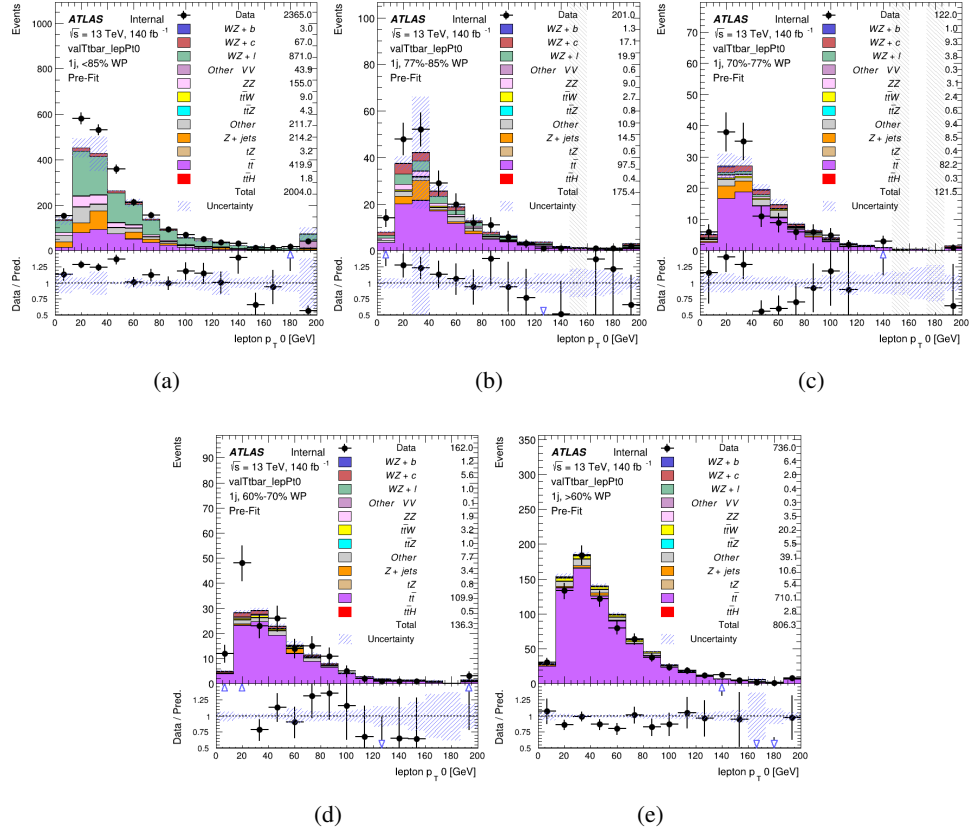


Figure .13: Comparisons between the data and MC distributions of the p_T of the OS lepton in the $t\bar{t}$ CR for each of the 1-jet b-tag working point regions

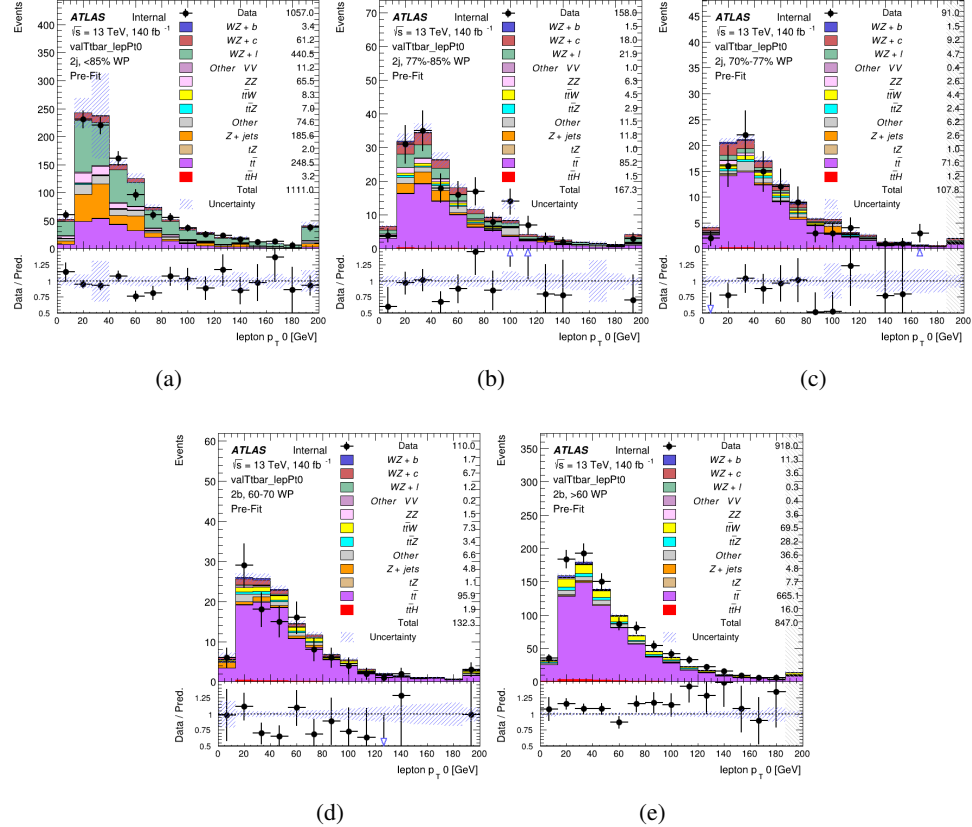


Figure 14: Comparisons between the data and MC distributions of the p_T of the OS lepton in the $t\bar{t}$ CR for each of the 2-jet b-tag working point regions

1823 .3 tZ Interference Studies

1824 Because it includes an on-shell Z boson as well as a b-jet and W from the top decay, tZ
1825 production represents an identical final state to WZ + b-jet. This implies the possibility of matrix
1826 level interference between these two processes not accounted for in the Monte Carlo simulations,
1827 which consider the two processes independently. Truth level studies are performed in order to
1828 estimate the impact of these interference effects.

1829 In order to estimate the matrix level interference effects between tZ and WZ + b-jet, two
1830 different sets of simulations are produced using MadGraph 5 [**Madgraph**] - one which simulates
1831 these two processes independently, and another where they are produced simultaneously, such
1832 that interference effects are present. These two sets of samples are then compared, and the
1833 difference between them can be taken to represent any interference effects.

1834 MadGraph simulations of 10,000 tZ and 10,000 WZ + b-jet events are produced, along
1835 with 20,000 events where both are present, in the fiducial region where three leptons and at least
1836 one jet are produced.

1837 A selection mimicking the preselection used in the main analysis is applied to the samples:
1838 The SS leptons are required to have $p_T > 20$ GeV, and > 10 GeV is required for the OS lepton.
1839 The associated b-jet is required to have $p_T > 25$ GeV, and all physics objects are required to fall
1840 in a range of $|\eta| < 2.5$.

1841 The kinematics of these samples after the selection has been applied are shown below:

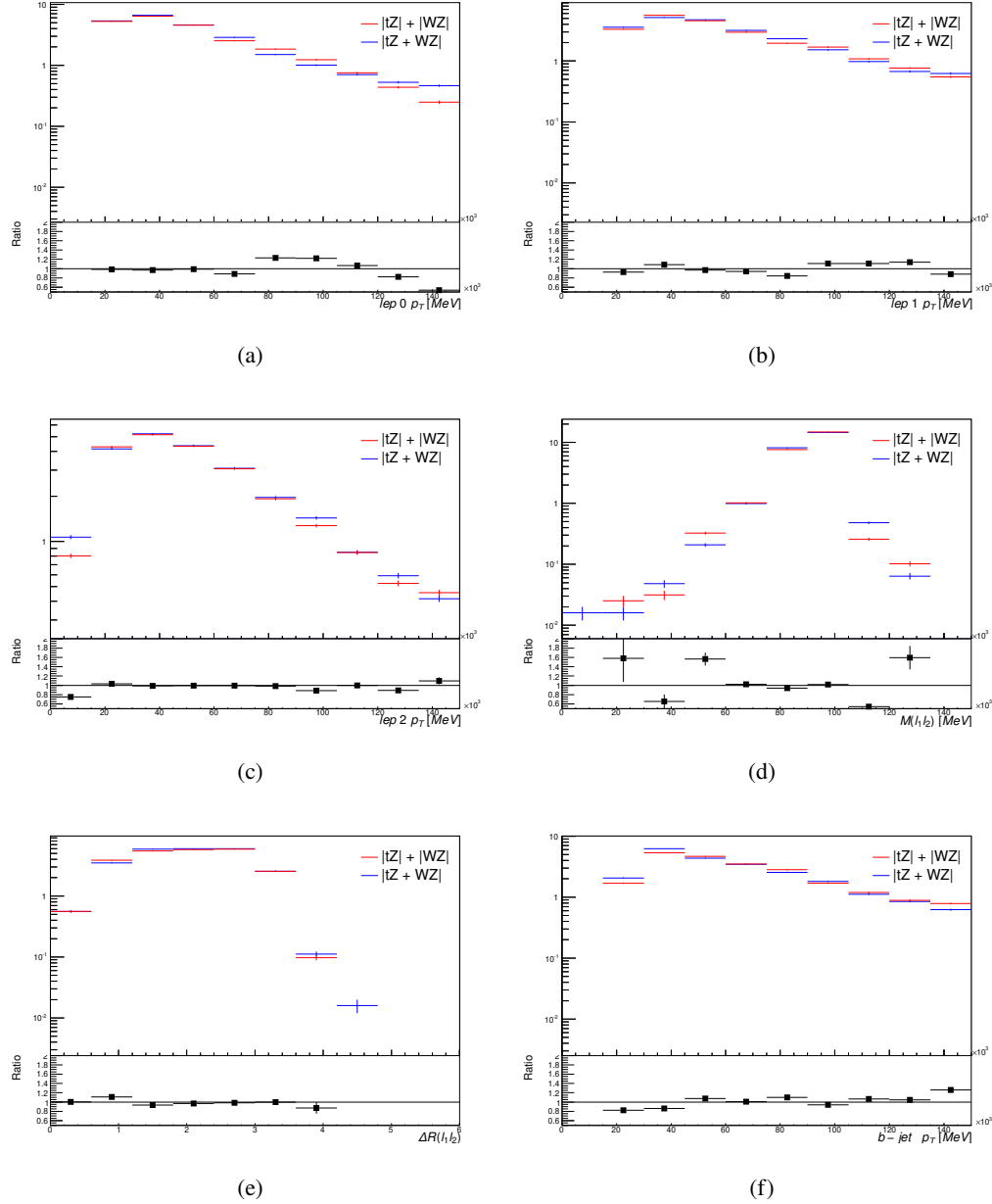


Figure .15: Comparisons between (a) the p_T of the lepton from the W, (b) and (c) show the p_T of the lepton from the Z, (d) the invariant mass of the Z-candidate, (e) ΔR of the leptons from the Z, and (f) the p_T of the b-jet, for WZ and tZ events generated with interference effects (blue) and without interference effects (red).

1842 The overall cross-section of the two methods agree within error, and no significant differ-
1843 ences in the kinematic distributions are seen. It is therefore concluded that interference effects
1844 do not significantly impact the results.

¹⁸⁴⁵ **.4 Alternate tZ Inclusive Fit**

1846 .4.1 tZ Inclusive Fit

1847 While tZ is often considered as a distinct process from WZ + b, this could also be considered part
 1848 of the signal. Alternate studies are performed where, using the same framework as the nominal
 1849 analysis, a measurement of WZ + b is performed that includes tZ as part of WZ+b.

1850 Because of this change, the tZ CR is no longer necessary, and only the five pseudo-
 1851 continuous b-tag regions are used in the fit. Further, systematics related to the tZ cross-section
 1852 are removed from the fit, as they are now encompassed by the normalization measurement of
 1853 WZ + b. All other systematic uncertainties are carried over from the nominal analysis.

1854 An expected WZ + b cross-section of $4.1^{+0.78}_{-0.74}(\text{stat})^{+0.53}_{-0.52}(\text{sys}) \text{ fb}$ is extracted from the fit,
 1855 with an expected significance of 4.0σ .

1856 The impact of the predominate systematics are summarized in Table 56.

Uncertainty Source	$\Delta\mu$	
WZ + light cross-section	0.08	-0.08
Jet Energy Scale	-0.06	0.08
Luminosity	-0.05	0.06
WZ + charm cross-section	-0.04	0.05
Other Diboson + b cross-section	-0.04	0.04
WZ cross-section - QCD scale	-0.04	0.03
t̄t cross-section	-0.03	0.03
Jet Energy Resolution	-0.03	0.03
Flavor tagging	-0.03	0.03
Z+jets cross section	-0.02	0.02
Total Systematic Uncertainty	-0.15	0.16

Table 56: Summary of the most significant sources of systematic uncertainty on the measurement of WZ + b with exactly one associated jet.

1857 **.4.2 Floating tZ**

1858 In order to quantify the impact of the tZ uncertainty on the fit, an alternate fit strategy is used
1859 where the tZ normalization is allowed to float. This normalization factor replaces the cross-
1860 section uncertainty on tZ, and all other parameters of the fit remain the same.

1861 An uncertainty of 17% on the normalization of tZ is extracted from the fit, compared to a
1862 theory uncertainty of 15% applied to the tZ cross-section. The measured uncertainties on WZ
1863 remain the same.

1864 .5 DSID list

Data:

```
data15_13TeV.AllYear.physics_Main.PhysCont.DAOD_HIGG8D1.grp15_v01_p4134
data16_13TeV.AllYear.physics_Main.PhysCont.DAOD_HIGG8D1.grp16_v01_p4134
data17_13TeV.AllYear.physics_Main.PhysCont.DAOD_HIGG8D1.grp17_v01_p4134
data18_13TeV.AllYear.physics_Main.PhysCont.DAOD_HIGG8D1.grp18_v01_p4134
```

mc16a:

```
mc16_13TeV.361603.PowhegPy8EG_CT10nloME_AZNLOCTEQ6L1_ZZllll_mll4.deriv.DAOD_HIGG8D1.e4475_s3126_r9364_r9315_p4133
mc16_13TeV.361602.PowhegPy8EG_CT10nloME_AZNLOCTEQ6L1_WZlvvv_mll4.deriv.DAOD_HIGG8D1.e4054_s3126_r9364_r9315_p4133
mc16_13TeV.361604.PowhegPy8EG_CT10nloME_AZNLOCTEQ6L1_ZZvvll_mll4.deriv.DAOD_HIGG8D1.e4475_s3126_r9364_r9315_p4133
mc16_13TeV.361600.PowhegPy8EG_CT10nloME_AZNLOCTEQ6L1_WWlvvv.deriv.DAOD_HIGG8D1.e4616_s3126_r9364_r9315_p4133
mc16_13TeV.361605.PowhegPy8EG_CT10nloME_AZNLOCTEQ6L1_ZZvvvv_mll4.deriv.DAOD_HIGG8D1.e4054_s3126_s3136_r9364_r9315_p4133
mc16_13TeV.361601.PowhegPy8EG_CT10nloME_AZNLOCTEQ6L1_WZlVll_mll4.deriv.DAOD_HIGG8D1.e4475_s3126_r9364_r9315_p4133
mc16_13TeV.364286.Sherpa_222_NNPDF30NNLO_llvjj_ss_EW4.deriv.DAOD_HIGG8D1.e6055_e5984_s3126_r9364_r9315_p3983 mc16_13TeV.364285.Sherpa_222_NNPDF30NNLO_llvjj_EW6_OFPlus.deriv.DAOD_HIGG8D1.e7421_e5984_s3126_r9364_r9315_p4133
mc16_13TeV.364740.MGPy8EG_NNPDF30NLO_A14NNPDF23LO_lvlljj_EW6_SFPlus.deriv.DAOD_HIGG8D1.e7421_e5984_s3126_r9364_r9315_p4133
mc16_13TeV.364742.MGPy8EG_NNPDF30NLO_A14NNPDF23LO_lvlljj_EW6_SFPlus.deriv.DAOD_HIGG8D1.e7421_e5984_s3126_r9364_r9315_p4133
mc16_13TeV.364253.Sherpa_222_NNPDF30NNLO_llv.deriv.DAOD_HIGG8D1.e5916_s3126_r9364_r9315_p4133
mc16_13TeV.364250.Sherpa_222_NNPDF30NNLO_lll.deriv.DAOD_HIGG8D1.e5894_s3126_r9364_r9315_p4133
mc16_13TeV.364254.Sherpa_222_NNPDF30NNLO_llv.deriv.DAOD_HIGG8D1.e5916_s3126_r9364_r9315_p4133
mc16_13TeV.364255.Sherpa_222_NNPDF30NNLO_lvvv.deriv.DAOD_HIGG8D1.e5916_s3126_r9364_r9315_p4133
mc16_13TeV.410155.aMcAtNloPythia8EvtGen_MEN30NLO_A14N23LO_ttW.deriv.DAOD_HIGG8D1.e5070_s3126_r9364_r9315_p4133
mc16_13TeV.410156.aMcAtNloPythia8EvtGen_MEN30NLO_A14N23LO_ttZnunu.deriv.DAOD_HIGG8D1.e5070_s3126_r9364_r9315_p4133
mc16_13TeV.410157.aMcAtNloPythia8EvtGen_MEN30NLO_A14N23LO_ttZqq.deriv.DAOD_HIGG8D1.e5070_s3126_r9364_r9315_p4133
mc16_13TeV.410218.aMcAtNloPythia8EvtGen_MEN30NLO_A14N23LO_ttee.deriv.DAOD_HIGG8D1.e5070_s3126_r9364_r9315_p4133
mc16_13TeV.410219.aMcAtNloPythia8EvtGen_MEN30NLO_A14N23LO_ttmumu.deriv.DAOD_HIGG8D1.e5070_s3126_r9364_r9315_p4133
mc16_13TeV.410220.aMcAtNloPythia8EvtGen_MEN30NLO_A14N23LO_ttautau.deriv.DAOD_HIGG8D1.e5070_s3126_r9364_r9315_p4133
mc16_13TeV.412063.aMcAtNloPythia8EvtGen_tllq_NNPDF30_nf4_A14.deriv.DAOD_TOPQ1.e7054_e5984_s3126_r9364_r9315_p4174
mc16_13TeV.410276.aMcAtNloPythia8EvtGen_MEN30NLO_A14N23LO_ttee_mll_1_5.deriv.DAOD_HIGG8D1.e6087_e5984_s3126_r9364_r9315_p4133
mc16_13TeV.410277.aMcAtNloPythia8EvtGen_MEN30NLO_A14N23LO_ttmumu_mll_1_5.deriv.DAOD_HIGG8D1.e6087_e5984_s3126_r9364_r9315_p4133
mc16_13TeV.410278.aMcAtNloPythia8EvtGen_MEN30NLO_A14N23LO_ttautau_mll_1_5.deriv.DAOD_HIGG8D1.e6087_e5984_s3126_r9364_r9315_p4133
mc16_13TeV.410397.MadGraphPythia8EvtGen_ttbar_wbee_MEN30LO_A14N23LO.deriv.DAOD_HIGG8D1.e6086_e5984_s3126_r9364_r9315_p4133
```

mc16_13TeV.410398.MadGraphPythia8EvtGen_ttbar_wbmumu_MEN30LO_A14N23LO.deriv.DAOD_HIGG8D1.e6086_e5984_s3126_r9364_r9315_p4133
 mc16_13TeV.410399.MadGraphPythia8EvtGen_ttbar_wbtautau_MEN30LO_A14N23LO.deriv.DAOD_HIGG8D1.e6086_e5984_s3126_r9364_r9315_p4133
 mc16_13TeV.410658.PhPy8EG_A14_tchan_BW50_lept_top.deriv.DAOD_HIGG8D1.e6671_e5984_s3126_r9364_r9315_p4133
 mc16_13TeV.410659.PhPy8EG_A14_tchan_BW50_lept_antitop.deriv.DAOD_HIGG8D1.e6671_e5984_s3126_r9364_r9315_p4133
 mc16_13TeV.410644.PowhegPythia8EvtGen_A14_singletop_schan_lept_top.deriv.DAOD_HIGG8D1.e6527_e5984_s3126_r9364_r9315_p4133
 mc16_13TeV.410645.PowhegPythia8EvtGen_A14_singletop_schan_lept_antitop.deriv.DAOD_HIGG8D1.e6527_e5984_s3126_r9364_r9315_p4133
 mc16_13TeV.304014.MadGraphPythia8EvtGen_A14NNPDF23_3top_SM.deriv.DAOD_HIGG8D1.e4324_s3126_r9364_r9315_p4133
 mc16_13TeV.410080.MadGraphPythia8EvtGen_A14NNPDF23_4topSM.deriv.DAOD_HIGG8D1.e4111_s3126_r9364_r9315_p4133
 mc16_13TeV.410081.MadGraphPythia8EvtGen_A14NNPDF23_ttbarWW.deriv.DAOD_HIGG8D1.e4111_s3126_r9364_r9315_p4133
 mc16_13TeV.364100.Sherpa_221_NNPDF30NNLO_Zmumu_MAXHTPTV0_70_CVetoBVeto.deriv.DAOD_HIGG8D1.e5271_s3126_r9364_r9315_p4133
 mc16_13TeV.364101.Sherpa_221_NNPDF30NNLO_Zmumu_MAXHTPTV0_70_CFilterBVeto.deriv.DAOD_HIGG8D1.e5271_s3126_r9364_r9315_p4133
 mc16_13TeV.364102.Sherpa_221_NNPDF30NNLO_Zmumu_MAXHTPTV0_70_BFilter.deriv.DAOD_HIGG8D1.e5271_s3126_r9364_r9315_p4133
 mc16_13TeV.364103.Sherpa_221_NNPDF30NNLO_Zmumu_MAXHTPTV70_140_CVetoBVeto.deriv.DAOD_HIGG8D1.e5271_s3126_r9364_r9315_p4133
 mc16_13TeV.364104.Sherpa_221_NNPDF30NNLO_Zmumu_MAXHTPTV70_140_CFilterBVeto.deriv.DAOD_HIGG8D1.e5271_s3126_r9364_r9315_p4133
 mc16_13TeV.364106.Sherpa_221_NNPDF30NNLO_Zmumu_MAXHTPTV140_280_CVetoBVeto.deriv.DAOD_HIGG8D1.e5271_s3126_r9364_r9315_p4133
 mc16_13TeV.364107.Sherpa_221_NNPDF30NNLO_Zmumu_MAXHTPTV140_280_CFilterBVeto.deriv.DAOD_HIGG8D1.e5271_s3126_r9364_r9315_p4133
 mc16_13TeV.364108.Sherpa_221_NNPDF30NNLO_Zmumu_MAXHTPTV140_280_BFilter.deriv.DAOD_HIGG8D1.e5271_s3126_r9364_r9315_p4133
 mc16_13TeV.364109.Sherpa_221_NNPDF30NNLO_Zmumu_MAXHTPTV280_500_CVetoBVeto.deriv.DAOD_HIGG8D1.e5271_s3126_r9364_r9315_p4133
 mc16_13TeV.364110.Sherpa_221_NNPDF30NNLO_Zmumu_MAXHTPTV280_500_CFilterBVeto.deriv.DAOD_HIGG8D1.e5271_s3126_r9364_r9315_p4133
 mc16_13TeV.364111.Sherpa_221_NNPDF30NNLO_Zmumu_MAXHTPTV280_500_BFilter.deriv.DAOD_HIGG8D1.e5271_e5984_s3126_r9364_r9315_p4133
 mc16_13TeV.364111.Sherpa_221_NNPDF30NNLO_Zmumu_MAXHTPTV280_500_BFilter.deriv.DAOD_HIGG8D1.e5271_s3126_r9364_r9315_p4133
 mc16_13TeV.364112.Sherpa_221_NNPDF30NNLO_Zmumu_MAXHTPTV500_1000.deriv.DAOD_HIGG8D1.e5271_s3126_r9364_r9315_p4133
 mc16_13TeV.364113.Sherpa_221_NNPDF30NNLO_Zmumu_MAXHTPTV1000_E_CMS.deriv.DAOD_HIGG8D1.e5271_s3126_r9364_r9315_p4133
 mc16_13TeV.364114.Sherpa_221_NNPDF30NNLO_Zee_MAXHTPTV0_70_CVetoBVeto.deriv.DAOD_HIGG8D1.e5299_s3126_r9364_r9315_p4133
 mc16_13TeV.364115.Sherpa_221_NNPDF30NNLO_Zee_MAXHTPTV0_70_CFilterBVeto.deriv.DAOD_HIGG8D1.e5299_s3126_r9364_r9315_p4133
 mc16_13TeV.364116.Sherpa_221_NNPDF30NNLO_Zee_MAXHTPTV0_70_BFilter.deriv.DAOD_HIGG8D1.e5299_s3126_r9364_r9315_p4133
 mc16_13TeV.364117.Sherpa_221_NNPDF30NNLO_Zee_MAXHTPTV70_140_CVetoBVeto.deriv.DAOD_HIGG8D1.e5299_s3126_r9364_r9315_p4133
 mc16_13TeV.364118.Sherpa_221_NNPDF30NNLO_Zee_MAXHTPTV70_140_CFilterBVeto.deriv.DAOD_HIGG8D1.e5299_s3126_r9364_r9315_p4133
 mc16_13TeV.364119.Sherpa_221_NNPDF30NNLO_Zee_MAXHTPTV70_140_BFilter.deriv.DAOD_HIGG8D1.e5299_s3126_r9364_r9315_p4133
 mc16_13TeV.364120.Sherpa_221_NNPDF30NNLO_Zee_MAXHTPTV140_280_CVetoBVeto.deriv.DAOD_HIGG8D1.e5299_s3126_r9364_r9315_p4133
 mc16_13TeV.364121.Sherpa_221_NNPDF30NNLO_Zee_MAXHTPTV140_280_CFilterBVeto.deriv.DAOD_HIGG8D1.e5299_s3126_r9364_r9315_p4133

mc16_13TeV.364122.Sherpa_221_NNPDF30NNLO_Zee_MAXHTPTV140_280_BFilter.deriv.DAOD_HIGG8D1.e5299_s3126_r9364_r9315_p4133
 mc16_13TeV.364123.Sherpa_221_NNPDF30NNLO_Zee_MAXHTPTV280_500_CVetoBVeto.deriv.DAOD_HIGG8D1.e5299_s3126_r9364_r9315_p4133
 mc16_13TeV.364124.Sherpa_221_NNPDF30NNLO_Zee_MAXHTPTV280_500_CFilterBVeto.deriv.DAOD_HIGG8D1.e5299_s3126_r9364_r9315_p4133
 mc16_13TeV.364125.Sherpa_221_NNPDF30NNLO_Zee_MAXHTPTV280_500_BFilter.deriv.DAOD_HIGG8D1.e5299_s3126_r9364_r9315_p4133
 mc16_13TeV.364125.Sherpa_221_NNPDF30NNLO_Zee_MAXHTPTV280_500_BFilter.deriv.DAOD_HIGG8D1.e5299_e5984_s3126_r9364_r9315_p4133
 mc16_13TeV.364126.Sherpa_221_NNPDF30NNLO_Zee_MAXHTPTV500_1000.deriv.DAOD_HIGG8D1.e5299_s3126_r9364_r9315_p4133
 mc16_13TeV.364127.Sherpa_221_NNPDF30NNLO_Zee_MAXHTPTV1000_E_CMS.deriv.DAOD_HIGG8D1.e5299_s3126_r9364_r9315_p4133
 mc16_13TeV.364128.Sherpa_221_NNPDF30NNLO_Ztautau_MAXHTPTV0_70_CVetoBVeto.deriv.DAOD_HIGG8D1.e5307_s3126_r9364_r9315_p4133
 mc16_13TeV.364129.Sherpa_221_NNPDF30NNLO_Ztautau_MAXHTPTV0_70_CFilterBVeto.deriv.DAOD_HIGG8D1.e5307_s3126_r9364_r9315_p4133
 mc16_13TeV.364130.Sherpa_221_NNPDF30NNLO_Ztautau_MAXHTPTV0_70_BFilter.deriv.DAOD_HIGG8D1.e5307_s3126_r9364_r9315_p4133
 mc16_13TeV.364131.Sherpa_221_NNPDF30NNLO_Ztautau_MAXHTPTV70_140_CVetoBVeto.deriv.DAOD_HIGG8D1.e5307_s3126_r9364_r9315_p4133
 mc16_13TeV.364132.Sherpa_221_NNPDF30NNLO_Ztautau_MAXHTPTV70_140_CFilterBVeto.deriv.DAOD_HIGG8D1.e5307_s3126_r9364_r9315_p4133
 mc16_13TeV.364133.Sherpa_221_NNPDF30NNLO_Ztautau_MAXHTPTV70_140_BFilter.deriv.DAOD_HIGG8D1.e5307_s3126_r9364_r9315_p4133
 mc16_13TeV.364134.Sherpa_221_NNPDF30NNLO_Ztautau_MAXHTPTV140_280_CVetoBVeto.deriv.DAOD_HIGG8D1.e5307_s3126_r9364_r9315_p4133
 mc16_13TeV.364135.Sherpa_221_NNPDF30NNLO_Ztautau_MAXHTPTV140_280_CFilterBVeto.deriv.DAOD_HIGG8D1.e5307_s3126_r9364_r9315_p4133
 mc16_13TeV.364136.Sherpa_221_NNPDF30NNLO_Ztautau_MAXHTPTV140_280_BFilter.deriv.DAOD_HIGG8D1.e5307_s3126_r9364_r9315_p4133
 mc16_13TeV.364137.Sherpa_221_NNPDF30NNLO_Ztautau_MAXHTPTV280_500_CVetoBVeto.deriv.DAOD_HIGG8D1.e5307_e5984_s3126_r9364_r9315_p4133
 mc16_13TeV.364137.Sherpa_221_NNPDF30NNLO_Ztautau_MAXHTPTV280_500_CVetoBVeto.deriv.DAOD_HIGG8D1.e5307_s3126_r9364_r9315_p4133
 mc16_13TeV.364138.Sherpa_221_NNPDF30NNLO_Ztautau_MAXHTPTV280_500_CFilterBVeto.deriv.DAOD_HIGG8D1.e5313_s3126_r9364_r9315_p4133
 mc16_13TeV.364139.Sherpa_221_NNPDF30NNLO_Ztautau_MAXHTPTV280_500_BFilter.deriv.DAOD_HIGG8D1.e5313_s3126_r9364_r9315_p4133
 mc16_13TeV.364140.Sherpa_221_NNPDF30NNLO_Ztautau_MAXHTPTV500_1000.deriv.DAOD_HIGG8D1.e5307_s3126_r9364_r9315_p4133
 mc16_13TeV.364141.Sherpa_221_NNPDF30NNLO_Ztautau_MAXHTPTV1000_E_CMS.deriv.DAOD_HIGG8D1.e5307_s3126_r9364_r9315_p4133
 mc16_13TeV.364198.Sherpa_221_NN30NNLO_Zmm_Mll10_40_MAXHTPTV0_70_BVeto.deriv.DAOD_HIGG8D1.e5421_s3126_r9364_r9315_p4133
 mc16_13TeV.364199.Sherpa_221_NN30NNLO_Zmm_Mll10_40_MAXHTPTV0_70_BFilter.deriv.DAOD_HIGG8D1.e5421_s3126_r9364_r9315_p4133
 mc16_13TeV.364200.Sherpa_221_NN30NNLO_Zmm_Mll10_40_MAXHTPTV70_280_BVeto.deriv.DAOD_HIGG8D1.e5421_s3126_r9364_r9315_p4133
 mc16_13TeV.364201.Sherpa_221_NN30NNLO_Zmm_Mll10_40_MAXHTPTV70_280_BFilter.deriv.DAOD_HIGG8D1.e5421_s3126_r9364_r9315_p4133
 mc16_13TeV.364202.Sherpa_221_NN30NNLO_Zmm_Mll10_40_MAXHTPTV280_E_CMS_BVeto.deriv.DAOD_HIGG8D1.e5421_s3126_r9364_r9315_p4133
 mc16_13TeV.364203.Sherpa_221_NN30NNLO_Zmm_Mll10_40_MAXHTPTV280_E_CMS_BFilter.deriv.DAOD_HIGG8D1.e5421_s3126_r9364_r9315_p4133
 mc16_13TeV.364204.Sherpa_221_NN30NNLO_Zee_Mll10_40_MAXHTPTV0_70_BVeto.deriv.DAOD_HIGG8D1.e5421_s3126_r9364_r9315_p4133
 mc16_13TeV.364205.Sherpa_221_NN30NNLO_Zee_Mll10_40_MAXHTPTV0_70_BFilter.deriv.DAOD_HIGG8D1.e5421_s3126_r9364_r9315_p4133
 mc16_13TeV.364206.Sherpa_221_NN30NNLO_Zee_Mll10_40_MAXHTPTV70_280_BVeto.deriv.DAOD_HIGG8D1.e5421_s3126_r9364_r9315_p4133

mc16_13TeV.364207.Sherpa_221_NN30NNLO_Zee_Mll10_40_MAXHTPTV70_280_BFilter.deriv.DAOD_HIGG8D1.e5421_s3126_r9364_r9315_p4133
 mc16_13TeV.364208.Sherpa_221_NN30NNLO_Zee_Mll10_40_MAXHTPTV280_E_CMS_BVeto.deriv.DAOD_HIGG8D1.e5421_s3126_r9364_r9315_p4133
 mc16_13TeV.364209.Sherpa_221_NN30NNLO_Zee_Mll10_40_MAXHTPTV280_E_CMS_BFilter.deriv.DAOD_HIGG8D1.e5421_s3126_r9364_r9315_p4133
 mc16_13TeV.364210.Sherpa_221_NN30NNLO_Ztt_Mll10_40_MAXHTPTV0_70_BVeto.deriv.DAOD_HIGG8D1.e5421_s3126_r9364_r9315_p4133
 mc16_13TeV.364211.Sherpa_221_NN30NNLO_Ztt_Mll10_40_MAXHTPTV0_70_BFilter.deriv.DAOD_HIGG8D1.e5421_s3126_r9364_r9315_p4133
 mc16_13TeV.364212.Sherpa_221_NN30NNLO_Ztt_Mll10_40_MAXHTPTV70_280_BVeto.deriv.DAOD_HIGG8D1.e5421_s3126_r9364_r9315_p4133
 mc16_13TeV.364213.Sherpa_221_NN30NNLO_Ztt_Mll10_40_MAXHTPTV70_280_BFilter.deriv.DAOD_HIGG8D1.e5421_s3126_r9364_r9315_p4133
 mc16_13TeV.364214.Sherpa_221_NN30NNLO_Ztt_Mll10_40_MAXHTPTV280_E_CMS_BVeto.deriv.DAOD_HIGG8D1.e5421_s3126_r9364_r9315_p4133
 mc16_13TeV.364215.Sherpa_221_NN30NNLO_Ztt_Mll10_40_MAXHTPTV280_E_CMS_BFilter.deriv.DAOD_HIGG8D1.e5421_s3126_r9364_r9315_p4133
 mc16_13TeV.364156.Sherpa_221_NNPDF30NNLO_Wmumu_MAXHTPTV0_70_CVetoBVeto.deriv.DAOD_HIGG8D1.e5340_s3126_r9364_r9315_p4133
 mc16_13TeV.364157.Sherpa_221_NNPDF30NNLO_Wmumu_MAXHTPTV0_70_CFilterBVeto.deriv.DAOD_HIGG8D1.e5340_s3126_r9364_r9315_p4133
 mc16_13TeV.364157.Sherpa_221_NNPDF30NNLO_Wmumu_MAXHTPTV0_70_CFilterBVeto.deriv.DAOD_HIGG8D1.e5340_e5984_s3126_r9364_r9315_p4133
 mc16_13TeV.364158.Sherpa_221_NNPDF30NNLO_Wmumu_MAXHTPTV0_70_BFilter.deriv.DAOD_HIGG8D1.e5340_s3126_r9364_r9315_p4133
 mc16_13TeV.364159.Sherpa_221_NNPDF30NNLO_Wmumu_MAXHTPTV70_140_CVetoBVeto.deriv.DAOD_HIGG8D1.e5340_s3126_r9364_r9315_p4133
 mc16_13TeV.364160.Sherpa_221_NNPDF30NNLO_Wmumu_MAXHTPTV70_140_CFilterBVeto.deriv.DAOD_HIGG8D1.e5340_s3126_r9364_r9315_p4133
 mc16_13TeV.364161.Sherpa_221_NNPDF30NNLO_Wmumu_MAXHTPTV70_140_BFilter.deriv.DAOD_HIGG8D1.e5340_s3126_r9364_r9315_p4133
 mc16_13TeV.364162.Sherpa_221_NNPDF30NNLO_Wmumu_MAXHTPTV140_280_CVetoBVeto.deriv.DAOD_HIGG8D1.e5340_s3126_r9364_r9315_p4133
 mc16_13TeV.364163.Sherpa_221_NNPDF30NNLO_Wmumu_MAXHTPTV140_280_CFilterBVeto.deriv.DAOD_HIGG8D1.e5340_s3126_r9364_r9315_p4133
 mc16_13TeV.364163.Sherpa_221_NNPDF30NNLO_Wmumu_MAXHTPTV140_280_CFilterBVeto.deriv.DAOD_HIGG8D1.e5340_e5984_s3126_s3136_r9364_r9315_p4133
 mc16_13TeV.364164.Sherpa_221_NNPDF30NNLO_Wmumu_MAXHTPTV140_280_BFilter.deriv.DAOD_HIGG8D1.e5340_s3126_r9364_r9315_p4133
 mc16_13TeV.364165.Sherpa_221_NNPDF30NNLO_Wmumu_MAXHTPTV280_500_CVetoBVeto.deriv.DAOD_HIGG8D1.e5340_s3126_r9364_r9315_p4133
 mc16_13TeV.364166.Sherpa_221_NNPDF30NNLO_Wmumu_MAXHTPTV280_500_CFilterBVeto.deriv.DAOD_HIGG8D1.e5340_s3126_r9364_r9315_p4133
 mc16_13TeV.364167.Sherpa_221_NNPDF30NNLO_Wmumu_MAXHTPTV280_500_BFilter.deriv.DAOD_HIGG8D1.e5340_e5984_s3126_r9364_r9315_p4133
 mc16_13TeV.364167.Sherpa_221_NNPDF30NNLO_Wmumu_MAXHTPTV280_500_BFilter.deriv.DAOD_HIGG8D1.e5340_s3126_r9364_r9315_p4133
 mc16_13TeV.364168.Sherpa_221_NNPDF30NNLO_Wmumu_MAXHTPTV500_1000.deriv.DAOD_HIGG8D1.e5340_s3126_r9364_r9315_p4133
 mc16_13TeV.364169.Sherpa_221_NNPDF30NNLO_Wmumu_MAXHTPTV1000_E_CMS.deriv.DAOD_HIGG8D1.e5340_s3126_r9364_r9315_p4133
 mc16_13TeV.364170.Sherpa_221_NNPDF30NNLO_Wenu_MAXHTPTV0_70_CVetoBVeto.deriv.DAOD_HIGG8D1.e5340_s3126_r9364_r9315_p4133
 mc16_13TeV.364171.Sherpa_221_NNPDF30NNLO_Wenu_MAXHTPTV0_70_CFilterBVeto.deriv.DAOD_HIGG8D1.e5340_e5984_s3126_r9364_r9315_p4133
 mc16_13TeV.364171.Sherpa_221_NNPDF30NNLO_Wenu_MAXHTPTV0_70_CFilterBVeto.deriv.DAOD_HIGG8D1.e5340_s3126_r9364_r9315_p4133
 mc16_13TeV.364172.Sherpa_221_NNPDF30NNLO_Wenu_MAXHTPTV0_70_BFilter.deriv.DAOD_HIGG8D1.e5340_s3126_r9364_r9315_p4133
 mc16_13TeV.364173.Sherpa_221_NNPDF30NNLO_Wenu_MAXHTPTV70_140_CVetoBVeto.deriv.DAOD_HIGG8D1.e5340_s3126_r9364_r9315_p4133

mc16_13TeV.364174.Sherpa_221_NNPDF30NNLO_Wenu_MAXHTPTV70_140_CFilterBVeto.deriv.DAOD_HIGG8D1.e5340_s3126_r9364_r9315_p4133
 mc16_13TeV.364175.Sherpa_221_NNPDF30NNLO_Wenu_MAXHTPTV70_140_BFilter.deriv.DAOD_HIGG8D1.e5340_e5984_s3126_s3136_r9364_r9315_p4133
 mc16_13TeV.364175.Sherpa_221_NNPDF30NNLO_Wenu_MAXHTPTV70_140_BFilter.deriv.DAOD_HIGG8D1.e5340_s3126_r9364_r9315_p4133
 mc16_13TeV.364176.Sherpa_221_NNPDF30NNLO_Wenu_MAXHTPTV140_280_CVetoBVeto.deriv.DAOD_HIGG8D1.e5340_s3126_r9364_r9315_p4133
 mc16_13TeV.364177.Sherpa_221_NNPDF30NNLO_Wenu_MAXHTPTV140_280_CFilterBVeto.deriv.DAOD_HIGG8D1.e5340_s3126_r9364_r9315_p4133
 mc16_13TeV.364177.Sherpa_221_NNPDF30NNLO_Wenu_MAXHTPTV140_280_CFilterBVeto.deriv.DAOD_HIGG8D1.e5340_e5984_s3126_s3136_r9364_r9315_p4133
 mc16_13TeV.364178.Sherpa_221_NNPDF30NNLO_Wenu_MAXHTPTV140_280_BFilter.deriv.DAOD_HIGG8D1.e5340_s3126_r9364_r9315_p4133
 mc16_13TeV.364179.Sherpa_221_NNPDF30NNLO_Wenu_MAXHTPTV280_500_CVetoBVeto.deriv.DAOD_HIGG8D1.e5340_s3126_r9364_r9315_p4133
 mc16_13TeV.364180.Sherpa_221_NNPDF30NNLO_Wenu_MAXHTPTV280_500_CFilterBVeto.deriv.DAOD_HIGG8D1.e5340_s3126_r9364_r9315_p4133
 mc16_13TeV.364181.Sherpa_221_NNPDF30NNLO_Wenu_MAXHTPTV280_500_BFilter.deriv.DAOD_HIGG8D1.e5340_e5984_s3126_r9364_r9315_p4133
 mc16_13TeV.364181.Sherpa_221_NNPDF30NNLO_Wenu_MAXHTPTV280_500_BFilter.deriv.DAOD_HIGG8D1.e5340_s3126_r9364_r9315_p4133
 mc16_13TeV.364182.Sherpa_221_NNPDF30NNLO_Wenu_MAXHTPTV500_1000.deriv.DAOD_HIGG8D1.e5340_s3126_r9364_r9315_p4133
 mc16_13TeV.364183.Sherpa_221_NNPDF30NNLO_Wenu_MAXHTPTV1000_E_CMS.deriv.DAOD_HIGG8D1.e5340_s3126_r9364_r9315_p4133
 mc16_13TeV.364184.Sherpa_221_NNPDF30NNLO_Wtaunu_MAXHTPTV0_70_CVetoBVeto.deriv.DAOD_HIGG8D1.e5340_s3126_r9364_r9315_p4133
 mc16_13TeV.364185.Sherpa_221_NNPDF30NNLO_Wtaunu_MAXHTPTV0_70_CFilterBVeto.deriv.DAOD_HIGG8D1.e5340_e5984_s3126_r9364_r9315_p4133
 mc16_13TeV.364185.Sherpa_221_NNPDF30NNLO_Wtaunu_MAXHTPTV0_70_CFilterBVeto.deriv.DAOD_HIGG8D1.e5340_s3126_r9364_r9315_p4133
 mc16_13TeV.364186.Sherpa_221_NNPDF30NNLO_Wtaunu_MAXHTPTV0_70_BFilter.deriv.DAOD_HIGG8D1.e5340_s3126_r9364_r9315_p4133
 mc16_13TeV.364187.Sherpa_221_NNPDF30NNLO_Wtaunu_MAXHTPTV70_140_CVetoBVeto.deriv.DAOD_HIGG8D1.e5340_s3126_r9364_r9315_p4133
 mc16_13TeV.364188.Sherpa_221_NNPDF30NNLO_Wtaunu_MAXHTPTV70_140_CFilterBVeto.deriv.DAOD_HIGG8D1.e5340_s3126_r9364_r9315_p4133
 mc16_13TeV.364189.Sherpa_221_NNPDF30NNLO_Wtaunu_MAXHTPTV70_140_BFilter.deriv.DAOD_HIGG8D1.e5340_s3126_r9364_r9315_p4133
 mc16_13TeV.364190.Sherpa_221_NNPDF30NNLO_Wtaunu_MAXHTPTV140_280_CVetoBVeto.deriv.DAOD_HIGG8D1.e5340_e5984_s3126_r9364_r9315_p4133
 mc16_13TeV.364190.Sherpa_221_NNPDF30NNLO_Wtaunu_MAXHTPTV140_280_CVetoBVeto.deriv.DAOD_HIGG8D1.e5340_s3126_r9364_r9315_p4133
 mc16_13TeV.364191.Sherpa_221_NNPDF30NNLO_Wtaunu_MAXHTPTV140_280_CFilterBVeto.deriv.DAOD_HIGG8D1.e5340_s3126_r9364_r9315_p4133
 mc16_13TeV.364191.Sherpa_221_NNPDF30NNLO_Wtaunu_MAXHTPTV140_280_CFilterBVeto.deriv.DAOD_HIGG8D1.e5340_e5984_s3126_s3136_r9364_r9315_p4133
 mc16_13TeV.364192.Sherpa_221_NNPDF30NNLO_Wtaunu_MAXHTPTV140_280_BFilter.deriv.DAOD_HIGG8D1.e5340_s3126_r9364_r9315_p4133
 mc16_13TeV.364193.Sherpa_221_NNPDF30NNLO_Wtaunu_MAXHTPTV280_500_CVetoBVeto.deriv.DAOD_HIGG8D1.e5340_s3126_r9364_r9315_p4133
 mc16_13TeV.364193.Sherpa_221_NNPDF30NNLO_Wtaunu_MAXHTPTV280_500_CVetoBVeto.deriv.DAOD_HIGG8D1.e5340_e5984_s3126_s3136_r9364_r9315_p4133
 mc16_13TeV.364194.Sherpa_221_NNPDF30NNLO_Wtaunu_MAXHTPTV280_500_CFilterBVeto.deriv.DAOD_HIGG8D1.e5340_e5984_s3126_s3136_r9364_r9315_p4133
 mc16_13TeV.364195.Sherpa_221_NNPDF30NNLO_Wtaunu_MAXHTPTV280_500_BFilter.deriv.DAOD_HIGG8D1.e5340_s3126_r9364_r9315_p4133
 mc16_13TeV.364196.Sherpa_221_NNPDF30NNLO_Wtaunu_MAXHTPTV500_1000.deriv.DAOD_HIGG8D1.e5340_s3126_r9364_r9315_p4133

mc16_13TeV.364197.Sherpa_221_NNPDF30NNLO_Wtaunu_MAXHTPTV1000_E_CMS.deriv.DAOD_HIGG8D1.e5340_s3126_r9364_r9315_p4133
 mc16_13TeV.364500.Sherpa_222_NNPDF30NNLO_eegamma_pty_7_15.deriv.DAOD_HIGG8D1.e5928_e5984_s3126_r9364_r9315_p4133
 mc16_13TeV.364501.Sherpa_222_NNPDF30NNLO_eegamma_pty_15_35.deriv.DAOD_HIGG8D1.e5928_e5984_s3126_r9364_r9315_p4133
 mc16_13TeV.364502.Sherpa_222_NNPDF30NNLO_eegamma_pty_35_70.deriv.DAOD_HIGG8D1.e5928_e5984_s3126_r9364_r9315_p4133
 mc16_13TeV.364503.Sherpa_222_NNPDF30NNLO_eegamma_pty_70_140.deriv.DAOD_HIGG8D1.e5928_e5984_s3126_r9364_r9315_p4133
 mc16_13TeV.364504.Sherpa_222_NNPDF30NNLO_eegamma_pty_140_E_CMS.deriv.DAOD_HIGG8D1.e5928_e5984_s3126_r9364_r9315_p4133
 mc16_13TeV.364505.Sherpa_222_NNPDF30NNLO_mumugamma_pty_7_15.deriv.DAOD_HIGG8D1.e5928_e5984_s3126_r9364_r9315_p4133
 mc16_13TeV.364506.Sherpa_222_NNPDF30NNLO_mumugamma_pty_15_35.deriv.DAOD_HIGG8D1.e5988_e5984_s3126_r9364_r9315_p4133
 mc16_13TeV.364507.Sherpa_222_NNPDF30NNLO_mumugamma_pty_35_70.deriv.DAOD_HIGG8D1.e5928_e5984_s3126_r9364_r9315_p4133
 mc16_13TeV.364508.Sherpa_222_NNPDF30NNLO_mumugamma_pty_70_140.deriv.DAOD_HIGG8D1.e5928_e5984_s3126_r9364_r9315_p4133
 mc16_13TeV.364509.Sherpa_222_NNPDF30NNLO_mumugamma_pty_140_E_CMS.deriv.DAOD_HIGG8D1.e5928_e5984_s3126_r9364_r9315_p4133
 mc16_13TeV.364510.Sherpa_222_NNPDF30NNLO_tautaugamma_pty_7_15.deriv.DAOD_HIGG8D1.e5928_s3126_r9364_r9315_p4133
 mc16_13TeV.364511.Sherpa_222_NNPDF30NNLO_tautaugamma_pty_15_35.deriv.DAOD_HIGG8D1.e5928_s3126_r9364_r9315_p4133
 mc16_13TeV.364512.Sherpa_222_NNPDF30NNLO_tautaugamma_pty_35_70.deriv.DAOD_HIGG8D1.e5928_s3126_r9364_r9315_p4133
 mc16_13TeV.364513.Sherpa_222_NNPDF30NNLO_tautaugamma_pty_70_140.deriv.DAOD_HIGG8D1.e5982_s3126_r9364_r9315_p4133
 mc16_13TeV.364514.Sherpa_222_NNPDF30NNLO_tautaugamma_pty_140_E_CMS.deriv.DAOD_HIGG8D1.e5928_s3126_r9364_r9315_p4133
 mc16_13TeV.364521.Sherpa_222_NNPDF30NNLO_enugamma_pty_7_15.deriv.DAOD_HIGG8D1.e5928_s3126_r9364_r9315_p4133
 mc16_13TeV.364522.Sherpa_222_NNPDF30NNLO_enugamma_pty_15_35.deriv.DAOD_HIGG8D1.e5928_s3126_r9364_r9315_p4133
 mc16_13TeV.364523.Sherpa_222_NNPDF30NNLO_enugamma_pty_35_70.deriv.DAOD_HIGG8D1.e5928_s3126_r9364_r9315_p4133
 mc16_13TeV.364524.Sherpa_222_NNPDF30NNLO_enugamma_pty_70_140.deriv.DAOD_HIGG8D1.e5928_s3126_r9364_r9315_p4133
 mc16_13TeV.364525.Sherpa_222_NNPDF30NNLO_enugamma_pty_140_E_CMS.deriv.DAOD_HIGG8D1.e5928_s3126_r9364_r9315_p4133
 mc16_13TeV.364526.Sherpa_222_NNPDF30NNLO_munugamma_pty_7_15.deriv.DAOD_HIGG8D1.e5928_s3126_r9364_r9315_p4133
 mc16_13TeV.364527.Sherpa_222_NNPDF30NNLO_munugamma_pty_15_35.deriv.DAOD_HIGG8D1.e5928_s3126_r9364_r9315_p4133
 mc16_13TeV.364528.Sherpa_222_NNPDF30NNLO_munugamma_pty_35_70.deriv.DAOD_HIGG8D1.e5928_s3126_r9364_r9315_p4133
 mc16_13TeV.364529.Sherpa_222_NNPDF30NNLO_munugamma_pty_70_140.deriv.DAOD_HIGG8D1.e5928_s3126_r9364_r9315_p4133
 mc16_13TeV.364530.Sherpa_222_NNPDF30NNLO_munugamma_pty_140_E_CMS.deriv.DAOD_HIGG8D1.e5928_s3126_r9364_r9315_p4133
 mc16_13TeV.364530.Sherpa_222_NNPDF30NNLO_munugamma_pty_140_E_CMS.deriv.DAOD_HIGG8D1.e5928_e5984_s3126_r9364_r9315_p4133
 mc16_13TeV.364531.Sherpa_222_NNPDF30NNLO_taunugamma_pty_7_15.deriv.DAOD_HIGG8D1.e5928_s3126_r9364_r9315_p4133
 mc16_13TeV.364532.Sherpa_222_NNPDF30NNLO_taunugamma_pty_15_35.deriv.DAOD_HIGG8D1.e5928_s3126_r9364_r9315_p4133
 mc16_13TeV.364533.Sherpa_222_NNPDF30NNLO_taunugamma_pty_35_70.deriv.DAOD_HIGG8D1.e5928_s3126_r9364_r9315_p4133

mc16_13TeV.364534.Sherpa_222_NNPDF30NNLO_taunugamma_pty_70_140.deriv.DAOD_HIGG8D1.e5928_s3126_r9364_r9315_p4133
 mc16_13TeV.364535.Sherpa_222_NNPDF30NNLO_taunugamma_pty_140_E_CMS.deriv.DAOD_HIGG8D1.e5928_s3126_r9364_r9315_p4133
 mc16_13TeV.364535.Sherpa_222_NNPDF30NNLO_taunugamma_pty_140_E_CMS.deriv.DAOD_HIGG8D1.e5928_e5984_s3126_r9364_r9315_p4133
 mc16_13TeV.410560.MadGraphPythia8EvtGen_A14_tZ_4fl_tchan_noAllHad.deriv.DAOD_HIGG8D1.e5803_s3126_r9364_r9315_p4133
 mc16_13TeV.410013.PowhegPythiaEvtGen_P2012_Wt_inclusive_top.deriv.DAOD_HIGG8D1.e3753_s3126_r9364_r9315_p4133
 mc16_13TeV.410014.PowhegPythiaEvtGen_P2012_Wt_inclusive_antitop.deriv.DAOD_HIGG8D1.e3753_s3126_r9364_r9315_p4133
 mc16_13TeV.410408.aMcAtNloPythia8EvtGen_tWZ_Ztoll_minDR1.deriv.DAOD_HIGG8D1.e6423_e5984_s3126_r9364_r9315_p4133
 mc16_13TeV.364242.Sherpa_222_NNPDF30NNLO_WWW_3l3v_EW6.deriv.DAOD_HIGG8D1.e5887_s3126_r9364_r9315_p4133
 mc16_13TeV.364243.Sherpa_222_NNPDF30NNLO_WWZ_4l2v_EW6.deriv.DAOD_HIGG8D1.e5887_s3126_r9364_r9315_p4133
 mc16_13TeV.364244.Sherpa_222_NNPDF30NNLO_WWZ_2l4v_EW6.deriv.DAOD_HIGG8D1.e5887_s3126_r9364_r9315_p4133
 mc16_13TeV.364245.Sherpa_222_NNPDF30NNLO_WZZ_5l1v_EW6.deriv.DAOD_HIGG8D1.e5887_s3126_r9364_r9315_p4133
 mc16_13TeV.364246.Sherpa_222_NNPDF30NNLO_WZZ_3l3v_EW6.deriv.DAOD_HIGG8D1.e5887_s3126_r9364_r9315_p4133
 mc16_13TeV.364247.Sherpa_222_NNPDF30NNLO_ZZZ_6l0v_EW6.deriv.DAOD_HIGG8D1.e5887_s3126_r9364_r9315_p4133
 mc16_13TeV.364248.Sherpa_222_NNPDF30NNLO_ZZZ_4l2v_EW6.deriv.DAOD_HIGG8D1.e5887_s3126_r9364_r9315_p4133
 mc16_13TeV.364249.Sherpa_222_NNPDF30NNLO_ZZZ_2l4v_EW6.deriv.DAOD_HIGG8D1.e5887_s3126_r9364_r9315_p4133
 mc16_13TeV.342284.Pythia8EvtGen_A14NNPDF23LO_WH125_inc.deriv.DAOD_HIGG8D1.e4246_s3126_r9364_r9315_p4133
 mc16_13TeV.342285.Pythia8EvtGen_A14NNPDF23LO_ZH125_inc.deriv.DAOD_HIGG8D1.e4246_s3126_r9364_r9315_p4133
 mc16_13TeV.341998.aMcAtNloHppEG_UEEE5_CTEQ6L1_CT10ME_tWH125_gamgam_yt_plus1.deriv.DAOD_HIGG8D1.e4394_e5984_s3126_r9364_r9315_p4133
 mc16_13TeV.410389.MadGraphPythia8EvtGen_A14NNPDF23_ttgamma_nonallhadronic.deriv.DAOD_HIGG8D1.e6155_e5984_s3126_r9364_r9315_p4133
 mc16_13TeV.410470.PhPy8EG_A14_ttbar_hdamp258p75_nonallhad.deriv.DAOD_HIGG8D1.e6337_e5984_s3126_r9364_r9315_p4133
 mc16_13TeV.410472.PhPy8EG_A14_ttbar_hdamp258p75_dil.deriv.DAOD_HIGG8D1.e6348_e5984_s3126_r9364_r9315_p4133
 mc16_13TeV.346343.PhPy8EG_A14NNPDF23_NNPDF30ME_ttH125_allhad.deriv.DAOD_HIGG8D1.e7148_e5984_s3126_r9364_r9315_p4133
 mc16_13TeV.346344.PhPy8EG_A14NNPDF23_NNPDF30ME_ttH125_semilep.deriv.DAOD_HIGG8D1.e7148_e5984_s3126_r9364_r9315_p4133
 mc16_13TeV.346345.PhPy8EG_A14NNPDF23_NNPDF30ME_ttH125_dilep.deriv.DAOD_HIGG8D1.e7148_e5984_s3126_r9364_r9315_p4133

mc16d:

mc16_13TeV.364253.Sherpa_222_NNPDF30NNLO_lllv.deriv.DAOD_HIGG8D1.e5916_e5984_s3126_r10201_r10210_p4133
 mc16_13TeV.364250.Sherpa_222_NNPDF30NNLO_llll.deriv.DAOD_HIGG8D1.e5894_e5984_s3126_r10201_r10210_p4133
 mc16_13TeV.364254.Sherpa_222_NNPDF30NNLO_llvv.deriv.DAOD_HIGG8D1.e5916_e5984_s3126_r10201_r10210_p4133
 mc16_13TeV.364255.Sherpa_222_NNPDF30NNLO_lvvv.deriv.DAOD_HIGG8D1.e5916_e5984_s3126_r10201_r10210_p4133
 mc16_13TeV.410155.aMcAtNloPythia8EvtGen_MEN30NLO_A14N23LO_ttW.deriv.DAOD_HIGG8D1.e5070_e5984_s3126_r10201_r10210_p4133

mc16_13TeV.410156.aMcAtNloPythia8EvtGen_MEN30NLO_A14N23LO_ttZnunu.deriv.DAOD_HIGG8D1.e5070_e5984_s3126_r10201_r10210_p4133
 mc16_13TeV.410157.aMcAtNloPythia8EvtGen_MEN30NLO_A14N23LO_ttZqq.deriv.DAOD_HIGG8D1.e5070_e5984_s3126_r10201_r10210_p4133
 mc16_13TeV.410218.aMcAtNloPythia8EvtGen_MEN30NLO_A14N23LO_ttee.deriv.DAOD_HIGG8D1.e5070_e5984_s3126_r10201_r10210_p4133
 mc16_13TeV.410219.aMcAtNloPythia8EvtGen_MEN30NLO_A14N23LO_ttmumu.deriv.DAOD_HIGG8D1.e5070_e5984_s3126_r10201_r10210_p4133
 mc16_13TeV.410220.aMcAtNloPythia8EvtGen_MEN30NLO_A14N23LO_ttautau.deriv.DAOD_HIGG8D1.e5070_e5984_s3126_r10201_r10210_p4133
 mc16_13TeV.410276.aMcAtNloPythia8EvtGen_MEN30NLO_A14N23LO_ttee_mll_1_5.deriv.DAOD_HIGG8D1.e6087_e5984_s3126_r10201_r10210_p4133
 mc16_13TeV.410277.aMcAtNloPythia8EvtGen_MEN30NLO_A14N23LO_ttmumu_mll_1_5.deriv.DAOD_HIGG8D1.e6087_e5984_s3126_r10201_r10210_p4133
 mc16_13TeV.410278.aMcAtNloPythia8EvtGen_MEN30NLO_A14N23LO_ttautau_mll_1_5.deriv.DAOD_HIGG8D1.e6087_e5984_s3126_r10201_r10210_p4133
 mc16_13TeV.410397.MadGraphPythia8EvtGen_ttbar_wbee_MEN30LO_A14N23LO.deriv.DAOD_HIGG8D1.e6086_e5984_s3126_r10201_r10210_p4133
 mc16_13TeV.410398.MadGraphPythia8EvtGen_ttbar_wbmumu_MEN30LO_A14N23LO.deriv.DAOD_HIGG8D1.e6086_e5984_s3126_r10201_r10210_p4133
 mc16_13TeV.410399.MadGraphPythia8EvtGen_ttbar_wbttau_MEN30LO_A14N23LO.deriv.DAOD_HIGG8D1.e6086_e5984_s3126_r10201_r10210_p4133
 mc16_13TeV.410658.PhPy8EG_A14_tchan_BW50_lept_top.deriv.DAOD_HIGG8D1.e6671_e5984_s3126_r10201_r10210_p4133
 mc16_13TeV.410659.PhPy8EG_A14_tchan_BW50_lept_antitop.deriv.DAOD_HIGG8D1.e6671_e5984_s3126_r10201_r10210_p4133
 mc16_13TeV.410644.PowhegPythia8EvtGen_A14_singletop_schan_lept_top.deriv.DAOD_HIGG8D1.e6527_e5984_s3126_r10201_r10210_p4133
 mc16_13TeV.410645.PowhegPythia8EvtGen_A14_singletop_schan_lept_antitop.deriv.DAOD_HIGG8D1.e6527_s3126_r10201_r10210_p4133
 mc16_13TeV.412063.aMcAtNloPythia8EvtGen_tllq_NNPDF30_nf4_A14.deriv.DAOD_TOPQ1.e7054_e5984_s3126_r10201_r10210_p4174
 mc16_13TeV.304014.MadGraphPythia8EvtGen_A14NNPDF23_3top_SM.deriv.DAOD_HIGG8D1.e4324_e5984_s3126_r10201_r10210_p4133
 mc16_13TeV.410080.MadGraphPythia8EvtGen_A14NNPDF23_4topSM.deriv.DAOD_HIGG8D1.e4111_e5984_s3126_r10201_r10210_p4133
 mc16_13TeV.410081.MadGraphPythia8EvtGen_A14NNPDF23_ttbarWW.deriv.DAOD_HIGG8D1.e4111_e5984_s3126_r10201_r10210_p4133
 mc16_13TeV.364100.Sherpa_221_NNPDF30NNLO_Zmumu_MAXHTPTV0_70_CVetoBVeto.deriv.DAOD_HIGG8D1.e5271_s3126_r10201_r10210_p4133
 mc16_13TeV.364101.Sherpa_221_NNPDF30NNLO_Zmumu_MAXHTPTV0_70_CFfilterBVeto.deriv.DAOD_HIGG8D1.e5271_s3126_r10201_r10210_p4133
 mc16_13TeV.364101.Sherpa_221_NNPDF30NNLO_Zmumu_MAXHTPTV0_70_CFfilterBVeto.deriv.DAOD_HIGG8D1.e5271_e5984_s3126_r10201_r10210_p4133
 mc16_13TeV.364102.Sherpa_221_NNPDF30NNLO_Zmumu_MAXHTPTV0_70_BFilter.deriv.DAOD_HIGG8D1.e5271_s3126_r10201_r10210_p4133
 mc16_13TeV.364103.Sherpa_221_NNPDF30NNLO_Zmumu_MAXHTPTV70_140_CVetoBVeto.deriv.DAOD_HIGG8D1.e5271_s3126_r10201_r10210_p4133
 mc16_13TeV.364104.Sherpa_221_NNPDF30NNLO_Zmumu_MAXHTPTV70_140_CFfilterBVeto.deriv.DAOD_HIGG8D1.e5271_s3126_r10201_r10210_p4133
 mc16_13TeV.364106.Sherpa_221_NNPDF30NNLO_Zmumu_MAXHTPTV140_280_CVetoBVeto.deriv.DAOD_HIGG8D1.e5271_s3126_r10201_r10210_p4133
 mc16_13TeV.364107.Sherpa_221_NNPDF30NNLO_Zmumu_MAXHTPTV140_280_CFfilterBVeto.deriv.DAOD_HIGG8D1.e5271_s3126_r10201_r10210_p4133
 mc16_13TeV.364108.Sherpa_221_NNPDF30NNLO_Zmumu_MAXHTPTV140_280_BFilter.deriv.DAOD_HIGG8D1.e5271_e5984_s3126_r10201_r10210_p4133
 mc16_13TeV.364109.Sherpa_221_NNPDF30NNLO_Zmumu_MAXHTPTV280_500_CVetoBVeto.deriv.DAOD_HIGG8D1.e5271_e5984_s3126_r10201_r10210_p4133
 mc16_13TeV.364109.Sherpa_221_NNPDF30NNLO_Zmumu_MAXHTPTV280_500_CVetoBVeto.deriv.DAOD_HIGG8D1.e5271_s3126_r10201_r10210_p4133

mc16_13TeV.364110.Sherpa_221_NNPDF30NNLO_Zmumu_MAXHTPTV280_500_CFilterBVeto.deriv.DAOD_HIGG8D1.e5271_s3126_r10201_r10210_p4133
mc16_13TeV.364111.Sherpa_221_NNPDF30NNLO_Zmumu_MAXHTPTV280_500_BFilter.deriv.DAOD_HIGG8D1.e5271_e5984_s3126_r10201_r10210_p4133
mc16_13TeV.364111.Sherpa_221_NNPDF30NNLO_Zmumu_MAXHTPTV280_500_BFilter.deriv.DAOD_HIGG8D1.e5271_s3126_r10201_r10210_p4133
mc16_13TeV.364112.Sherpa_221_NNPDF30NNLO_Zmumu_MAXHTPTV500_1000.deriv.DAOD_HIGG8D1.e5271_e5984_s3126_r10201_r10210_p4133
mc16_13TeV.364112.Sherpa_221_NNPDF30NNLO_Zmumu_MAXHTPTV500_1000.deriv.DAOD_HIGG8D1.e5271_s3126_r10201_r10210_p4133
mc16_13TeV.364113.Sherpa_221_NNPDF30NNLO_Zmumu_MAXHTPTV1000_E_CMS.deriv.DAOD_HIGG8D1.e5271_s3126_r10201_r10210_p4133
mc16_13TeV.364114.Sherpa_221_NNPDF30NNLO_Zee_MAXHTPTV0_70_CVetoBVeto.deriv.DAOD_HIGG8D1.e5299_s3126_r10201_r10210_p4133
mc16_13TeV.364115.Sherpa_221_NNPDF30NNLO_Zee_MAXHTPTV0_70_CFilterBVeto.deriv.DAOD_HIGG8D1.e5299_e5984_s3126_r10201_r10210_p4133
mc16_13TeV.364116.Sherpa_221_NNPDF30NNLO_Zee_MAXHTPTV0_70_BFilter.deriv.DAOD_HIGG8D1.e5299_e5984_s3126_r10201_r10210_p4133
mc16_13TeV.364117.Sherpa_221_NNPDF30NNLO_Zee_MAXHTPTV70_140_CVetoBVeto.deriv.DAOD_HIGG8D1.e5299_e5984_s3126_r10201_r10210_p4133
mc16_13TeV.364118.Sherpa_221_NNPDF30NNLO_Zee_MAXHTPTV70_140_CFilterBVeto.deriv.DAOD_HIGG8D1.e5299_e5984_s3126_r10201_r10210_p4133
mc16_13TeV.364119.Sherpa_221_NNPDF30NNLO_Zee_MAXHTPTV70_140_BFilter.deriv.DAOD_HIGG8D1.e5299_e5984_s3126_r10201_r10210_p4133
mc16_13TeV.364120.Sherpa_221_NNPDF30NNLO_Zee_MAXHTPTV140_280_CVetoBVeto.deriv.DAOD_HIGG8D1.e5299_e5984_s3126_r10201_r10210_p4133
mc16_13TeV.364121.Sherpa_221_NNPDF30NNLO_Zee_MAXHTPTV140_280_CFilterBVeto.deriv.DAOD_HIGG8D1.e5299_e5984_s3126_r10201_r10210_p4133
mc16_13TeV.364122.Sherpa_221_NNPDF30NNLO_Zee_MAXHTPTV140_280_BFilter.deriv.DAOD_HIGG8D1.e5299_e5984_s3126_r10201_r10210_p4133
mc16_13TeV.364123.Sherpa_221_NNPDF30NNLO_Zee_MAXHTPTV280_500_CVetoBVeto.deriv.DAOD_HIGG8D1.e5299_e5984_s3126_r10201_r10210_p4133
mc16_13TeV.364124.Sherpa_221_NNPDF30NNLO_Zee_MAXHTPTV280_500_CFilterBVeto.deriv.DAOD_HIGG8D1.e5299_e5984_s3126_r10201_r10210_p4133
mc16_13TeV.364125.Sherpa_221_NNPDF30NNLO_Zee_MAXHTPTV280_500_BFilter.deriv.DAOD_HIGG8D1.e5299_e5984_s3126_r10201_r10210_p4133
mc16_13TeV.364126.Sherpa_221_NNPDF30NNLO_Zee_MAXHTPTV500_1000.deriv.DAOD_HIGG8D1.e5299_e5984_s3126_r10201_r10210_p4133
mc16_13TeV.364127.Sherpa_221_NNPDF30NNLO_Zee_MAXHTPTV1000_E_CMS.deriv.DAOD_HIGG8D1.e5299_e5984_s3126_r10201_r10210_p4133
mc16_13TeV.364128.Sherpa_221_NNPDF30NNLO_Ztautau_MAXHTPTV0_70_CVetoBVeto.deriv.DAOD_HIGG8D1.e5307_e5984_s3126_r10201_r10210_p4133
mc16_13TeV.364129.Sherpa_221_NNPDF30NNLO_Ztautau_MAXHTPTV0_70_CFilterBVeto.deriv.DAOD_HIGG8D1.e5307_e5984_s3126_r10201_r10210_p4133
mc16_13TeV.364130.Sherpa_221_NNPDF30NNLO_Ztautau_MAXHTPTV0_70_BFilter.deriv.DAOD_HIGG8D1.e5307_e5984_s3126_r10201_r10210_p4133
mc16_13TeV.364131.Sherpa_221_NNPDF30NNLO_Ztautau_MAXHTPTV70_140_CVetoBVeto.deriv.DAOD_HIGG8D1.e5307_e5984_s3126_r10201_r10210_p4133
mc16_13TeV.364132.Sherpa_221_NNPDF30NNLO_Ztautau_MAXHTPTV70_140_CFilterBVeto.deriv.DAOD_HIGG8D1.e5307_e5984_s3126_r10201_r10210_p4133
mc16_13TeV.364133.Sherpa_221_NNPDF30NNLO_Ztautau_MAXHTPTV70_140_BFilter.deriv.DAOD_HIGG8D1.e5307_e5984_s3126_r10201_r10210_p4133
mc16_13TeV.364134.Sherpa_221_NNPDF30NNLO_Ztautau_MAXHTPTV140_280_CVetoBVeto.deriv.DAOD_HIGG8D1.e5307_e5984_s3126_r10201_r10210_p4133
mc16_13TeV.364135.Sherpa_221_NNPDF30NNLO_Ztautau_MAXHTPTV140_280_CFilterBVeto.deriv.DAOD_HIGG8D1.e5307_e5984_s3126_r10201_r10210_p4133
mc16_13TeV.364136.Sherpa_221_NNPDF30NNLO_Ztautau_MAXHTPTV140_280_BFilter.deriv.DAOD_HIGG8D1.e5307_e5984_s3126_r10201_r10210_p4133
mc16_13TeV.364137.Sherpa_221_NNPDF30NNLO_Ztautau_MAXHTPTV280_500_CVetoBVeto.deriv.DAOD_HIGG8D1.e5307_e5984_s3126_r10201_r10210_p4133
mc16_13TeV.364138.Sherpa_221_NNPDF30NNLO_Ztautau_MAXHTPTV280_500_CFilterBVeto.deriv.DAOD_HIGG8D1.e5313_e5984_s3126_r10201_r10210_p4133

mc16_13TeV.364139.Sherpa_221_NNPDF30NNLO_Ztautau_MAXHTPTV280_500_BFilter.deriv.DAOD_HIGG8D1.e5313_e5984_s3126_r10201_r10210_p4133
 mc16_13TeV.364140.Sherpa_221_NNPDF30NNLO_Ztautau_MAXHTPTV500_1000.deriv.DAOD_HIGG8D1.e5307_e5984_s3126_r10201_r10210_p4133
 mc16_13TeV.364141.Sherpa_221_NNPDF30NNLO_Ztautau_MAXHTPTV1000_E_CMS.deriv.DAOD_HIGG8D1.e5307_e5984_s3126_r10201_r10210_p4133
 mc16_13TeV.364198.Sherpa_221_NN30NNLO_Zmm_Mll10_40_MAXHTPTV0_70_BVeto.deriv.DAOD_HIGG8D1.e5421_e5984_s3126_r10201_r10210_p4133
 mc16_13TeV.364199.Sherpa_221_NN30NNLO_Zmm_Mll10_40_MAXHTPTV0_70_BFilter.deriv.DAOD_HIGG8D1.e5421_e5984_s3126_r10201_r10210_p4133
 mc16_13TeV.364200.Sherpa_221_NN30NNLO_Zmm_Mll10_40_MAXHTPTV70_280_BVeto.deriv.DAOD_HIGG8D1.e5421_e5984_s3126_r10201_r10210_p4133
 mc16_13TeV.364201.Sherpa_221_NN30NNLO_Zmm_Mll10_40_MAXHTPTV70_280_BFilter.deriv.DAOD_HIGG8D1.e5421_e5984_s3126_r10201_r10210_p4133
 mc16_13TeV.364202.Sherpa_221_NN30NNLO_Zmm_Mll10_40_MAXHTPTV280_E_CMS_BVeto.deriv.DAOD_HIGG8D1.e5421_e5984_s3126_r10201_r10210_p4133
 mc16_13TeV.364203.Sherpa_221_NN30NNLO_Zmm_Mll10_40_MAXHTPTV280_E_CMS_BFilter.deriv.DAOD_HIGG8D1.e5421_e5984_s3126_r10201_r10210_p4133
 mc16_13TeV.364204.Sherpa_221_NN30NNLO_Zee_Mll10_40_MAXHTPTV0_70_BVeto.deriv.DAOD_HIGG8D1.e5421_e5984_s3126_r10201_r10210_p4133
 mc16_13TeV.364205.Sherpa_221_NN30NNLO_Zee_Mll10_40_MAXHTPTV0_70_BFilter.deriv.DAOD_HIGG8D1.e5421_e5984_s3126_r10201_r10210_p4133
 mc16_13TeV.364206.Sherpa_221_NN30NNLO_Zee_Mll10_40_MAXHTPTV70_280_BVeto.deriv.DAOD_HIGG8D1.e5421_e5984_s3126_r10201_r10210_p4133
 mc16_13TeV.364207.Sherpa_221_NN30NNLO_Zee_Mll10_40_MAXHTPTV70_280_BFilter.deriv.DAOD_HIGG8D1.e5421_e5984_s3126_r10201_r10210_p4133
 mc16_13TeV.364208.Sherpa_221_NN30NNLO_Zee_Mll10_40_MAXHTPTV280_E_CMS_BVeto.deriv.DAOD_HIGG8D1.e5421_e5984_s3126_r10201_r10210_p4133
 mc16_13TeV.364209.Sherpa_221_NN30NNLO_Zee_Mll10_40_MAXHTPTV280_E_CMS_BFilter.deriv.DAOD_HIGG8D1.e5421_e5984_s3126_r10201_r10210_p4133
 mc16_13TeV.364210.Sherpa_221_NN30NNLO_Ztt_Mll10_40_MAXHTPTV0_70_BVeto.deriv.DAOD_HIGG8D1.e5421_e5984_s3126_r10201_r10210_p4133
 mc16_13TeV.364211.Sherpa_221_NN30NNLO_Ztt_Mll10_40_MAXHTPTV0_70_BFilter.deriv.DAOD_HIGG8D1.e5421_e5984_s3126_r10201_r10210_p4133
 mc16_13TeV.364212.Sherpa_221_NN30NNLO_Ztt_Mll10_40_MAXHTPTV70_280_BVeto.deriv.DAOD_HIGG8D1.e5421_e5984_s3126_r10201_r10210_p4133
 mc16_13TeV.364213.Sherpa_221_NN30NNLO_Ztt_Mll10_40_MAXHTPTV70_280_BFilter.deriv.DAOD_HIGG8D1.e5421_e5984_s3126_r10201_r10210_p4133
 mc16_13TeV.364214.Sherpa_221_NN30NNLO_Ztt_Mll10_40_MAXHTPTV280_E_CMS_BVeto.deriv.DAOD_HIGG8D1.e5421_e5984_s3126_r10201_r10210_p4133
 mc16_13TeV.364215.Sherpa_221_NN30NNLO_Ztt_Mll10_40_MAXHTPTV280_E_CMS_BFilter.deriv.DAOD_HIGG8D1.e5421_e5984_s3126_r10201_r10210_p4133
 mc16_13TeV.364156.Sherpa_221_NNPDF30NNLO_Wmunu_MAXHTPTV0_70_CVetoBVeto.deriv.DAOD_HIGG8D1.e5340_s3126_r10201_r10210_p4133
 mc16_13TeV.364156.Sherpa_221_NNPDF30NNLO_Wmunu_MAXHTPTV0_70_CVetoBVeto.deriv.DAOD_HIGG8D1.e5340_e5984_s3126_s3136_r10201_r10210_p4133
 mc16_13TeV.364157.Sherpa_221_NNPDF30NNLO_Wmunu_MAXHTPTV0_70_CFilterBVeto.deriv.DAOD_HIGG8D1.e5340_e5984_s3126_s3136_r10201_r10210_p4133
 mc16_13TeV.364157.Sherpa_221_NNPDF30NNLO_Wmunu_MAXHTPTV0_70_CFilterBVeto.deriv.DAOD_HIGG8D1.e5340_s3126_r10201_r10210_p4133
 mc16_13TeV.364158.Sherpa_221_NNPDF30NNLO_Wmunu_MAXHTPTV0_70_BFilter.deriv.DAOD_HIGG8D1.e5340_e5984_s3126_s3136_r10201_r10210_p4133
 mc16_13TeV.364158.Sherpa_221_NNPDF30NNLO_Wmunu_MAXHTPTV0_70_BFilter.deriv.DAOD_HIGG8D1.e5340_s3126_r10201_r10210_p4133
 mc16_13TeV.364159.Sherpa_221_NNPDF30NNLO_Wmunu_MAXHTPTV70_140_CVetoBVeto.deriv.DAOD_HIGG8D1.e5340_s3126_r10201_r10210_p4133
 mc16_13TeV.364159.Sherpa_221_NNPDF30NNLO_Wmunu_MAXHTPTV70_140_CVetoBVeto.deriv.DAOD_HIGG8D1.e5340_e5984_s3126_r10201_r10210_p4133
 mc16_13TeV.364159.Sherpa_221_NNPDF30NNLO_Wmunu_MAXHTPTV70_140_CVetoBVeto.deriv.DAOD_HIGG8D1.e5340_e5984_s3126_s3136_r10201_r10210_p4133

mc16_13TeV.364160.Sherpa_221_NNPDF30NNLO_Wmunu_MAXHTPTV70_140_CFilterBVeto.deriv.DAOD_HIGG8D1.e5340_e5984_s3126_r10201_r10210_p4133
 mc16_13TeV.364160.Sherpa_221_NNPDF30NNLO_Wmunu_MAXHTPTV70_140_CFilterBVeto.deriv.DAOD_HIGG8D1.e5340_s3126_r10201_r10210_p4133
 mc16_13TeV.364161.Sherpa_221_NNPDF30NNLO_Wmunu_MAXHTPTV70_140_BFilter.deriv.DAOD_HIGG8D1.e5340_s3126_r10201_r10210_p4133
 mc16_13TeV.364161.Sherpa_221_NNPDF30NNLO_Wmunu_MAXHTPTV70_140_BFilter.deriv.DAOD_HIGG8D1.e5340_e5984_s3126_s3136_r10201_r10210_p4133
 mc16_13TeV.364162.Sherpa_221_NNPDF30NNLO_Wmunu_MAXHTPTV140_280_CVetoBVeto.deriv.DAOD_HIGG8D1.e5340_s3126_r10201_r10210_p4133
 mc16_13TeV.364162.Sherpa_221_NNPDF30NNLO_Wmunu_MAXHTPTV140_280_CVetoBVeto.deriv.DAOD_HIGG8D1.e5340_e5984_s3126_s3136_r10201_r10210_p4133
 mc16_13TeV.364163.Sherpa_221_NNPDF30NNLO_Wmunu_MAXHTPTV140_280_CFilterBVeto.deriv.DAOD_HIGG8D1.e5340_s3126_r10201_r10210_p4133
 mc16_13TeV.364163.Sherpa_221_NNPDF30NNLO_Wmunu_MAXHTPTV140_280_CFilterBVeto.deriv.DAOD_HIGG8D1.e5340_e5984_s3126_s3136_r10201_r10210_p4133
 mc16_13TeV.364163.Sherpa_221_NNPDF30NNLO_Wmunu_MAXHTPTV140_280_CFilterBVeto.deriv.DAOD_HIGG8D1.e5340_e5984_s3126_r10201_r10210_p4133
 mc16_13TeV.364164.Sherpa_221_NNPDF30NNLO_Wmunu_MAXHTPTV140_280_BFilter.deriv.DAOD_HIGG8D1.e5340_s3126_r10201_r10210_p4133
 mc16_13TeV.364164.Sherpa_221_NNPDF30NNLO_Wmunu_MAXHTPTV140_280_BFilter.deriv.DAOD_HIGG8D1.e5340_e5984_s3126_s3136_r10201_r10210_p4133
 mc16_13TeV.364165.Sherpa_221_NNPDF30NNLO_Wmunu_MAXHTPTV280_500_CVetoBVeto.deriv.DAOD_HIGG8D1.e5340_e5984_s3126_s3136_r10201_r10210_p4133
 mc16_13TeV.364166.Sherpa_221_NNPDF30NNLO_Wmunu_MAXHTPTV280_500_CFilterBVeto.deriv.DAOD_HIGG8D1.e5340_s3126_r10201_r10210_p4133
 mc16_13TeV.364166.Sherpa_221_NNPDF30NNLO_Wmunu_MAXHTPTV280_500_CFilterBVeto.deriv.DAOD_HIGG8D1.e5340_e5984_s3126_s3136_r10201_r10210_p4133
 mc16_13TeV.364167.Sherpa_221_NNPDF30NNLO_Wmunu_MAXHTPTV280_500_BFilter.deriv.DAOD_HIGG8D1.e5340_s3126_r10201_r10210_p4133
 mc16_13TeV.364167.Sherpa_221_NNPDF30NNLO_Wmunu_MAXHTPTV280_500_BFilter.deriv.DAOD_HIGG8D1.e5340_e5984_s3126_r10201_r10210_p4133
 mc16_13TeV.364168.Sherpa_221_NNPDF30NNLO_Wmunu_MAXHTPTV500_1000.deriv.DAOD_HIGG8D1.e5340_s3126_r10201_r10210_p4133
 mc16_13TeV.364168.Sherpa_221_NNPDF30NNLO_Wmunu_MAXHTPTV500_1000.deriv.DAOD_HIGG8D1.e5340_e5984_s3126_s3136_r10201_r10210_p4133
 mc16_13TeV.364169.Sherpa_221_NNPDF30NNLO_Wmunu_MAXHTPTV1000_E_CMS.deriv.DAOD_HIGG8D1.e5340_s3126_r10201_r10210_p4133
 mc16_13TeV.364169.Sherpa_221_NNPDF30NNLO_Wmunu_MAXHTPTV1000_E_CMS.deriv.DAOD_HIGG8D1.e5340_e5984_s3126_s3136_r10201_r10210_p4133
 mc16_13TeV.364170.Sherpa_221_NNPDF30NNLO_Wenu_MAXHTPTV0_70_CVetoBVeto.deriv.DAOD_HIGG8D1.e5340_e5984_s3126_s3136_r10201_r10210_p4133
 mc16_13TeV.364170.Sherpa_221_NNPDF30NNLO_Wenu_MAXHTPTV0_70_CVetoBVeto.deriv.DAOD_HIGG8D1.e5340_s3126_r10201_r10210_p4133
 mc16_13TeV.364171.Sherpa_221_NNPDF30NNLO_Wenu_MAXHTPTV0_70_CFilterBVeto.deriv.DAOD_HIGG8D1.e5340_e5984_s3126_r10201_r10210_p4133
 mc16_13TeV.364171.Sherpa_221_NNPDF30NNLO_Wenu_MAXHTPTV0_70_CFilterBVeto.deriv.DAOD_HIGG8D1.e5340_s3126_r10201_r10210_p4133
 mc16_13TeV.364171.Sherpa_221_NNPDF30NNLO_Wenu_MAXHTPTV0_70_CFilterBVeto.deriv.DAOD_HIGG8D1.e5340_e5984_s3126_s3136_r10201_r10210_p4133
 mc16_13TeV.364172.Sherpa_221_NNPDF30NNLO_Wenu_MAXHTPTV0_70_BFilter.deriv.DAOD_HIGG8D1.e5340_e5984_s3126_s3136_r10201_r10210_p4133
 mc16_13TeV.364172.Sherpa_221_NNPDF30NNLO_Wenu_MAXHTPTV0_70_BFilter.deriv.DAOD_HIGG8D1.e5340_e5984_s3126_r10201_r10210_p4133
 mc16_13TeV.364173.Sherpa_221_NNPDF30NNLO_Wenu_MAXHTPTV70_140_CVetoBVeto.deriv.DAOD_HIGG8D1.e5340_s3126_r10201_r10210_p4133
 mc16_13TeV.364173.Sherpa_221_NNPDF30NNLO_Wenu_MAXHTPTV70_140_CVetoBVeto.deriv.DAOD_HIGG8D1.e5340_e5984_s3126_r10201_r10210_p4133

mc16_13TeV.364174.Sherpa_221_NNPDF30NNLO_Wenu_MAXHTPTV70_140_CFilterBVeto.deriv.DAOD_HIGG8D1.e5340_s3126_r10201_r10210_p4133
 mc16_13TeV.364174.Sherpa_221_NNPDF30NNLO_Wenu_MAXHTPTV70_140_CFilterBVeto.deriv.DAOD_HIGG8D1.e5340_e5984_s3126_r10201_r10210_p4133
 mc16_13TeV.364175.Sherpa_221_NNPDF30NNLO_Wenu_MAXHTPTV70_140_BFilter.deriv.DAOD_HIGG8D1.e5340_e5984_s3126_r10201_r10210_p4133
 mc16_13TeV.364175.Sherpa_221_NNPDF30NNLO_Wenu_MAXHTPTV70_140_BFilter.deriv.DAOD_HIGG8D1.e5340_e5984_s3126_s3136_r10201_r10210_p4133
 mc16_13TeV.364175.Sherpa_221_NNPDF30NNLO_Wenu_MAXHTPTV70_140_BFilter.deriv.DAOD_HIGG8D1.e5340_s3126_r10201_r10210_p4133
 mc16_13TeV.364176.Sherpa_221_NNPDF30NNLO_Wenu_MAXHTPTV140_280_CVetoBVeto.deriv.DAOD_HIGG8D1.e5340_e5984_s3126_s3136_r10201_r10210_p4133
 mc16_13TeV.364176.Sherpa_221_NNPDF30NNLO_Wenu_MAXHTPTV140_280_CVetoBVeto.deriv.DAOD_HIGG8D1.e5340_s3126_r10201_r10210_p4133
 mc16_13TeV.364177.Sherpa_221_NNPDF30NNLO_Wenu_MAXHTPTV140_280_CFilterBVeto.deriv.DAOD_HIGG8D1.e5340_s3126_r10201_r10210_p4133
 mc16_13TeV.364177.Sherpa_221_NNPDF30NNLO_Wenu_MAXHTPTV140_280_CFilterBVeto.deriv.DAOD_HIGG8D1.e5340_e5984_s3126_s3136_r10201_r10210_p4133
 mc16_13TeV.364177.Sherpa_221_NNPDF30NNLO_Wenu_MAXHTPTV140_280_CFilterBVeto.deriv.DAOD_HIGG8D1.e5340_e5984_s3126_s3136_r10201_r10210_p4133
 mc16_13TeV.364177.Sherpa_221_NNPDF30NNLO_Wenu_MAXHTPTV140_280_CFilterBVeto.deriv.DAOD_HIGG8D1.e5340_e5984_s3126_r10201_r10210_p4133
 mc16_13TeV.364178.Sherpa_221_NNPDF30NNLO_Wenu_MAXHTPTV140_280_BFilter.deriv.DAOD_HIGG8D1.e5340_s3126_r10201_r10210_p4133
 mc16_13TeV.364178.Sherpa_221_NNPDF30NNLO_Wenu_MAXHTPTV140_280_BFilter.deriv.DAOD_HIGG8D1.e5340_s3126_r10201_r10210_p4133
 mc16_13TeV.364179.Sherpa_221_NNPDF30NNLO_Wenu_MAXHTPTV280_500_CVetoBVeto.deriv.DAOD_HIGG8D1.e5340_s3126_r10201_r10210_p4133
 mc16_13TeV.364179.Sherpa_221_NNPDF30NNLO_Wenu_MAXHTPTV280_500_CVetoBVeto.deriv.DAOD_HIGG8D1.e5340_e5984_s3126_r10201_r10210_p4133
 mc16_13TeV.364180.Sherpa_221_NNPDF30NNLO_Wenu_MAXHTPTV280_500_CFilterBVeto.deriv.DAOD_HIGG8D1.e5340_e5984_s3126_s3136_r10201_r10210_p4133
 mc16_13TeV.364180.Sherpa_221_NNPDF30NNLO_Wenu_MAXHTPTV280_500_CFilterBVeto.deriv.DAOD_HIGG8D1.e5340_s3126_r10201_r10210_p4133
 mc16_13TeV.364181.Sherpa_221_NNPDF30NNLO_Wenu_MAXHTPTV280_500_BFilter.deriv.DAOD_HIGG8D1.e5340_e5984_s3126_r10201_r10210_p4133
 mc16_13TeV.364181.Sherpa_221_NNPDF30NNLO_Wenu_MAXHTPTV280_500_BFilter.deriv.DAOD_HIGG8D1.e5340_s3126_r10201_r10210_p4133
 mc16_13TeV.364182.Sherpa_221_NNPDF30NNLO_Wenu_MAXHTPTV500_1000.deriv.DAOD_HIGG8D1.e5340_s3126_r10201_r10210_p4133
 mc16_13TeV.364182.Sherpa_221_NNPDF30NNLO_Wenu_MAXHTPTV500_1000.deriv.DAOD_HIGG8D1.e5340_e5984_s3126_s3136_r10201_r10210_p4133
 mc16_13TeV.364183.Sherpa_221_NNPDF30NNLO_Wenu_MAXHTPTV1000_E_CMS.deriv.DAOD_HIGG8D1.e5340_e5984_s3126_r10201_r10210_p4133
 mc16_13TeV.364184.Sherpa_221_NNPDF30NNLO_Wtaunu_MAXHTPTV0_70_CVetoBVeto.deriv.DAOD_HIGG8D1.e5340_e5984_s3126_r10201_r10210_p4133
 mc16_13TeV.364184.Sherpa_221_NNPDF30NNLO_Wtaunu_MAXHTPTV0_70_CVetoBVeto.deriv.DAOD_HIGG8D1.e5340_s3126_r10201_r10210_p4133
 mc16_13TeV.364185.Sherpa_221_NNPDF30NNLO_Wtaunu_MAXHTPTV0_70_CFilterBVeto.deriv.DAOD_HIGG8D1.e5340_e5984_s3126_r10201_r10210_p4133
 mc16_13TeV.364186.Sherpa_221_NNPDF30NNLO_Wtaunu_MAXHTPTV0_70_BFilter.deriv.DAOD_HIGG8D1.e5340_e5984_s3126_r10201_r10210_p4133
 mc16_13TeV.364187.Sherpa_221_NNPDF30NNLO_Wtaunu_MAXHTPTV70_140_CVetoBVeto.deriv.DAOD_HIGG8D1.e5340_e5984_s3126_r10201_r10210_p4133
 mc16_13TeV.364188.Sherpa_221_NNPDF30NNLO_Wtaunu_MAXHTPTV70_140_CFilterBVeto.deriv.DAOD_HIGG8D1.e5340_e5984_s3126_r10201_r10210_p4133
 mc16_13TeV.364189.Sherpa_221_NNPDF30NNLO_Wtaunu_MAXHTPTV70_140_BFilter.deriv.DAOD_HIGG8D1.e5340_s3126_r10201_r10210_p4133
 mc16_13TeV.364190.Sherpa_221_NNPDF30NNLO_Wtaunu_MAXHTPTV140_280_CVetoBVeto.deriv.DAOD_HIGG8D1.e5340_s3126_r10201_r10210_p4133
 mc16_13TeV.364190.Sherpa_221_NNPDF30NNLO_Wtaunu_MAXHTPTV140_280_CVetoBVeto.deriv.DAOD_HIGG8D1.e5340_e5984_s3126_s3136_r10201_r10210_p4133

mc16_13TeV.364191.Sherpa_221_NNPDF30NNLO_Wtaunu_MAXHTPTV140_280_CFilterBVeto.deriv.DAOD_HIGG8D1.e5340_e5984_s3126_s3136_r10201_r10210_p4133
mc16_13TeV.364191.Sherpa_221_NNPDF30NNLO_Wtaunu_MAXHTPTV140_280_CFilterBVeto.deriv.DAOD_HIGG8D1.e5340_s3126_r10201_r10210_p4133
mc16_13TeV.364192.Sherpa_221_NNPDF30NNLO_Wtaunu_MAXHTPTV140_280_BFilter.deriv.DAOD_HIGG8D1.e5340_e5984_s3126_r10201_r10210_p4133
mc16_13TeV.364193.Sherpa_221_NNPDF30NNLO_Wtaunu_MAXHTPTV280_500_CVetoBVeto.deriv.DAOD_HIGG8D1.e5340_e5984_s3126_r10201_r10210_p4133
mc16_13TeV.364193.Sherpa_221_NNPDF30NNLO_Wtaunu_MAXHTPTV280_500_CVetoBVeto.deriv.DAOD_HIGG8D1.e5340_e5984_s3126_s3136_r10201_r10210_p4133
mc16_13TeV.364194.Sherpa_221_NNPDF30NNLO_Wtaunu_MAXHTPTV280_500_CFilterBVeto.deriv.DAOD_HIGG8D1.e5340_e5984_s3126_r10201_r10210_p4133
mc16_13TeV.364194.Sherpa_221_NNPDF30NNLO_Wtaunu_MAXHTPTV280_500_CFilterBVeto.deriv.DAOD_HIGG8D1.e5340_s3126_r10201_r10210_p4133
mc16_13TeV.364194.Sherpa_221_NNPDF30NNLO_Wtaunu_MAXHTPTV280_500_BFilter.deriv.DAOD_HIGG8D1.e5340_e5984_s3126_r10201_r10210_p4133
mc16_13TeV.364194.Sherpa_221_NNPDF30NNLO_Wtaunu_MAXHTPTV280_500_BFilter.deriv.DAOD_HIGG8D1.e5340_s3126_s3136_r10201_r10210_p4133
mc16_13TeV.364195.Sherpa_221_NNPDF30NNLO_Wtaunu_MAXHTPTV280_500_BFilter.deriv.DAOD_HIGG8D1.e5340_e5984_s3126_r10201_r10210_p4133
mc16_13TeV.364195.Sherpa_221_NNPDF30NNLO_Wtaunu_MAXHTPTV280_500_BFilter.deriv.DAOD_HIGG8D1.e5340_s3126_r10201_r10210_p4133
mc16_13TeV.364196.Sherpa_221_NNPDF30NNLO_Wtaunu_MAXHTPTV500_1000.deriv.DAOD_HIGG8D1.e5340_e5984_s3126_s3136_r10201_r10210_p4133
mc16_13TeV.364196.Sherpa_221_NNPDF30NNLO_Wtaunu_MAXHTPTV500_1000.deriv.DAOD_HIGG8D1.e5340_s3126_r10201_r10210_p4133
mc16_13TeV.364197.Sherpa_221_NNPDF30NNLO_Wtaunu_MAXHTPTV1000_E_CMS.deriv.DAOD_HIGG8D1.e5340_e5984_s3126_r10201_r10210_p4133
mc16_13TeV.364500.Sherpa_222_NNPDF30NNLO_eegamma_pty_7_15.deriv.DAOD_HIGG8D1.e5928_e5984_s3126_r10201_r10210_p4133
mc16_13TeV.364501.Sherpa_222_NNPDF30NNLO_eegamma_pty_15_35.deriv.DAOD_HIGG8D1.e5928_e5984_s3126_r10201_r10210_p4133
mc16_13TeV.364502.Sherpa_222_NNPDF30NNLO_eegamma_pty_35_70.deriv.DAOD_HIGG8D1.e5928_e5984_s3126_r10201_r10210_p4133
mc16_13TeV.364503.Sherpa_222_NNPDF30NNLO_eegamma_pty_70_140.deriv.DAOD_HIGG8D1.e5928_e5984_s3126_r10201_r10210_p4133
mc16_13TeV.364504.Sherpa_222_NNPDF30NNLO_eegamma_pty_140_E_CMS.deriv.DAOD_HIGG8D1.e5928_e5984_s3126_r10201_r10210_p4133
mc16_13TeV.364505.Sherpa_222_NNPDF30NNLO_mumugamma_pty_7_15.deriv.DAOD_HIGG8D1.e5928_e5984_s3126_r10201_r10210_p4133
mc16_13TeV.364506.Sherpa_222_NNPDF30NNLO_mumugamma_pty_15_35.deriv.DAOD_HIGG8D1.e5928_e5984_s3126_r10201_r10210_p4133
mc16_13TeV.364507.Sherpa_222_NNPDF30NNLO_mumugamma_pty_35_70.deriv.DAOD_HIGG8D1.e5928_e5984_s3126_r10201_r10210_p4133
mc16_13TeV.364508.Sherpa_222_NNPDF30NNLO_mumugamma_pty_70_140.deriv.DAOD_HIGG8D1.e5928_e5984_s3126_r10201_r10210_p4133
mc16_13TeV.364509.Sherpa_222_NNPDF30NNLO_mumugamma_pty_140_E_CMS.deriv.DAOD_HIGG8D1.e5928_e5984_s3126_r10201_r10210_p4133
mc16_13TeV.364510.Sherpa_222_NNPDF30NNLO_tautaugamma_pty_7_15.deriv.DAOD_HIGG8D1.e5928_e5984_s3126_r10201_r10210_p4133
mc16_13TeV.364511.Sherpa_222_NNPDF30NNLO_tautaugamma_pty_15_35.deriv.DAOD_HIGG8D1.e5928_e5984_s3126_r10201_r10210_p4133
mc16_13TeV.364512.Sherpa_222_NNPDF30NNLO_tautaugamma_pty_35_70.deriv.DAOD_HIGG8D1.e5928_e5984_s3126_r10201_r10210_p4133
mc16_13TeV.364513.Sherpa_222_NNPDF30NNLO_tautaugamma_pty_70_140.deriv.DAOD_HIGG8D1.e5982_e5984_s3126_r10201_r10210_p4133
mc16_13TeV.364513.Sherpa_222_NNPDF30NNLO_tautaugamma_pty_70_140.deriv.DAOD_HIGG8D1.e5928_e5984_s3126_r10201_r10210_p4133
mc16_13TeV.364514.Sherpa_222_NNPDF30NNLO_tautaugamma_pty_140_E_CMS.deriv.DAOD_HIGG8D1.e5928_e5984_s3126_r10201_r10210_p4133
mc16_13TeV.364521.Sherpa_222_NNPDF30NNLO_enugamma_pty_7_15.deriv.DAOD_HIGG8D1.e5928_e5984_s3126_r10201_r10210_p4133
mc16_13TeV.364522.Sherpa_222_NNPDF30NNLO_enugamma_pty_15_35.deriv.DAOD_HIGG8D1.e5928_e5984_s3126_r10201_r10210_p4133

mc16_13TeV.364523.Sherpa_222_NNPDF30NNLO_enugamma_pty_35_70.deriv.DAOD_HIGG8D1.e5928_e5984_s3126_r10201_r10210_p4133
 mc16_13TeV.364524.Sherpa_222_NNPDF30NNLO_enugamma_pty_70_140.deriv.DAOD_HIGG8D1.e5928_e5984_s3126_r10201_r10210_p4133
 mc16_13TeV.364525.Sherpa_222_NNPDF30NNLO_enugamma_pty_140_E_CMS.deriv.DAOD_HIGG8D1.e5928_e5984_s3126_r10201_r10210_p4133
 mc16_13TeV.364526.Sherpa_222_NNPDF30NNLO_munugamma_pty_7_15.deriv.DAOD_HIGG8D1.e5928_e5984_s3126_r10201_r10210_p4133
 mc16_13TeV.364527.Sherpa_222_NNPDF30NNLO_munugamma_pty_15_35.deriv.DAOD_HIGG8D1.e5928_e5984_s3126_r10201_r10210_p4133
 mc16_13TeV.364528.Sherpa_222_NNPDF30NNLO_munugamma_pty_35_70.deriv.DAOD_HIGG8D1.e5928_e5984_s3126_r10201_r10210_p4133
 mc16_13TeV.364529.Sherpa_222_NNPDF30NNLO_munugamma_pty_70_140.deriv.DAOD_HIGG8D1.e5928_e5984_s3126_r10201_r10210_p4133
 mc16_13TeV.364530.Sherpa_222_NNPDF30NNLO_munugamma_pty_140_E_CMS.deriv.DAOD_HIGG8D1.e5928_e5984_s3126_r10201_r10210_p4133
 mc16_13TeV.364531.Sherpa_222_NNPDF30NNLO_taunugamma_pty_7_15.deriv.DAOD_HIGG8D1.e5928_e5984_s3126_r10201_r10210_p4133
 mc16_13TeV.364532.Sherpa_222_NNPDF30NNLO_taunugamma_pty_15_35.deriv.DAOD_HIGG8D1.e5928_e5984_s3126_r10201_r10210_p4133
 mc16_13TeV.364533.Sherpa_222_NNPDF30NNLO_taunugamma_pty_35_70.deriv.DAOD_HIGG8D1.e5928_e5984_s3126_r10201_r10210_p4133
 mc16_13TeV.364534.Sherpa_222_NNPDF30NNLO_taunugamma_pty_70_140.deriv.DAOD_HIGG8D1.e5928_e5984_s3126_r10201_r10210_p4133
 mc16_13TeV.364535.Sherpa_222_NNPDF30NNLO_taunugamma_pty_140_E_CMS.deriv.DAOD_HIGG8D1.e5928_e5984_s3126_r10201_r10210_p4133
 mc16_13TeV.410560.MadGraphPythia8EvtGen_A14_tZ_4fl_tchan_noAllHad.deriv.DAOD_HIGG8D1.e5803_e5984_s3126_r10201_r10210_p4133
 mc16_13TeV.410013.PowhegPythiaEvtGen_P2012_Wt_inclusive_top.deriv.DAOD_HIGG8D1.e3753_s3126_r10201_r10210_p4133
 mc16_13TeV.410014.PowhegPythiaEvtGen_P2012_Wt_inclusive_antitop.deriv.DAOD_HIGG8D1.e3753_s3126_r10201_r10210_p4133
 mc16_13TeV.410408.aMcAtNloPythia8EvtGen_tWZ_Ztoll_minDR1.deriv.DAOD_HIGG8D1.e6423_e5984_s3126_r10201_r10210_p4133
 mc16_13TeV.364242.Sherpa_222_NNPDF30NNLO_WWW_3l3v_EW6.deriv.DAOD_HIGG8D1.e5887_e5984_s3126_r10201_r10210_p4133
 mc16_13TeV.364243.Sherpa_222_NNPDF30NNLO_WWZ_4l2v_EW6.deriv.DAOD_HIGG8D1.e5887_e5984_s3126_r10201_r10210_p4133
 mc16_13TeV.364244.Sherpa_222_NNPDF30NNLO_WWZ_2l4v_EW6.deriv.DAOD_HIGG8D1.e5887_e5984_s3126_r10201_r10210_p4133
 mc16_13TeV.364245.Sherpa_222_NNPDF30NNLO_WZZ_5l1v_EW6.deriv.DAOD_HIGG8D1.e5887_e5984_s3126_r10201_r10210_p4133
 mc16_13TeV.364246.Sherpa_222_NNPDF30NNLO_WZZ_3l3v_EW6.deriv.DAOD_HIGG8D1.e5887_e5984_s3126_r10201_r10210_p4133
 mc16_13TeV.364247.Sherpa_222_NNPDF30NNLO_ZZZ_6l0v_EW6.deriv.DAOD_HIGG8D1.e5887_e5984_s3126_r10201_r10210_p4133
 mc16_13TeV.364248.Sherpa_222_NNPDF30NNLO_ZZZ_4l2v_EW6.deriv.DAOD_HIGG8D1.e5887_e5984_s3126_r10201_r10210_p4133
 mc16_13TeV.364249.Sherpa_222_NNPDF30NNLO_ZZZ_2l4v_EW6.deriv.DAOD_HIGG8D1.e5887_e5984_s3126_r10201_r10210_p4133
 mc16_13TeV.342284.Pythia8EvtGen_A14NNPDF23LO_WH125_inc.deriv.DAOD_HIGG8D1.e4246_e5984_s3126_r10201_r10210_p4133
 mc16_13TeV.342285.Pythia8EvtGen_A14NNPDF23LO_ZH125_inc.deriv.DAOD_HIGG8D1.e4246_e5984_s3126_r10201_r10210_p4133
 mc16_13TeV.341998.aMcAtNloHppEG_UEEE5_CTEQ6L1_CT10ME_tWH125_gamgam_yt_plus1.deriv.DAOD_HIGG8D1.e4394_e5984_s3126_r10201_r10210_p4133
 mc16_13TeV.410470.PhPy8EG_A14_ttbar_hdamp258p75_nonallhad.deriv.DAOD_HIGG8D1.e6337_e5984_s3126_r10201_r10210_p4133
 mc16_13TeV.410472.PhPy8EG_A14_ttbar_hdamp258p75_dil.deriv.DAOD_HIGG8D1.e6348_e5984_s3126_r10201_r10210_p4133
 mc16_13TeV.346343.PhPy8EG_A14NNPDF23_NNPDF30ME_ttH125_allhad.deriv.DAOD_HIGG8D1.e7148_e5984_s3126_r10201_r10210_p4133

mc16_13TeV.346344.PhPy8EG_A14NNPDF23_NNPDF30ME_ttH125_semilep.deriv.DAOD_HIGG8D1.e7148_e5984_a875_r10201_r10210_p4133

mc16_13TeV.346345.PhPy8EG_A14NNPDF23_NNPDF30ME_ttH125_dilep.deriv.DAOD_HIGG8D1.e7148_e5984_a875_r10201_r10210_p4133

mc16e:

mc16_13TeV.361605.PowhegPy8EG_CT10nloME_AZNLOCTEQ6L1_ZZvvvv_mll4.deriv.DAOD_HIGG8D1.e4054_e5984_s3126_r10724_r10726_p4133

mc16_13TeV.361602.PowhegPy8EG_CT10nloME_AZNLOCTEQ6L1_WZlvvv_mll4.deriv.DAOD_HIGG8D1.e4054_e5984_s3126_r10724_r10726_p4133

mc16_13TeV.361601.PowhegPy8EG_CT10nloME_AZNLOCTEQ6L1_WZlvl_l_mll4.deriv.DAOD_HIGG8D1.e4475_e5984_s3126_r10724_r10726_p4133

mc16_13TeV.361600.PowhegPy8EG_CT10nloME_AZNLOCTEQ6L1_WWlvvv.deriv.DAOD_HIGG8D1.e4616_e5984_s3126_r10724_r10726_p4133

mc16_13TeV.361603.PowhegPy8EG_CT10nloME_AZNLOCTEQ6L1_ZZllll_mll4.deriv.DAOD_HIGG8D1.e4475_e5984_s3126_r10724_r10726_p4133

mc16_13TeV.361604.PowhegPy8EG_CT10nloME_AZNLOCTEQ6L1_ZZvvll_mll4.deriv.DAOD_HIGG8D1.e4475_e5984_s3126_r10724_r10726_p4133

mc16_13TeV.364288.Sherpa_222_NNPDF30NNLO_llll_lowMllPtComplement.deriv.DAOD_HIGG8D1.e6096_s3126_r10724_p3983 mc16_13TeV.364287.Sherpa_222_NNPDF

mc16_13TeV.364285.Sherpa_222_NNPDF30NNLO_llvjj_EW6.deriv.DAOD_HIGG8D1.e6055_e5984_s3126_r10724_r10726_p3983

mc16_13TeV.364284.Sherpa_222_NNPDF30NNLO_llvjj_EW6.deriv.DAOD_HIGG8D1.e6055_s3126_r10724_p3983

mc16_13TeV.364283.Sherpa_222_NNPDF30NNLO_lllljj_EW6.deriv.DAOD_HIGG8D1.e6055_s3126_r10724_p3983

mc16_13TeV.364739.MGPy8EG_NNPDF30NLO_A14NNPDF23LO_lvlljjEW6_OFMinus.deriv.DAOD_HIGG8D1.e7421_e5984_s3126_r10724_r10726_p4133

mc16_13TeV.364742.MGPy8EG_NNPDF30NLO_A14NNPDF23LO_lvlljjEW6_SFPlus.deriv.DAOD_HIGG8D1.e7421_e5984_s3126_r10724_r10726_p4133

mc16_13TeV.364740.MGPy8EG_NNPDF30NLO_A14NNPDF23LO_lvlljjEW6_OFPlus.deriv.DAOD_HIGG8D1.e7421_e5984_s3126_r10724_r10726_p4133

mc16_13TeV.364741.MGPy8EG_NNPDF30NLO_A14NNPDF23LO_lvlljjEW6_SFMinus.deriv.DAOD_HIGG8D1.e7421_e5984_s3126_r10724_r10726_p4133

mc16_13TeV.364253.Sherpa_222_NNPDF30NNLO_llv.deriv.DAOD_HIGG8D1.e5916_e5984_s3126_r10724_r10726_p4133

mc16_13TeV.364250.Sherpa_222_NNPDF30NNLO_llll.deriv.DAOD_HIGG8D1.e5894_e5984_s3126_r10724_r10726_p4133

mc16_13TeV.364254.Sherpa_222_NNPDF30NNLO_llv.deriv.DAOD_HIGG8D1.e5916_e5984_s3126_r10724_r10726_p4133

mc16_13TeV.364255.Sherpa_222_NNPDF30NNLO_lvvv.deriv.DAOD_HIGG8D1.e5916_e5984_s3126_r10724_r10726_p4133

mc16_13TeV.410155.aMcAtNloPythia8EvtGen_MEN30NLO_A14N23LO_ttW.deriv.DAOD_HIGG8D1.e5070_e5984_s3126_r10724_r10726_p4133

mc16_13TeV.410156.aMcAtNloPythia8EvtGen_MEN30NLO_A14N23LO_ttZnuuu.deriv.DAOD_HIGG8D1.e5070_e5984_s3126_r10724_r10726_p4133

mc16_13TeV.410157.aMcAtNloPythia8EvtGen_MEN30NLO_A14N23LO_ttZqq.deriv.DAOD_HIGG8D1.e5070_e5984_s3126_r10724_r10726_p4133

mc16_13TeV.410218.aMcAtNloPythia8EvtGen_MEN30NLO_A14N23LO_ttee.deriv.DAOD_HIGG8D1.e5070_e5984_s3126_r10724_r10726_p4133

mc16_13TeV.410219.aMcAtNloPythia8EvtGen_MEN30NLO_A14N23LO_ttmumu.deriv.DAOD_HIGG8D1.e5070_e5984_s3126_r10724_r10726_p4133

mc16_13TeV.410220.aMcAtNloPythia8EvtGen_MEN30NLO_A14N23LO_ttautau.deriv.DAOD_HIGG8D1.e5070_e5984_s3126_r10724_r10726_p4133

mc16_13TeV.410276.aMcAtNloPythia8EvtGen_MEN30NLO_A14N23LO_ttee_mll_1_5.deriv.DAOD_HIGG8D1.e6087_e5984_s3126_r10724_r10726_p4133

mc16_13TeV.410277.aMcAtNloPythia8EvtGen_MEN30NLO_A14N23LO_ttmumu_mll_1_5.deriv.DAOD_HIGG8D1.e6087_e5984_s3126_r10724_r10726_p4133

mc16_13TeV.410278.aMcAtNloPythia8EvtGen_MEN30NLO_A14N23LO_ttautau_mll_1_5.deriv.DAOD_HIGG8D1.e6087_e5984_s3126_r10724_r10726_p4133

mc16_13TeV.410397.MadGraphPythia8EvtGen_ttbar_wbee_MEN30LO_A14N23LO.deriv.DAOD_HIGG8D1.e6086_e5984_s3126_r10724_r10726_p4133
 mc16_13TeV.410398.MadGraphPythia8EvtGen_ttbar_wbmumu_MEN30LO_A14N23LO.deriv.DAOD_HIGG8D1.e6086_e5984_s3126_r10724_r10726_p4133
 mc16_13TeV.410399.MadGraphPythia8EvtGen_ttbar_wbttau_MEN30LO_A14N23LO.deriv.DAOD_HIGG8D1.e6086_e5984_s3126_r10724_r10726_p4133
 mc16_13TeV.410658.PhPy8EG_A14_tchan_BW50_lept_top.deriv.DAOD_HIGG8D1.e6671_e5984_s3126_s3136_r10724_r10726_p4133
 mc16_13TeV.410659.PhPy8EG_A14_tchan_BW50_lept_antitop.deriv.DAOD_HIGG8D1.e6671_e5984_s3126_s3136_r10724_r10726_p4133
 mc16_13TeV.410644.PowhegPythia8EvtGen_A14_singletop_schan_lept_top.deriv.DAOD_HIGG8D1.e6527_e5984_s3126_r10724_r10726_p4133
 mc16_13TeV.410645.PowhegPythia8EvtGen_A14_singletop_schan_lept_antitop.deriv.DAOD_HIGG8D1.e6527_e5984_s3126_r10724_r10726_p4133
 mc16_13TeV.412063.aMcAtNloPythia8EvtGen_llq_NNPDF30_nf4_A14.deriv.DAOD_TOPQ1.e7054_e5984_s3126_r10724_r10726_p4174
 mc16_13TeV.304014.MadGraphPythia8EvtGen_A14NNPDF23_3top_SM.deriv.DAOD_HIGG8D1.e4324_e5984_s3126_r10724_r10726_p4133
 mc16_13TeV.410080.MadGraphPythia8EvtGen_A14NNPDF23_4topSM.deriv.DAOD_HIGG8D1.e4111_e5984_s3126_r10724_r10726_p4133
 mc16_13TeV.410081.MadGraphPythia8EvtGen_A14NNPDF23_ttbarWW.deriv.DAOD_HIGG8D1.e4111_e5984_s3126_r10724_r10726_p4133
 mc16_13TeV.364100.Sherpa_221_NNPDF30NNLO_Zmumu_MAXHTPTV0_70_CVetoBVeto.deriv.DAOD_HIGG8D1.e5271_e5984_s3126_s3136_r10724_r10726_p4133
 mc16_13TeV.364100.Sherpa_221_NNPDF30NNLO_Zmumu_MAXHTPTV0_70_CVetoBVeto.deriv.DAOD_HIGG8D1.e5271_e5984_s3126_r10724_r10726_p4133
 mc16_13TeV.364101.Sherpa_221_NNPDF30NNLO_Zmumu_MAXHTPTV0_70_CFilterBVeto.deriv.DAOD_HIGG8D1.e5271_e5984_s3126_r10724_r10726_p4133
 mc16_13TeV.364102.Sherpa_221_NNPDF30NNLO_Zmumu_MAXHTPTV0_70_BFilter.deriv.DAOD_HIGG8D1.e5271_e5984_s3126_s3136_r10724_r10726_p4133
 mc16_13TeV.364102.Sherpa_221_NNPDF30NNLO_Zmumu_MAXHTPTV0_70_BFilter.deriv.DAOD_HIGG8D1.e5271_e5984_s3126_r10724_r10726_p4133
 mc16_13TeV.364103.Sherpa_221_NNPDF30NNLO_Zmumu_MAXHTPTV70_140_CVetoBVeto.deriv.DAOD_HIGG8D1.e5271_e5984_s3126_r10724_r10726_p4133
 mc16_13TeV.364103.Sherpa_221_NNPDF30NNLO_Zmumu_MAXHTPTV70_140_CVetoBVeto.deriv.DAOD_HIGG8D1.e5271_e5984_s3126_s3136_r10724_r10726_p4133
 mc16_13TeV.364104.Sherpa_221_NNPDF30NNLO_Zmumu_MAXHTPTV70_140_CFilterBVeto.deriv.DAOD_HIGG8D1.e5271_e5984_s3126_r10724_r10726_p4133
 mc16_13TeV.364104.Sherpa_221_NNPDF30NNLO_Zmumu_MAXHTPTV70_140_CFilterBVeto.deriv.DAOD_HIGG8D1.e5271_e5984_s3126_s3136_r10724_r10726_p4133
 mc16_13TeV.364106.Sherpa_221_NNPDF30NNLO_Zmumu_MAXHTPTV140_280_CVetoBVeto.deriv.DAOD_HIGG8D1.e5271_e5984_s3126_s3136_r10724_r10726_p4133
 mc16_13TeV.364107.Sherpa_221_NNPDF30NNLO_Zmumu_MAXHTPTV140_280_CFilterBVeto.deriv.DAOD_HIGG8D1.e5271_e5984_s3126_r10724_r10726_p4133
 mc16_13TeV.364107.Sherpa_221_NNPDF30NNLO_Zmumu_MAXHTPTV140_280_CFilterBVeto.deriv.DAOD_HIGG8D1.e5271_e5984_s3126_s3136_r10724_r10726_p4133
 mc16_13TeV.364108.Sherpa_221_NNPDF30NNLO_Zmumu_MAXHTPTV140_280_BFilter.deriv.DAOD_HIGG8D1.e5271_e5984_s3126_r10724_r10726_p4133
 mc16_13TeV.364109.Sherpa_221_NNPDF30NNLO_Zmumu_MAXHTPTV280_500_CVetoBVeto.deriv.DAOD_HIGG8D1.e5271_e5984_s3126_r10724_r10726_p4133
 mc16_13TeV.364110.Sherpa_221_NNPDF30NNLO_Zmumu_MAXHTPTV280_500_CFilterBVeto.deriv.DAOD_HIGG8D1.e5271_e5984_s3126_r10724_r10726_p4133
 mc16_13TeV.364110.Sherpa_221_NNPDF30NNLO_Zmumu_MAXHTPTV280_500_CFilterBVeto.deriv.DAOD_HIGG8D1.e5271_e5984_s3126_s3136_r10724_r10726_p4133
 mc16_13TeV.364111.Sherpa_221_NNPDF30NNLO_Zmumu_MAXHTPTV280_500_BFilter.deriv.DAOD_HIGG8D1.e5271_e5984_s3126_s3136_r10724_r10726_p4133
 mc16_13TeV.364111.Sherpa_221_NNPDF30NNLO_Zmumu_MAXHTPTV280_500_BFilter.deriv.DAOD_HIGG8D1.e5271_e5984_s3126_r10724_r10726_p4133
 mc16_13TeV.364112.Sherpa_221_NNPDF30NNLO_Zmumu_MAXHTPTV500_1000.deriv.DAOD_HIGG8D1.e5271_e5984_s3126_r10724_r10726_p4133

mc16_13TeV.364113.Sherpa_221_NNPDF30NNLO_Zmumu_MAXHTPTV1000_E_CMS.deriv.DAOD_HIGG8D1.e5271_e5984_s3126_r10724_r10726_p4133
 mc16_13TeV.364113.Sherpa_221_NNPDF30NNLO_Zmumu_MAXHTPTV1000_E_CMS.deriv.DAOD_HIGG8D1.e5271_e5984_s3126_s3136_r10724_r10726_p4133
 mc16_13TeV.364114.Sherpa_221_NNPDF30NNLO_Zee_MAXHTPTV0_70_CVetoBVeto.deriv.DAOD_HIGG8D1.e5299_e5984_s3126_s3136_r10724_r10726_p4133
 mc16_13TeV.364114.Sherpa_221_NNPDF30NNLO_Zee_MAXHTPTV0_70_CVetoBVeto.deriv.DAOD_HIGG8D1.e5299_e5984_s3126_r10724_r10726_p4133
 mc16_13TeV.364115.Sherpa_221_NNPDF30NNLO_Zee_MAXHTPTV0_70_CFilterBVeto.deriv.DAOD_HIGG8D1.e5299_e5984_s3126_s3136_r10724_r10726_p4133
 mc16_13TeV.364115.Sherpa_221_NNPDF30NNLO_Zee_MAXHTPTV0_70_CFilterBVeto.deriv.DAOD_HIGG8D1.e5299_e5984_s3126_r10724_r10726_p4133
 mc16_13TeV.364116.Sherpa_221_NNPDF30NNLO_Zee_MAXHTPTV0_70_BFilter.deriv.DAOD_HIGG8D1.e5299_e5984_s3126_r10724_r10726_p4133
 mc16_13TeV.364117.Sherpa_221_NNPDF30NNLO_Zee_MAXHTPTV70_140_CVetoBVeto.deriv.DAOD_HIGG8D1.e5299_e5984_s3126_s3136_r10724_r10726_p4133
 mc16_13TeV.364117.Sherpa_221_NNPDF30NNLO_Zee_MAXHTPTV70_140_CVetoBVeto.deriv.DAOD_HIGG8D1.e5299_e5984_s3126_r10724_r10726_p4133
 mc16_13TeV.364118.Sherpa_221_NNPDF30NNLO_Zee_MAXHTPTV70_140_CFilterBVeto.deriv.DAOD_HIGG8D1.e5299_e5984_s3126_s3136_r10724_r10726_p4133
 mc16_13TeV.364118.Sherpa_221_NNPDF30NNLO_Zee_MAXHTPTV70_140_CFilterBVeto.deriv.DAOD_HIGG8D1.e5299_e5984_s3126_r10724_r10726_p4133
 mc16_13TeV.364119.Sherpa_221_NNPDF30NNLO_Zee_MAXHTPTV70_140_BFilter.deriv.DAOD_HIGG8D1.e5299_e5984_s3126_r10724_r10726_p4133
 mc16_13TeV.364120.Sherpa_221_NNPDF30NNLO_Zee_MAXHTPTV140_280_CVetoBVeto.deriv.DAOD_HIGG8D1.e5299_e5984_s3126_r10724_r10726_p4133
 mc16_13TeV.364121.Sherpa_221_NNPDF30NNLO_Zee_MAXHTPTV140_280_CFilterBVeto.deriv.DAOD_HIGG8D1.e5299_e5984_s3126_r10724_r10726_p4133
 mc16_13TeV.364122.Sherpa_221_NNPDF30NNLO_Zee_MAXHTPTV140_280_BFilter.deriv.DAOD_HIGG8D1.e5299_e5984_s3126_s3136_r10724_r10726_p4133
 mc16_13TeV.364122.Sherpa_221_NNPDF30NNLO_Zee_MAXHTPTV140_280_BFilter.deriv.DAOD_HIGG8D1.e5299_e5984_s3126_r10724_r10726_p4133
 mc16_13TeV.364123.Sherpa_221_NNPDF30NNLO_Zee_MAXHTPTV280_500_CVetoBVeto.deriv.DAOD_HIGG8D1.e5299_e5984_s3126_r10724_r10726_p4133
 mc16_13TeV.364124.Sherpa_221_NNPDF30NNLO_Zee_MAXHTPTV280_500_CFilterBVeto.deriv.DAOD_HIGG8D1.e5299_e5984_s3126_r10724_r10726_p4133
 mc16_13TeV.364125.Sherpa_221_NNPDF30NNLO_Zee_MAXHTPTV280_500_BFilter.deriv.DAOD_HIGG8D1.e5299_e5984_s3126_s3136_r10724_r10726_p4133
 mc16_13TeV.364125.Sherpa_221_NNPDF30NNLO_Zee_MAXHTPTV280_500_BFilter.deriv.DAOD_HIGG8D1.e5299_e5984_s3126_r10724_r10726_p4133
 mc16_13TeV.364126.Sherpa_221_NNPDF30NNLO_Zee_MAXHTPTV500_1000.deriv.DAOD_HIGG8D1.e5299_e5984_s3126_r10724_r10726_p4133
 mc16_13TeV.364126.Sherpa_221_NNPDF30NNLO_Zee_MAXHTPTV500_1000.deriv.DAOD_HIGG8D1.e5299_e5984_s3126_s3136_r10724_r10726_p4133
 mc16_13TeV.364127.Sherpa_221_NNPDF30NNLO_Zee_MAXHTPTV1000_E_CMS.deriv.DAOD_HIGG8D1.e5299_e5984_s3126_s3136_r10724_r10726_p4133
 mc16_13TeV.364127.Sherpa_221_NNPDF30NNLO_Zee_MAXHTPTV1000_E_CMS.deriv.DAOD_HIGG8D1.e5299_e5984_s3126_r10724_r10726_p4133
 mc16_13TeV.364128.Sherpa_221_NNPDF30NNLO_Ztautau_MAXHTPTV0_70_CVetoBVeto.deriv.DAOD_HIGG8D1.e5307_e5984_s3126_s3136_r10724_r10726_p4133
 mc16_13TeV.364128.Sherpa_221_NNPDF30NNLO_Ztautau_MAXHTPTV0_70_CVetoBVeto.deriv.DAOD_HIGG8D1.e5307_e5984_s3126_r10724_r10726_p4133
 mc16_13TeV.364129.Sherpa_221_NNPDF30NNLO_Ztautau_MAXHTPTV0_70_CFilterBVeto.deriv.DAOD_HIGG8D1.e5307_e5984_s3126_r10724_r10726_p4133
 mc16_13TeV.364129.Sherpa_221_NNPDF30NNLO_Ztautau_MAXHTPTV0_70_CFilterBVeto.deriv.DAOD_HIGG8D1.e5307_e5984_s3126_s3136_r10724_r10726_p4133
 mc16_13TeV.364130.Sherpa_221_NNPDF30NNLO_Ztautau_MAXHTPTV0_70_BFilter.deriv.DAOD_HIGG8D1.e5307_e5984_s3126_s3136_r10724_r10726_p4133
 mc16_13TeV.364130.Sherpa_221_NNPDF30NNLO_Ztautau_MAXHTPTV0_70_BFilter.deriv.DAOD_HIGG8D1.e5307_e5984_s3126_r10724_r10726_p4133
 mc16_13TeV.364131.Sherpa_221_NNPDF30NNLO_Ztautau_MAXHTPTV70_140_CVetoBVeto.deriv.DAOD_HIGG8D1.e5307_e5984_s3126_r10724_r10726_p4133

mc16_13TeV.364132.Sherpa_221_NNPDF30NNLO_Ztautau_MAXHTPTV70_140_CFilterBVeto.deriv.DAOD_HIGG8D1.e5307_e5984_s3126_r10724_r10726_p4133
 mc16_13TeV.364132.Sherpa_221_NNPDF30NNLO_Ztautau_MAXHTPTV70_140_CFilterBVeto.deriv.DAOD_HIGG8D1.e5307_e5984_s3126_s3136_r10724_r10726_p4133
 mc16_13TeV.364133.Sherpa_221_NNPDF30NNLO_Ztautau_MAXHTPTV70_140_BFilter.deriv.DAOD_HIGG8D1.e5307_e5984_s3126_r10724_r10726_p4133
 mc16_13TeV.364134.Sherpa_221_NNPDF30NNLO_Ztautau_MAXHTPTV140_280_CVetoBVeto.deriv.DAOD_HIGG8D1.e5307_e5984_s3126_r10724_r10726_p4133
 mc16_13TeV.364135.Sherpa_221_NNPDF30NNLO_Ztautau_MAXHTPTV140_280_CFilterBVeto.deriv.DAOD_HIGG8D1.e5307_e5984_s3126_r10724_r10726_p4133
 mc16_13TeV.364135.Sherpa_221_NNPDF30NNLO_Ztautau_MAXHTPTV140_280_CFilterBVeto.deriv.DAOD_HIGG8D1.e5307_e5984_s3126_s3136_r10724_r10726_p4133
 mc16_13TeV.364136.Sherpa_221_NNPDF30NNLO_Ztautau_MAXHTPTV140_280_BFilter.deriv.DAOD_HIGG8D1.e5307_e5984_s3126_r10724_r10726_p4133
 mc16_13TeV.364137.Sherpa_221_NNPDF30NNLO_Ztautau_MAXHTPTV280_500_CVetoBVeto.deriv.DAOD_HIGG8D1.e5307_e5984_s3126_r10724_r10726_p4133
 mc16_13TeV.364138.Sherpa_221_NNPDF30NNLO_Ztautau_MAXHTPTV280_500_CFilterBVeto.deriv.DAOD_HIGG8D1.e5313_e5984_s3126_s3136_r10724_r10726_p4133
 mc16_13TeV.364138.Sherpa_221_NNPDF30NNLO_Ztautau_MAXHTPTV280_500_CFilterBVeto.deriv.DAOD_HIGG8D1.e5313_e5984_s3126_r10724_r10726_p4133
 mc16_13TeV.364139.Sherpa_221_NNPDF30NNLO_Ztautau_MAXHTPTV280_500_BFilter.deriv.DAOD_HIGG8D1.e5313_e5984_s3126_r10724_r10726_p4133
 mc16_13TeV.364139.Sherpa_221_NNPDF30NNLO_Ztautau_MAXHTPTV280_500_BFilter.deriv.DAOD_HIGG8D1.e5313_e5984_s3126_s3136_r10724_r10726_p4133
 mc16_13TeV.364140.Sherpa_221_NNPDF30NNLO_Ztautau_MAXHTPTV500_1000.deriv.DAOD_HIGG8D1.e5307_e5984_s3126_r10724_r10726_p4133
 mc16_13TeV.364140.Sherpa_221_NNPDF30NNLO_Ztautau_MAXHTPTV500_1000.deriv.DAOD_HIGG8D1.e5307_e5984_s3126_s3136_r10724_r10726_p4133
 mc16_13TeV.364141.Sherpa_221_NNPDF30NNLO_Ztautau_MAXHTPTV1000_E_CMS.deriv.DAOD_HIGG8D1.e5307_e5984_s3126_s3136_r10724_r10726_p4133
 mc16_13TeV.364141.Sherpa_221_NNPDF30NNLO_Ztautau_MAXHTPTV1000_E_CMS.deriv.DAOD_HIGG8D1.e5307_e5984_s3126_r10724_r10726_p4133
 mc16_13TeV.364198.Sherpa_221_NN30NNLO_Zmm_Mll10_40_MAXHTPTV0_70_BVeto.deriv.DAOD_HIGG8D1.e5421_e5984_s3126_r10724_r10726_p4133
 mc16_13TeV.364199.Sherpa_221_NN30NNLO_Zmm_Mll10_40_MAXHTPTV0_70_BFilter.deriv.DAOD_HIGG8D1.e5421_e5984_s3126_r10724_r10726_p4133
 mc16_13TeV.364200.Sherpa_221_NN30NNLO_Zmm_Mll10_40_MAXHTPTV70_280_BVeto.deriv.DAOD_HIGG8D1.e5421_e5984_s3126_r10724_r10726_p4133
 mc16_13TeV.364201.Sherpa_221_NN30NNLO_Zmm_Mll10_40_MAXHTPTV70_280_BFilter.deriv.DAOD_HIGG8D1.e5421_e5984_s3126_r10724_r10726_p4133
 mc16_13TeV.364202.Sherpa_221_NN30NNLO_Zmm_Mll10_40_MAXHTPTV280_E_CMS_BVeto.deriv.DAOD_HIGG8D1.e5421_e5984_s3126_r10724_r10726_p4133
 mc16_13TeV.364203.Sherpa_221_NN30NNLO_Zmm_Mll10_40_MAXHTPTV280_E_CMS_BFilter.deriv.DAOD_HIGG8D1.e5421_e5984_s3126_r10724_r10726_p4133
 mc16_13TeV.364204.Sherpa_221_NN30NNLO_Zee_Mll10_40_MAXHTPTV0_70_BVeto.deriv.DAOD_HIGG8D1.e5421_e5984_s3126_r10724_r10726_p4133
 mc16_13TeV.364205.Sherpa_221_NN30NNLO_Zee_Mll10_40_MAXHTPTV0_70_BFilter.deriv.DAOD_HIGG8D1.e5421_e5984_s3126_r10724_r10726_p4133
 mc16_13TeV.364206.Sherpa_221_NN30NNLO_Zee_Mll10_40_MAXHTPTV70_280_BVeto.deriv.DAOD_HIGG8D1.e5421_e5984_s3126_r10724_r10726_p4133
 mc16_13TeV.364207.Sherpa_221_NN30NNLO_Zee_Mll10_40_MAXHTPTV70_280_BFilter.deriv.DAOD_HIGG8D1.e5421_e5984_s3126_r10724_r10726_p4133
 mc16_13TeV.364208.Sherpa_221_NN30NNLO_Zee_Mll10_40_MAXHTPTV280_E_CMS_BVeto.deriv.DAOD_HIGG8D1.e5421_e5984_s3126_r10724_r10726_p4133
 mc16_13TeV.364209.Sherpa_221_NN30NNLO_Zee_Mll10_40_MAXHTPTV280_E_CMS_BFilter.deriv.DAOD_HIGG8D1.e5421_e5984_s3126_r10724_r10726_p4133
 mc16_13TeV.364210.Sherpa_221_NN30NNLO_Ztt_Mll10_40_MAXHTPTV0_70_BVeto.deriv.DAOD_HIGG8D1.e5421_e5984_s3126_r10724_r10726_p4133
 mc16_13TeV.364211.Sherpa_221_NN30NNLO_Ztt_Mll10_40_MAXHTPTV0_70_BFilter.deriv.DAOD_HIGG8D1.e5421_e5984_s3126_r10724_r10726_p4133
 mc16_13TeV.364212.Sherpa_221_NN30NNLO_Ztt_Mll10_40_MAXHTPTV70_280_BVeto.deriv.DAOD_HIGG8D1.e5421_e5984_s3126_r10724_r10726_p4133

mc16_13TeV.364213.Sherpa_221_NN30NNLO_Ztt_Mll10_40_MAXHTPTV70_280_BFilter.deriv.DAOD_HIGG8D1.e5421_e5984_s3126_r10724_r10726_p4133
 mc16_13TeV.364214.Sherpa_221_NN30NNLO_Ztt_Mll10_40_MAXHTPTV280_E_CMS_BVeto.deriv.DAOD_HIGG8D1.e5421_e5984_s3126_r10724_r10726_p4133
 mc16_13TeV.364215.Sherpa_221_NN30NNLO_Ztt_Mll10_40_MAXHTPTV280_E_CMS_BFilter.deriv.DAOD_HIGG8D1.e5421_e5984_s3126_r10724_r10726_p4133
 mc16_13TeV.364156.Sherpa_221_NNPDF30NNLO_Wmunu_MAXHTPTV0_70_CVetoBVeto.deriv.DAOD_HIGG8D1.e5340_e5984_s3126_r10724_r10726_p4133
 mc16_13TeV.364157.Sherpa_221_NNPDF30NNLO_Wmunu_MAXHTPTV0_70_CFilterBVeto.deriv.DAOD_HIGG8D1.e5340_e5984_s3126_r10724_r10726_p4133
 mc16_13TeV.364158.Sherpa_221_NNPDF30NNLO_Wmunu_MAXHTPTV0_70_BFilter.deriv.DAOD_HIGG8D1.e5340_e5984_s3126_s3136_r10724_r10726_p4133
 mc16_13TeV.364158.Sherpa_221_NNPDF30NNLO_Wmunu_MAXHTPTV0_70_BFilter.deriv.DAOD_HIGG8D1.e5340_e5984_s3126_r10724_r10726_p4133
 mc16_13TeV.364159.Sherpa_221_NNPDF30NNLO_Wmunu_MAXHTPTV70_140_CVetoBVeto.deriv.DAOD_HIGG8D1.e5340_e5984_s3126_s3136_r10724_r10726_p4133
 mc16_13TeV.364160.Sherpa_221_NNPDF30NNLO_Wmunu_MAXHTPTV70_140_CFilterBVeto.deriv.DAOD_HIGG8D1.e5340_e5984_s3126_s3136_r10724_r10726_p4133
 mc16_13TeV.364160.Sherpa_221_NNPDF30NNLO_Wmunu_MAXHTPTV70_140_CFilterBVeto.deriv.DAOD_HIGG8D1.e5340_e5984_s3126_r10724_r10726_p4133
 mc16_13TeV.364161.Sherpa_221_NNPDF30NNLO_Wmunu_MAXHTPTV70_140_BFilter.deriv.DAOD_HIGG8D1.e5340_e5984_s3126_r10724_r10726_p4133
 mc16_13TeV.364162.Sherpa_221_NNPDF30NNLO_Wmunu_MAXHTPTV140_280_CVetoBVeto.deriv.DAOD_HIGG8D1.e5340_e5984_s3126_r10724_r10726_p4133
 mc16_13TeV.364163.Sherpa_221_NNPDF30NNLO_Wmunu_MAXHTPTV140_280_CFilterBVeto.deriv.DAOD_HIGG8D1.e5340_e5984_s3126_s3136_r10724_r10726_p4133
 mc16_13TeV.364163.Sherpa_221_NNPDF30NNLO_Wmunu_MAXHTPTV140_280_CFilterBVeto.deriv.DAOD_HIGG8D1.e5340_e5984_s3126_r10724_r10726_p4133
 mc16_13TeV.364164.Sherpa_221_NNPDF30NNLO_Wmunu_MAXHTPTV140_280_BFilter.deriv.DAOD_HIGG8D1.e5340_e5984_s3126_r10724_r10726_p4133
 mc16_13TeV.364165.Sherpa_221_NNPDF30NNLO_Wmunu_MAXHTPTV280_500_CVetoBVeto.deriv.DAOD_HIGG8D1.e5340_e5984_s3126_r10724_r10726_p4133
 mc16_13TeV.364165.Sherpa_221_NNPDF30NNLO_Wmunu_MAXHTPTV280_500_CVetoBVeto.deriv.DAOD_HIGG8D1.e5340_e5984_s3126_s3136_r10724_r10726_p4133
 mc16_13TeV.364166.Sherpa_221_NNPDF30NNLO_Wmunu_MAXHTPTV280_500_CFilterBVeto.deriv.DAOD_HIGG8D1.e5340_e5984_s3126_s3136_r10724_r10726_p4133
 mc16_13TeV.364166.Sherpa_221_NNPDF30NNLO_Wmunu_MAXHTPTV280_500_CFilterBVeto.deriv.DAOD_HIGG8D1.e5340_e5984_s3126_r10724_r10726_p4133
 mc16_13TeV.364167.Sherpa_221_NNPDF30NNLO_Wmunu_MAXHTPTV280_500_BFilter.deriv.DAOD_HIGG8D1.e5340_e5984_s3126_r10724_r10726_p4133
 mc16_13TeV.364167.Sherpa_221_NNPDF30NNLO_Wmunu_MAXHTPTV280_500_BFilter.deriv.DAOD_HIGG8D1.e5340_e5984_s3126_s3136_r10724_r10726_p4133
 mc16_13TeV.364168.Sherpa_221_NNPDF30NNLO_Wmunu_MAXHTPTV500_1000.deriv.DAOD_HIGG8D1.e5340_e5984_s3126_r10724_r10726_p4133
 mc16_13TeV.364168.Sherpa_221_NNPDF30NNLO_Wmunu_MAXHTPTV500_1000.deriv.DAOD_HIGG8D1.e5340_e5984_s3126_s3136_r10724_r10726_p4133
 mc16_13TeV.364169.Sherpa_221_NNPDF30NNLO_Wmunu_MAXHTPTV1000_E_CMS.deriv.DAOD_HIGG8D1.e5340_e5984_s3126_s3136_r10724_r10726_p4133
 mc16_13TeV.364169.Sherpa_221_NNPDF30NNLO_Wmunu_MAXHTPTV1000_E_CMS.deriv.DAOD_HIGG8D1.e5340_e5984_s3126_r10724_r10726_p4133
 mc16_13TeV.364170.Sherpa_221_NNPDF30NNLO_Wenu_MAXHTPTV0_70_CVetoBVeto.deriv.DAOD_HIGG8D1.e5340_e5984_s3126_r10724_r10726_p4133
 mc16_13TeV.364171.Sherpa_221_NNPDF30NNLO_Wenu_MAXHTPTV0_70_CFilterBVeto.deriv.DAOD_HIGG8D1.e5340_e5984_s3126_r10724_r10726_p4133
 mc16_13TeV.364172.Sherpa_221_NNPDF30NNLO_Wenu_MAXHTPTV0_70_BFilter.deriv.DAOD_HIGG8D1.e5340_e5984_s3126_r10724_r10726_p4133
 mc16_13TeV.364173.Sherpa_221_NNPDF30NNLO_Wenu_MAXHTPTV70_140_CVetoBVeto.deriv.DAOD_HIGG8D1.e5340_e5984_s3126_s3136_r10724_r10726_p4133
 mc16_13TeV.364174.Sherpa_221_NNPDF30NNLO_Wenu_MAXHTPTV70_140_CFilterBVeto.deriv.DAOD_HIGG8D1.e5340_e5984_s3126_r10724_r10726_p4133
 mc16_13TeV.364175.Sherpa_221_NNPDF30NNLO_Wenu_MAXHTPTV70_140_BFilter.deriv.DAOD_HIGG8D1.e5340_e5984_s3126_s3136_r10724_r10726_p4133

mc16_13TeV.364176.Sherpa_221_NNPDF30NNLO_Wenu_MAXHTPTV140_280_CVetoBVeto.deriv.DAOD_HIGG8D1.e5340_e5984_s3126_r10724_r10726_p4133
 mc16_13TeV.364177.Sherpa_221_NNPDF30NNLO_Wenu_MAXHTPTV140_280_CFilterBVeto.deriv.DAOD_HIGG8D1.e5340_e5984_s3126_r10724_r10726_p4133
 mc16_13TeV.364177.Sherpa_221_NNPDF30NNLO_Wenu_MAXHTPTV140_280_CFilterBVeto.deriv.DAOD_HIGG8D1.e5340_e5984_s3126_s3136_r10724_r10726_p4133
 mc16_13TeV.364178.Sherpa_221_NNPDF30NNLO_Wenu_MAXHTPTV140_280_BFilter.deriv.DAOD_HIGG8D1.e5340_e5984_s3126_r10724_r10726_p4133
 mc16_13TeV.364179.Sherpa_221_NNPDF30NNLO_Wenu_MAXHTPTV280_500_CVetoBVeto.deriv.DAOD_HIGG8D1.e5340_e5984_s3126_r10724_r10726_p4133
 mc16_13TeV.364179.Sherpa_221_NNPDF30NNLO_Wenu_MAXHTPTV280_500_CVetoBVeto.deriv.DAOD_HIGG8D1.e5340_e5984_s3126_s3136_r10724_r10726_p4133
 mc16_13TeV.364180.Sherpa_221_NNPDF30NNLO_Wenu_MAXHTPTV280_500_CFilterBVeto.deriv.DAOD_HIGG8D1.e5340_e5984_s3126_s3136_r10724_r10726_p4133
 mc16_13TeV.364180.Sherpa_221_NNPDF30NNLO_Wenu_MAXHTPTV280_500_CFilterBVeto.deriv.DAOD_HIGG8D1.e5340_e5984_s3126_r10724_r10726_p4133
 mc16_13TeV.364181.Sherpa_221_NNPDF30NNLO_Wenu_MAXHTPTV280_500_BFilter.deriv.DAOD_HIGG8D1.e5340_e5984_s3126_s3136_r10724_r10726_p4133
 mc16_13TeV.364181.Sherpa_221_NNPDF30NNLO_Wenu_MAXHTPTV280_500_BFilter.deriv.DAOD_HIGG8D1.e5340_e5984_s3126_r10724_r10726_p4133
 mc16_13TeV.364182.Sherpa_221_NNPDF30NNLO_Wenu_MAXHTPTV500_1000.deriv.DAOD_HIGG8D1.e5340_e5984_s3126_s3136_r10724_r10726_p4133
 mc16_13TeV.364182.Sherpa_221_NNPDF30NNLO_Wenu_MAXHTPTV500_1000.deriv.DAOD_HIGG8D1.e5340_e5984_s3126_r10724_r10726_p4133
 mc16_13TeV.364183.Sherpa_221_NNPDF30NNLO_Wenu_MAXHTPTV1000_E_CMS.deriv.DAOD_HIGG8D1.e5340_e5984_s3126_r10724_r10726_p4133
 mc16_13TeV.364183.Sherpa_221_NNPDF30NNLO_Wenu_MAXHTPTV1000_E_CMS.deriv.DAOD_HIGG8D1.e5340_e5984_s3126_s3136_r10724_r10726_p4133
 mc16_13TeV.364184.Sherpa_221_NNPDF30NNLO_Wtaunu_MAXHTPTV0_70_CVetoBVeto.deriv.DAOD_HIGG8D1.e5340_e5984_s3126_r10724_r10726_p4133
 mc16_13TeV.364185.Sherpa_221_NNPDF30NNLO_Wtaunu_MAXHTPTV0_70_CFilterBVeto.deriv.DAOD_HIGG8D1.e5340_e5984_s3126_r10724_r10726_p4133
 mc16_13TeV.364186.Sherpa_221_NNPDF30NNLO_Wtaunu_MAXHTPTV0_70_BFilter.deriv.DAOD_HIGG8D1.e5340_e5984_s3126_s3136_r10724_r10726_p4133
 mc16_13TeV.364186.Sherpa_221_NNPDF30NNLO_Wtaunu_MAXHTPTV0_70_BFilter.deriv.DAOD_HIGG8D1.e5340_e5984_s3126_r10724_r10726_p4133
 mc16_13TeV.364187.Sherpa_221_NNPDF30NNLO_Wtaunu_MAXHTPTV70_140_CVetoBVeto.deriv.DAOD_HIGG8D1.e5340_e5984_s3126_r10724_r10726_p4133
 mc16_13TeV.364188.Sherpa_221_NNPDF30NNLO_Wtaunu_MAXHTPTV70_140_CFilterBVeto.deriv.DAOD_HIGG8D1.e5340_e5984_s3126_r10724_r10726_p4133
 mc16_13TeV.364189.Sherpa_221_NNPDF30NNLO_Wtaunu_MAXHTPTV70_140_BFilter.deriv.DAOD_HIGG8D1.e5340_e5984_s3126_r10724_r10726_p4133
 mc16_13TeV.364189.Sherpa_221_NNPDF30NNLO_Wtaunu_MAXHTPTV70_140_BFilter.deriv.DAOD_HIGG8D1.e5340_e5984_s3126_s3136_r10724_r10726_p4133
 mc16_13TeV.364190.Sherpa_221_NNPDF30NNLO_Wtaunu_MAXHTPTV140_280_CVetoBVeto.deriv.DAOD_HIGG8D1.e5340_e5984_s3126_r10724_r10726_p4133
 mc16_13TeV.364190.Sherpa_221_NNPDF30NNLO_Wtaunu_MAXHTPTV140_280_CVetoBVeto.deriv.DAOD_HIGG8D1.e5340_e5984_s3126_s3136_r10724_r10726_p4133
 mc16_13TeV.364191.Sherpa_221_NNPDF30NNLO_Wtaunu_MAXHTPTV140_280_CFilterBVeto.deriv.DAOD_HIGG8D1.e5340_e5984_s3126_r10724_r10726_p4133
 mc16_13TeV.364191.Sherpa_221_NNPDF30NNLO_Wtaunu_MAXHTPTV140_280_CFilterBVeto.deriv.DAOD_HIGG8D1.e5340_e5984_s3126_s3136_r10724_r10726_p4133
 mc16_13TeV.364192.Sherpa_221_NNPDF30NNLO_Wtaunu_MAXHTPTV140_280_BFilter.deriv.DAOD_HIGG8D1.e5340_e5984_s3126_s3136_r10724_r10726_p4133
 mc16_13TeV.364192.Sherpa_221_NNPDF30NNLO_Wtaunu_MAXHTPTV140_280_BFilter.deriv.DAOD_HIGG8D1.e5340_e5984_s3126_r10724_r10726_p4133
 mc16_13TeV.364193.Sherpa_221_NNPDF30NNLO_Wtaunu_MAXHTPTV280_500_CVetoBVeto.deriv.DAOD_HIGG8D1.e5340_e5984_s3126_r10724_r10726_p4133
 mc16_13TeV.364193.Sherpa_221_NNPDF30NNLO_Wtaunu_MAXHTPTV280_500_CVetoBVeto.deriv.DAOD_HIGG8D1.e5340_e5984_s3126_s3136_r10724_r10726_p4133
 mc16_13TeV.364194.Sherpa_221_NNPDF30NNLO_Wtaunu_MAXHTPTV280_500_CFilterBVeto.deriv.DAOD_HIGG8D1.e5340_e5984_s3126_s3136_r10724_r10726_p4133

mc16_13TeV.364194.Sherpa_221_NNPDF30NNLO_Wtaunu_MAXHTPTV280_500_CFilterBVeto.deriv.DAOD_HIGG8D1.e5340_e5984_s3126_r10724_r10726_p4133
 mc16_13TeV.364195.Sherpa_221_NNPDF30NNLO_Wtaunu_MAXHTPTV280_500_BFilter.deriv.DAOD_HIGG8D1.e5340_e5984_s3126_s3136_r10724_r10726_p4133
 mc16_13TeV.364195.Sherpa_221_NNPDF30NNLO_Wtaunu_MAXHTPTV280_500_BFilter.deriv.DAOD_HIGG8D1.e5340_e5984_s3126_r10724_r10726_p4133
 mc16_13TeV.364196.Sherpa_221_NNPDF30NNLO_Wtaunu_MAXHTPTV500_1000.deriv.DAOD_HIGG8D1.e5340_e5984_s3126_s3136_r10724_r10726_p4133
 mc16_13TeV.364196.Sherpa_221_NNPDF30NNLO_Wtaunu_MAXHTPTV500_1000.deriv.DAOD_HIGG8D1.e5340_e5984_s3126_r10724_r10726_p4133
 mc16_13TeV.364197.Sherpa_221_NNPDF30NNLO_Wtaunu_MAXHTPTV1000_E_CMS.deriv.DAOD_HIGG8D1.e5340_e5984_s3126_s3136_r10724_r10726_p4133
 mc16_13TeV.364197.Sherpa_221_NNPDF30NNLO_Wtaunu_MAXHTPTV1000_E_CMS.deriv.DAOD_HIGG8D1.e5340_e5984_s3126_r10724_r10726_p4133
 mc16_13TeV.364500.Sherpa_222_NNPDF30NNLO_eegamma_pty_7_15.deriv.DAOD_HIGG8D1.e5928_e5984_s3126_r10724_r10726_p4133
 mc16_13TeV.364501.Sherpa_222_NNPDF30NNLO_eegamma_pty_15_35.deriv.DAOD_HIGG8D1.e5928_e5984_s3126_r10724_r10726_p4133
 mc16_13TeV.364502.Sherpa_222_NNPDF30NNLO_eegamma_pty_35_70.deriv.DAOD_HIGG8D1.e5928_e5984_s3126_r10724_r10726_p4133
 mc16_13TeV.364503.Sherpa_222_NNPDF30NNLO_eegamma_pty_70_140.deriv.DAOD_HIGG8D1.e5928_e5984_s3126_r10724_r10726_p4133
 mc16_13TeV.364504.Sherpa_222_NNPDF30NNLO_eegamma_pty_140_E_CMS.deriv.DAOD_HIGG8D1.e5928_e5984_s3126_r10724_r10726_p4133
 mc16_13TeV.364505.Sherpa_222_NNPDF30NNLO_mumugamma_pty_7_15.deriv.DAOD_HIGG8D1.e5928_e5984_s3126_r10724_r10726_p4133
 mc16_13TeV.364506.Sherpa_222_NNPDF30NNLO_mumugamma_pty_15_35.deriv.DAOD_HIGG8D1.e5928_e5984_s3126_r10724_r10726_p4133
 mc16_13TeV.364507.Sherpa_222_NNPDF30NNLO_mumugamma_pty_35_70.deriv.DAOD_HIGG8D1.e5928_e5984_s3126_r10724_r10726_p4133
 mc16_13TeV.364508.Sherpa_222_NNPDF30NNLO_mumugamma_pty_70_140.deriv.DAOD_HIGG8D1.e5928_e5984_s3126_r10724_r10726_p4133
 mc16_13TeV.364509.Sherpa_222_NNPDF30NNLO_mumugamma_pty_140_E_CMS.deriv.DAOD_HIGG8D1.e5928_e5984_s3126_r10724_r10726_p4133
 mc16_13TeV.364511.Sherpa_222_NNPDF30NNLO_tautaugamma_pty_15_35.deriv.DAOD_HIGG8D1.e5928_e5984_s3126_r10724_r10726_p4133
 mc16_13TeV.364512.Sherpa_222_NNPDF30NNLO_tautaugamma_pty_35_70.deriv.DAOD_HIGG8D1.e5928_e5984_s3126_r10724_r10726_p4133
 mc16_13TeV.364513.Sherpa_222_NNPDF30NNLO_tautaugamma_pty_70_140.deriv.DAOD_HIGG8D1.e5982_e5984_s3126_r10724_r10726_p4133
 mc16_13TeV.364514.Sherpa_222_NNPDF30NNLO_tautaugamma_pty_140_E_CMS.deriv.DAOD_HIGG8D1.e5928_e5984_s3126_r10724_r10726_p4133
 mc16_13TeV.364522.Sherpa_222_NNPDF30NNLO_enugamma_pty_15_35.deriv.DAOD_HIGG8D1.e5928_e5984_s3126_r10724_r10726_p4133
 mc16_13TeV.364523.Sherpa_222_NNPDF30NNLO_enugamma_pty_35_70.deriv.DAOD_HIGG8D1.e5928_e5984_s3126_r10724_r10726_p4133
 mc16_13TeV.364524.Sherpa_222_NNPDF30NNLO_enugamma_pty_70_140.deriv.DAOD_HIGG8D1.e5928_e5984_s3126_r10724_r10726_p4133
 mc16_13TeV.364525.Sherpa_222_NNPDF30NNLO_enugamma_pty_140_E_CMS.deriv.DAOD_HIGG8D1.e5928_e5984_s3126_r10724_r10726_p4133
 mc16_13TeV.364527.Sherpa_222_NNPDF30NNLO_munugamma_pty_15_35.deriv.DAOD_HIGG8D1.e5928_e5984_s3126_r10724_r10726_p4133
 mc16_13TeV.364528.Sherpa_222_NNPDF30NNLO_munugamma_pty_35_70.deriv.DAOD_HIGG8D1.e5928_e5984_s3126_r10724_r10726_p4133
 mc16_13TeV.364529.Sherpa_222_NNPDF30NNLO_munugamma_pty_70_140.deriv.DAOD_HIGG8D1.e5928_e5984_s3126_r10724_r10726_p4133
 mc16_13TeV.364530.Sherpa_222_NNPDF30NNLO_munugamma_pty_140_E_CMS.deriv.DAOD_HIGG8D1.e5928_e5984_s3126_r10724_r10726_p4133
 mc16_13TeV.364532.Sherpa_222_NNPDF30NNLO_taunugamma_pty_15_35.deriv.DAOD_HIGG8D1.e5928_e5984_s3126_r10724_r10726_p4133
 mc16_13TeV.364533.Sherpa_222_NNPDF30NNLO_taunugamma_pty_35_70.deriv.DAOD_HIGG8D1.e5928_e5984_s3126_r10724_r10726_p4133

mc16_13TeV.364534.Sherpa_222_NNPDF30NNLO_taunugamma_pty_70_140.deriv.DAOD_HIGG8D1.e5928_e5984_s3126_r10724_r10726_p4133
mc16_13TeV.364535.Sherpa_222_NNPDF30NNLO_taunugamma_pty_140_E_CMS.deriv.DAOD_HIGG8D1.e5928_e5984_s3126_r10724_r10726_p4133
mc16_13TeV.410560.MadGraphPythia8EvtGen_A14_tZ_4fl_tchan_noAllHad.deriv.DAOD_HIGG8D1.e5803_e5984_s3126_r10724_r10726_p4133
mc16_13TeV.410408.aMcAtNloPythia8EvtGen_tWZ_Ztoll_minDR1.deriv.DAOD_HIGG8D1.e6423_e5984_s3126_r10724_r10726_p4133
mc16_13TeV.364242.Sherpa_222_NNPDF30NNLO_WWW_3l3v_EW6.deriv.DAOD_HIGG8D1.e5887_e5984_s3126_r10724_r10726_p4133
mc16_13TeV.364243.Sherpa_222_NNPDF30NNLO_WWZ_4l2v_EW6.deriv.DAOD_HIGG8D1.e5887_e5984_s3126_r10724_r10726_p4133
mc16_13TeV.364244.Sherpa_222_NNPDF30NNLO_WWZ_2l4v_EW6.deriv.DAOD_HIGG8D1.e5887_e5984_s3126_r10724_r10726_p4133
mc16_13TeV.364245.Sherpa_222_NNPDF30NNLO_WZZ_5l1v_EW6.deriv.DAOD_HIGG8D1.e5887_e5984_s3126_r10724_r10726_p4133
mc16_13TeV.364246.Sherpa_222_NNPDF30NNLO_WZZ_3l3v_EW6.deriv.DAOD_HIGG8D1.e5887_e5984_s3126_r10724_r10726_p4133
mc16_13TeV.364247.Sherpa_222_NNPDF30NNLO_ZZZ_6l0v_EW6.deriv.DAOD_HIGG8D1.e5887_e5984_s3126_r10724_r10726_p4133
mc16_13TeV.364248.Sherpa_222_NNPDF30NNLO_ZZZ_4l2v_EW6.deriv.DAOD_HIGG8D1.e5887_e5984_s3126_r10724_r10726_p4133
mc16_13TeV.364249.Sherpa_222_NNPDF30NNLO_ZZZ_2l4v_EW6.deriv.DAOD_HIGG8D1.e5887_e5984_s3126_r10724_r10726_p4133
mc16_13TeV.342284.Pythia8EvtGen_A14NNPDF23LO_WH125_inc.deriv.DAOD_HIGG8D1.e4246_e5984_s3126_r10724_r10726_p4133
mc16_13TeV.342285.Pythia8EvtGen_A14NNPDF23LO_ZH125_inc.deriv.DAOD_HIGG8D1.e4246_e5984_s3126_r10724_r10726_p4133
mc16_13TeV.341998.aMcAtNloHppEG_UEEE5_CTEQ6L1_CT10ME_tWH125_gamgam_yt_plus1.deriv.DAOD_HIGG8D1.e4394_e5984_s3126_r10724_r10726_p4133
mc16_13TeV.410389.MadGraphPythia8EvtGen_A14NNPDF23_ttgamma_nonallhadronic.deriv.DAOD_HIGG8D1.e6155_e5984_s3126_r10724_r10726_p4133
mc16_13TeV.410470.PhPy8EG_A14_ttbar_hdamp258p75_nonallhad.deriv.DAOD_HIGG8D1.e6337_e5984_s3126_r10724_r10726_p4133
mc16_13TeV.410472.PhPy8EG_A14_ttbar_hdamp258p75_dil.deriv.DAOD_HIGG8D1.e6348_e5984_s3126_r10724_r10726_p4133
mc16_13TeV.346343.PhPy8EG_A14NNPDF23_NNPDF30ME_ttH125_allhad.deriv.DAOD_HIGG8D1.e7148_e5984_s3126_r10724_r10726_p4133
mc16_13TeV.346343.PhPy8EG_A14NNPDF23_NNPDF30ME_ttH125_allhad.deriv.DAOD_HIGG8D1.e7148_e5984_a875_r10724_r10726_p4133
mc16_13TeV.346344.PhPy8EG_A14NNPDF23_NNPDF30ME_ttH125_semilep.deriv.DAOD_HIGG8D1.e7148_e5984_a875_r10724_r10726_p4133
mc16_13TeV.346344.PhPy8EG_A14NNPDF23_NNPDF30ME_ttH125_semilep.deriv.DAOD_HIGG8D1.e7148_e5984_s3126_r10724_r10726_p4133
mc16_13TeV.346345.PhPy8EG_A14NNPDF23_NNPDF30ME_ttH125_dilep.deriv.DAOD_HIGG8D1.e7148_e5984_a875_r10724_r10726_p4133
mc16_13TeV.346345.PhPy8EG_A14NNPDF23_NNPDF30ME_ttH125_dilep.deriv.DAOD_HIGG8D1.e7148_e5984_s3126_r10724_r10726_p4133

1865 **A Machine Learning Models**

1866 The following section provides details of the various MVAs as well as a few studies performed
1867 in support of this analysis, exploring alternate decisions and strategies.

1868 **A.1 Higgs Reconstruction Model Details**

1869 **A.1.1 b-jet Identification Features - 2lSS**

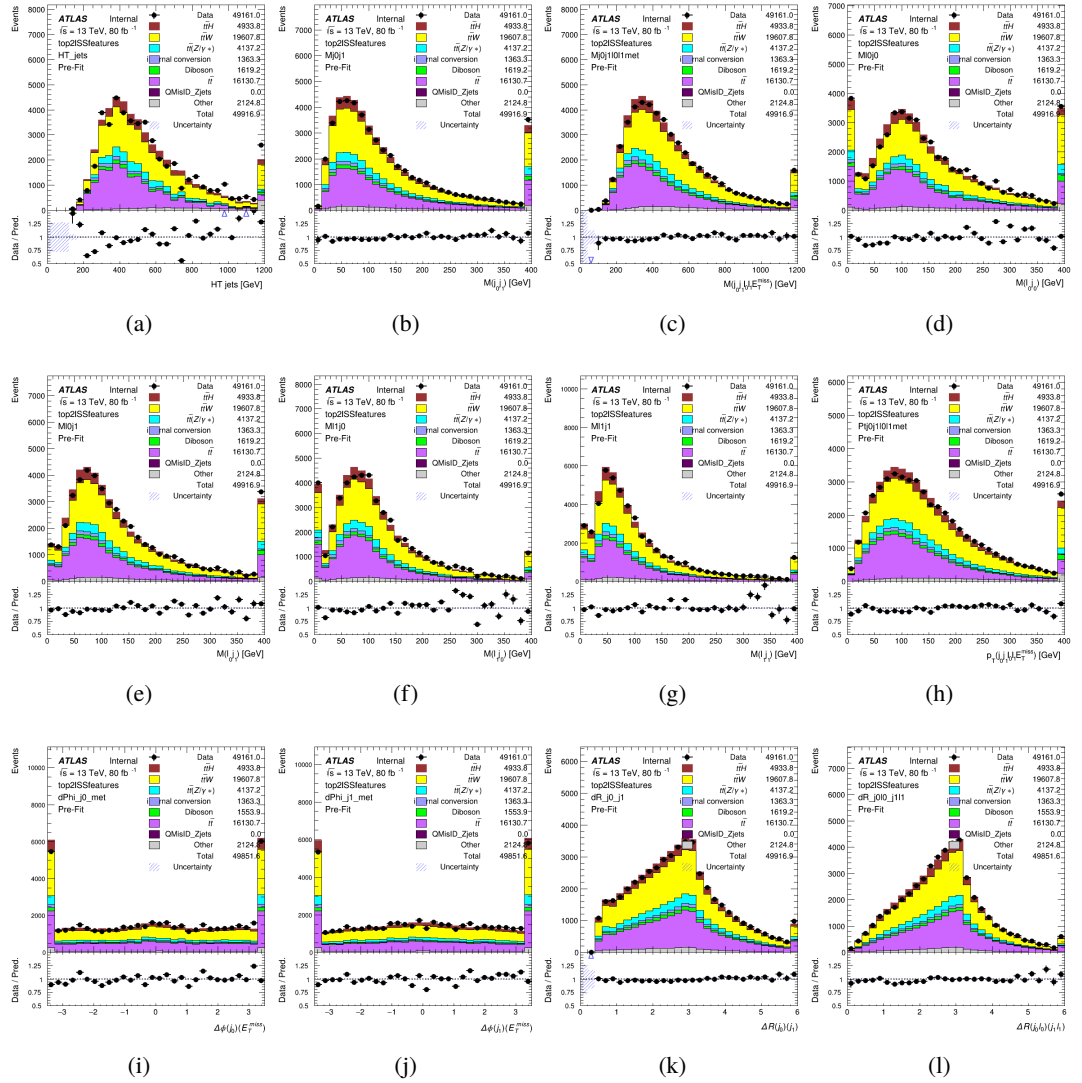


Figure A.1: Input features for top2lSS

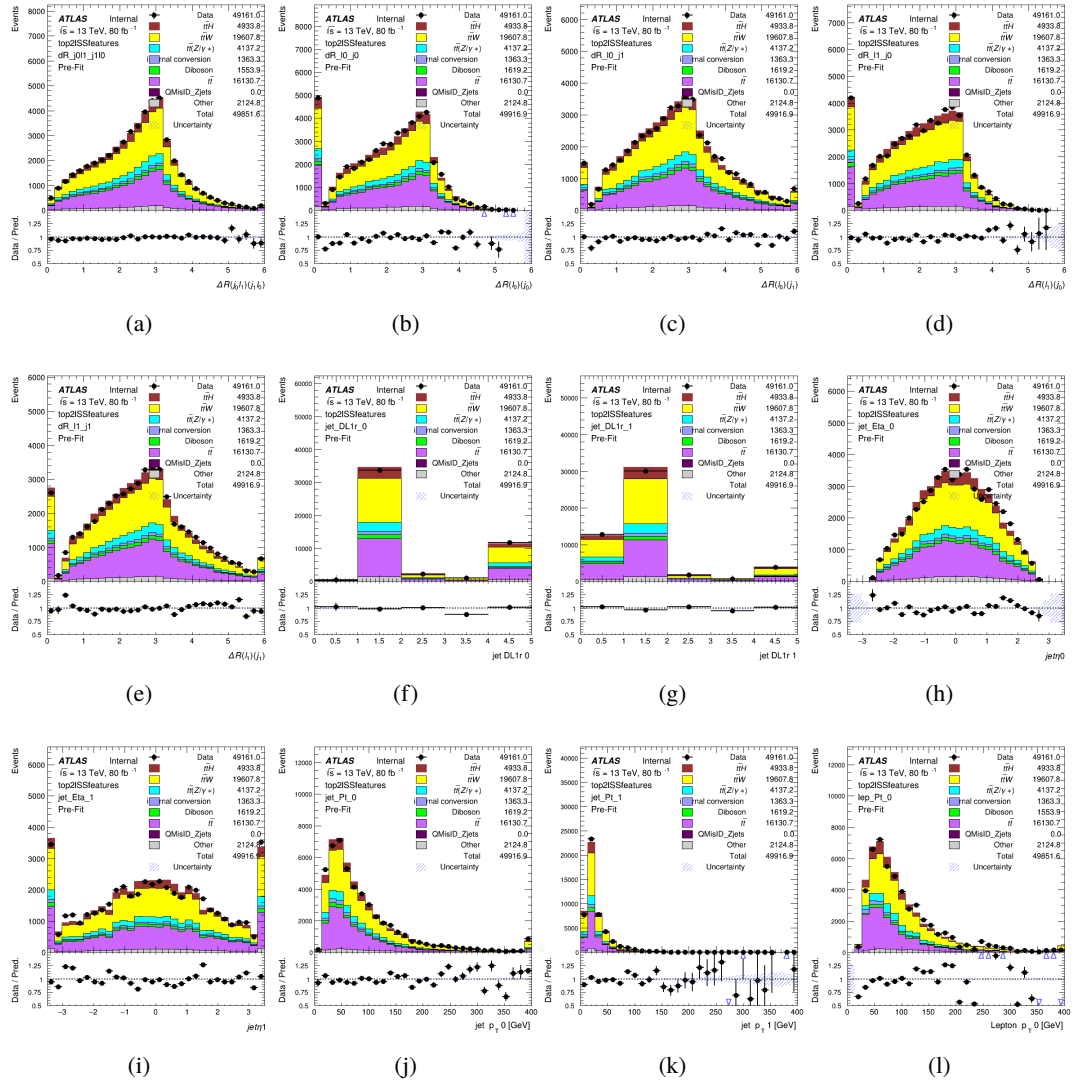


Figure A.2: Input features for top2lSS

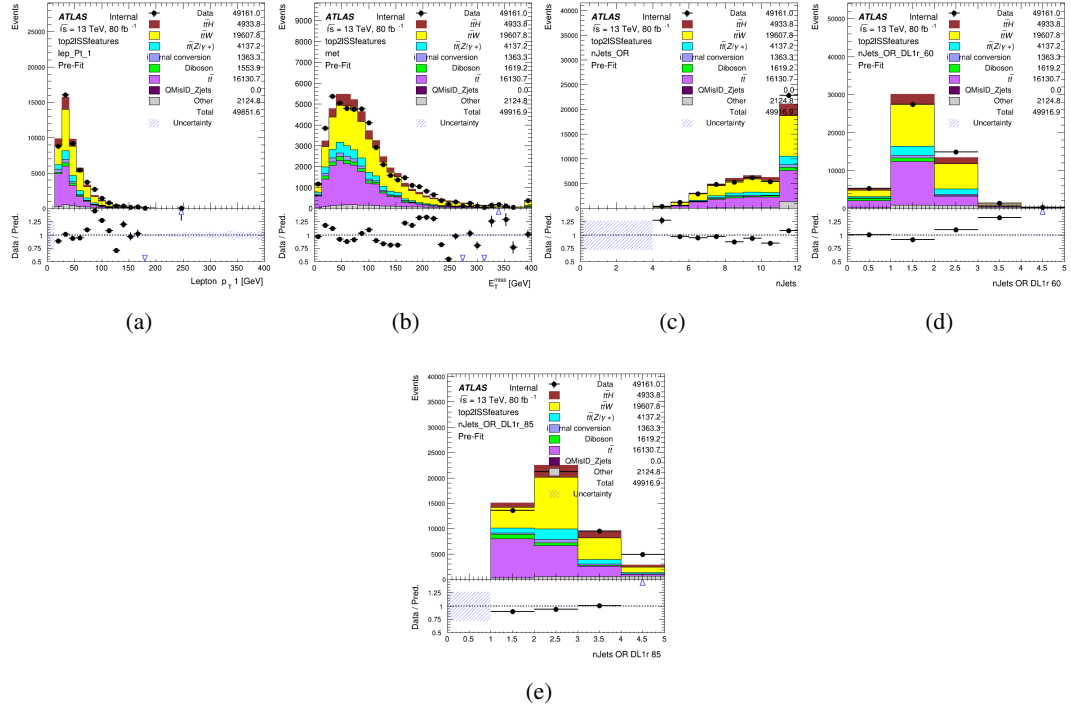


Figure A.3: Input features for top2ISS

¹⁸⁷⁰ **A.1.2 b-jet Identification Features - 3l**

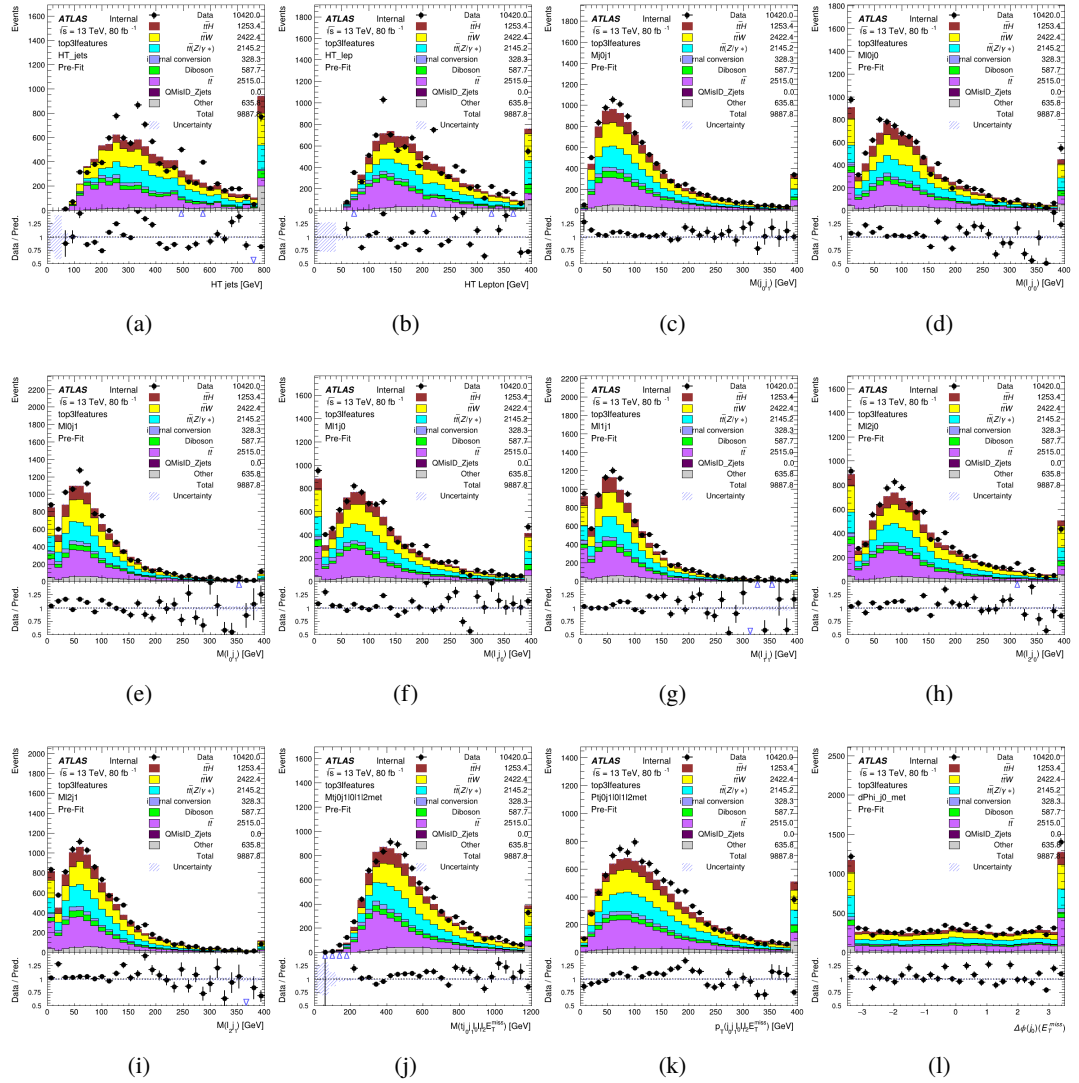


Figure A.4: Input features for top31

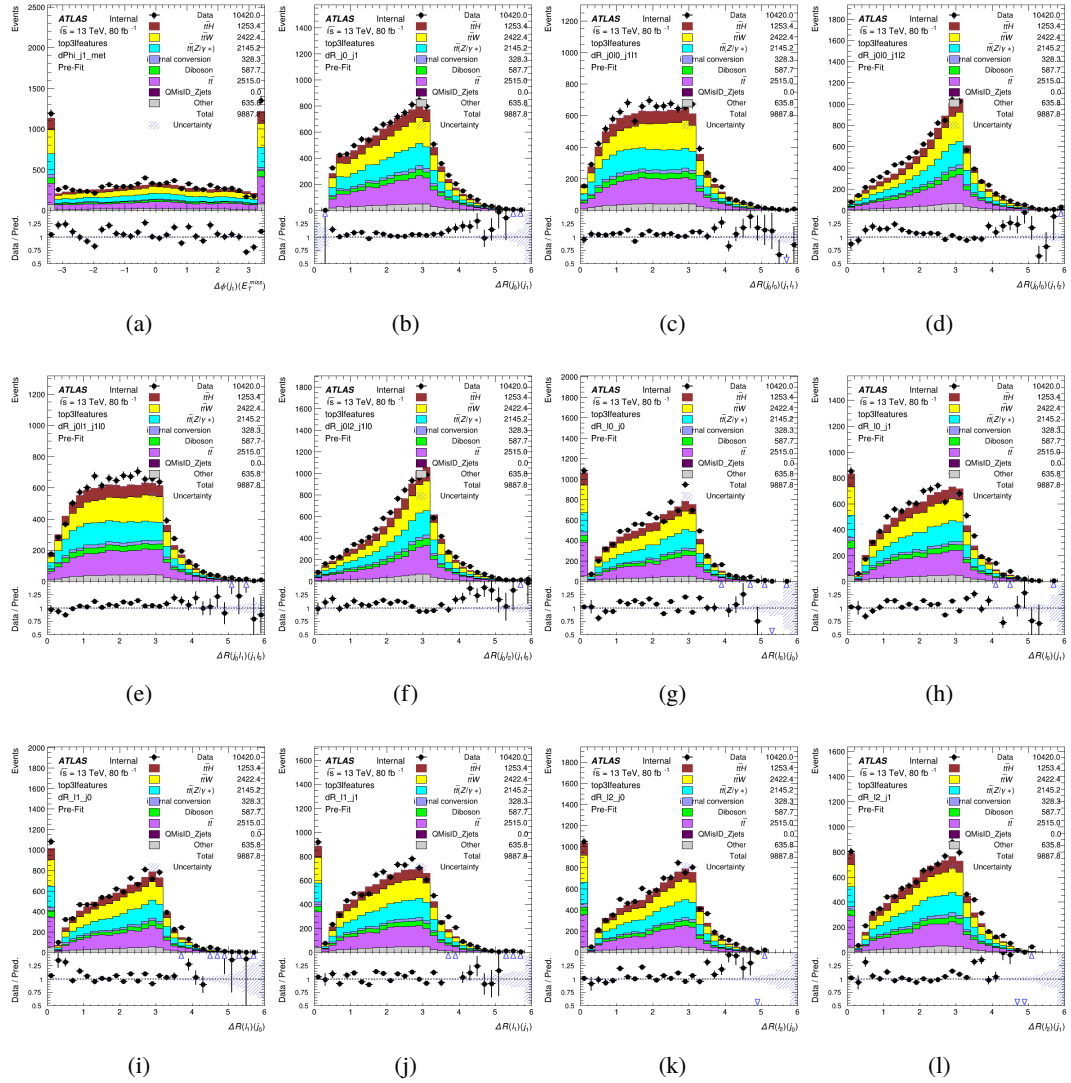


Figure A.5: Input features for top31

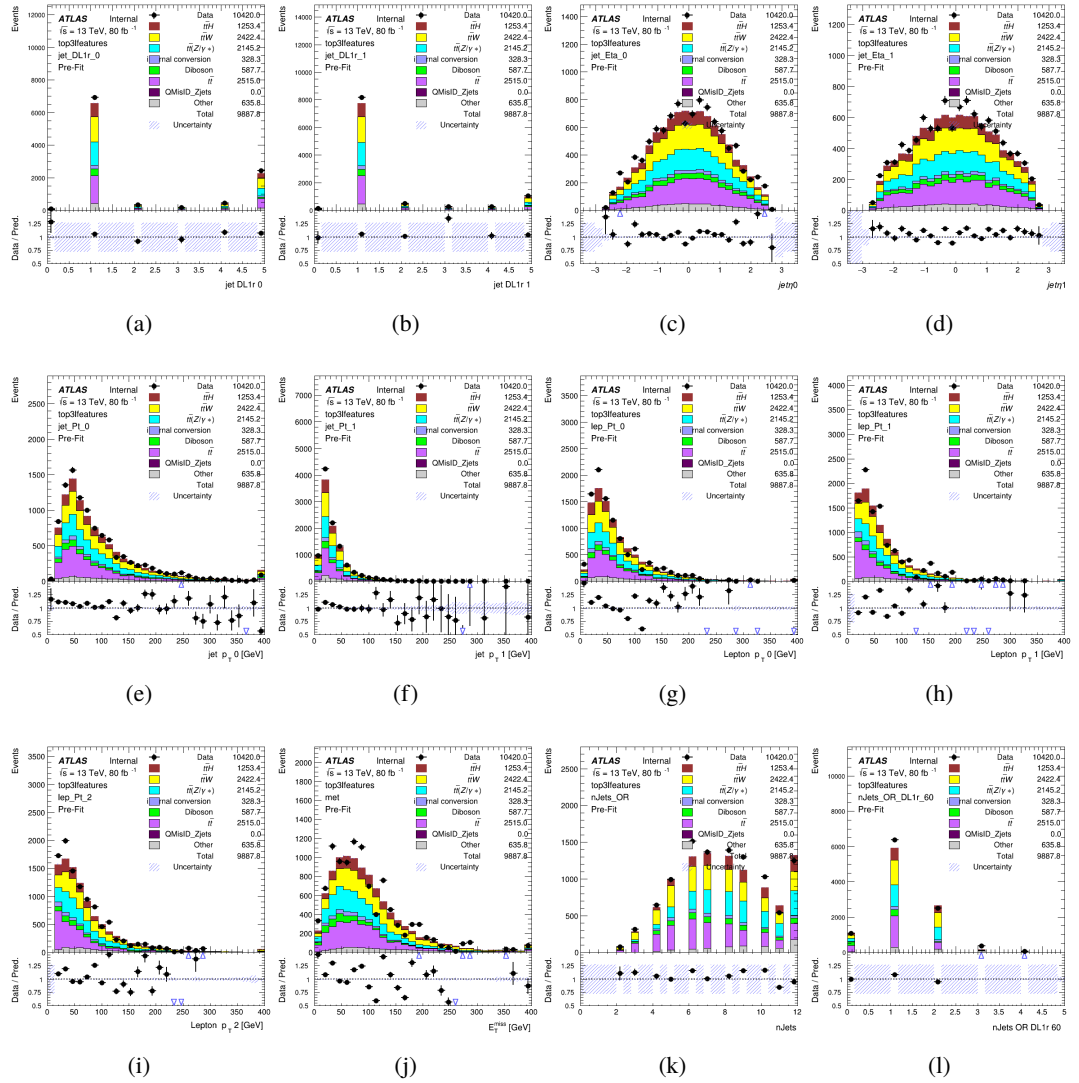
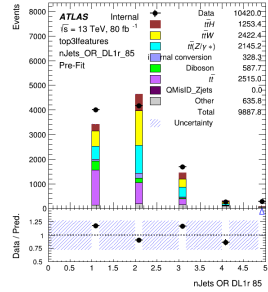


Figure A.6: Input features for top31



(a)

Figure A.7: Input features for top31

¹⁸⁷¹ **A.1.3 Higgs Reconstruction Features - 2lSS**

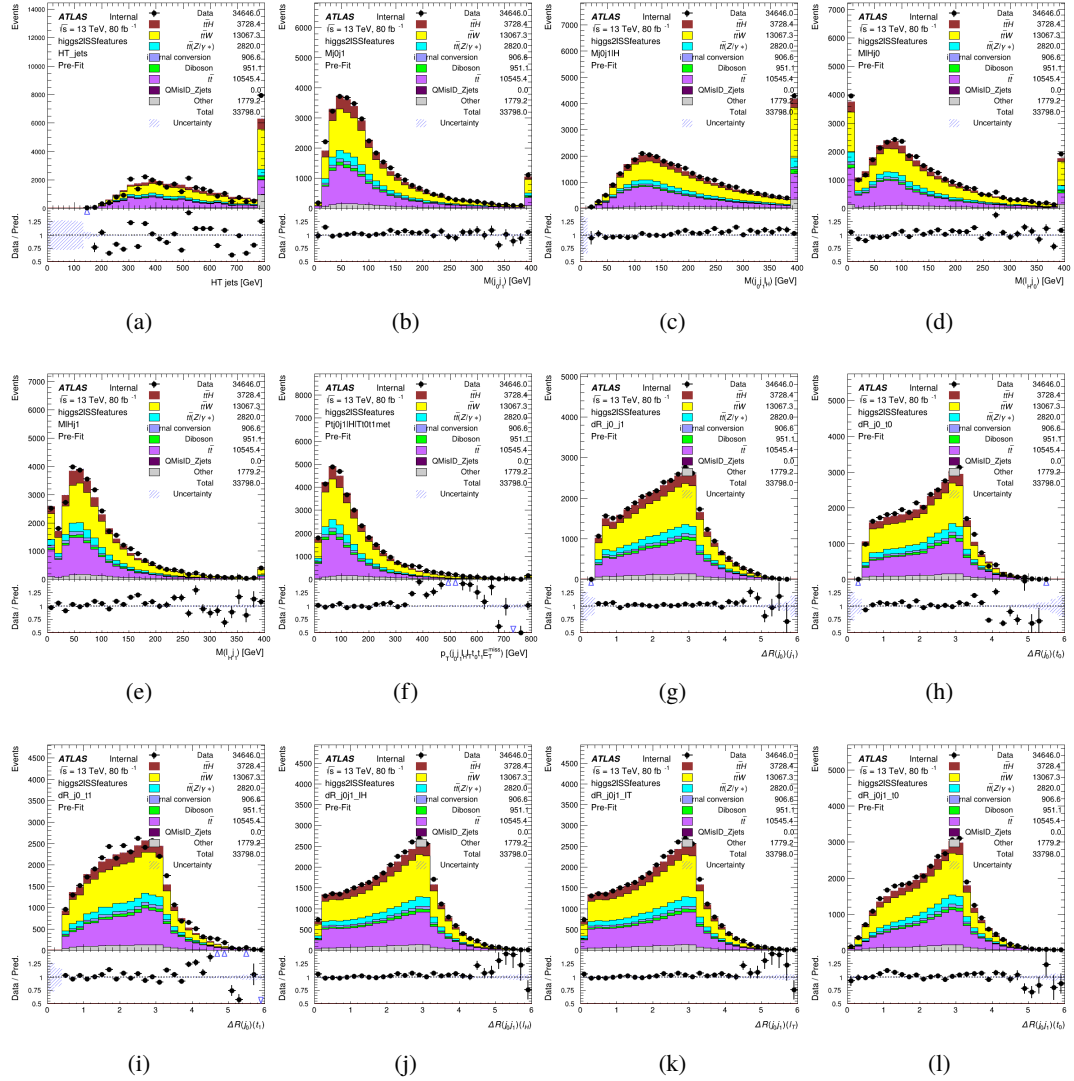


Figure A.8: Input features for higgs2lSS

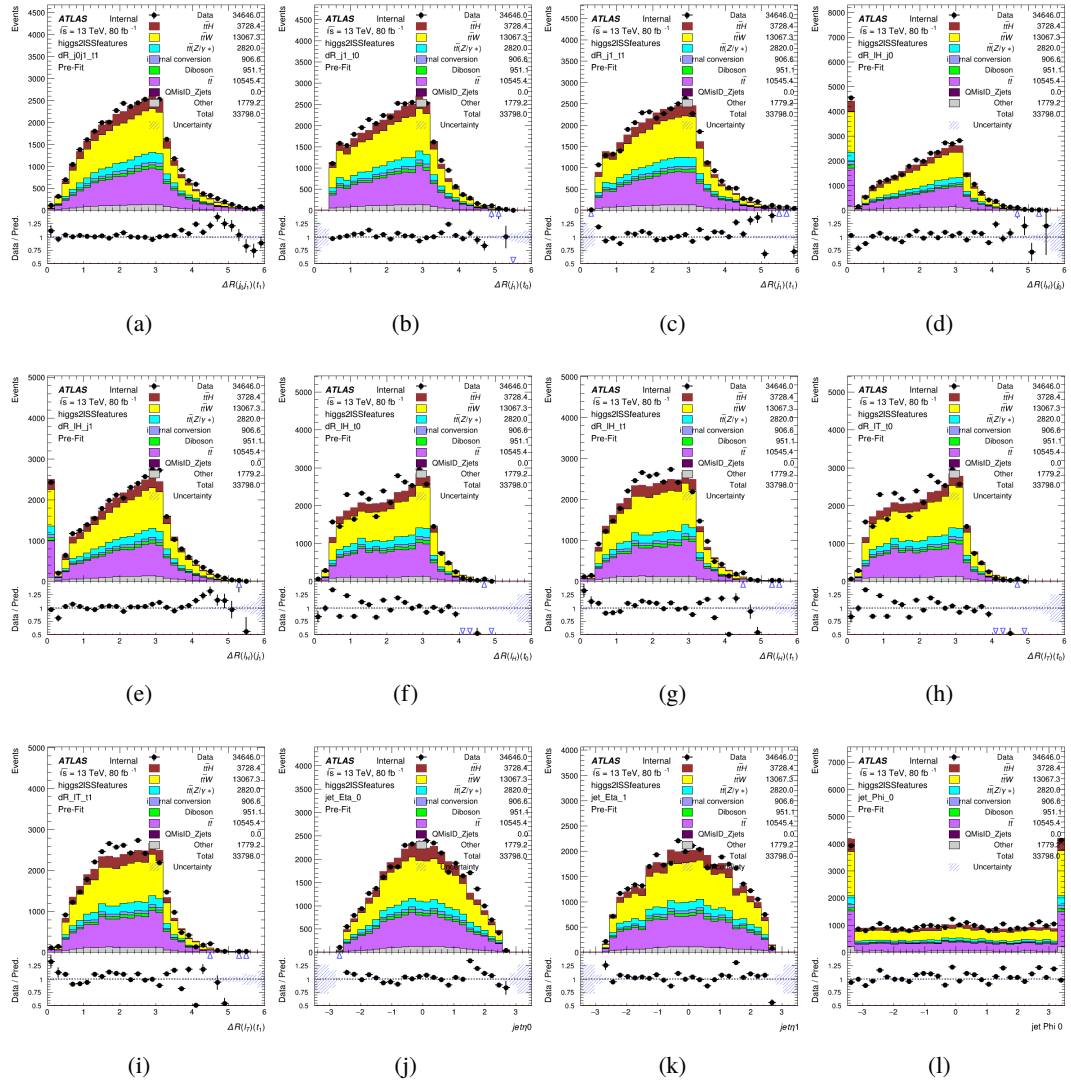


Figure A.9: Input features for higgs2lSS

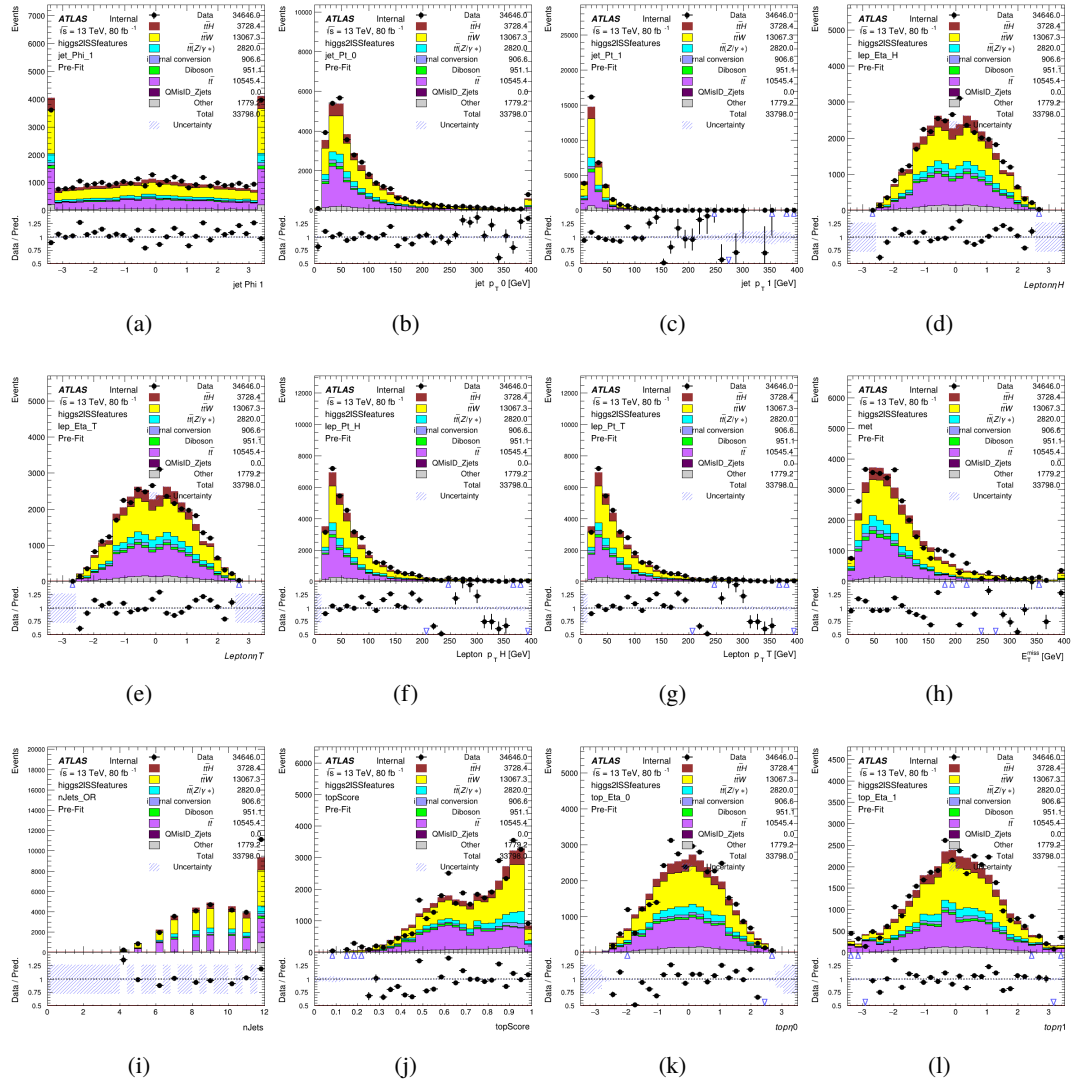


Figure A.10: Input features for higgs2IS

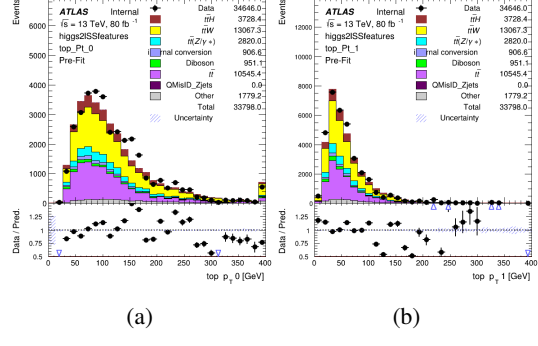


Figure A.11: Input features for higgs2lSS

1872 **A.1.4 Higgs Reconstruction Features - 3lS**

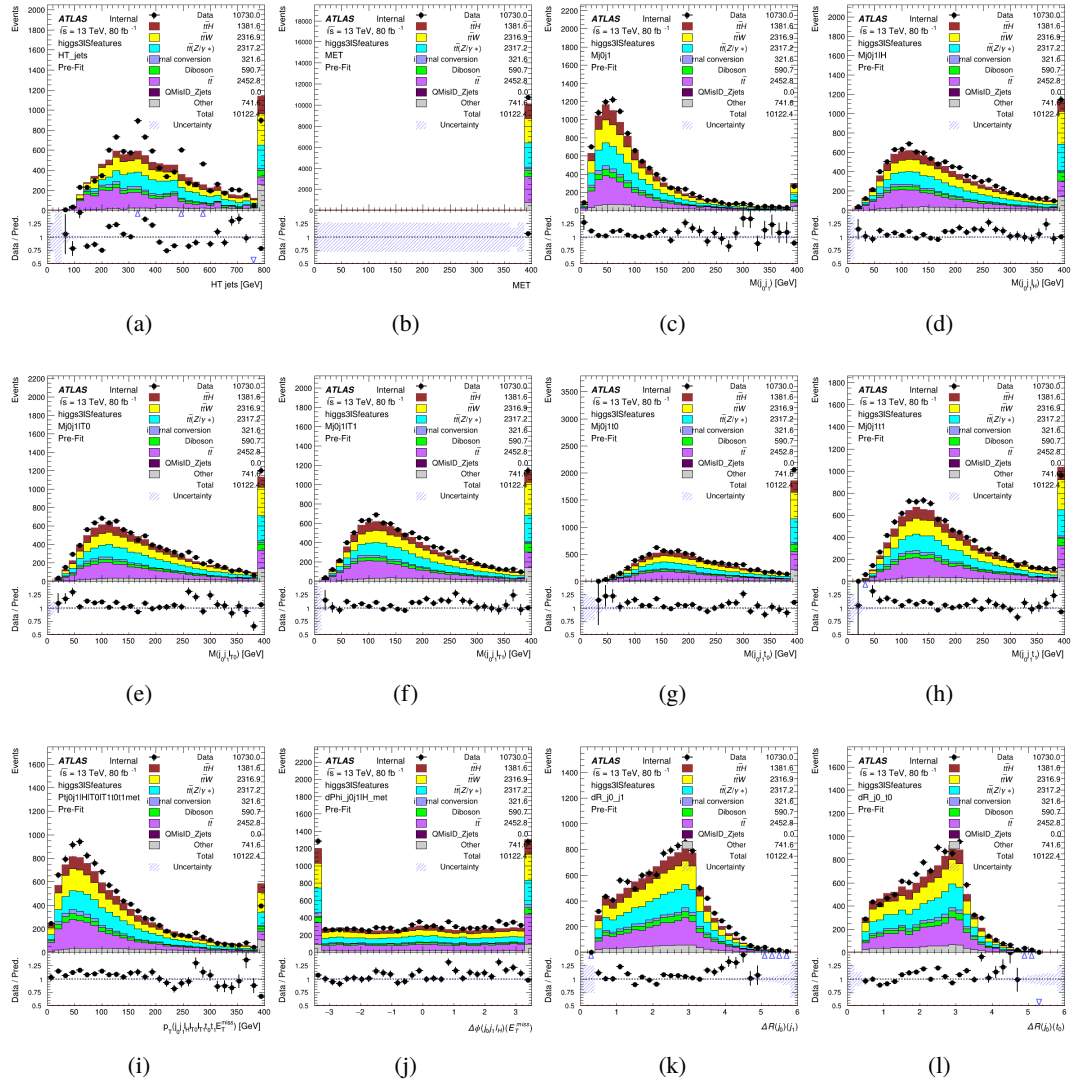


Figure A.12: Input features for higgs3IS

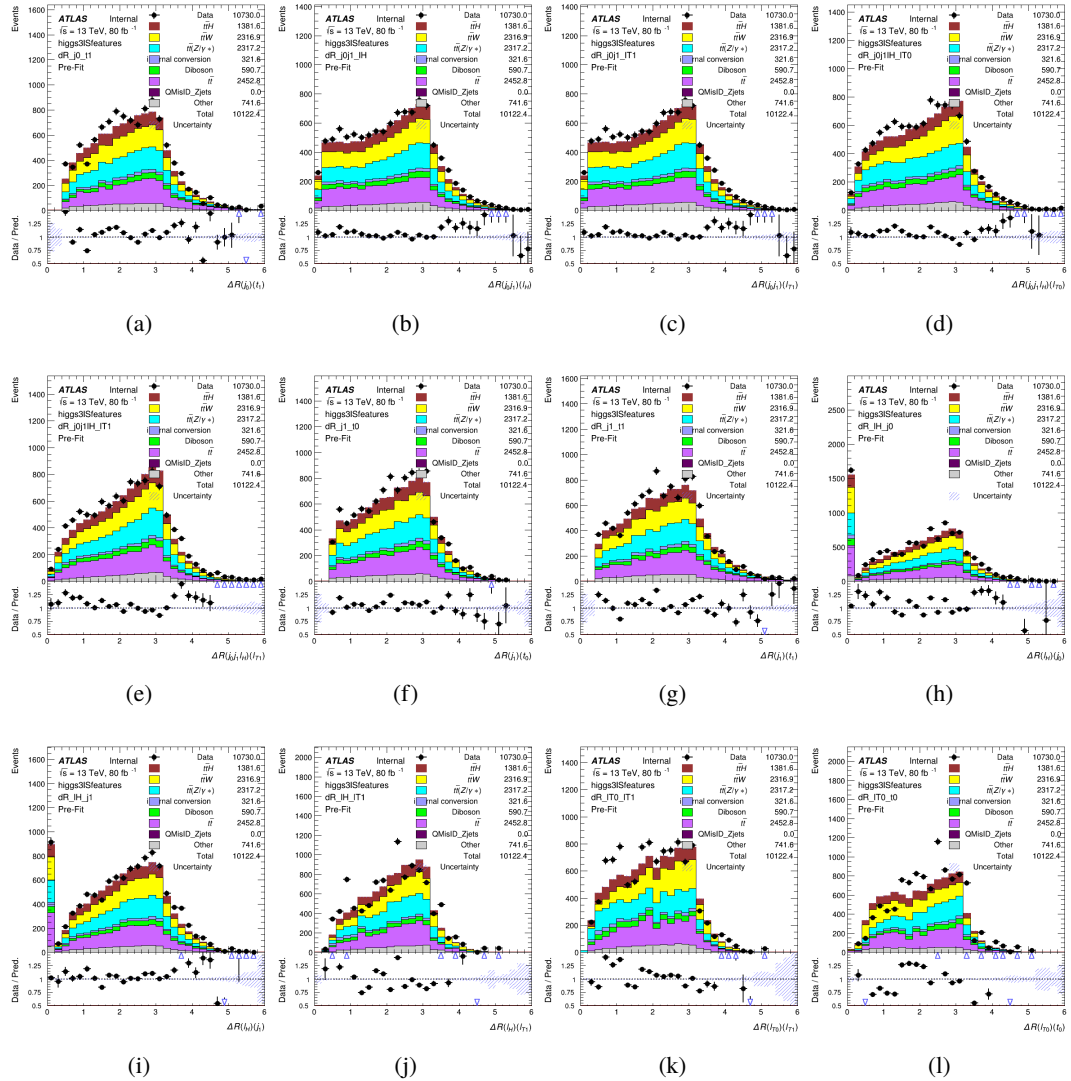


Figure A.13: Input features for higgs3S1S

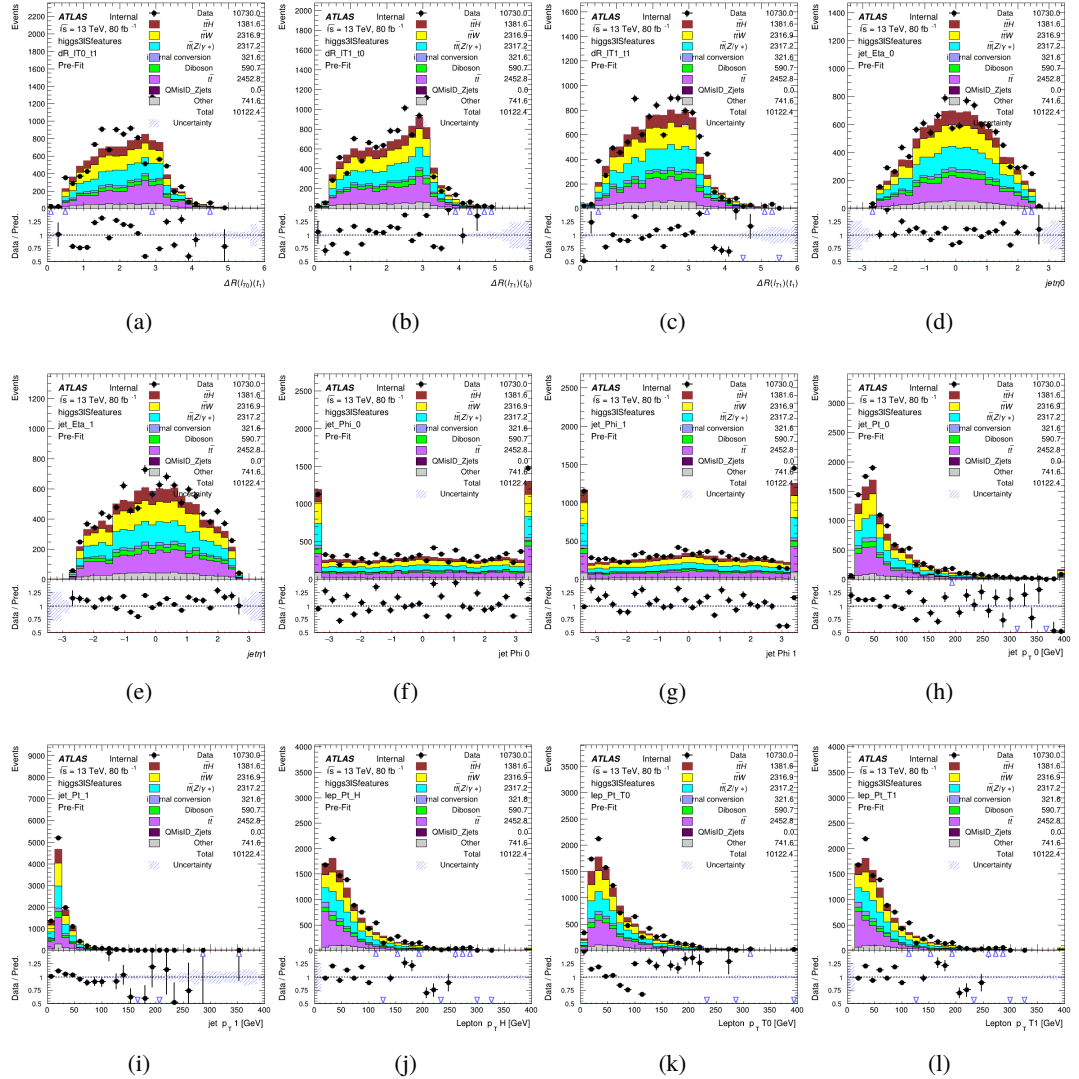


Figure A.14: Input features for higgs3IS

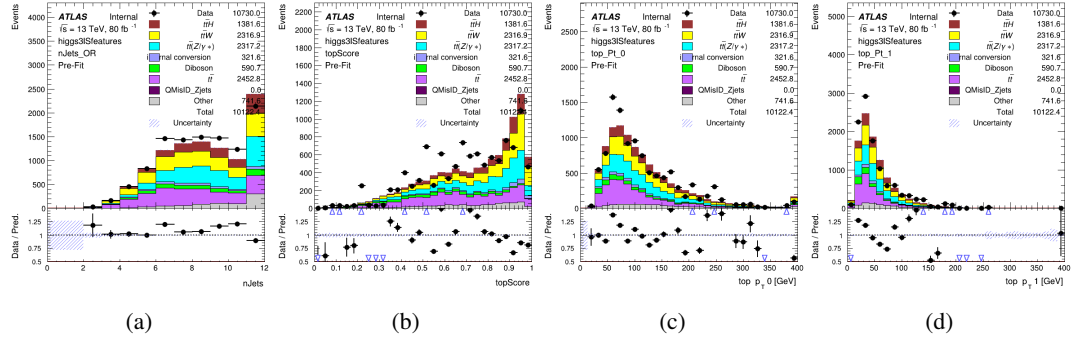


Figure A.15: Input features for higgs3IS

1873 **A.1.5 Higgs Reconstruction Features - 3lF**

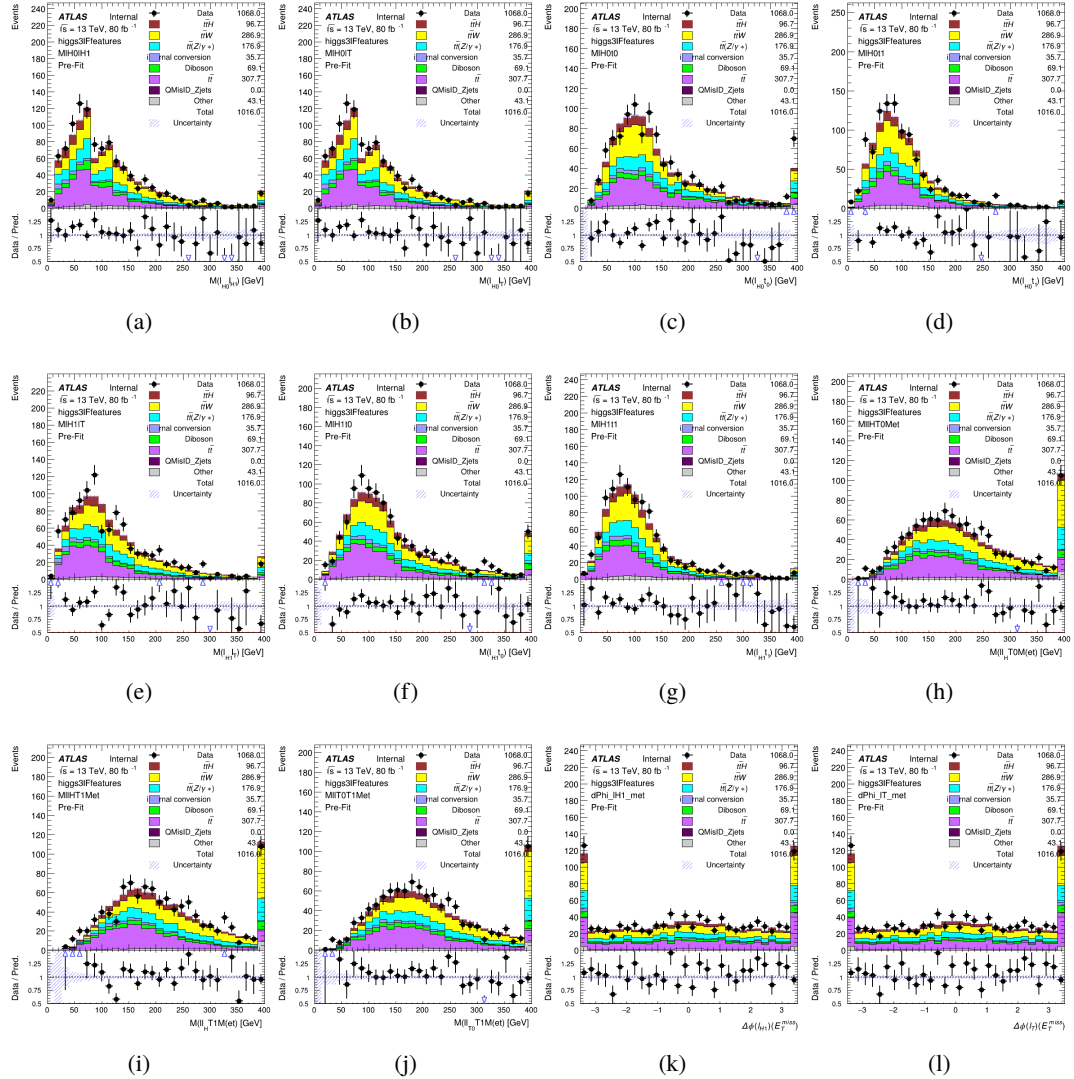


Figure A.16: Input features for higgs3IF

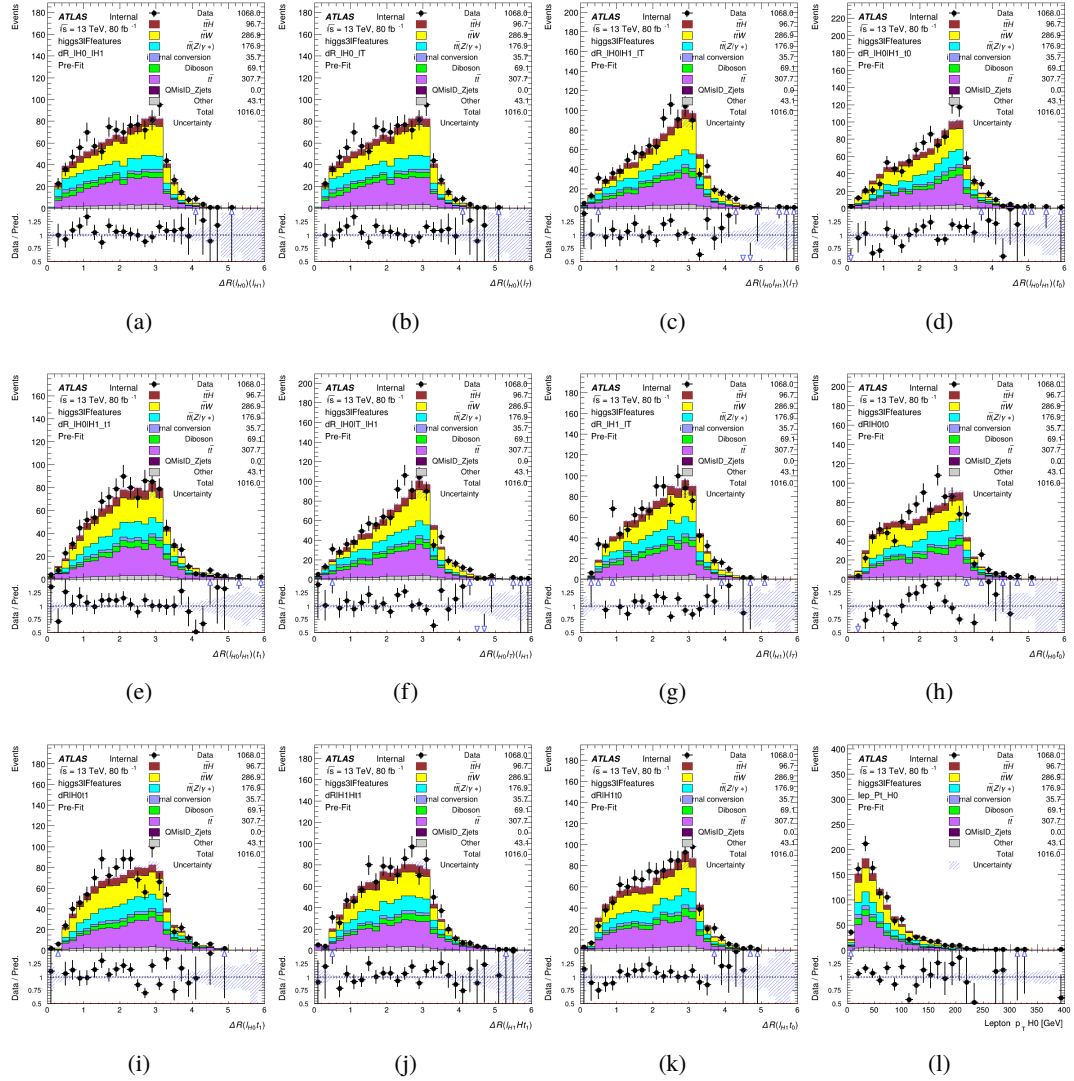


Figure A.17: Input features for higgs3IF

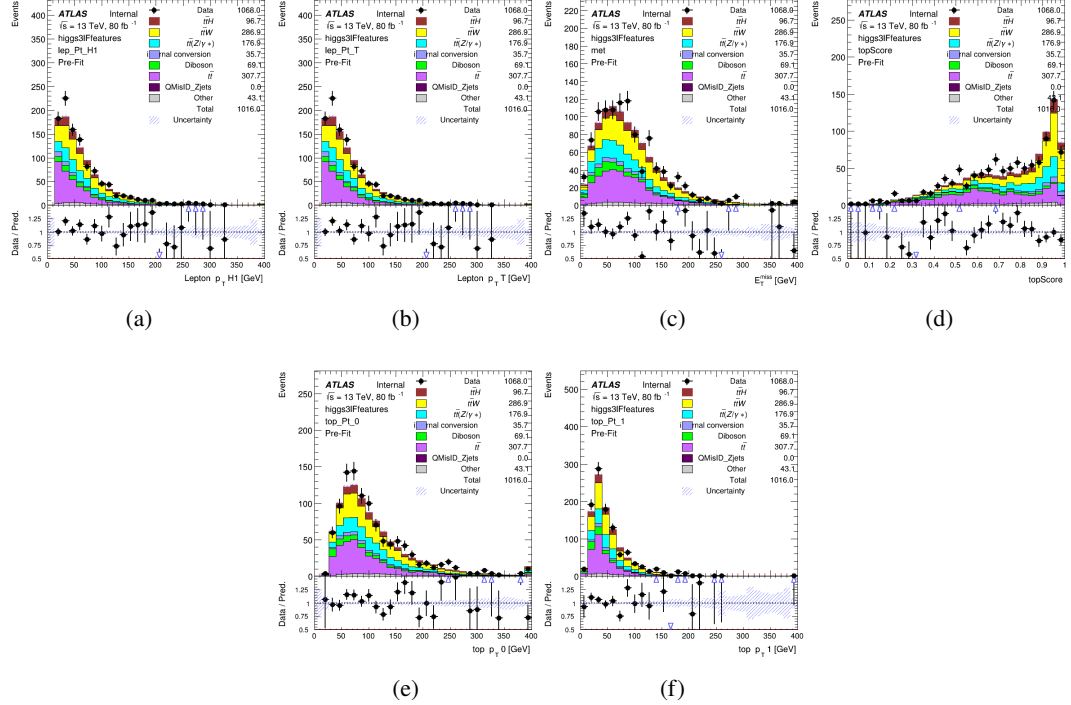


Figure A.18: Input features for higgs3lF

¹⁸⁷⁴ **A.2 Background Rejection MVA Details**

¹⁸⁷⁵ **A.2.1 Background Rejection MVA Features - 2ISS**

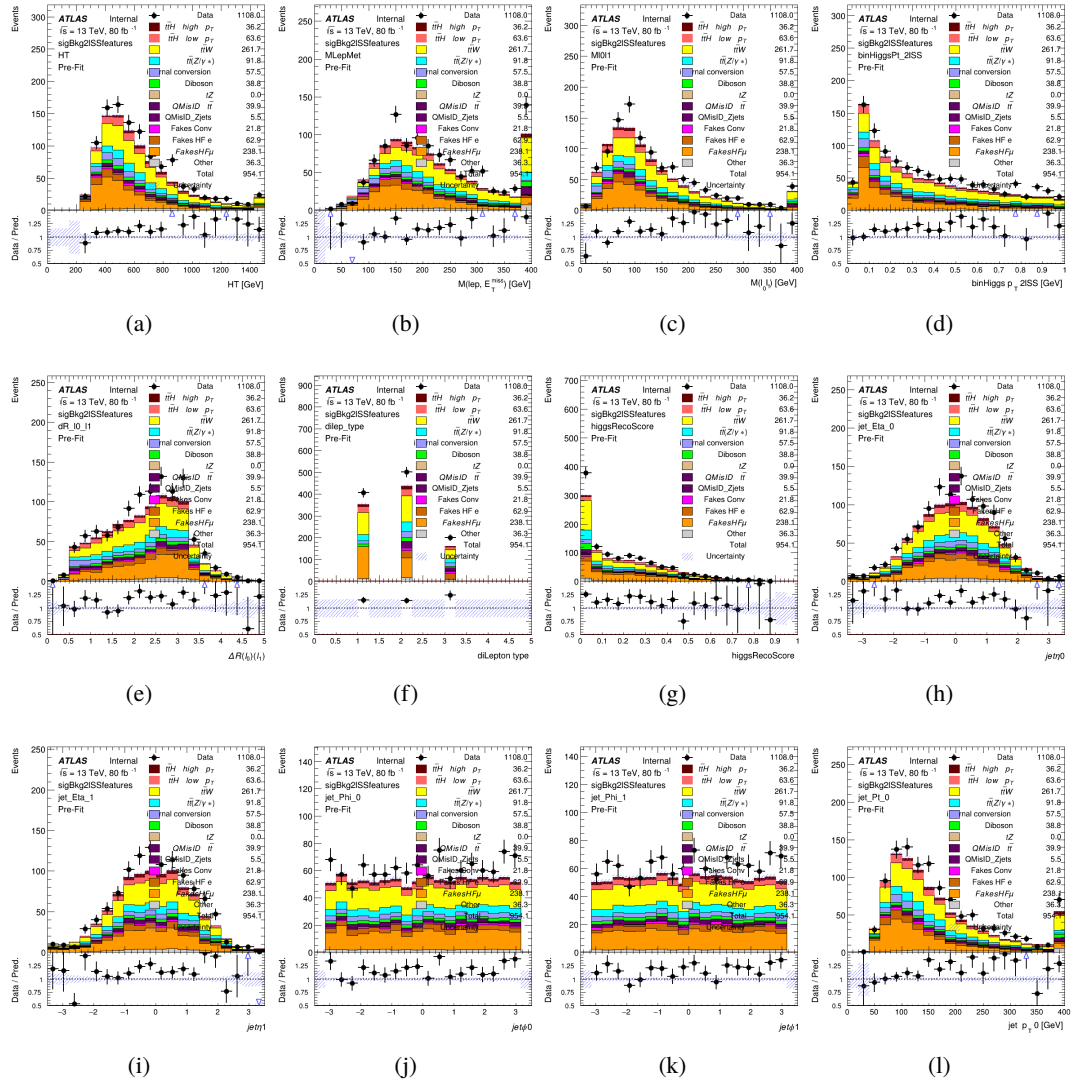
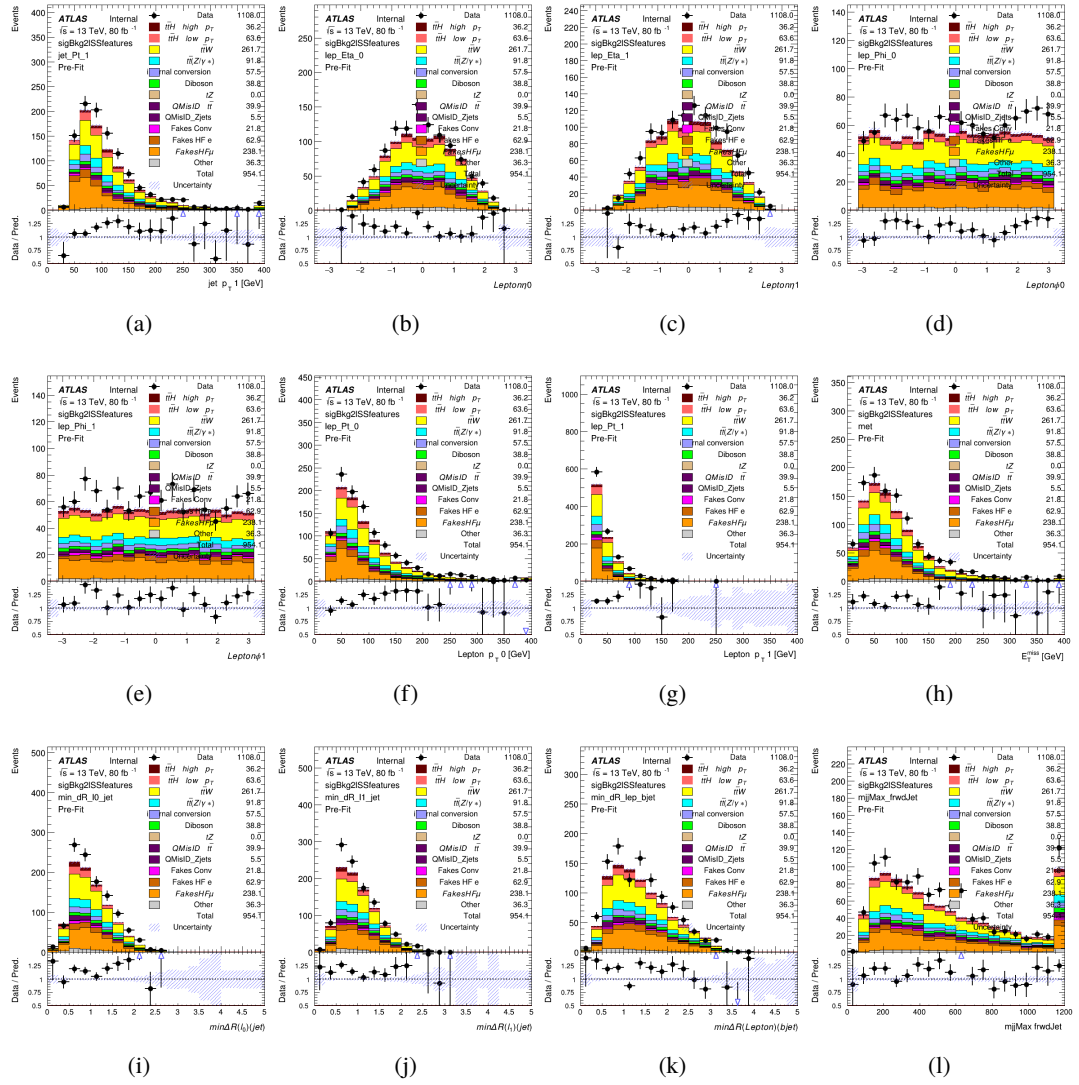


Figure A.19: Input features for sigBkg2lSS

Figure A.20: Input features for `sigBkg2lSS`

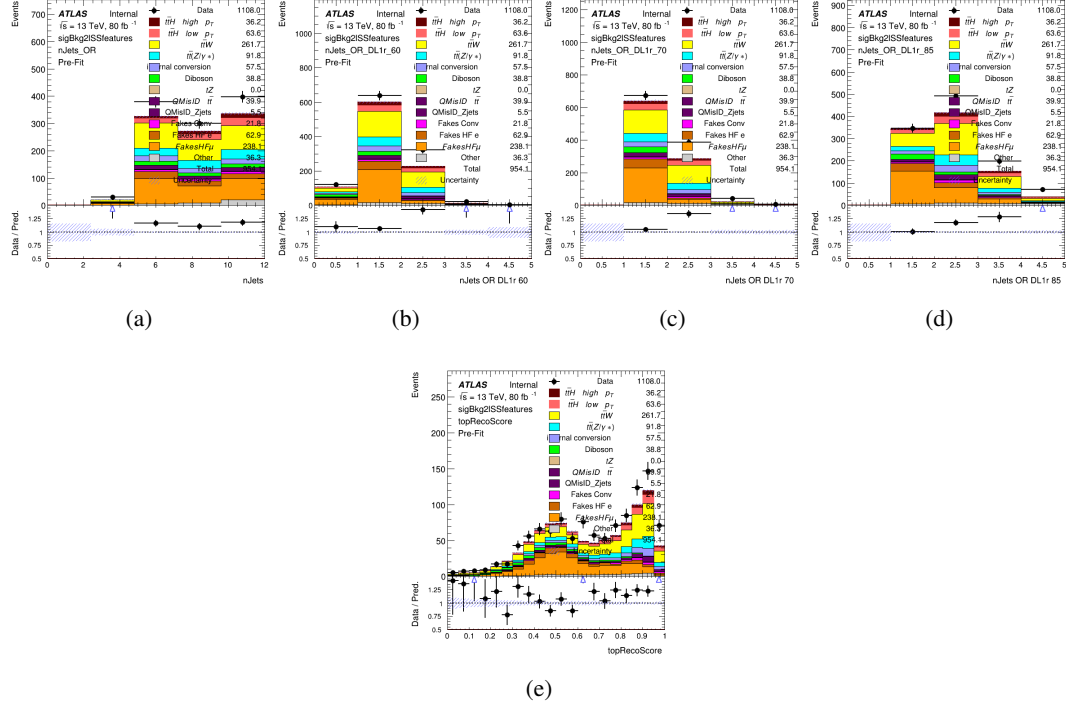
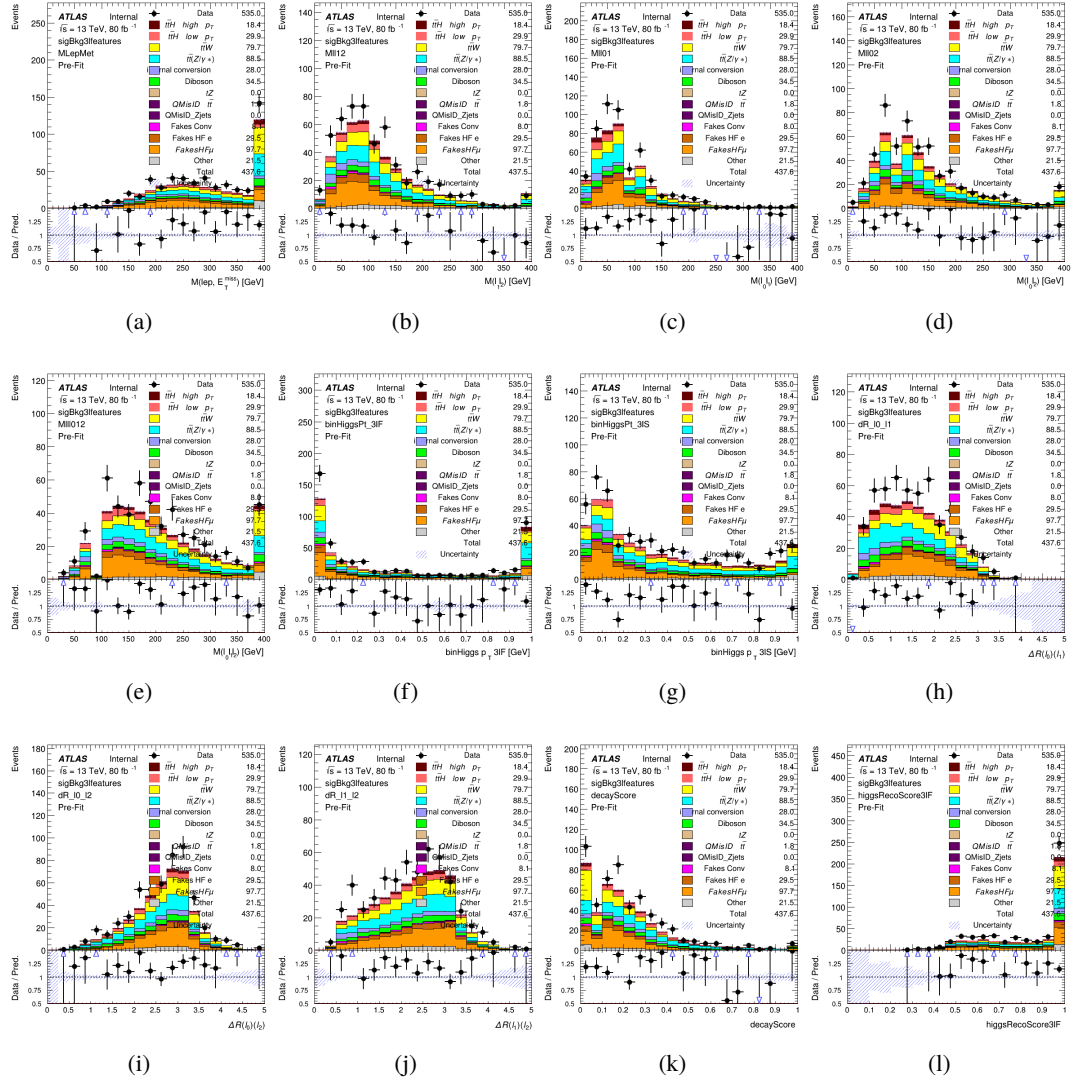


Figure A.21: Input features for sigBkg2lSS

¹⁸⁷⁶ **A.2.2 Background Rejection MVA Features - 3l**

Figure A.22: Input features for `sigBkg3l`

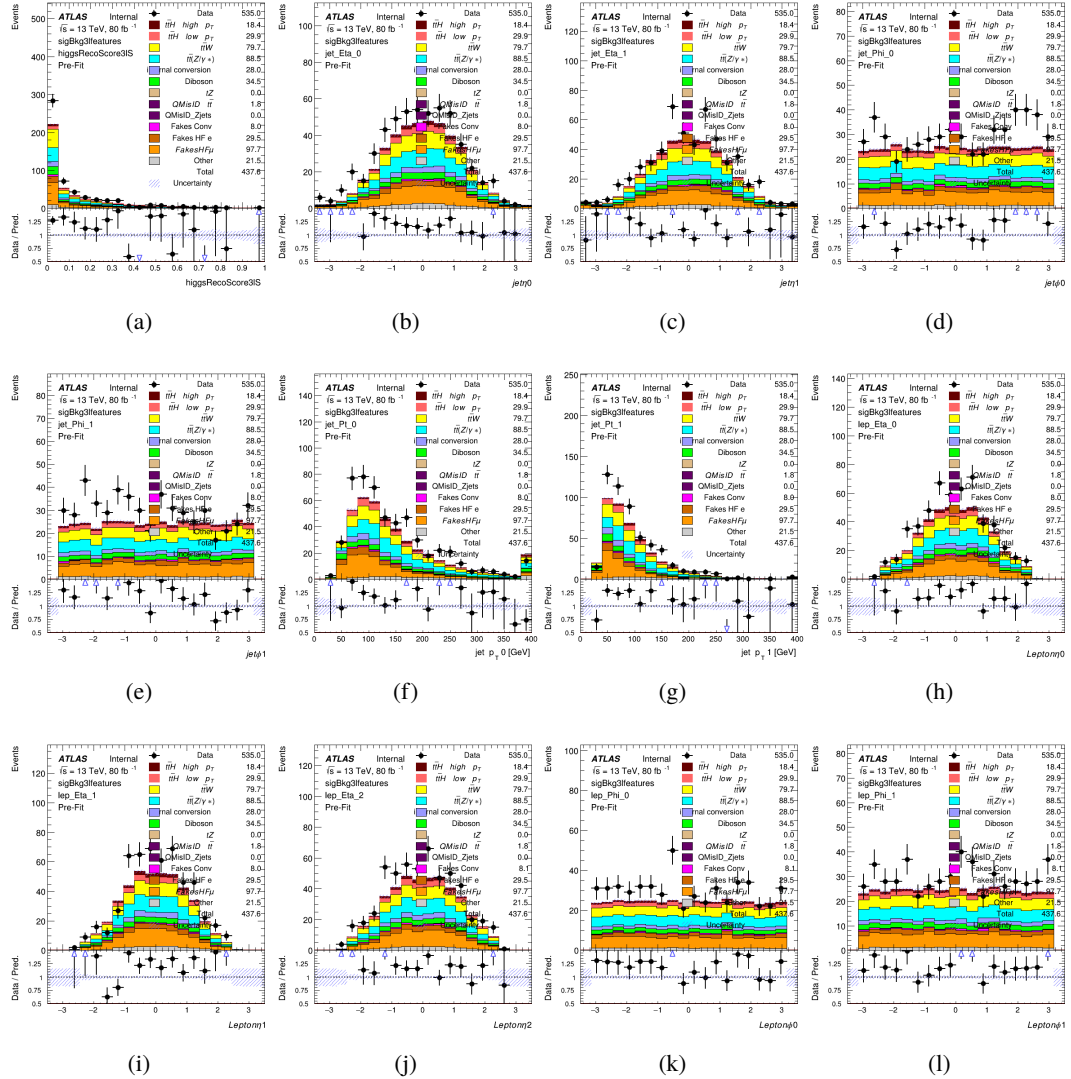
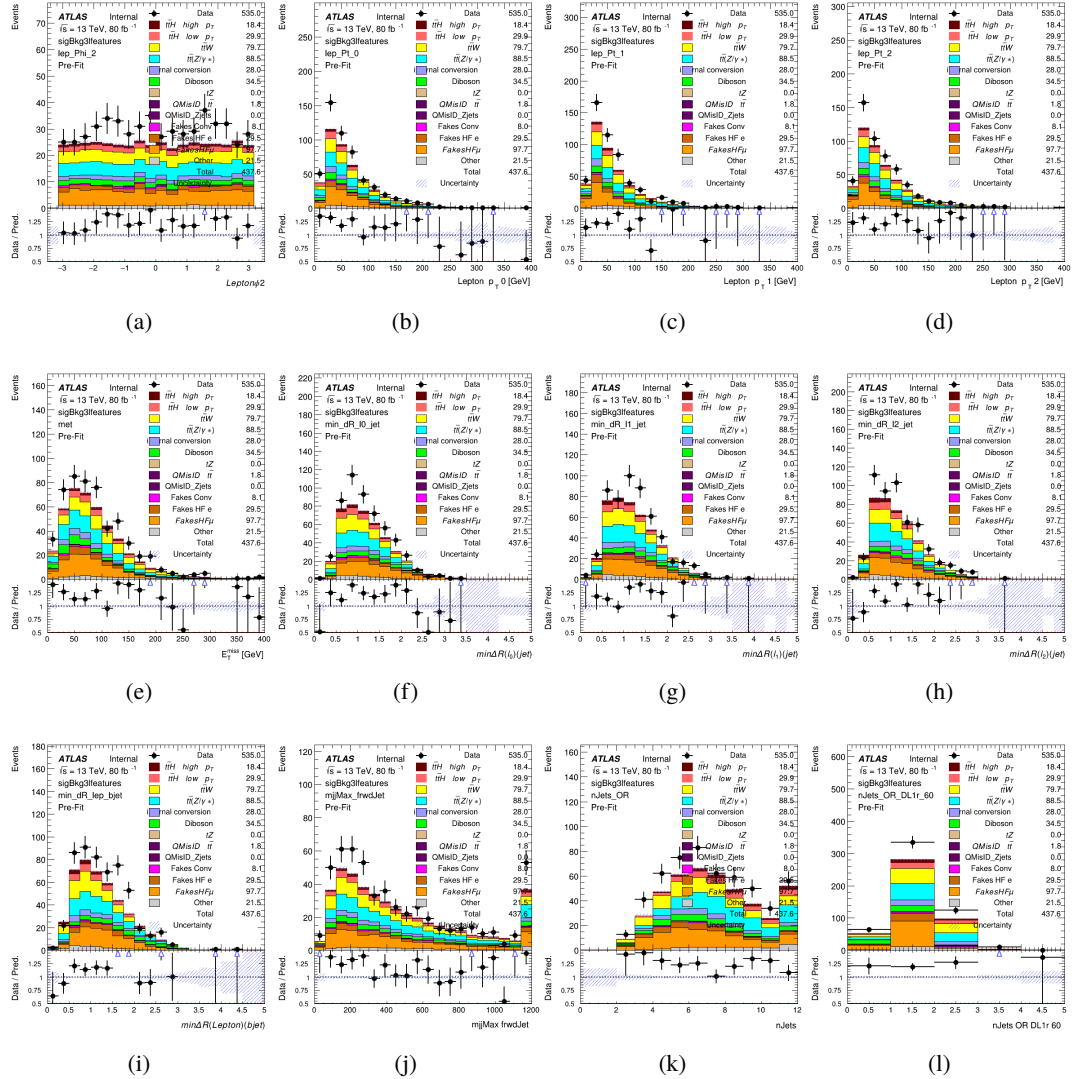


Figure A.23: Input features for sigBkg3l

Figure A.24: Input features for `sigBkg3l`

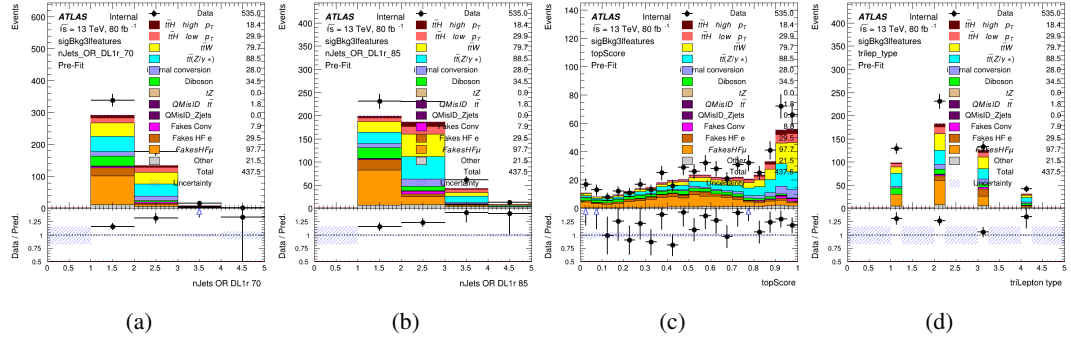


Figure A.25: Input features for sigBkg3l

1877 A.3 Truth Level Studies

1878 Attempts to identify the decay products of the Higgs are motivated by the ability to reconstruct
 1879 the Higgs momentum based on their kinematics. In order to demonstrate that this is case, the
 1880 kinematics of reconstructed objects that are truth matched to the Higgs decay are used as inputs
 1881 to a neural network which is designed to predict of the momentum of the Higgs. This is done in
 1882 the 2lSS channel, as it proves to be the most challenging for p_T reconstruction.

1883 Only leptons and jets which are truth matched to the Higgs are used as inputs for the
 1884 model; events where the lepton and both jets are not reconstructed are not included. The model
 1885 uses the same feature set and network architecture as the p_T prediction model used in the main
 1886 analysis, as described in Section 18.5.1.

1887 The results of the model are summarized below:

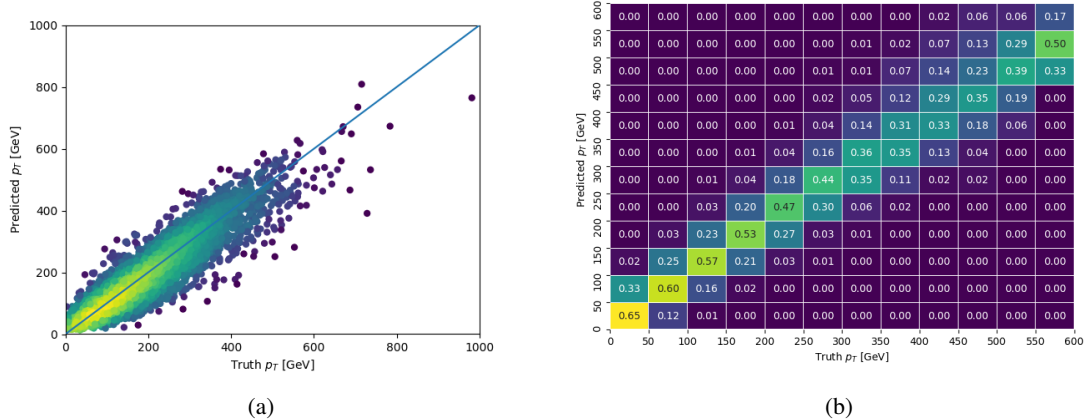


Figure A.26: The regressed Higgs momentum spectrum as a function of the truth p_T for 2lSS $t\bar{H}$ events in (a) a scatterplot, where the color of each point represents the log of the point density, based on Gaussian Kernel Density Estimation, and (b) a histogram where each column has been normalized to one.

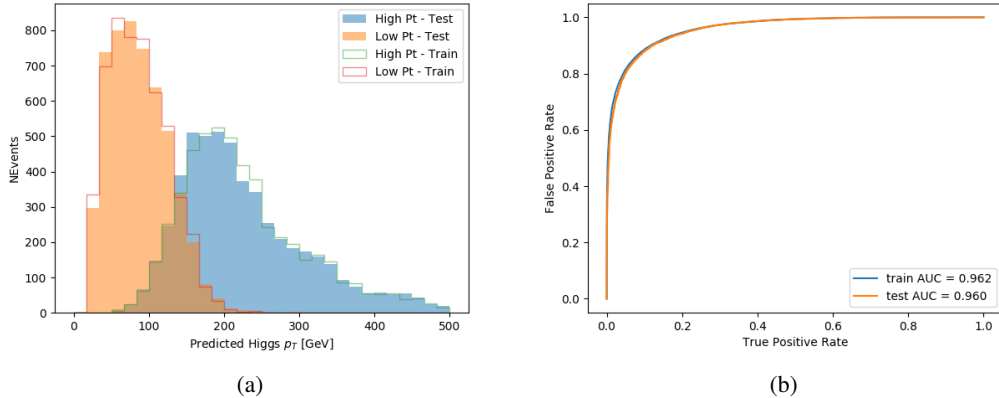


Figure A.27: (a) shows the reconstructed Higgs p_T for 2lSS events with truth $p_T > 150$ GeV and < 150 GeV, while (b) shows the ROC curve for those two sets of events.

1888 Based on the performance of the model, as shown Figures A.26 and A.27, the Higgs
 1889 momentum can be reconstructed with fairly high precision when its decay products are correctly
 1890 identified.

1891 A.4 Alternate b-jet Identification Algorithm

1892 The nominal analysis reconstructs the b-jets by considering different combinations of jets, and
 1893 asking a neural network to determine whether each combination consists of b-jets from top quark
 1894 decays. An alternate approach would be to give the neural network about all of the jets in an event
 1895 at once, and train it to select which two are most likely to be the b-jets from top decay. It was
 1896 hypothesized that this could perform better than considering each combination independently, as
 1897 the neural network could consider the event as a whole. While this is not found to be the case,
 1898 these studies are documented here as a point of interest and comparison.

1899 For these studies, the kinematics of the 10 highest p_T jets in each event are used for
 1900 training. This includes the vast majority of truth b-jets. Specifically the p_T , η , ϕ , E , and DL1r
 1901 score of each jet are used. For events with fewer than 10 jets, these values are substituted with 0.
 1902 The p_T , η , ϕ , and E of the leptons and E_T^{miss} are included as well. Categorical cross entropy is
 1903 used as the loss function.

Table 58: Accuracy of the NN in identifying b-jets from tops in 2lSS events for the alternate categorical method compared to the nominal method.

Channel	Categorical	Nominal
2lSS	70.6%	73.9%
3l	76.1%	79.8%

1904 A.5 Binary Classification of the Higgs p_T

1905 A two bin fit of the Higgs momentum is used because statistics are insufficient for any finer
 1906 resolution. This means separating high and low p_T events is sufficient for this analysis. As
 1907 such, rather than attempting the reconstruct the full Higgs p_T spectrum, a binary classification
 1908 approach is explored.

1909 A model is built to determine whether $t\bar{t}H$ events include a high p_T (>150 GeV) or low
 1910 p_T (<150 GeV) Higgs Boson. While this is now a classification model, it uses the same input
 1911 features described in section 18.5. Binary crossentropy is used as the loss function.

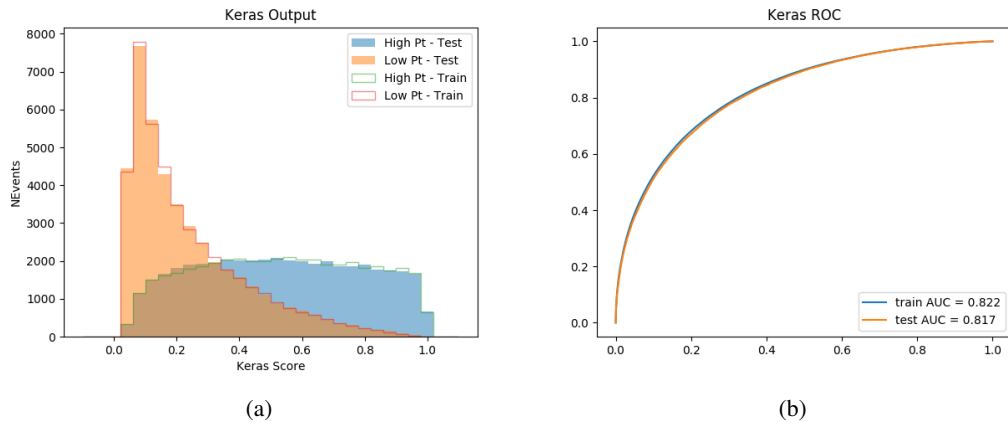


Figure A.28: Output distribution of the NN score for the binary high/low p_T separation model in the 2lSS channel.

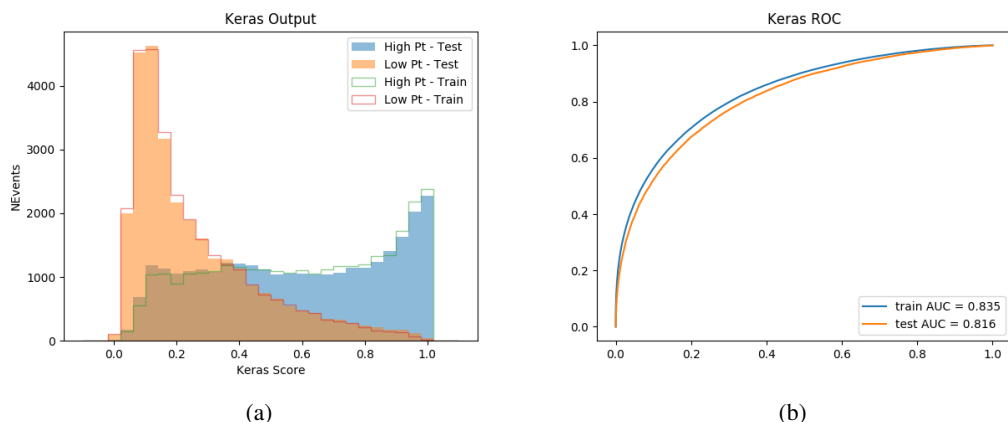


Figure A.29: Output distribution of the NN score for the binary high/low p_T separation model in the 3lS channel.

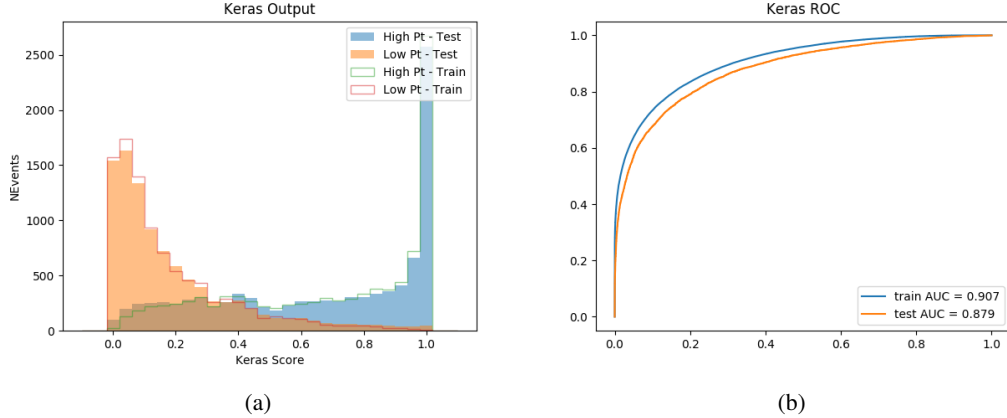


Figure A.30: Output distribution of the NN score for the binary high/low p_T separation model in the 3lS channel.

1912 A.6 Impact of Alternative Jet Selection

1913 A relatively low p_T threshold of 15 GeV is used to determine jet candidates, as the jets originating
1914 from the Higgs decay are found to fall between 15 and 25 GeV a large fraction of the time. The
1915 impact of different jet p_T cuts on our ability to reconstruct the Higgs p_T is explored here.

1916 The models are retrained in the 2lSS channel with the same parameters as those used in the
1917 nominal analysis, but the jet p_T threshold is altered. The performance of the Higgs p_T prediction
1918 models for jet p_T cuts of 20 and 25 GeV are shown below.

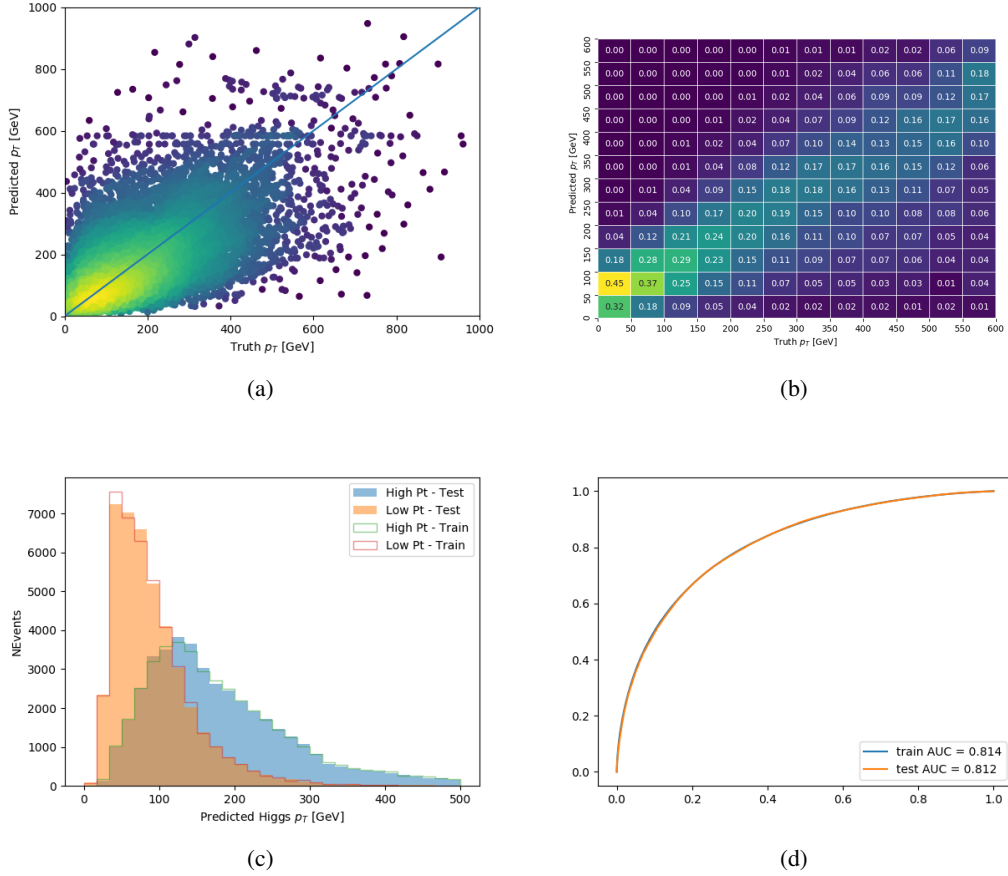
Jet $p_T > 20$ GeV

Figure A.31: Output of the model designed to predict the Higgs momentum in the 2LSS channel, with the jet p_T cutoff used is raised to 20 GeV.

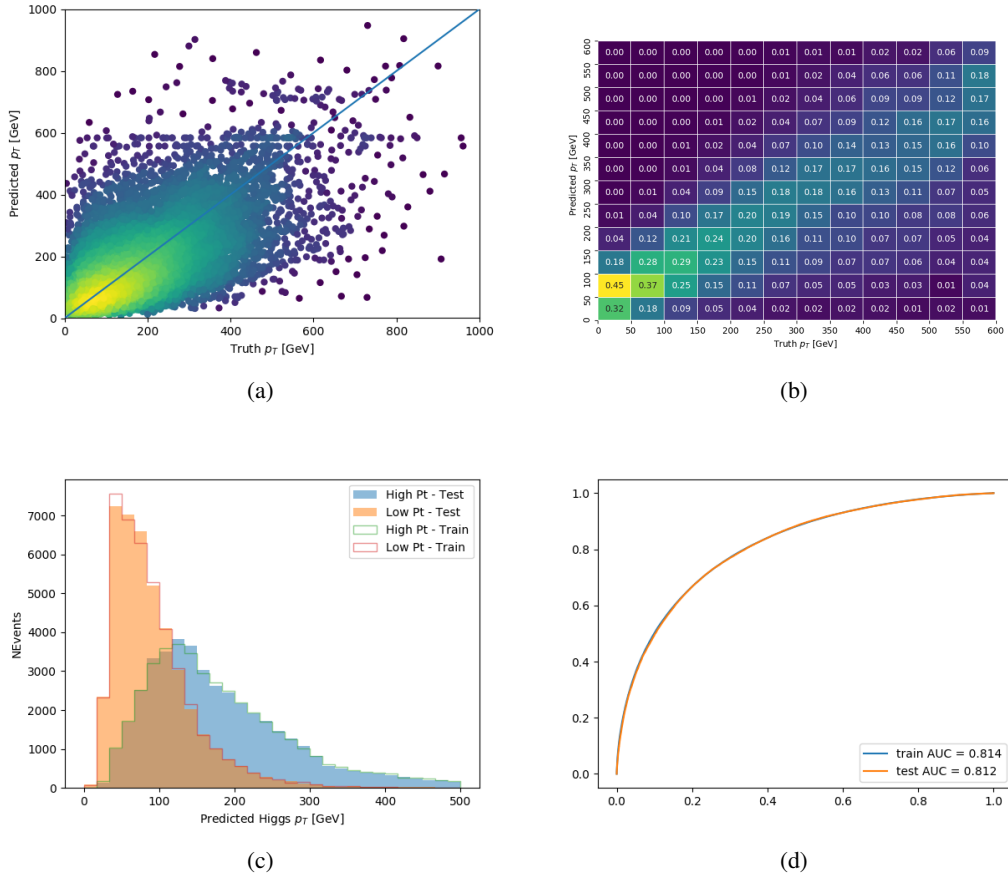
Jet $p_T > 25 \text{ GeV}$ 

Figure A.32: Output of the model designed to predict the Higgs momentum in the 2LSS channel, with the jet p_T cutoff used is raised to 25 GeV.

1919 **B**